INNOVATIVE METHODS FOR NON-INVASIVE MONITORING OF HYDROLOGICAL PROCESSES FROM FIELD TO CATCHMENT SCALE

EDITED BY: Heye Reemt Bogena, Clara Christabel Chew, Andreas Güntner, Martin Schrön and Virginia Strati

PUBLISHED IN: Frontiers in Water

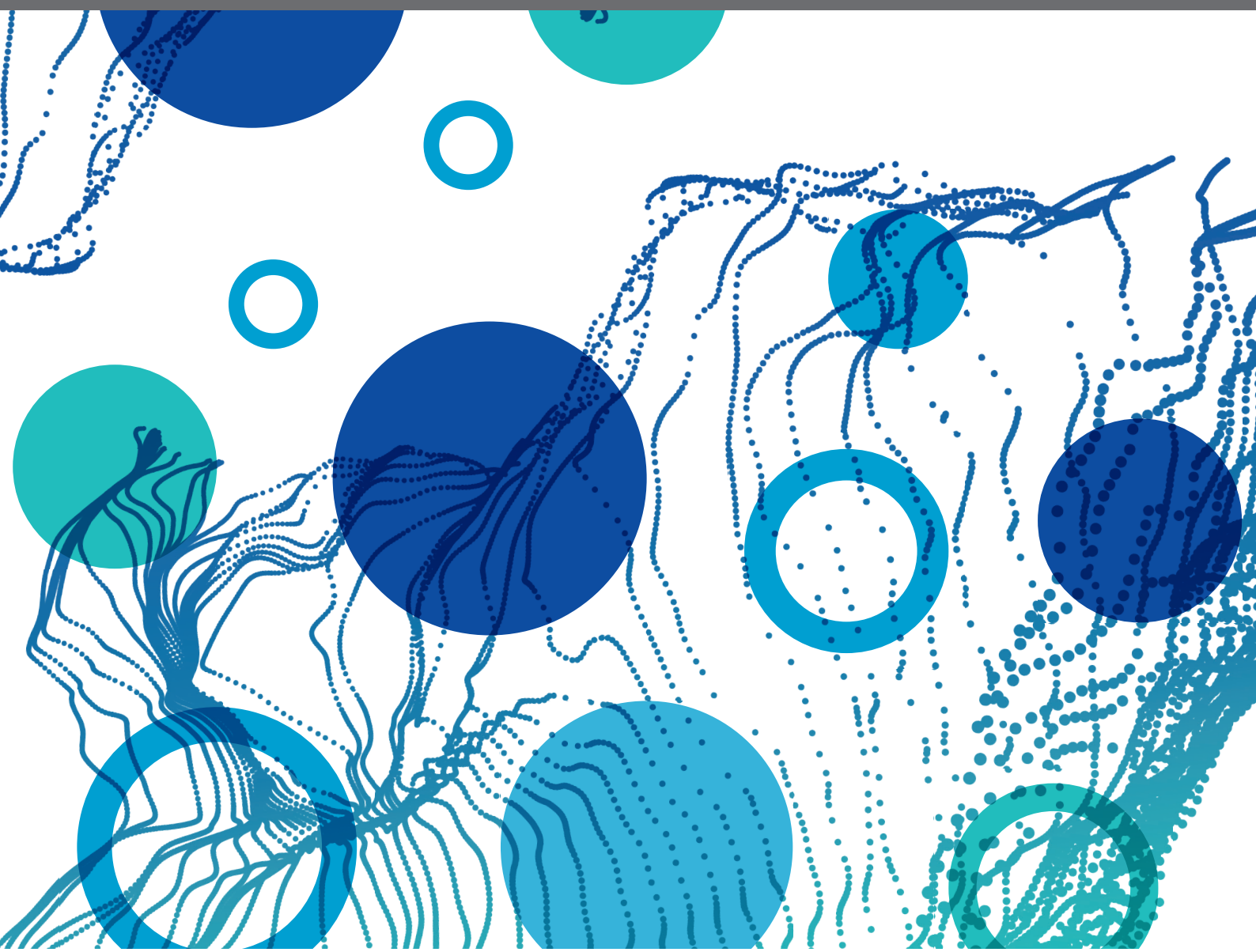

frontiers Research Topics

ISSN 1664-8714
ISBN 978-2-88966-703-1
DOI 10.3389/978-2-88966-703-1

About Frontiers

Frontiers is more than just an open-access publisher of scholarly articles: it is a pioneering approach to the world of academia, radically improving the way scholarly research is managed. The grand vision of Frontiers is a world where all people have an equal opportunity to seek, share and generate knowledge. Frontiers provides immediate and permanent online open access to all its publications, but this alone is not enough to realize our grand goals.

Frontiers Journal Series

The Frontiers Journal Series is a multi-tier and interdisciplinary set of open-access, online journals, promising a paradigm shift from the current review, selection and dissemination processes in academic publishing. All Frontiers journals are driven by researchers for researchers; therefore, they constitute a service to the scholarly community. At the same time, the Frontiers Journal Series operates on a revolutionary invention, the tiered publishing system, initially addressing specific communities of scholars, and gradually climbing up to broader public understanding, thus serving the interests of the lay society, too.

Dedication to Quality

Each Frontiers article is a landmark of the highest quality, thanks to genuinely collaborative interactions between authors and review editors, who include some of the world's best academicians. Research must be certified by peers before entering a stream of knowledge that may eventually reach the public - and shape society; therefore, Frontiers only applies the most rigorous and unbiased reviews.
Frontiers revolutionizes research publishing by freely delivering the most outstanding research, evaluated with no bias from both the academic and social point of view. By applying the most advanced information technologies, Frontiers is catapulting scholarly publishing into a new generation.

What are Frontiers Research Topics?

Frontiers Research Topics are very popular trademarks of the Frontiers Journals Series: they are collections of at least ten articles, all centered on a particular subject. With their unique mix of varied contributions from Original Research to Review Articles, Frontiers Research Topics unify the most influential researchers, the latest key findings and historical advances in a hot research area! Find out more on how to host your own Frontiers Research Topic or contribute to one as an author by contacting the Frontiers Editorial Office: frontiersin.org/about/contact

INNOVATIVE METHODS FOR NON-INVASIVE MONITORING OF HYDROLOGICAL PROCESSES FROM FIELD TO CATCHMENT SCALE

Topic Editors:
Heye Reemt Bogena, Helmholtz-Verband Deutscher Forschungszentren (HZ), Germany
Clara Christabel Chew, University Corporation for Atmospheric Research (UCAR), United States
Andreas Güntner, Helmholtz Centre Potsdam, Germany
Martin Schrön, Helmholtz Centre for Environmental Research (UFZ), Germany
Virginia Strati, University of Ferrara, Italy

Citation: Bogena, H. R., Chew, C. C., Güntner, A., Schrön, M., Strati, V., eds. (2021). Innovative Methods for Non-invasive Monitoring of Hydrological Processes from Field to Catchment Scale. Lausanne: Frontiers Media SA. doi: 10.3389/978-2-88966-703-1

Table of Contents

frontiers in Water

EDITORIAL
published: 16 March 2021
doi: 10.3389/frwa.2021.641458

Editorial: Innovative Methods for Non-invasive Monitoring of Hydrological Processes From Field to Catchment Scale

Heye R. Bogena[1]*, *Virginia Strati*[2,3], *Andreas Güntner*[4,5], *Clara C. Chew*[6] and *Martin Schrön*[7]

[1] Forschungszentrum Jülich GmbH, Institute of Bio- and Geosciences, Agrosphere Institute (IBG-3), Jülich, Germany, [2] Department of Physics and Earth Sciences, Università of Ferrara, Ferrara, Italy, [3] Istituto Nazionale di Fisica Nucleare, Ferrara Section, Ferrara, Italy, [4] GFZ German Research Centre for Geosciences, Potsdam, Germany, [5] Institute of Environmental Science and Geography, University of Potsdam, Potsdam, Germany, [6] Earth Observation and Data Science, University Corporation for Atmospheric Research (UCAR), Boulder, NV, United States, [7] Helmholtz Centre for Environmental Research (UFZ), Leipzig, Germany

Keywords: soil moisture, non-invasive measurement techniques, cosmic-ray neutron probes, field scale, catchment, land surface

Editorial on the Research Topic

Innovative Methods for Non-invasive Monitoring of Hydrological Processes From Field to Catchment Scale

OPEN ACCESS

Edited by:
Luca Brocca,
National Research Council (CNR), Italy

Reviewed by:
Tiejun Wang,
Tianjin University, China
Georgia Papacharalampous,
Roma Tre University, Italy

****Correspondence:***
Heye R. Bogena
h.bogena@fz-juelich.de

Specialty section:
This article was submitted to Water and Hydrocomplexity, a section of the journal Frontiers in Water

Received: *14 December 2020*
Accepted: *16 February 2021*
Published: *16 March 2021*

Citation:
Bogena HR, Strati V, Güntner A, Chew CC and Schrön M (2021) Editorial: Innovative Methods for Non-invasive Monitoring of Hydrological Processes From Field to Catchment Scale. Front. Water 3:641458. doi: 10.3389/frwa.2021.641458

The advancement of hydrological research relies on innovative methods to determine water states and fluxes at high spatiotemporal resolution and covering large areas. The emergence of novel measurement techniques has been and will continue to be an important driver for the ability to analyze hydrological processes and to evaluate process-based models (Bogena et al., 2015). Soil moisture is an important state variable as it controls the exchange of water and energy between the land surface and the atmosphere. Information on soil moisture dynamics is also important for agricultural practices and management, and for a better understanding of biogeochemical, vadose zone, and atmospheric processes. To date, soil moisture is mostly measured with *in-situ* electromagnetic soil moisture sensors for a relatively small volume of soil (Jonard et al., 2018). However, soil moisture shows strong spatial variability at the field scale that is not well-covered by *in-situ* sensors (Vereecken et al., 2014). Recent advances in non-invasive measurement techniques, such as cosmic-ray neutron probes (CRNP), GNSS (global navigation satellite system) reflectometry, ground-based microwave radiometry, gamma-ray monitoring and terrestrial gravimetry, allow continuous non-invasive soil moisture measurements that integrate over the field to the catchment scale (Bogena et al., 2015).

The purpose of this Research Topic is to share recent advances in CRNP-based techniques that detect fluctuations of neutron intensities at the land surface resulting from high-energy particles from space and hydrogen distribution in and on soil at the land surface to provide continuous non-invasive measurements of soil moisture dynamics from the field to catchment scale. This Research Topic features seven articles, which are briefly introduced in the following:

Franz et al. applied established data analysis approaches to deriving novel CRNP data products: smoothed soil moisture time series, landscape average rainfall, and root zone soil moisture. The authors take a significant step forward by enhancing CRNS soil moisture data to provide stakeholders with value-added data products. The presented results could serve as a critical step toward the adoption of CRNP data for practical applications.

Jakobi et al. quantified the uncertainty in soil moisture estimation from cosmic ray neutron measurements with an easy-to-use 3rd order Taylor expansion approach. This approach is

particularly useful for neutron rover measurements, since the soil moisture estimates obtained with this approach are typically more uncertain than those obtained with stationary CRNPs. Thus, the presented method has great potential for planning and evaluating rover experiments and to find a suitable trade-off between measurement accuracy, aggregation, and the associated spatial resolution of the resulting soil moisture products. The authors also published a companion Corrigendum paper (Jakobi et al.).

Bogena et al. used long-term CRNP measurements in the Pinios Hydrologic Observatory (PHO), Greece, to test different methods for converting neutron count rates to snow pack characteristics. These methods include linear regression methods based on thermal and epithermal neutrons, the standard N0-calibration function, and a physics-based calibration approach. They found that the N0-calibration function and the physics-based calibration performed the best and the ratio of thermal to epithermal neutrons performed the worst. They concluded that CRNP-based SWE (snow water equivalent) determination at the field scale is a potential alternative to established methods based on point-based snow depth observations.

Nasta et al. compared data from CRNP and SoilNet wireless *in-situ* sensor networks at two sites in the Alento catchment, Italy. They found discrepancies in the data of the two sensor types related to the effects of the time-varying vertical measurement footprint of the CRNP. Furthermore, they showed that the bimodality of the Soil Moisture Index (SMI) derived from SoilNet data was not well-captured by CRNP and that SMI contrasts between the two different test sites can be explained by soil texture or terrain characteristics. Finally, the authors also derived field-scale water retention functions from CRNP and SoilNet data for the analysis of hydrological processes.

Weimar et al. examined critical properties of neutron detectors specifically designed for CRNP applications. The authors introduced a large-scale detector setup by optimizing the moderator thickness and the spatial dimensions of the moderator housing in order to increase the count rate. They also discussed the effect of non-neutron radiation and its influence on the overall signal quality. The novel detection system achieves count rates that are much higher than usual systems with higher signal-to-noise ratio. Moreover, the lower relative statistical uncertainty leads to more precise soil moisture measurements at short time scales.

González-Sanchis et al. compared the capability of *in-situ* soil sensors and CRNP in assessing soil water dynamics as a key variable that reflects the effects of forest management in a semi-arid environment. To this end, two experimental plots were established in Sierra Calderona, Spain, in a post-fire regeneration Aleppo pine forest. They found that the performance of CRNP was better under semi-arid than under extremely dry conditions. Forest biomass and litter layer led to an overestimation of CRNP-derived soil moisture. Both sensor systems were capable to reproduce tree transpiration affected by soil moisture, environmental variables, and thinning, with CRNP being affected by atmospheric forcing.

Köhli et al. proposed a new analytical method to estimate the neutron response to soil moisture and air humidity. Comparing two Monte-Carlo neutron transport simulations, URANOS and MCNP, their findings revealed a systematic deviation of the standard relationship between the neutron count rate and soil moisture especially for extremely dry conditions. The authors also discussed the importance of detector-specific response functions, various model concepts and atmospheric humidity. The new analytical relationship has been tested at two exemplary CRNP monitoring sites and it outperformed the hitherto standard approach.

We are convinced that the presented advances in CRNP-based techniques will improve the description of local-scale processes related to hydrological fluxes and storage variations, which is of key importance to reduce the large uncertainties that are still present in large-scale models used to predict soil water dynamics.

AUTHOR CONTRIBUTIONS

HB had the idea for this Research Topic and has invited the guest editors. HB, MS, VS, AG, and CC invited authors and did article review and editing. HB wrote the editorial, which was then edited by MS, VS, AG, and CC. All authors contributed to the article and approved the submitted version.

ACKNOWLEDGMENTS

We would like to thank the authors for their contributions and patience, the many reviewers for their time and effort, the Specialty Chief Editor, Harrie-Jan Hendricks Franssen, for organizing the entire review process, and the Frontiers editorial team for their administrative and logistical support throughout the process.

REFERENCES

Bogena, H. R., Huisman, J. A., Hübner, C., Kusche, J., Jonard, F., Vey, S., et al. (2015). Emerging methods for non-invasive sensing of soil moisture dynamics from field to catchment scale: a review. *WIREs Water* 2, 635–647. doi: 10.1002/wat2.1097

Jonard, F., Bogena, H., Caterina, D., Garré S., Klotzsche, A., Monerris, A., et al. (2018). "Ground-based soil moisture determination," in *Observation and Measurement*. eds X. Li and H. Vereecken (Berlin; Heidelberg: Springer, Ecohydrology). doi: 10.1007/978-3-662-47871-4_2-2

Vereecken, H., Huisman, J. A., Pachepsky, Y., Montzka, C., van der Kruk, J., Bogena, H., et al. (2014). On the spatio-temporal dynamics of soil water content at the field scale. *J. Hydrol.* 516, 76–96. doi: 10.1016/j.jhydrol.2013.11.061

Conflict of Interest: The authors declare that the research was conducted in the absence of any commercial or financial relationships that could be construed as a potential conflict of interest.

frontiers in Water

ORIGINAL RESEARCH
published: 16 April 2020
doi: 10.3389/frwa.2020.00009

Practical Data Products From Cosmic-Ray Neutron Sensing for Hydrological Applications

Trenton E. Franz[1], Ammar Wahbi[2,3], Jie Zhang[2,4], Mariette Vreugdenhil[5,6], Lee Heng[2], Gerd Dercon[2], Peter Strauss[7], Luca Brocca[8] and Wolfgang Wagner[6]*

[1] School of Natural Resources, University of Nebraska-Lincoln, Lincoln, NE, United States, [2] Soil and Water Management & Crop Nutrition Subprogramme, Joint FAO/IAEA Division of Nuclear Techniques in Food and Agriculture, International Atomic Energy Agency (IAEA), Vienna, Austria, [3] Arid Land Research Center, Tottori University, Tottori, Japan, [4] College of Land Science and Technology, China Agricultural University, Beijing, China, [5] Centre for Water Resource Systems, Vienna University of Technology (TU Wien), Vienna, Austria, [6] Department of Geodesy and Geoinformation, Vienna University of Technology (TU Wien), Vienna, Austria, [7] Federal Agency for Water Management, Institute for Land and Water Management Research, Petzenkirchen, Austria, [8] National Research Council, Research Institute for Geo-Hydrological Protection, Perugia, Italy

OPEN ACCESS

Edited by:
Heye Reemt Bogena, Helmholtz Association of German Research Centers (HZ), Germany

Reviewed by:
Martin Schrön, Helmholtz Centre for Environmental Research (UFZ), Germany
Rui Jin, Northwest Institute of Eco-Environment and Resources (CAS), China

****Correspondence:***
Trenton E. Franz
tfranz2@unl.edu

Specialty section:
This article was submitted to Water and Hydrocomplexity, a section of the journal Frontiers in Water

Received: *22 October 2019*
Accepted: *24 March 2020*
Published: *16 April 2020*

Citation:
Franz TE, Wahbi A, Zhang J, Vreugdenhil M, Heng L, Dercon G, Strauss P, Brocca L and Wagner W (2020) Practical Data Products From Cosmic-Ray Neutron Sensing for Hydrological Applications. Front. Water 2:9. doi: 10.3389/frwa.2020.00009

The Cosmic-Ray Neutron Sensor (CRNS) technique for estimating landscape average soil water content (SWC) is now a decade old and includes many practical methods for implementing measurements, such as identification of detection area and depth and determining crop biomass water equivalent. However, in order to maximize the societal relevance of CRNS SWC data, practical value-added products need to be developed that can estimate both water flux (i.e., rainfall, deep percolation, evapotranspiration) and root zone SWC changes. In particular, simple methods that can be used to estimate daily values at landscape average scales are needed by decision makers and stakeholders interested in utilizing this technique. Moreover, landscape average values are necessary for better comparisons with remote sensing products. In this work we utilize three well-established algorithms to enhance the usability of the CRNS data. The algorithms aim to: (1) temporally smooth the neutron intensity and SWC time series, (2) estimate a daily rainfall product using the Soil Moisture 2 Rain (SM2RAIN) algorithm, and (3) estimate daily root zone SWC using an exponential filter algorithm. The algorithms are tested on the CRNS site at the Hydrological Open Air Laboratory experiment in Petzenkirchen, Austria over a 3 years period. Independent observations of rainfall and point SWC data are used to calibrate the algorithms. With respect to the neutron filter, we found the Savitzky-Golay (SG) had the best results in preserving the amplitude and timing of the SWC response to rainfall as compared to the Moving Average (MA), which shifted the SWC peak by 2–4 h. With respect to daily rainfall using the SM2RAIN algorithm, we found the MA and SG filters had similar results for a range of temporal windows (3–13 h) with cumulative errors of $<9\%$ against the observations. With respect to daily root zone SWC, we found all filters behaved well (Kling-Gupta-Efficiency criteria > 0.9). A methodological framework is presented that summarizes the different processes, required data, algorithms, and products.

Keywords: soil water, agriculture, root zone, landscape average, rainfall

INTRODUCTION

The Cosmic-Ray Neutron Sensor (CRNS) is an *in situ* technique that is unique in its capability to estimate soil water content (SWC) at scales from ∼1 to 10 ha using stationary and mobile platforms (c.f. Zreda et al., 2008, 2012; Desilets et al., 2010; Franz et al., 2015; Kohli et al., 2015; Andreasen et al., 2017). Several studies have used CRNS data to support precision agriculture (Finkenbiner et al., 2019), catchment hydrology (Fersch et al., 2018), snow hydrology (Schattan et al., 2017), land surface modeling (Rosolem et al., 2014; Baatz et al., 2017; Lawston et al., 2017), validation of remote sensing products (Montzka et al., 2017; Babaeian et al., 2018), and understanding vegetation dynamics (Franz et al., 2013). In order to maximize the societal and scientific relevance of SWC data (Vereecken et al., 2008), practical value-added products need to be developed that can estimate both water flux and root zone SWC changes. In particular, simple methods that can be used to estimate daily values at landscape average scales are needed by stakeholders as well as for better comparisons with remote sensing products (e.g., soil moisture products from Metop Advanced SCAT Scatterometer (ASCAT), NASA's Soil Moisture Active Passive mission (SMAP), ESA's Soil Moisture Ocean Salinity mission (SMOS), and Sentinel-1, see McCabe et al. (2017) for details on current and planned missions for measuring hydrologic fluxes and state variables).

While remote sensing has made significant progress in recent years (McCabe et al., 2017), significant gaps in spatial and temporal resolution and latency of images makes practical applications of retrieved hydrologic products challenging for stakeholders. For example, microwave instruments like ASCAT, SMOS, and SMAP offer a shallow (0 to ∼3 cm, Jackson et al., 1997) SWC estimate at a snapshot in time and at a spatial resolution of tens of kilometers every 1–3 days. Sentinel-1 provides SWC estimates at a spatial resolution of 1 km and temporal resolution of 1.5–4 days over Europe (Bauer-Marschallingere et al., 2019). However, this is not available globally and temporal resolution of Sentinel-1 is decreased outside of Europe. Blending of different datasets can further increase the spatial and temporal resolution (e.g., SMAP and Sentinel for a 3 km product every 2–3 days). A critical and likely remaining gap for agricultural stakeholders, is providing daily field and subfield scale (0.1–10 ha) root zone SWC data (0 to ∼1 m). With the inability of satellites to directly estimate root zone SWC, indirect methods using a combination of satellites, ground sensors, and models are needed to produce root zone SWC data.

The CRNS technology offers part of the solution to fill this critical measurement gap at the field scale given its ability to measure landscape average SWC over hundreds of meters horizontally and tens of centimeters vertically. Over the past decade since its development CRNS theory and best practices for equipment have greatly matured. Nonetheless, practical implementation of using the CRNS data by stakeholders requires further developing value-added products. In this methodological study, we will apply and evaluate three well-established algorithms used within the science community to increase the practical use of CRNS data. The three algorithms aim to: (1) temporally smooth the neutron intensity and SWC time series, (2) estimate a daily rainfall product using the Soil Moisture 2 Rain (SM2RAIN) algorithm (Brocca et al., 2014), and (3) estimate daily root zone SWC using an exponential filter algorithm (Wagner et al., 1999; Albergel et al., 2008). The remainder of the manuscript is organized as follows. In section Materials and methods the three algorithms will be described in detail. In section Results the algorithms will be tested on the CRNS site established in 2013 at the Hydrological Open Air Laboratory (HOAL) in Petzenkirchen, Austria (Blöschl et al., 2016) using independent observations of rainfall and a network of *in situ* point SWC data. Finally, in section Summary and Conclusions, we will present a summary and future recommendations.

MATERIALS AND METHODS

In order to provide the reader a clear outline of the manuscript **Figure 1** provides a methodological framework. The framework describes the various processes, data sources, algorithms, and value-added products covered in this study.

Study Area

A CRNS (Model # CRS 1000/B, HydroInnova LLC, Albuquerque, NM, USA) was installed at the study area in northeast Austria (48.1547°N, 15.1483°E, elevation 277 m, average slope of 8%) on 11 December 2013 and has continuously operated since (Franz et al., 2016). The study site, the Hydrological Open Air Laboratory (HOAL) (Blöschl et al., 2016), which is a cooperation project between the Federal Agency for Water Management (BAW Petzenkirchen) and the Vienna University of Technology (TU Wien), is located in Petzenkirchen, about 100 km west of Vienna. HOAL receives an annual average 823 mm of rainfall, the average annual temperature is 9.5°C, and the mean annual evapotranspiration estimated by the water balance is 628 mm/yr (1990–2014) (Blöschl et al., 2016). The research station is located in an undulating agricultural landscape, characterized by Cambisols (56%), Planosols (21%), Anthrosols (17%), Gleysols (6%), and Histosols (<1%) (United Nations, 2007). Infiltration capacities tend to be medium to low, water storage capacities tend to be high, and shrinking cracks may occur in summer due to high clay contents (Blöschl et al., 2016). The main crops are winter wheat, barley, maize, and rape. The land use at the study site consists of various parcel sizes making up a patchwork of different crops. As previously summarized by Franz et al. (2016), the location of the CRNS within the various land use parcels makes landscape average measurements of SWC challenging (Franz et al., 2016). Full details of the study site, available datasets, overarching research questions, and specific hypotheses can be found in Blöschl et al. (2016).

A network of Time-Domain Transmissivity (TDT) sensors (SPADE, Julich, Germany) were installed in the second half of 2013 and available for a portion of 2014. The TDT sensors record hourly SWC at a point and were installed at 31 sites distributed around the study area (Blöschl et al., 2016; Franz et al., 2016). At each site four TDT sensors were

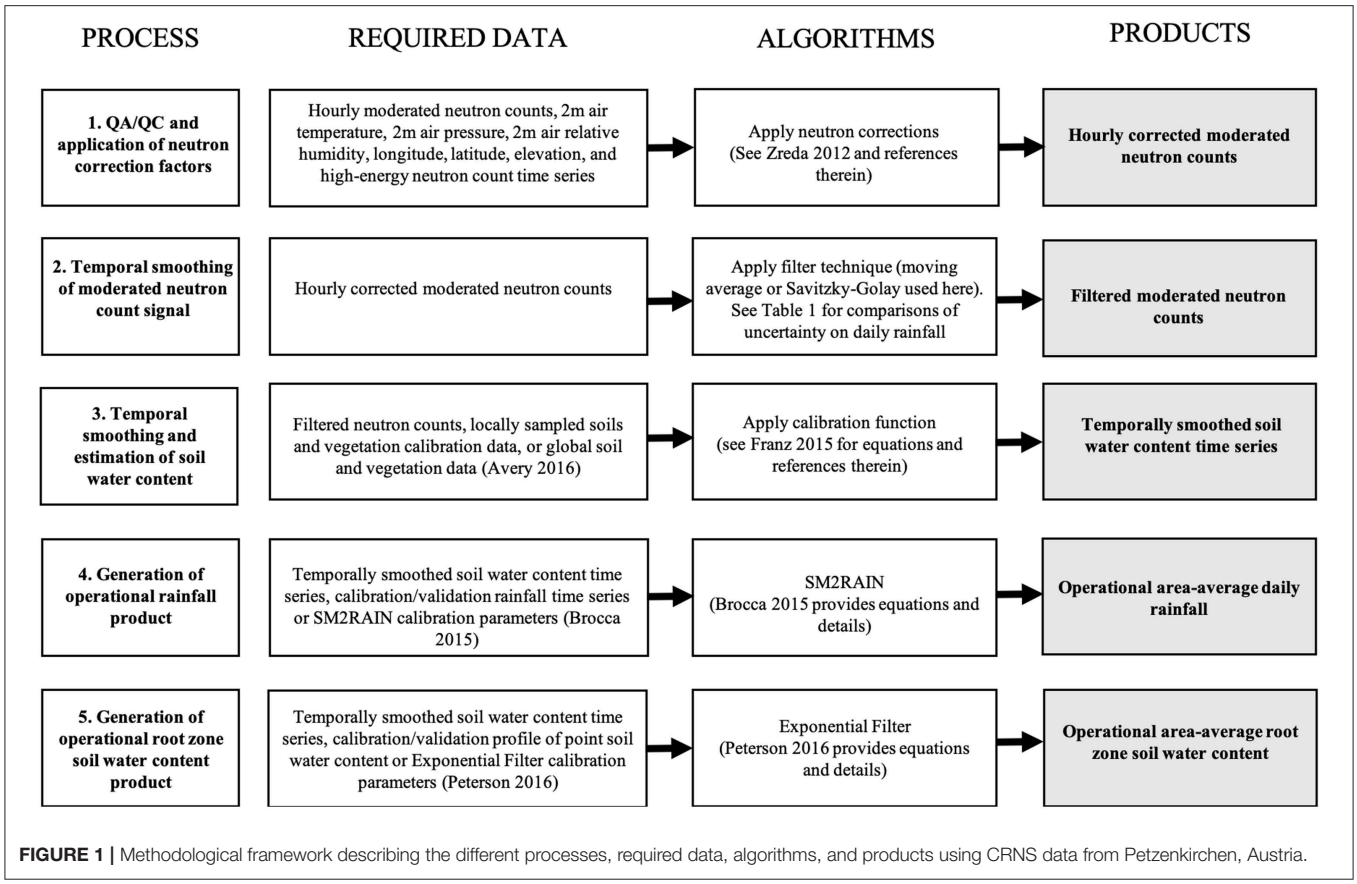

FIGURE 1 | Methodological framework describing the different processes, required data, algorithms, and products using CRNS data from Petzenkirchen, Austria.

installed horizontally at four depths (5, 10, 20, and 50 cm). Depending on routine agricultural operations and location of the stations, 11 TDT stations were removed at various times throughout the year. In this study we only use the sensors which are located within the footprint of the CRNS. **Figures 2A–D** illustrates the individual TDT site time series and the large degree of spatial variation in space and time at the site. In order to compare the TDT data against the CRNS neutron data, the spatial average of each sensor depth is illustrated in **Figure 2E** (ignoring sensor locations with time gaps). The daily rainfall onsite is shown in **Figure 2F**. Lastly, weighted sums over the profile from 0–30 to 0–60 cm are computed based on sensor insertion depth. In order to compute the profile weighted averages first the arithmetic mean from all locations was computed by depth. Next a weight was assigned between the midpoint for each successive TDT sensor depth, that is a weight of 7.5 for the 5 cm sensor, 7.5 for the 10 cm probe, and 15 for the 20 cm sensor for the 0–30 cm profile average. The same process was repeated using the 50 cm sensor for the 0–60 cm profile average. The profile sums are used in this study as calibration for the exponential filter algorithm.

Temporal Filtering of CRNS Data

The CRNS technique works by counting low-energy neutrons (∼0.5–1000 eV) from a moderated detector over a certain time interval (typically 1 h for stationary sensors) (see Zreda et al., 2008, 2012; Desilets et al., 2010; Andreasen et al., 2017 for details). The uncertainty of CRNS neutron count rates follows Poisson statistics (Knoll, 2000; Zreda et al., 2012), where the standard deviation is equal to the square root of the total counts. For example, 1,000 counts per hour (cph) would have an uncertainty of 31.6 cph or 3.16%. Because of the inherent counting statistics, plots of hourly neutron counts and SWC appear noisy with random fluctuations around a mean value. In order to produce a smoothed SWC time series, a temporal filter is applied to the corrected neutron data. Following the standard set of corrections for time-varying barometric pressure, high-energy incoming neutron intensity, and atmospheric water vapor (Zreda et al., 2012; Rosolem et al., 2013), a time series filter can be applied. Here we compared the 1 h corrected neutron counts vs. a Moving Average (MA) filter with different temporal windows (3–24 h) and vs. a Savitzky-Golay (SG) filter with different ordered polynomials (1st−3rd order) and temporal windows (3–25 h) (see Savitzky and Golay, 1964; Orfanidis, 1996 for full details). In general, the 1 h neutron count data had large fluctuations for this site, the MA filter is simple and widely used but the smoothed data distorted the location of the neutron trough after a rainfall event, thus affecting the timing and magnitude of the SWC peak. The SG filter was evaluated here because it is known for better balancing the degree of smoothing while minimizing the distortion of the sharp decreases/increases in the data, which

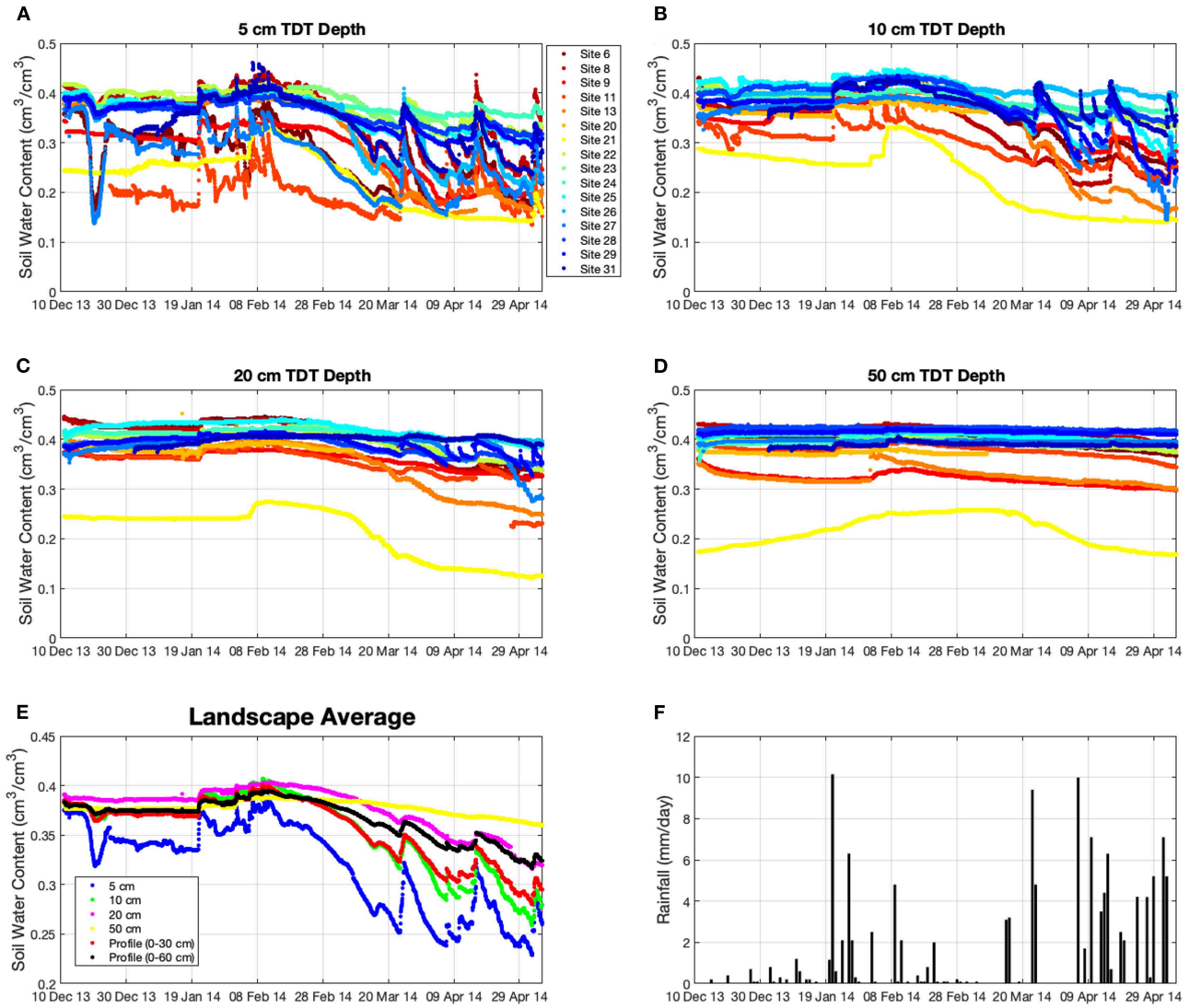

FIGURE 2 | Time series of TDT probes organized by depth **(A–D)** and by site location illustrating the wide range of SWC encountered. All TDT sensors were installed in the second half of 2013 but removed over time on different dates due to the various soil cultivation and harvest times of each of the land use parcels. See Figure 2a in Franz et al. (2016) for spatial locations. **(E)** Time series of landscape average SWC by TDT depth and profile weighted averages of 0–30 and 0–60 cm. **(F)** Time series of daily rainfall data.

is useful in preserving the amplitude and timing of neutron count decreases following a rain event. In this work we will quantify how the different neutron filter methods translate into hourly SWC, daily rainfall with the SM2RAIN algorithm and root zone SWC using the exponential filter.

Estimation of Landscape Average Rainfall Using SM2RAIN Algorithm

Given the challenge of estimating landscape average rainfall from ground based observations and top down approaches using satellites, additional sources of rainfall data are greatly needed (McCabe et al., 2017). One recently proposed approach is the Soil Moisture 2 Rain (SM2RAIN) algorithm (http://hydrology.irpi.cnr.it/research/sm2rain/ and Brocca et al., 2014; Chiaravalloti et al., 2018). SM2RAIN assumes that the soil acts like a bucket and that measurements of SWC can be inverted to estimate rainfall from a bottom up approach (Brocca et al., 2014). Following the bucket analogy the following equations can be used to describe the mass balance:

$$Z^* \frac{ds(t)}{dt} = p(t) - r(t) - e(t) - g(t) \quad (1)$$

where Z^* is the soil water capacity equal to soil depth times porosity, $s(t)$ is relative soil moisture (=SWC/porosity) as function of time t, $p(t)$ is precipitation, $r(t)$ is surface runoff, $e(t)$ is evaporation, and $g(t) = as(t)^b$ is deep drainage and a and b are calibration coefficients. During rainfall, surface runoff

and evapotranspiration are assumed to be negligible at the daily timescale. This assumption will be discussed more in section Limitations of Study. Thus, precipitation can be estimated as:

$$p(t) = Z^* \frac{ds(t)}{dt} + as(t)^b \quad (2)$$

thereby leaving three parameters to calibrate (Z^*, a, b) using of observations of SWC and rainfall.

Given the wide array of SWC products at different scales the SM2RAIN algorithm has been applied and validated across time and space. By using the European Space Agency Climate Change Initiative (ESA CCI) soil moisture product, Ciabatta et al. (2018) developed a global scale SM2RAIN-CCI rainfall product that has been compared with five different global rainfall products showing good correlation at 1° spatial resolution and 5 day accumulated totals against gridded rain gauge-based rainfall observations (assumed to be the actual true rainfall). Spatial correlations range from 0.3 to 0.8 across a wide portion of the global land surface. At finer spatial (12.5 km) and temporal (1-day) resolutions, the SM2RAIN algorithm has been recently applied to the EUMETSAT Satellite Application Facility on Support to Operational Hydrology and Water Management (HSAF) soil moisture product (Brocca et al., 2019) showing better performance than a state-of-the-art satellite rainfall product (i.e., Global Precipitation Measurement, GPM) over Africa and South America. From a study in Italy, Chiaravalloti et al. (2018) compared *in-situ* rain gauges vs. satellite remote sensing products obtaining a correlation of around 0.7 for 24-h periods. Brocca et al. (2015) applied the SM2RAIN algorithm to *in situ* soil moisture observations across Europe, but the algorithm has been never applied to CRNS. Therefore, the potential of the method to obtain landscape average rainfall estimates at field scale is tested here for the first time.

Estimation of Root Zone Soil Water Content Using an Exponential Filter

A common problem with remotely sensed SWC data is that only the near surface (∼0–3 cm) is directly observed using microwave wavelengths (Jackson et al., 1997). In order for these satellite products to be useful, SWC storage must be extrapolated across a plant root zone. This extrapolation can be accomplished in a number of ways using simple linear interpolation to a full data assimilation approach using a physically based water and energy balance model. However, given the computational demands, lack of boundary conditions, initial conditions, and model parameters this approach can be challenging. A fairly simple method to do root zone SWC extrapolation uses the idea of an exponential filter to solve for the time delay between surface soil response and deeper soils (Wagner et al., 1999). The exponential filter has been used with great success for remote sensing products, *in-situ* point scale networks (Paulik et al., 2014; Wang et al., 2017), and recently CRNS (Peterson et al., 2016).

In this study, we utilized the continuous CRNS SWC data, and assumed a depth of ∼0-20 cm based on expected effective depth of the site (see Franz et al., 2012a; Kohli et al., 2015 for details on effective depth calculation). In addition, by using the seasonal TDT data from 2014 at Petzenkirchen we can parameterize the exponential filter approach, thus being able to produce an operational root zone storage product from the CRNS data henceforth. The exponential filter model considers the water balance model of a two-layer soil profile. Layer 1 has historically been set to the depth of the remote sensing product (0–3 cm) but 0–20 cm will be used here for CRNS applications. Layer 2 has been set to a root zone depth around ∼1 m depending on vegetation type and local soil depths. The exponential filter approach is flexible allowing the user to specify a desired depth, given the stated assumptions about the method remain valid. Here, we will assume layer 1 is the surface layer (provided by the continuous CRNS SWC data ∼0–20 cm, denoted by SWC_1), and layer 2 is the lower soil layer of interest (here an integrated root zone storage estimate constrained by the depth of the TDT sensors in order to calibrate the exponential filter approach). For demonstration purposes here a layer 2 depth of 0–30 and 0–60 cm will be provided in the following examples. Having two different root zone depths may be important to relate the available SWC with different growth stages of crop over the growing season. SWC of layer 2 (denoted by SWC_2) is described as:

$$L\frac{dSWC_2}{dt} = C(SWC_1 - SWC_2) \quad (3)$$

where t is time, L is the depth of layer 2, and C is an area-representative pseudo-diffusivity constant. This approach assumes that plant transpiration and drainage losses from the lower layer are negligible, and that hydraulic diffusivity between the soil layers is constant (Wagner et al., 1999). These limitations will be further discussed in section Limitations of Study. Equation (3) can be solved using a recursive formulation following (Albergel et al., 2008):

$$SWI_{2(t)} = SWI_{2(t-1)} * (1 - K_t) + SWI_{1(t)} * K_t \quad (4)$$

where $SWI_{2(t)}$ and $SWI_{1(t)}$ are the Soil Water Index (SWI) of layer 2 and layer 1, respectively, t is a time index, and K_t is the gain. Soil water index is the SWC scaled between 0 and 1 using assumed minimum and maximum values, SWI$= \left(\frac{SWC - SWC_{min}}{SWC_{max} - SWC_{min}}\right)$. For layer 1, the SWC is bounded by the minimum and maximum of the hourly CRNS observations. We note that the lower bound is dependent on the length of CRNS record and drier periods may be experienced in future drought periods. For layer 2, previous work has bounded SWC by the wilting point as the minimum value, and the mid-point between field capacity and porosity as the maximum value. Soil data or calibration of the model is thus required. The gain K_t ranges from 0 to 1 and is calculated as:

$$K_t = \frac{K_{t-1}}{K_{t-1} + exp(-\Delta t/T)} \quad (5)$$

where $K_{t-1}$is the gain of the previous time step, Δt is the time step (here 1 day), and T is a characteristic time length (equal

to L/C from Equation 3). The filter is initialized by setting $K_t = 1$ and $SWI_{2(1)} = SWI_{1(1)}$. The characteristic time length (T) is dependent on a variety of factors, including thickness of layer 2, topographic complexity (Paulik et al., 2014), and soil properties that may influence water movement (flux) rates (Albergel et al., 2008) thus requiring local calibration. Here we followed the same methodology as Peterson et al. (2016), which calibrated three parameters, T and the layer 2 minimum and maximum SWC (T, SWC_{2min}, SWC_{2max}). In order to perform the calibration we used the *in-situ* TDT data and a Monte Carlo approach varying the three parameters over their expected range (SWC_{2min} from 0.01 to 0.25 every 0.005 cm^3/cm^3, SWC_{2max} from 0.36 to 0.75 every 0.005 cm^3/cm^3, and T from 10 to 70 every 2 days). The three optimal model parameters were selected based on the objective function of maximizing the Kling-Gupta-Efficiency (KGE) criteria (Gupta et al., 2009), where a perfect fit would be KGE equal to 1. KGE has been shown to be a superior metric in hydrologic model calibration (Gupta et al., 2009) as it is based on weighting the correlation, the mean, and standard deviation between the observed and predicted time series.

RESULTS

Temporal Filtering of CRNS Data

Table 1 provides a comparison of the 24 different neutron filters propagated through the SM2RAIN algorithm for estimating daily rainfall. Using the cumulative sum percent error and KGE we selected the best MA (8 h) and SG (3rd order, 13 h) filters. These two filters and the 1 h data will be used for visual purposes for the remainder of analyses. **Figure 3A** illustrates the 1 h corrected neutron counts (black dots), the MA 8 h (blue dots and line) and SG 3rd order, 13 h filtered neutrons counts (red dots and line) for the Petzenkirchen site from 2013 to mid 2014 corresponding to the available TDT data. Following the neutron count filtering, the standard calibration function of Desilets et al. (2010) was applied to all datasets and SWC can be estimated, **Figure 3B** (see Franz et al., 2016 for on-site parameters and **Supplemental Data**). **Figure 3C** illustrates the daily liquid observed rainfall time series. Note, we also apply a porosity upper bound (=0.6 cm^3/cm^3 based on the sites soil bulk density, see Franz et al., 2016) to the SWC data. Neutron counts that result in SWC above porosity are due to the presence of liquid or solid water on the surface.

TABLE 1 | Summary of daily rainfall error analysis using different filtering techniques on moderated neutron counts and propagating calculated SWC data through SM2RAIN algorithm.

Neutron filter method	SM2RAIN estimated rainfall (mm)	Rainfall difference, SM2RAIN-observed (mm)	% Error	*R*-value	RMSE (mm/day)	Bias (mm/day)	KGE	Z*	A	b
1 h raw data	3104.7	876.7	39.4	0.598	4.20	0.79	0.481	20.00	3.81	49.92
MA 3 h	2225.2	−2.8	0.1	0.694	3.57	0.00	0.559	31.43	5.37	29.71
MA 6 h	2239.5	11.5	0.5	0.738	3.34	0.01	0.623	56.98	6.97	50.00
MA 8 h*	2144.2	−83.8	3.8	0.743	3.32	−0.08	0.615	69.65	3.32	46.85
MA 10 h	2090.0	−138.0	6.2	0.721	3.44	−0.12	0.609	81.58	0.00	50.00
MA 12 h	2051.8	−176.2	7.9	0.736	3.36	−0.16	0.629	91.43	0.00	50.00
MA 24 h	1919.5	−308.5	13.8	0.753	3.27	−0.28	0.641	139.02	0.00	50.00
SG 1st order, 3 h	2062.9	−165.2	7.4	0.686	3.62	−0.15	0.518	30.28	8.54	47.32
SG 2nd order, 3 h	3104.7	876.7	39.4	0.598	4.20	0.79	0.410	20.00	3.81	49.93
SG 1st order, 7 h	2140.4	−87.6	3.9	0.731	3.38	−0.08	0.601	63.28	7.94	49.97
SG 2nd order, 7 h	2162.8	−65.2	2.9	0.701	3.54	−0.06	0.555	32.35	4.97	49.70
SG 3rd order, 7 h	2162.8	−65.2	2.9	0.701	3.54	−0.06	0.555	32.35	4.97	49.70
SG 1st order, 9 h	2148.5	−79.5	3.6	0.728	3.40	−0.07	0.619	77.32	1.04	46.90
SG 2nd order, 9 h	2023.8	−204.2	9.2	0.713	3.49	−0.18	0.536	39.60	4.24	49.93
SG 3rd order, 9 h	2064.1	−163.9	7.4	0.711	3.50	−0.15	0.547	40.23	4.27	49.93
SG 1st order, 11 h	2094.8	−133.2	6.0	0.719	3.45	−0.12	0.606	86.95	2.85	49.96
SG 2nd order, 11 h	2116.2	−111.8	5.0	0.704	3.52	−0.10	0.577	46.68	3.40	10.36
SG 3rd order, 11 h	2116.2	−111.8	5.0	0.704	3.52	−0.10	0.577	46.68	3.40	10.36
SG 1st order, 13 h	2051.8	−176.2	7.9	0.710	3.50	−0.16	0.593	97.39	0.41	49.98
SG 2nd order, 13 h	2193.9	−34.1	1.5	0.733	3.37	−0.03	0.631	53.17	2.20	5.62
SG 3rd order, 13 h*	2193.7	−34.3	1.5	0.733	3.37	−0.03	0.631	53.17	2.20	5.62
SG 1st order, 25 h	1895.8	−332.3	14.9	0.693	3.60	−0.30	0.583	139.97	0.07	50.00
SG 2nd order, 25 h	1965.4	−262.6	11.8	0.702	3.54	−0.24	0.579	97.91	0.00	49.99
SG 3rd order, 25 h	1965.4	−262.6	11.8	0.702	3.54	−0.24	0.579	97.91	0.00	49.99

MA stands for moving average and SG for Savitzky-Golay.
Record Period 12/13/2013 to 12/31/2016, 2228.0 mm of observed rainfall.
** Denotes selected method for each filtering technique.*

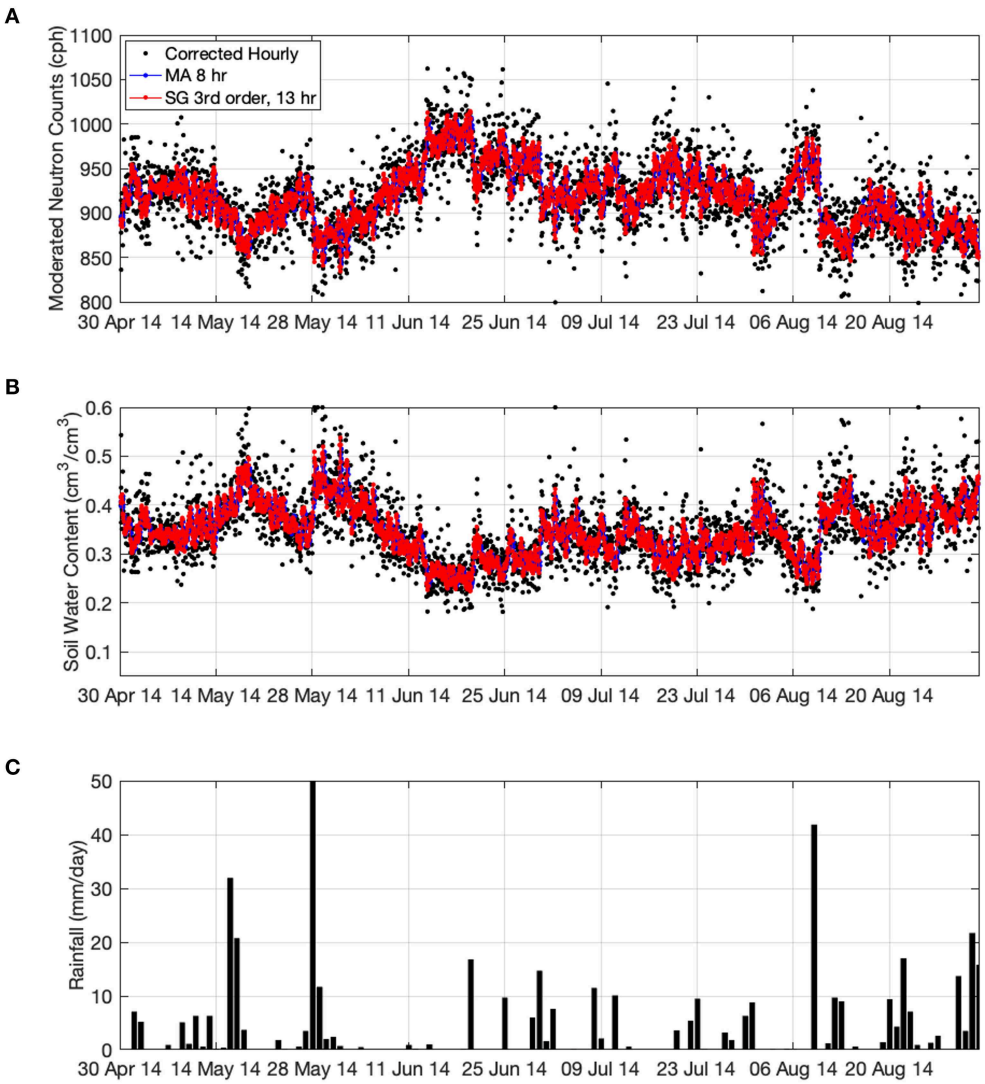

FIGURE 3 | Time series of **(A)** hourly corrected neutron counts (black dots), MA (blue dots with line) and SG filtered neutrons (red dots with line), **(B)** hourly SWC using the Desilets et al. (2010) equation and **(C)** daily rainfall observed study site for the same time period as TDT observations.

Given the closeness of the SG and MA time series, **Figure 4** provides a zoomed in view between May and June 2014. From **Figures 3A**, **4A** the connection between rainfall events and sharp decrease in neutron count rates is evident. Also note that for periods between rainfall events a steady increase in neutron counts is observed as more water is being transported to the atmosphere and soil via evapotranspiration (soil evaporation and plant transpiration). From **Figures 3**, **4** it is evident that both the MA and SG filter time series follow the central tendency of the black dot data cloud. However, **Figure 4B** illustrates that the MA filter changes the SWC peak by 2–4 h and slightly decreases the amplitude compared to the SG filter. The change in amplitude and timing of the SWC peak will affect surface runoff generation and connections to the watershed discharge (Dingman, 2002). Here our study only focused on the connection of CRNS data to daily rainfall and root zone SWC but future work should also investigate the connections to surface runoff and discharge.

Estimation of Landscape Average Rainfall Using SM2RAIN Algorithm

Table 1 summarizes the 24 different neutron filters using the SM2RAIN algorithm and rain gauge observations at Petzenkirchen. The rainfall observations are used to select the three free parameters (Z^*, a, b) in Equation (2) by minimizing the root mean square error (RMSE) between observed and estimated daily rainfall. The 1 h data results in a poor comparison with the observed data as the cumulative sum is 39.4% larger than the observations (3104.7 vs. 2,228 mm over the 3 year period, 2013–2016). The MA filter with a temporal window of 3–12 h resulted in small cumulative error (<8%). The SG filter with 1st−3rd order polynomials and temporal windows of 7–13 h also had small cumulative error (<9%). The other statistical metrics (Pearson correlation (R), KGE, Bias) were also comparable for these neutron filters.

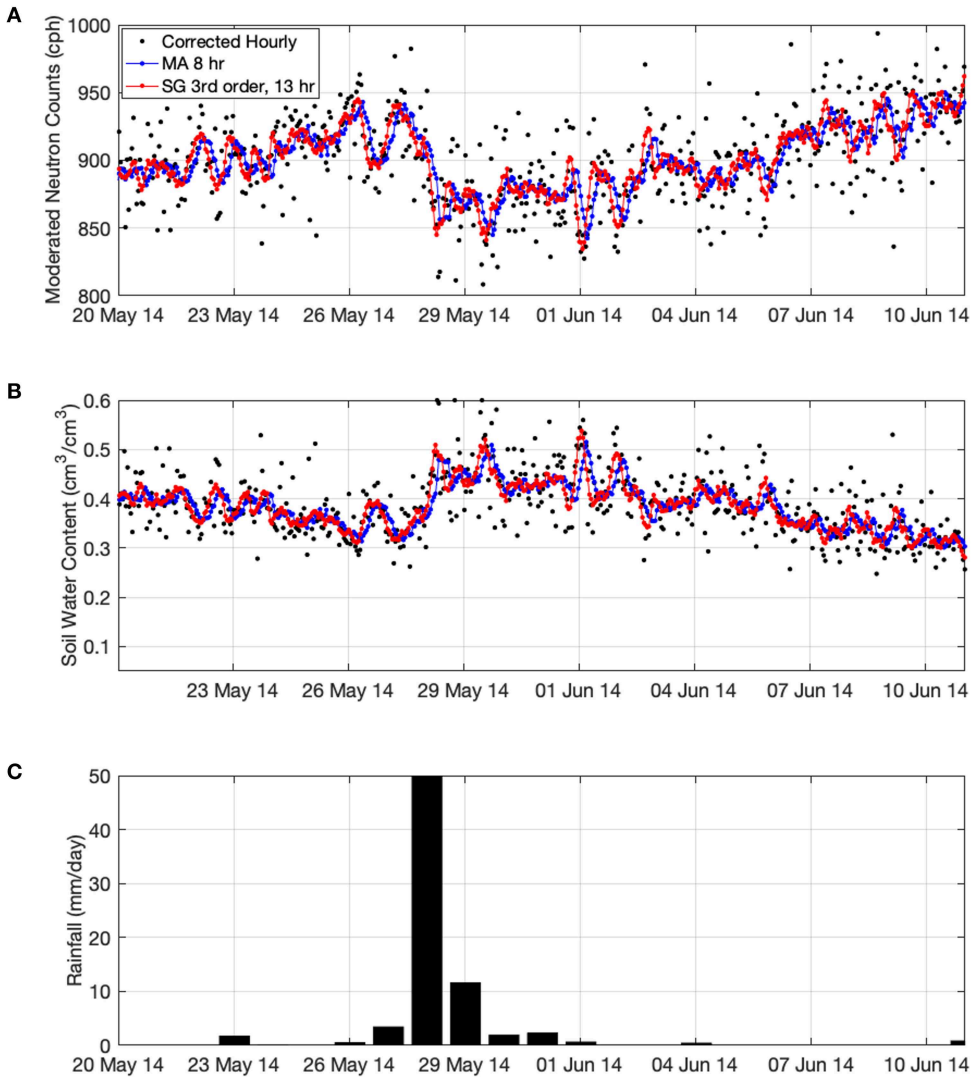

FIGURE 4 | Zoomed in times series of **Figure 3** better illustrating the 2–4 h shift in the timing of rainfall using the MA filter the Petzenkirchen. **(A)** Hourly corrected neutron counts (black dots), MA (blue dots with line) and SG filtered neutrons (red dots with line), **(B)** hourly SWC using the Desilets et al. (2010) equation and **(C)** daily rainfall observed study site for the same time period.

Comparing the three parameters with Brocca et al. (2015) we find different values. This is expected as the CRNS depth and remote sensing depths are different (∼20 vs. 3 cm). At the daily level, a R-value of 0.74 and 0.73 is found for the study site for the optimal MA and SG filters, which is comparable with the results obtained with satellite soil moisture products (e.g., Chiaravalloti et al., 2018; Brocca et al., 2019). **Figure 5** illustrates the daily cumulative sum of the three selected filters vs. the observed rainfall, again showing excellent agreement for the SG and MA filters. There are a few periods early in the record that show small deviations. If compared with the results obtained with classical *in situ* measurements shown in Brocca et al. (2015), in which the range of R-values is between 0.75 and 0.95, the performance with CRNS SWC are in the lower range but with the significant added-value to provide landscape average rainfall estimates. **Table 2** includes summary statistics for rainfall accumulations of 1, 3, and 5 days. For increasing integration time the statistical metrics improve to levels reported by Brocca et al. (2015) and Chiaravalloti et al. (2018). With respect to error the World Meteorological Organization (De Valle et al., 2007 and https://www.wmo-sat.info/oscar/variables/view/1) reports rain gage error around 1 and 2–4 mm/day for satellite estimates, however each method has different spatial resolution and coverage. The CRNS derived rainfall provides a missing and critical gap at the 1–10 ha scale.

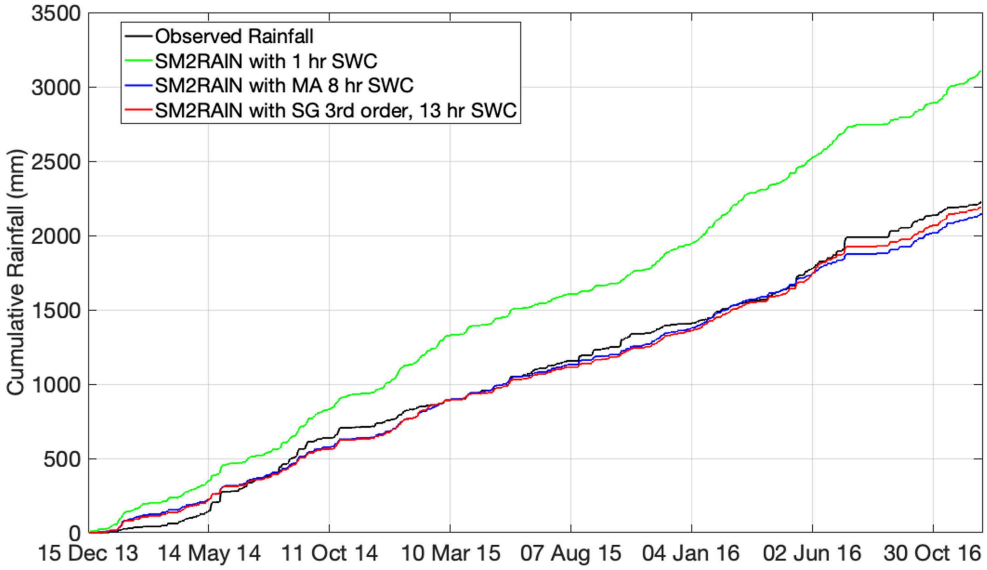

FIGURE 5 | Cumulative sums of observed rainfall and SM2RAIN estimates using three neutron filters. See **Table 1** for full summary.

TABLE 2 | Summary of SM2RAIN algorithm statistical performance at Petzenkirchen for different integration periods.

Neutron filter method	integration period (days)	R	RMSE (mm/day)	KGE	SM2RAIN estimated rainfall (mm)	Rainfall difference, SM2RAIN-observed (mm)	% Error
1 h raw data	1	0.598	4.20	0.41	3104.74	876.74	39.4
MA8 h	1	0.743	3.32	0.62	2144.23	−83.77	3.8
SG 3rd order, 13 h	1	0.733	3.37	0.63	2193.72	−34.28	1.5
1 h raw data	3	0.635	2.72	0.45	3085.45	857.44	38.5
MA 8 h	3	0.788	2.00	0.68	2299.48	71.48	3.2
SG 3rd order, 13 h	3	0.788	1.99	0.68	2238.16	10.15	0.5
1 h raw data	5	0.652	2.15	0.48	3062.31	834.31	37.4
MA 8 h	5	0.791	1.55	0.69	2274.14	46.14	2.1
SG 3rd order, 13 h	5	0.753	1.67	0.65	2158.14	−69.86	3.1

MA stands for moving average and SG for Savitzky-Golay.

Estimation of Root Zone Soil Water Content Using an Exponential Filter

Figure 2E illustrates the time series of landscape average TDT sensors by depth that were available at the HOAL from 2013 to 2014. Due to various land management operations the sensors were removed from different land uses at different times. In order to calibrate the exponential filter model to a root zone product a profile SWC was estimated from a weighted average of TDT sensors within those 0–30 and 0–60 cm profiles. Using the CRNS SWC data as layer 1 and the SWC profile 0–30 and 0–60 cm data as layer 2, the three free parameters for the exponential filter model (Equations 3, 4) were estimated using a Monte Carlo approach. The objective function was maximizing KGE between the observed and modeled SWC time series. **Table 3** provides the summary results illustrating that all three methods had large KGE values of >0.9. Estimates of SWC_{2max} and T were very similar for all methods. SWC_{1min} was lower for the 1 h neutron data due to the higher random fluctuations. As expected T was larger for the 0–60 cm layer. Following calibration **Figures 6A,B** illustrate the comparison of SWC between the exponential filter fit and the TDT landscape averages for both depths. With respect to estimating the critical parameter T, Paulik et al. (2014) used the International Soil Moisture Network (Dorigo et al., 2013) data to compare T vs. different environmental covariates. Paulik et al. (2014) found depth and topographic complexity were most correlated to T. In contrast, Wang et al. (2017) used the Nebraska Mesonet sites (same sensor type) and found that T was strongly correlated to depth and soil texture (percent sand and clay). We note that a relatively new commercial product exists that uses the exponential filter with a combination of passive microwave sensors to produce an operational daily 100 m SWC product at 10, 20, and 40 cm (https://www.vandersat.com/soil-moisture-monitoring).

Using the CNRS SWC data and the exponential model fits in **Table 3** an operational daily SWC product for 0–30 and 0–60 cm can be produced. **Figure 7** illustrates the CRNS SWC, 0–30 cm SWC, and 0–60 cm SWC products. By tracking changes in SWC over these depths in real-time stakeholders will be able to make more informed decisions about irrigation, fertilization rates, and other management operations.

TABLE 3 | Summary of calibration fit and three parameter estimates for the 0–30 and 0–60 cm exponential filter models for different neutron filters.

Calibration of CRNS vs. TDT					
Neutron filter method	**Depth (cm)**	**KGE**	**SWC_{2min} (cm^3/cm^3)**	**SWC_{2max} (cm^3/cm^3)**	**T (days)**
Daily SWC, 1 h data	30	0.911	0.01	0.675	50
Daily SWC, MA 8 h	30	0.909	0.045	0.68	48
Daily SWC, SG 3rd order, 13 h	30	0.908	0.035	0.68	50
Daily SWC, 1 h data	60	0.914	0.125	0.585	64
Daily SWC, MA 8 h	60	0.913	0.15	0.59	62
Daily SWC, SG 3rd order, 13 h	60	0.912	0.145	0.59	64

MA stands for moving average and SG for Savitzky-Golay.

Limitations of Study

The key limitation of this work is that only a single CRNS site was used, mainly due to the challenge of having a high-density *in-situ* SWC network to calibrate the algorithms. Several other studies have such networks (e.g., Franz et al., 2012a,b; Bogena et al., 2013; Lv et al., 2014) and would be good candidates to validate and extend this work. Another limitation of this work is that the optimal filter window for the MA and SG methods is dependent on the total counts, which are related to the site location (i.e., geomagnetic latitude), elevation, and detector size/type. We anticipate the optimal window size will decrease with increased total counts. This is important for use of the MA filter, particularly in minimizing any shifts in timing or amplitude of the SWC peak following a rain event. Accurate depiction of the SWC peak is critical for understanding the connection between CRNS data and

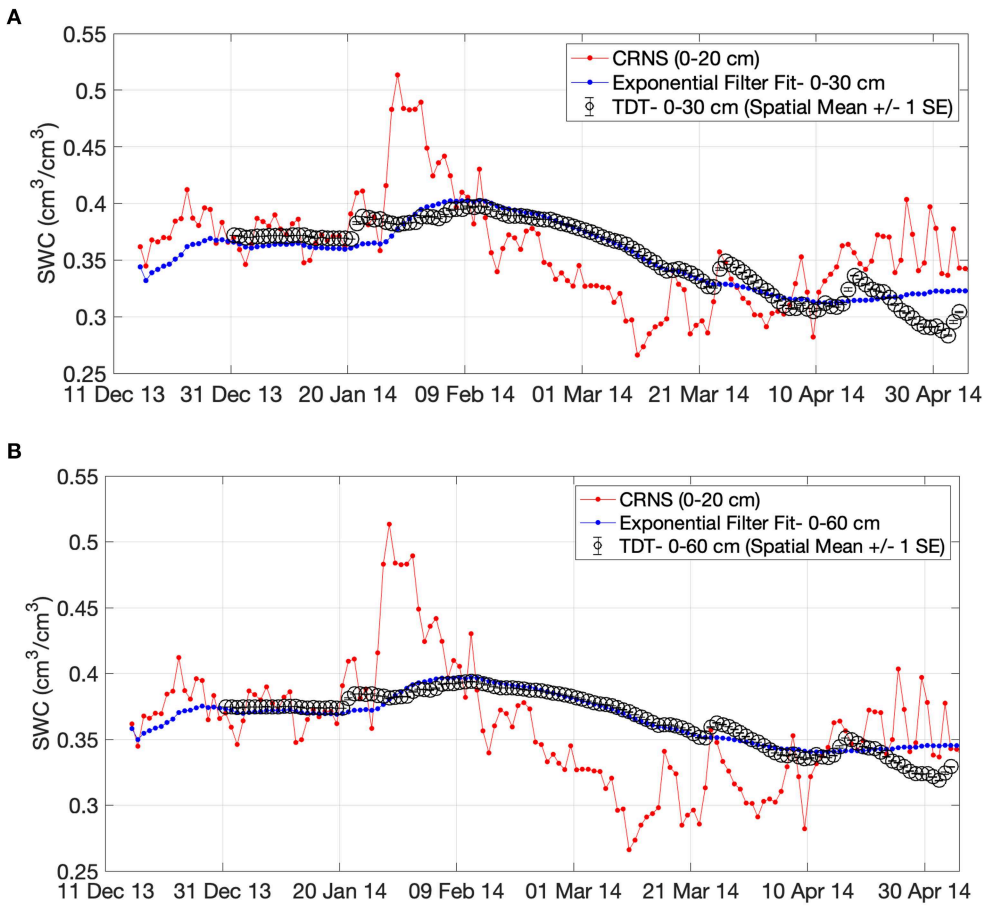

FIGURE 6 | Comparison of SWC for the CRNS (neutron filter SG 3rd order, 13 h), fitted exponential model, and observed landscape average TDT data for the **(A)** 0–30 cm and **(B)** 0–60 cm products.

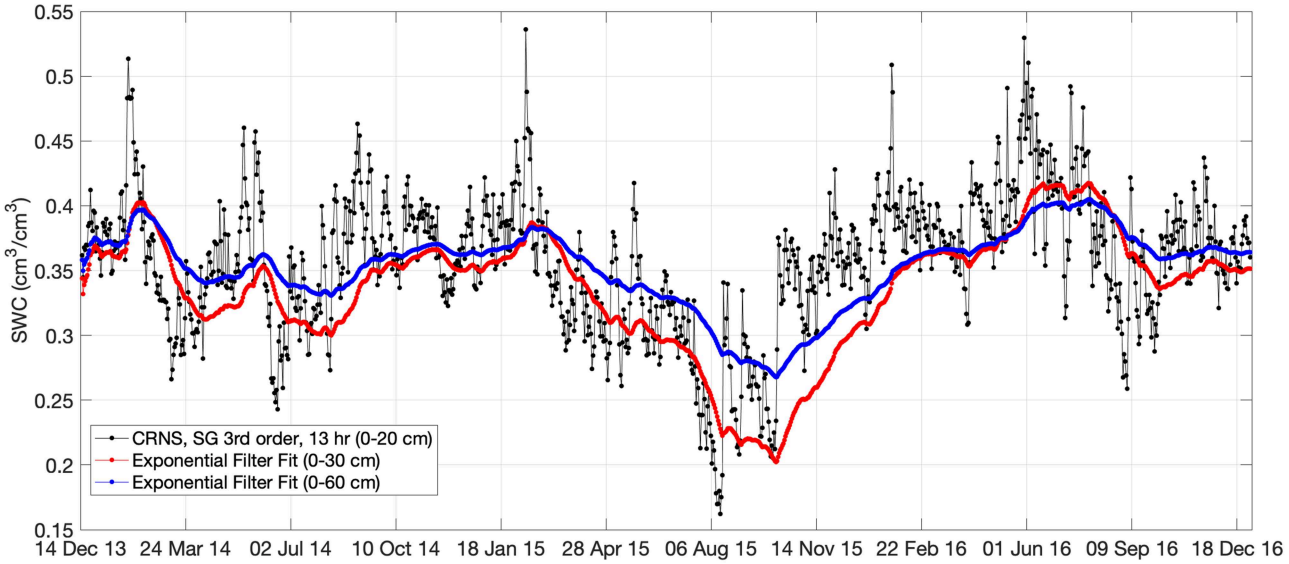

FIGURE 7 | Time series of SWC for CRNS, 0–30 cm exponential filter product, and 0–60 cm exponential filter product for the 3 years period.

surface runoff and discharge. This topic was beyond the scope of the current study but deserves more attention in the future.

With respect to the SM2RAIN algorithm, the CRNS data performed comparable to rain gage and satellite products for the MA and SG neutron filters. The 1 h data lead to a 39.4% overestimation of rainfall due to the random fluctuations in the neutron counts. The key assumption for the SM2RAIN method is that no surface runoff is generated during rainfall, which may be violated for certain sites. In addition, selection of the three parameters did vary with choice of neutron filter algorithm. Current versions of the SM2RAIN algorithm do include a self-calibration procedure. We did find that adding the criteria of cumulative sum percent error against the observed rainfall was helpful in selecting appropriate window sizes for evaluating the filters and conserving water mass balance.

With respect to daily root zone SWC, all three neutron filtering techniques worked well, albeit the 1 h data had a different SWC_{2min} parameter. The main challenge of the exponential filter approach is selection of the T parameter for novel sites where *in-situ* data may be unavailable. Paulik et al. (2014) found using the ISMN SWC data that depth and topographic complexity were most correlated to T, whereas Wang et al. (2017) found T was highly correlated to depth and soil texture for the Nebraska Mesonet site data. What is clear is that caution should be used when applying the exponential filter approach for sites with shallow water tables, large topographic relief, and dense vegetation. Given these limitations, the method's simplicity and widespread operational use in remote sensing and commercial products make it a viable candidate for extending the use of CRNS SWC data.

SUMMARY AND CONCLUSIONS

This methodological paper provides the background, equations, and example calculations from the Petzenkirchen CRNS study site using three well-established algorithms summarized in the methodological framework in **Figure 1** and available for general use (see Data Availability Statement). The algorithms make the essential step of enhancing the CRNS SWC data for providing stakeholders with the value-added products of a smoothed SWC time series, landscape average rainfall, and root zone SWC data in order to make decisions. While the provided examples are written in the computer program MATLAB R2018b mostly used by engineers and academics, next steps require the data and value-added products and code be made available on web-based data portals, code sharing environments and smartphone applications for use by stakeholders. Therefore, this paper serves as a critical but only a first step toward adoption of CRNS data toward practical applications. Future work with CRNS and available *in situ* SWC data should further validate these approaches and their use in complex environments.

DATA AVAILABILITY STATEMENT

The datasets generated for this study can be found in the Mendeley Repository with the citation- Franz, Trenton (2020), Data for Cosmic-Ray Neutron Sensor: Practical Data Products from Cosmic-Ray Neutron Sensing for Hydrological Applications, Mendeley Data, V2, doi: 10.17632/cxzjjm2txx.2. The neutron intensity smoothing and exponential filter code written in MATLAB R2018b are available upon written request to the corresponding author (tfranz2@unl.edu). The SM2RAIN code is available from LB

at http://hydrology.irpi.cnr.it/research/sm2rain/ for a variety of platforms.

AUTHOR CONTRIBUTIONS

TF performed the primary data analysis and wrote the manuscript. AW and JZ assisted with data analysis and edited the manuscript. LH and GD provided funding, laboratory access, and edited the manuscript. PS and MV provided datasets from HOAL and edited the manuscript. LB provided access to SM2RAIN algorithm, assisted with data analysis, and edited the manuscript. WW edited the manuscript.

FUNDING

Financial support was provided by the Joint FAO/IAEA Programme of Nuclear Techniques in Food and Agriculture through the Coordinated Research Project (CRP) D1.50.17 Nuclear Techniques for a Better Understanding of the Impact of Climate Change on Soil Erosion in Upland Agro ecosystems (2015–2020) and CRP D1.20.14 Enhancing agricultural resilience and water security using Cosmic-Ray Neutron Sensor (2019–2024).

ACKNOWLEDGMENTS

The authors would like to acknowledge the support of the Hydrological Open Air Laboratory, the Soil and Water Management & Crop Nutrition Laboratory of the Joint Division of Nuclear Techniques in Food and Agriculture, the Vienna Doctoral Programme on Water Resources Systems and Georg Weltin in the installation and maintenance of the CRNS.

SUPPLEMENTARY MATERIAL

The Supplementary Material for this article can be found online at: https://www.frontiersin.org/articles/10.3389/frwa.2020.00009/full#supplementary-material

Supplemental Data | Containing the raw and processed data.

REFERENCES

Albergel, C., Rudiger, C., Pellarin, T., Calvet, J. C., Fritz, N., Roissard, R., et al. (2008). From near-surface to root-zone soil moisture using an exponential filter: an assessment of the method based on *in-situ* observations and model simulations. *Hydrol. Earth Syst. Sci.* 12, 1323–1337. doi: 10.5194/hess-12-1323-2008

Andreasen, M., Jensen, K. H., Desilets, D., Franz, T., Zreda, M., Bogena, H. R., et al. (2017). Status and perspectives on the cosmic-ray neutron method for soil moisture estimation and other environmental science applications. *Vadose Zone J.* 16:11. doi: 10.2136/vzj2017.04.0086

Avery, W., Finkenbiner, C., Franz, T. E., Wang, T., Nguy-Roberston, A., Arkebauer, T., et al. (2016). Incorporation of globally available datasets into the roving cosmic-ray neutron probe method for estimating field-scale soil water content. *Hydrol. Earth Syst. Sci. Discuss.* 20, 3859–3872. doi: 10.5194/hess-20-3859-2016

Baatz, R., Franssen, H. J. H., Han, X., Hoar, T., Vereecken, H., Bogena, H. R., et al. (2017). Evaluation of a cosmic-ray neutron sensor network for improved land surface model prediction. *Hydrol. Earth Syst. Sci.* 21, 2509–2530. doi: 10.5194/hess-21-2509-2017

Babaeian, E., Sadeghi, M., Franz, T. E., Jones, S., and Tuller, M. (2018). Mapping soil moisture with the OPtical TRApezoid Model (OPTRAM) based on long-term MODIS observations. *Remote Sens. Environ.* 211, 425–440. doi: 10.1016/j.rse.2018.04.029

Bauer-Marschallingere, B., Freeman, V., Cao, S., Paulik, C., Schaufler, S., Stachl, T., et al. (2019). Toward global soil moisture monitoring with sentinel-1: harnessing assets and overcoming obstacles. *IEEE Trans. Geosci. Remote Sens.* 57, 520–539. doi: 10.1109/TGRS.2018.2858004

Blöschl, G., Blaschke, A. P., Broer, M., Bucher, C., Carr, G., Chen, X., et al. (2016). The Hydrological Open Air Laboratory (HOAL) in Petzenkirchen: a hypotheses-driven observatory. *Hydrol. Earth Syst. Sci.* 20, 227–255. doi: 10.5194/hess-20-227-2016

Bogena, H. R., Huisman, J. A., Baatz, R., and Franssen, H. J. H. (2013). Accuracy of the cosmic-ray soil water content probe in humid forest ecosystems: the worst case scenario. *Water Resour. Res.* 49, 5778–5791. doi: 10.1002/wrcr.20463

Brocca, L., Ciabatta, L., Massari, C., Moramarco, T., Hahn, S., Hasenauer, S., et al. (2014). Soil as a natural rain gauge: estimating global rainfall from satellite soil moisture data. *J. Geophys. Res. Atmos.* 119, 5128–5141. doi: 10.1002/2014JD021489

Brocca, L., Filippucci, P., Hahn, S., Ciabatta, L., Massari, C., Camici, S., et al. (2019). SM2RAIN-ASCAT (2007-2018): global daily satellite rainfall from ASCAT soil moisture. *Earth Syst. Sci. Data* 11, 1583–1601. doi: 10.5194/essd-11-1583-2019

Brocca, L., Massari, C., Ciabatta, L., Moramarco, T., Penna, D., Zuecco, G., et al. (2015). Rainfall estimation from *in situ* soil moisture observations at several sites in Europe: an evaluation of SM2RAIN algorithm. *J. Hydrol. Hydromech.* 63, 201–209. doi: 10.1515/johh-2015-0016

Chiaravalloti, F., Brocca, L., Procopio, A., Massari, C., and Gabriele, S. (2018). Assessment of GPM and SM2RAIN-ASCAT rainfall products over complex terrain in southern Italy. *Atmos. Res.* 206, 64–74. doi: 10.1016/j.atmosres.2018.02.019

Ciabatta, L., Massari, C., Brocca, L., Gruber, A., Reimer, C., Hahn, S., et al. (2018). SM2RAIN-CCI: a new global long-term rainfall data set derived from ESA CCI soil moisture. *Earth Syst. Sci. Data* 10, 267–280. doi: 10.5194/essd-10-267-2018

De Valle, V., Vuerich, E., Monesi, C., Lanza, L. G., Stagi, L., and Lanzinger, E., (2007). *WMO Field Intercomparison of Rainfall Intensity Gauges*. World Meteorological Organization instruments and observing methods report no. 99. Geneva: World Meteorological Organization.

Desilets, D., Zreda, M., and Ferre, T. P. A. (2010). Nature's neutron probe: land surface hydrology at an elusive scale with cosmic rays. *Water Resour. Res.* 46:W11505. doi: 10.1029/2009WR008726

Dingman, L. S. (2002). *Physical Hydrology, 2ndEdn.* Upper Saddle River, NJ: Prentice-Hall Inc.

Dorigo, W. A., Xaver, A., Vreugdenhil, M., Gruber, A., Hegyiova, A., Sanchis-Dufau, A., et al. (2013). Global automated quality control of *in situ* oil moisture data from the international soil moisture network. *Vadose Zone J.* 12:21. doi: 10.2136/vzj2012.0097

Fersch, B., Jagdhuber, T., Schron, M., Volksch, I., and Jager, M. (2018). Synergies for soil moisture retrieval across scales from airborne polarimetric SAR cosmic ray neutron roving, and an *in situ* sensor network. *Water Resour. Res.* 54, 9364–9383. doi: 10.1029/2018WR023337

Finkenbiner, C. E., Franz, T. E., Gibson, J., Heeren, D. M., and Luck, J. (2019). Integration of hydrogeophysical datasets and empirical orthogonal functions for improved irrigation water management. *Precis. Agric.* 20, 78–100. doi: 10.1007/s11119-018-9582-5

Franz, T. E., Wahbi, A., Vreugdenhil, M., Weltin, G., Heng, L., Oismueller, M., et al. (2016). Using cosmic-ray neutron probes to monitor landscape scale soil water content in mixed land use agricultural systems. *Appl. Environ. Soil Sci.* 2016:1–11. doi: 10.1155/2016/4323742

Franz, T. E., Wang, T., Avery, W., Finkenbiner, C., and Brocca, L. (2015). Combined analysis of soil moisture measurements from roving and fixed

cosmic ray neutron probes for multiscale real-time monitoring. *Geophys. Res. Lett.* 42, 3389–3396. doi: 10.1002/2015GL063963

Franz, T. E., Zreda, M., Ferre, P. A., Rosolem, R., Zweck, C., Stillman, S., et al. (2012a). Measurement depth of the cosmic-ray soil moisture probe affected by hydrogen from various sources. *Water Resour. Res.* 48:8515. doi: 10.1029/2012WR011871

Franz, T. E., Zreda, M., Rosolem, R., and Ferre, P. A. (2012b). Field validation of cosmic-ray soil moisture sensor using a distributed sensor network. *Vadose Zone J.* 11. doi: 10.2136/vzj2012.0046

Franz, T. E., Zreda, M., Rosolem, R., Hornbuckle, B., Irvin, S., Adams, H., et al. (2013). Ecosystem scale measurements of biomass water using cosmic-ray neutrons. *Geophys. Res. Lett.* 40, 3929–3933. doi: 10.1002/grl.50791

Gupta, H. V., Kling, H., Yilmaz, K. K., and Martinez, G. F. (2009). Decomposition of the mean squared error and NSE performance criteria: implications for improving hydrological modelling. *J. Hydrol.* 377, 80–91. doi: 10.1016/j.jhydrol.2009.08.003

Jackson, T. J., Oneill, P. E., and Swift, C. T. (1997). Passive microwave observation of diurnal surface soil moisture. *IEEE Trans. Geosci. Remote Sens.* 35, 1210–1222. doi: 10.1109/36.628788

Knoll, G. F. (2000). *Radiation Detection and Measurement*. Hoboken, NJ: John Wiley & Sons, Inc.

Kohli, M., Schron, M., Zreda, M., Schmidt, U., Dietrich, P., and Zacharias, S. (2015). Footprint characteristics revised for field-scale soil moisture monitoring with cosmic-ray neutrons. *Water Resour. Res.* 51, 5772–5790. doi: 10.1002/2015WR017169

Lawston, P. M., Santanello, J. A., Franz, T. E., and Rodell, M. (2017). Assessment of irrigation physics in a land surface modeling framework using non-traditional and human-practice datasets. *Hydrol. Earth Syst. Sci.* 21, 2953–2966. doi: 10.5194/hess-21-2953-2017

Lv, L., Franz, T. E., Robinson, D. A., and Jones, S. (2014). Measured and mpodeled soil moisture compared with cosmic-ray neutron robe estimates in a mixed forest. *Vadose Zone J.* 13:13. doi: 10.2136/vzj2014.06.0077

McCabe, M. F., Rodell, M., Alsdorf, D. E., Miralles, D. G., Uijlenhoet, R., Wagner, W., et al. (2017). The future of earth observation in hydrology. *Hydrol. Earth Syst. Sci.* 21, 3879–3914. doi: 10.5194/hess-21-3879-2017

Montzka, C., Bogena, H. R., Zreda, M., Monerris, A., Morrison, R., Muddu, S., et al. (2017). Validation of spaceborne and modelled surface soil moisture products with cosmic-ray neutron probes. *Remote Sens.* 9:103. doi: 10.3390/rs9020103

Orfanidis, S. J. (1996). *Introduction to Signal Processing*. Englewood Cliffs, NJ: Prentice-Hall.

Paulik, C., Dorigo, W., Wagner, W., and Kidd, R. (2014), Validation of the ASCAT Soil Water Index using in situ data from the International Soil Moisture Network. *Int. J. Appl. Earth Obs. Geoinf.* 30, 1–8. doi: 10.1016/j.jag.2014.01.007

Peterson, A. M., Helgason, W. D., and Ireson, A. M. (2016). Estimating field-scale root zone soil moisture using the cosmic-ray neutron probe. *Hydrol. Earth Syst. Sci.* 20, 1373–1385. doi: 10.5194/hess-20-1373-2016

Rosolem, R., Hoar, T., Arellano, A., Anderson, J. L., Shuttleworth, W., Zeng, X., et al. (2014). Translating aboveground cosmic-ray neutron intensity to high-frequency soil moisture profiles at sub-kilometer scale. *Hydrol. Earth Syst. Sci.* 18, 4363–4379. doi: 10.5194/hess-18-4363-2014

Rosolem, R., Shuttleworth, W. J., Zreda, M., Franz, T. E., Zeng, X., Papuga, S., et al. (2013). The effect of atmospheric water vapor on the cosmic-ray soil moisture signal. *J. Hydrometeorol.* 14, 1659–1671. doi: 10.1175/JHM-D-12-0120.1

Savitzky, A., and Golay, M. J. E. (1964). Smoothing and differentiation of data by simplified least square procedure. *Anal. Chem.* 36, 1627–1639. doi: 10.1021/ac60214a047

Schattan, P., Baroni, G., Oswald, S. E., Schober, J., Fey, C., Kormann, C., et al. (2017). Continuous monitoring of snowpack dynamics in alpine terrain by aboveground neutron sensing. *Water Resour. Res.* 53, 3615–3634. doi: 10.1002/2016WR020234

United Nations (2007). *World Reference Base for Soil Resources 2006*. World Soil Resources Reports No. 103. United Nations Food and Agriculture Organization, IUSS Working Group WRB, FAO, Rome. Available online at: http://www.fao.org/fileadmin/templates/nr/images/resources/pdf_documents/

Vereecken, H., Huisman, J. A., Bogena, H., Vanderborght, J., Vrugt, J., Hopmans, J. W., et al. (2008). On the value of soil moisture measurements in vadose zone hydrology: a review. *Water Resour. Res.* 44:W00D06. doi: 10.1029/2008WR006829

Wagner, W., Lemoine, G., and Rott, H. (1999). A method for estimating soil moisture from ERS scatterometer and soil data. *Remote Sens. Environ.* 70, 191–207. doi: 10.1016/S0034-4257(99)00036-X

Wang, T. J., Franz, T. E., You, J. S., Shulski, M., and Ray, C. (2017). Evaluating controls of soil properties and climatic conditions on the use of an exponential filter for converting near surface to root zone soil moisture contents. *J. Hydrol.* 548, 683–696. doi: 10.1016/j.jhydrol.2017.03.055

Zreda, M., Desilets, D., Ferre, T. P. A., and Scott, R. L. (2008). Measuring soil moisture content non-invasively at intermediate spatial scale using cosmic-ray neutrons. *Geophys. Res. Lett.* 35:L21402. doi: 10.1029/2008GL035655

Zreda, M., Shuttleworth, W. J., Xeng, X., Zweck, C., Desilets, D., Franz, T., et al. (2012). COSMOS: the COsmic-ray soil moisture observing system. *Hydrol. Earth Syst. Sci.* 16, 4079–4099. doi: 10.5194/hess-16-4079-2012

Conflict of Interest: The authors declare that the research was conducted in the absence of any commercial or financial relationships that could be construed as a potential conflict of interest.

frontiers in Water

ORIGINAL RESEARCH
published: 14 May 2020
doi: 10.3389/frwa.2020.00010

Error Estimation for Soil Moisture Measurements With Cosmic Ray Neutron Sensing and Implications for Rover Surveys

Jannis Jakobi[1], Johan A. Huisman[1], Martin Schrön[2], Justus Fiedler[1], Cosimo Brogi[1], Harry Vereecken[1] and Heye R. Bogena[1]*

[1] Agrosphere Institute (IBG-3), Forschungszentrum Jülich GmbH, Jülich, Germany, [2] Department of Monitoring and Exploration Technologies, Helmholtz-Zentrum für Umweltforschung GmbH-UFZ, Leipzig, Germany

Cosmic ray neutron (CRN) sensing allows for non-invasive soil moisture measurements at the field scale and relies on the inverse correlation between aboveground measured epithermal neutron intensity (1 eV−100 keV) and environmental water content. The measurement uncertainty follows Poisson statistics and thus increases with decreasing neutron intensity, which corresponds to increasing soil moisture. In order to reduce measurement uncertainty, the neutron count rate is usually aggregated over 12 or 24 h time windows for stationary CRN probes. To obtain accurate soil moisture estimates with mobile CRN rover applications, the aggregation of neutron measurements is also necessary and should consider soil wetness and driving speed. To date, the optimization of spatial aggregation of mobile CRN observations in order to balance measurement accuracy and spatial resolution of soil moisture patterns has not been investigated in detail. In this work, we present and apply an easy-to-use method based on Gaussian error propagation theory for uncertainty quantification of soil moisture measurements obtained with CRN sensing. We used a 3rd order Taylor expansion for estimating the soil moisture uncertainty from uncertainty in neutron counts and compared the results to a Monte Carlo approach with excellent agreement. Furthermore, we applied our method with selected aggregation times to investigate how CRN rover survey design affects soil moisture estimation uncertainty. We anticipate that the new approach can be used to improve the strategic planning and evaluation of CRN rover surveys based on uncertainty requirements.

Keywords: cosmic ray neutron sensing, error propagation, aggregation, cosmic ray rover, uncertainty

OPEN ACCESS

Edited by:
Jianzhi Dong,
Agricultural Research Service (USDA), United States

Reviewed by:
Trenton Franz,
University of Nebraska-Lincoln, United States
Linna Chai,
Beijing Normal University, China

****Correspondence:***
Jannis Jakobi
j.jakobi@fz-juelich.de

Specialty section:
This article was submitted to Water and Hydrocomplexity, a section of the journal Frontiers in Water

Received: *23 January 2020*
Accepted: *14 April 2020*
Published: *14 May 2020*

Citation:
Jakobi J, Huisman JA, Schrön M, Fiedler J, Brogi C, Vereecken H and Bogena HR (2020) Error Estimation for Soil Moisture Measurements With Cosmic Ray Neutron Sensing and Implications for Rover Surveys. Front. Water 2:10. doi: 10.3389/frwa.2020.00010

INTRODUCTION

Soil moisture is an essential variable of the terrestrial system as it governs the transfer of both water and energy between the land surface and the atmosphere (Vereecken et al., 2015). Accurate information on soil moisture dynamics is vital for a better understanding of processes in the vadose zone, because it controls major subsurface processes, such as ground water recharge, runoff, and infiltration. Furthermore, soil moisture dynamics are important for the optimization of agricultural management because they determine crop growth, leaching processes, and the fate of fertilizers applied to soils. Soil moisture is highly variable in both space and time, with typical length and time

scales ranging from a few centimeters to several kilometers and from minutes to years, respectively (Robinson et al., 2008; Vereecken et al., 2008).

Recent advances in non-invasive monitoring techniques enable continuous and contactless measurements of soil moisture dynamics at the field scale (Bogena et al., 2015). Among other methods, the cosmic ray neutron sensing (CRNS) method has become increasingly popular for soil moisture estimation since its introduction by Zreda et al. (2008). The CRNS method relies on the inverse relationship between soil moisture and the amount of aboveground epithermal neutrons (energy range from ∼0.2 eV to 100 keV) (Köhli et al., 2018). The measurement footprint ranges from 130 to 240 m radius around the neutron detector with a penetration depth ranging between 15 and 80 cm depending on soil moisture and other parameters (Köhli et al., 2015). Typically, stationary CRNS probes are used to obtain continuous information on field scale soil moisture dynamics (Zreda et al., 2012; Andreasen et al., 2017; Schrön et al., 2018a). More recently, mobile applications of CRNS probes (i.e., CRN roving) have been introduced, which enable to measure spatial soil moisture variability at the larger catchment scale (Chrisman and Zreda, 2013; Dong et al., 2014; Franz et al., 2015; Avery et al., 2016; McJannet et al., 2017; Schrön et al., 2018b).

Measurement uncertainty is an important quantity that should accompany every geophysical data set. The systematic uncertainty has been analyzed by Baroni et al. (2018), who quantified the influence of environmental factors, such as vegetation or soil properties, on the CRNS product. The present study investigates the statistical uncertainty of CRNS soil moisture estimates, which depends on the detector configuration, i.e., the number of counts in a given period of time. This count rate, however, is inversely related to soil moisture, such that dryer soil leads to more precise measurements (cf. Desilets et al., 2010; Bogena et al., 2013). In CRN rover applications, this translates to the number of detected neutrons in a specific spatial unit that is passed during the record period of the detector. Hence, the traveling speed determines the spatial resolution and is an important factor for the quantification of measurement uncertainty.

Various neutron detectors exist of different size and efficiency. Typically, a larger detector volume improves the counting statistics, and thus reduces the uncertainty of the soil moisture product. The record period of most mobile neutron detectors is between 10 s and 1 min, while typical driving speeds range from 2 to 10 km/h on agricultural fields (Schrön et al., 2018b; Fentanes et al., 2019) to ∼50 km/h for large-scale surveys (e.g., Chrisman and Zreda, 2013; Dong et al., 2014; McJannet et al., 2017; Dong and Ochsner, 2018). In most studies, additional spatial smoothing was applied to the CRN rover measurements by using a temporal moving window filter in order to reduce the uncertainty in the soil moisture estimates (e.g., Schrön et al., 2018b: window size of 3 measurements; Chrisman and Zreda, 2013: window size of 7 measurements). However, long record periods as well as large averaging window sizes lead to elongated measurement footprints in the direction of data acquisition and thus to a decrease in spatial resolution (Chrisman and Zreda, 2013; Fersch et al., 2018; Schrön et al., 2018b). For instance, aggregated neutron counts for 1, 3, 5, and 7 min time periods acquired with an average driving speed of 50 km/h correspond to elongated footprints where the longer axis is 0.8, 2.5, 4.2, and 5.8 km long, respectively. More advanced approaches for data aggregation have also been proposed. Some studies assigned the average of all raw neutron measurements within a fixed radius to a grid (e.g. Dong and Ochsner, 2018; Gibson and Franz, 2018; Finkenbiner et al., 2019). In a further processing step, inverse distance weighting was used to further sharpen the image and to increase resolution (Gibson and Franz, 2018; Finkenbiner et al., 2019).

Bogena et al. (2013) and Schrön et al. (2018a) have already analyzed the dependence of the accuracy of CRN-based soil moisture measurements on the time integration for a stationary CRNS probe. In principle, this method can also be applied to mobile CRN rovers by taking spatial aggregation into account. Nevertheless, the effects of the spatial aggregation of neutron counts on the soil moisture measurement accuracy have not yet been investigated in detail. A comprehensive method to determine uncertainty in soil moisture from uncertainty in neutron counts would allow for the discrimination of statistical effects from the effects of environmental water. In earlier CRN rover studies, such undetermined features could not be assessed in full detail (e.g., Dong et al., 2014; Franz et al., 2015; Dong and Ochsner, 2018; Schrön et al., 2018b).

In this study, we aim to analyze how temporal and spatial aggregation of neutron counts affects the accuracy of soil moisture measurements with CRNS technology with a focus on mobile CRN roving. To this end, analytical expressions for error propagation are introduced that allow to assess the accuracy of soil moisture estimates from uncertain neutron count rates. The appropriateness of the analytical expressions is evaluated using Monte Carlo simulations. The applicability of the analytical expressions is tested using experimental data from three different CRN rover campaigns with different spatial scales in Germany and in Oklahoma (USA).

MATERIALS AND METHODS

Jülich CRN Rover

The Jülich CRN rover consists of an array of nine neutron detector units (Hydroinnova LLC, Albuquerque, NM, USA) each holding four $_{10}BF^3$-filled tubes, which amounts to a total number of 36 neutron detector tubes located in 9 detector housings. The housing of the detector tubes was designed such that the moderating High Density Polyethylene (HDPE) can be removed on demand. This allows to convert the neutron detector tubes from epithermal (with HDPE) to thermal neutron sensitive (without HDPE) and back. During the presented measurement campaigns, the Jülich CRN rover was configured to measure epithermal neutrons with five detector units. Three of these units were mounted in vertical orientation, while the other two units were oriented horizontally (**Figure 1**). The remaining four detector units measured thermal neutrons during the experiments to calculate the thermal-to-epithermal neutron ratio (N_r). The N_r ratio has already been successfully used in previous studies to estimate surface biomass and to correct the influence

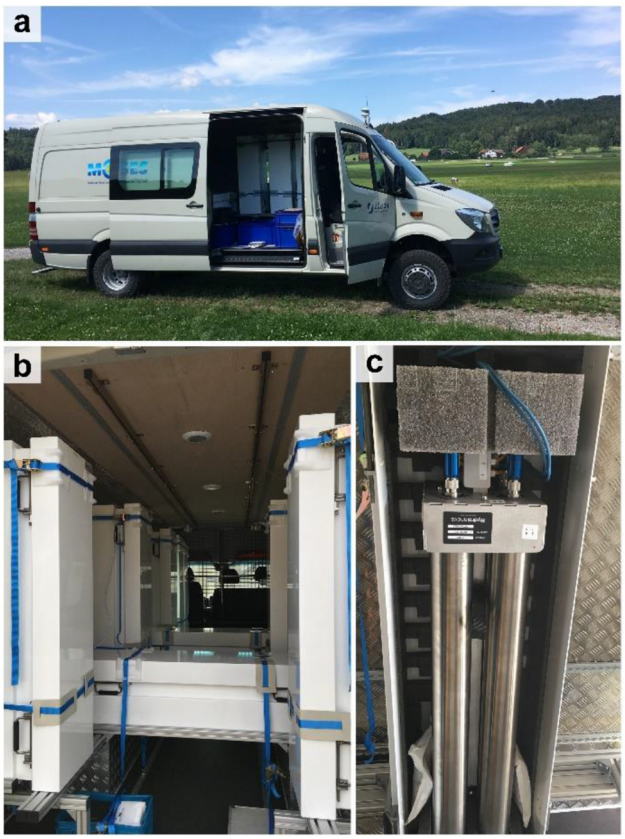

FIGURE 1 | Jülich Cosmic rover in the field at the TERENO research site Fendt **(a)**. Setup of the nine detector units inside the car **(b)**. Example of one detector unit consisting of four detector tubes—here shown without the moderating HDPE **(c)**.

of surface biomass on soil moisture from cosmic ray neutrons (Tian et al., 2016; Jakobi et al., 2018). The driving speed during the presented measurement campaigns with the Jülich CRN rover was 4–5 km/h, and the time interval of the raw neutron count measurements was 10 s.

Experimental Sites

Fendt Site (Germany, Experiment A)

The long-term research site Fendt (47°50'N, 11°3.6'E) belongs to the Pre-Alpine observatory (Wolf et al., 2016; Kiese et al., 2018) of the TERENO (TERrestrial ENvironmental Observatories) network (Zacharias et al., 2011; Bogena et al., 2012). The Fendt site is located at the south-eastern tip of the Rott catchment (55 km^2) at about 595 m a.s.l. The soils are dominated by Cambrian stagnosols and land use consists mainly of pasture and forest. The Fendt site has a temperate marine climate with an average annual rainfall of 1,033 mm and temperature of 8.6°C (Fu et al., 2017). For more detailed information on site characteristics, we refer to Kiese et al. (2018).

The CRN rover measurements on the Fendt research site were carried out as part of a joint field campaign of the CosmicSense project (for more information please visit the project webpage: https://www.uni-potsdam.de/en/cosmicsense.html). We drove back and forth along a ∼350 m long grass road for 4 h at the lowest possible speed of 4–5 km/h on 14 April 2019. For reference, shallow soil moisture (0–7 cm depth) was measured at 155 locations a few meters off the road using HydraProbe soil moisture sensors (Hydra Go Field Version, Stevens Water Monitoring Systems, Inc., Portland, USA). The measurement transect was bordered by a road in the west and a small stream in the east.

Selhausen Site (Germany, Experiment B)

The research site Selhausen (50°52'N, 6°27'E) covers an area of ∼1 × 1 km and is part of the Lower Rhine Valley/Eifel Observatory of the TERENO network (Bogena et al., 2018). The Selhausen site is located in the eastern part of the Rur catchment (2,354 km^2) and is characterized by an eastern upper terrace composed of Pleistocene sand and gravel sediments that are buried in loess sediments and by a western lower terrace that is generally dominated by Pleistocene/Holocene loess sediments (Weihermüller et al., 2007). The soils in the area consist of Cambisols, Luvisols, Planosols, and Stagnosols (Rudolph et al., 2015). Generally, all fields within the study area are used for agriculture. The crops that are most commonly grown are winter cereals, sugar beet and silage maize (Reichenau et al., 2016). The site has a temperate maritime climate with a mean annual precipitation and temperature of 714 mm and 10.2°C, respectively (Korres et al., 2015). Detailed information on the Selhausen research site can be found in Bogena et al. (2018) and Brogi et al. (2020).

The CRN rover measurements at the Selhausen site were collected as part of a MOSES (Modular Observation Solutions for Earth Systems) test campaign. MOSES is an infrastructure program funded by the Helmholtz Association (https://www.ufz.de/moses/). The campaign was carried out on 11 July 2018 and we mostly drove on the roads in the research area. Whenever it was possible, we also drove on the agricultural fields. Some of the fields in the northwest and southeast of the area were irrigated during the CRN rover measurements. Reference soil moisture measurements were again made with HydraProbe sensors as in the Fendt experiment at 738 locations distributed over a large fraction of the experimental area with a focus on sites where earlier studies were based (e.g., Rudolph et al., 2015; Jakobi et al., 2018; Brogi et al., 2019). This was done to limit the amount of work associated with taking reference measurements (4 people were measuring for ∼4 h).

For this site, the bulk density of the fine fraction ($\varrho_{bd<2}$) was estimated to be 1.32 g/cm^3 from literature values (Ehlers et al., 1983; Unger and Jones, 1998) and from previous sampling campaigns conducted within the study area. These values were modified using gravel content as successfully done by Brogi et al. (2020) for the simulation of crop growth in this study area. For this, a high-resolution soil map produced from a combination of electromagnetic induction measurements and direct soil sampling (Brogi et al., 2019) was used to retrieve spatially distributed gravel content. This map divides the study area in 18 soil units, each provided with information on gravel content for each horizon. To obtain bulk density (ϱ_{bd}) values

considering gravel content, the method proposed by Brakensiek and Rawls (1994) was used:

$$\varrho_{bd} = \varrho_{bd<2} + Z2\,(\varrho_{bd>2} - \varrho_{bd<2}) \quad (1)$$

where $\varrho_{bd>2}$is the bulk density of rock fragments (2.65 g/cm^3, Brakensiek and Rawls, 1994) and Z2 [g/cm^3] is the volume of rock fragments (Flint and Childs, 1984), which was approximated according to Brakensiek and Rawls (1994) with:

$$Z2 = Z1/(2 - Z1) \quad (2)$$

where $Z1$ is the gravel content in % of weight relative to the total weight of dry samples. The same map was used to determine the sum of lattice water and organic matter (θ_{off}) for the Selhausen site with the loss-on-ignition method by heating mixed samples of the 18 soil units to 1,000°C for 12 h (Zreda et al., 2012; Baatz et al., 2015). The samples were obtained from mixed top soil material (30–40 cm depth) from a total of 200 measurement locations in the area. The reference soil moisture, ϱ_{bd} and θ_{off} were horizontally weighted to match the CRN rover measurement locations (Schrön et al., 2017).

Oklahoma Site (USA, Experiment C)

The Oklahoma site is located in the Cimarron River catchment in the central north of Oklahoma, USA. The soil is dominated by Mollisols, Alfisols and Inzeptisols with loamy texture in the central part of the transect and sandy texture in the western part of the transect (SSURGO database, https://websoilsurvey.sc.egov.usda.gov/). The land use consists mainly of warm seasonal grasses, winter wheat and small patches of deciduous forests. The average annual precipitation ranges from 880 mm in the east to 732 mm in the west (Dong and Ochsner, 2018).

CRN rover measurements were performed 18 times on a ∼150 km long unpaved road. The resulting dataset was analyzed by Dong and Ochsner (2018) to determine controlling factors for mesoscale soil moisture patterns. The CRN rover used at this site consists of two epithermal neutron detectors, each holding two ^{3}He-filled detector tubes (Hydroinnova LLC, Albuquerque, NM, USA). The aggregation interval of the raw neutron count measurements was 1 min and the driving speed varied according to the local conditions. The average speed was 48 km/h (Dong and Ochsner, 2018).

For the Oklahoma study area, we extracted ϱ_{bd} and clay content of the top soil from the SSURGO database and converted it to a 200 × 200 m resolution grid as described by Dong and Ochsner (2018). In a further step, we used their linear relation to derive lattice water (θ_{off}) from clay content. The hydrogen pool of the soil organic matter was not considered by Dong and Ochsner (2018). Next, average values of ϱ_{bd} and θ_{off} in a 200 m radius were assigned to the CRN rover measurement locations.

Data Acquisition and Standard Processing

Both CRN rovers recorded GPS locations at the end of each aggregation interval. These were set to half the distance traveled between two recordings so that the location better reflected the origin of the accumulated neutron counts (Dong and Ochsner, 2018; Schrön et al., 2018b). In addition, absolute humidity (calculated from measured air temperature and relative humidity) and atmospheric pressure were recorded with both CRN rovers. The corrected neutron counts (N_{cor}) for the Jülich CRN rover were obtained by applying standard correction procedures for atmospheric pressure (Desilets and Zreda, 2003), absolute humidity (Rosolem et al., 2013) and variation in incoming cosmic radiation (Desilets and Zreda, 2001). The correction procedures are described in detail in Jakobi et al. (2018, Appendix B). The reference incoming cosmic radiation was obtained from the neutron monitor at Jungfraujoch (JUNG, available via the NMDB neutron monitor database at www.nmdb.eu). The hourly incoming cosmic ray data were interpolated linearly to the respective time stamps of the measurements with the Jülich CRN rover. For the Oklahoma CRN rover, we used the raw and corrected neutron counts as published by Dong and Ochsner (2018).

Conversion of Neutron Counts to Soil Moisture

We converted the corrected neutron count rates to gravimetric soil moisture (θ_g [g/g]) with the approach of Desilets et al. (2010):

$$\theta_g = a_0 \left(\frac{N_{cor}}{N_0} - a_1 \right)^{-1} - a_2 - \theta_{off} \quad (3)$$

where N_0 is a free parameter that is usually calibrated with independent *in-situ* soil moisture reference measurements, and a_i = (0.0808, 0.372, 0.115) are fitting parameters determined by Desilets et al. (2010) and validated in many publications thereafter. Estimated hydrogen content within the CRN probe footprint stored in pools other than soil moisture (θ_{off} [g/g], i.e., lattice water and organic matter) is subtracted from the CRN soil moisture estimate (Franz et al., 2012). As in previous CRN rover studies, we only considered lattice water and organic matter here (e.g., Avery et al., 2016; McJannet et al., 2017). The conversion from gravimetric to volumetric soil moisture (θ_v [m^3/m^3]) is known as:

$$\theta_v = \varrho_{bd}\,\theta_g \quad (4)$$

For the Fendt site, we used a constant ϱ_{bd} = 1.028 g/m^3 and θ_{off} = 0.072 g/g, which were sampled ∼150 m northeast of the measurement transect by Fersch et al. (2018). The *in-situ* soil moisture measurements were used to calibrate N_0 in Equation 3, which resulted in a value of 753 cts/min for the Fendt site. For the N_0 calibration of the CRN rover application at the Selhausen site, all reference *in-situ* soil moisture were used with four different aggregation methods (moving window and nearest neighbor aggregation of 3 and 9 measurements, respectively). Subsequently, the four aggregated N_0 values were averaged, resulting in a mean N_0 value of 720 cts/min for the Selhausen site. In this way, we did not favor any of the aggregation strategies used in this study. For the conversion of measured neutron counts to soil moisture at the Oklahoma site, we used N_0 = 556 cts/min. This value was obtained by Dong and Ochsner (2018) using calibration against reference data from four stations of the Oklahoma Mesonet.

Quantification of Measurement Accuracy

The measurement accuracy of CRN rover measurements was quantified using the standard deviation (σ) and the root mean squared error (RMSE). Both have a similar meaning and are therefore directly comparable. The standard deviation σ is given by:

$$\sigma(c) = \sqrt{\frac{1}{A(c)-1}\sum_{i=1}^{A(c)}\left|x(c)_i - \overline{x(c)}\right|^2} \tag{5}$$

where x and $\bar{x}$ are the measurements and their mean, respectively, and A is the total number of measurements, which scales with the aggregation size c. The RMSE is given by:

$$RMSE(c) = \sqrt{\frac{1}{A(c)}\sum_{i=1}^{A(c)}\left|x(c)_i - x_2(c)_i\right|^2} \tag{6}$$

where x_2 are the reference measurements for a given level of aggregation.

Expected Measurement Accuracy Due to Uncertain Neutron Count Rates

Measurements of a proportional neutron detector system are governed by counting statistics that follow a Poissonian probability distribution (Zreda et al., 2012). For a large number of events per unit time, the Poisson distribution converges to a normal distribution. Therefore, the expected uncertainty in the neutron count rate N is defined by the standard deviation $\sqrt{N}$. Consequently, increasing neutron count rates lead to decreasing relative measurement uncertainty as well as decreasing absolute soil moisture uncertainty (Schrön, 2017). It is important to realize that the basic uncertainty is introduced by the raw count rate rather than the processed neutron counts after correction. Therefore, the uncertainty analysis must be based on the raw measurement N and propagated to the corrected neutron counts with the factor s, the product of the correction factors for pressure, humidity and incoming cosmic radiation:

$$\sigma_N = s\sqrt{N} \tag{7}$$

In order to obtain the expected standard deviation of soil moisture, the uncertainty of the neutron count rates must be propagated through Equation 3. One possible approach is the approximation by an analytical Taylor expansion. We used the method presented by Mekid and Vaja (2008), which develops the Taylor expansion up to the 3rd polynomial order and considers six central moments in the uncertainty distribution. Since the random detection of neutron counts follow a symmetric Gaussian normal distribution, only the 2nd, 4th, and 6th—moments are relevant in this calculation. The 1st, 2nd, and 3rd order approximation of the propagated uncertainty of θ_g (σ_{θ_g} [g/g]) are given by:

$$\sigma_{\theta_g}(N) = \sqrt{\boxed{\boxed{\theta'(N)^2\sigma_N{}^2} + \frac{1}{2}\theta''(N)^2\sigma_N{}^4} + \theta'(N)\theta'''(N)\sigma_N{}^4 + \frac{15}{36}\theta'''(N)^2\sigma_N{}^6} \tag{8}$$

where the rectangles from small to large denote increasing order of approximation (Mekid and Vaja, 2008). Equation 8 requires the 1st, 2nd, and 3rd derivatives of Equation 3, which are given by:

$$\begin{aligned}
\theta'(N) &= -\frac{a_0}{N_0\left(\frac{N_{cor}}{N_0} - a_1\right)^2} \\
\theta''(N) &= \frac{2a_0}{{N_0}^2\left(\frac{N_{cor}}{N_0} - a_1\right)^3} \\
\theta'''(N) &= -\frac{6a_0}{{N_0}^3\left(\frac{N_{cor}}{N_0} - a_1\right)^4}
\end{aligned} \tag{9}$$

For easier implementation of the 3rd order uncertainty approximation, the expressions given in Equations 8 and 9 can be simplified to:

$$\sigma_{\theta_g}(N) = \sigma_N \frac{a_0 N_0}{(N_{cor} - a_1 N_0)^4} \sqrt{(N_{cor} - a_1 N_0)^4 + 8\sigma_N{}^2(N_{cor} - a_1 N_0)^2 + 15\sigma_N{}^4} \tag{10}$$

To convert the expected standard deviation from gravimetric to volumetric units (σ_{θ_v} [m^3/m^3]) we used:

$$\sigma_{\theta_v}(N) = \varrho_{bd}\,\sigma_{\theta_g} \tag{11}$$

To validate the proposed Taylor expansion approach, we used a more computationally intensive Monte Carlo uncertainty analysis (e.g., Bogena et al., 2013; Baroni et al., 2018). For this, we calculated neutron count rates representative for volumetric soil moisture ranging from 0.0 to 0.7 m^3/m^3. This was done using Equations 3 and 4 by assuming Fendt site conditions (i.e., ϱ_{bd}, θ_{off}, and s) and N_0 values ranging from 0 to 45,000 cts. These values were chosen since they cover typical N_0 values for the counting periods of CRN rovers (e.g., Avery et al., 2016: 518 cts/min; Dong and Ochsner, 2018: 556 cts/min; Vather et al., 2019: 133 cts/min) aggregated up to 1 h (e.g., Dong and Ochsner, 2018: 33,360 cts/h), as well as typical N_0 values for long aggregation periods of stationary cosmic ray probes (e.g., Baatz et al., 2014: 936–1,242 cts/h; Baroni et al., 2018: 1,438 and 1,531 cts/h) aggregated up to 24 h. Subsequently, the synthetic mean neutron count rates were recalculated to raw neutron count rates with $N_{in} = \frac{1}{s}N_{cor}$ assuming the average conditions of the Fendt experiment and used to generate large sets of draws from the appropriate Poisson distribution (N_{out}). These were rescaled again with $N_{poisson} = sN_{out}$ and converted to soil moisture. The standard deviation of the resulting soil moisture distributions was

used to obtain the measurement accuracy as a function of soil moisture, aggregation time and N_0.

It should be noted that the non-linear behavior of Equation 3 transforms the Gaussian probability distribution of N to a skewed distribution of θ_g. Consequently, the uncertainty of θ_g is asymmetric, which cannot be expressed by a single standard deviation as obtained from the uncertainty approximation methods used in this study. However, since the focus is the optimization of CRNS rover surveys, we are confident that the presented approaches represent the uncertainty in soil moisture estimates from uncertain neutron count rates sufficiently well.

Since uncertainties of rover measurements are often more prone to areal than to temporal variation in soil moisture, we also converted aggregation time to aggregation length for 5, 10, 50, and 100 km/h driving speed using:

$$Aggregation\ length\ \left[km\right] = Speed\ \left[\frac{km}{h}\right] \cdot Aggregation\ time\ [h] \tag{12}$$

Other Sources of Uncertainty

Additional uncertainties for the estimation of soil moisture with the CRNS method, such as the uncertainties in the amount of biomass (Avery et al., 2016), N_0, the incoming cosmic ray flux (Baroni et al., 2018), air pressure (Gugerli et al., 2019), and humidity are not investigated in this manuscript. However, due to the linear dependency of σ_{θ_v} and soil bulk density (Equation 11), the uncertainty in soil bulk density ($\sigma_{\varrho_{bd}}$) is known to have a particularly strong influence on the volumetric soil moisture product (Avery et al., 2016; Baroni et al., 2018). According to error propagation theory, the relative uncertainty of soil bulk density and gravimetric soil moisture in Equation 11 sum up, which leads to the following calculation of volumetric soil moisture uncertainty:

$$\sigma_{\theta_v}(N,\ \varrho_{bd}) = \varrho_{bd}\sigma_{\theta_g} + \sigma_{\varrho_{bd}}\,\theta_g \tag{13}$$

Neutron Aggregation Strategies

For the Fendt experiment, we subdivided the measurement transect into equally long sections while assuring that each section contained at least 100 neutron count measurements. This resulted in ten sections, for which we assumed constant soil moisture during the 4 h measurement campaign. Within each of the sections, we defined a central location using the respective means of the east-west distance and the north-south distance. Subsequently, we selected the ten measurements nearest to the central location and calculated the standard deviation of the first aggregation step using Equation 5. In the next aggregation step, the twenty nearest measurements were selected. Then, the 1st and 11th, 2nd and 12th measurement, etc., were added to obtain 10 aggregated neutron count rates, and the standard deviation was calculated again. This process was continued until less than ten measurement were left. Finally, we used Equations 3 and 4 to convert the corrected neutron counts to volumetric soil moisture.

As mentioned above, the neutron count statistics of CRN rover measurements are usually improved by using a moving window filter. However, in many locations more local information is available where streets are intersecting. Therefore, using a nearest neighbor average should improve the measurement accuracy in these locations. We used the Selhausen experiment to compare a moving window aggregation strategy with a nearest neighbor aggregation strategy. We used a moving average filter with a window size of three and nine measurements along the driven route. Analogously, we averaged the neutron counts at each location with the nearest neighbor measurements in a way that the same number of measurements can be compared (e.g., a moving window of nine subsequent measurements is compared to the average of the location and the eight nearest neighbors).

For the Oklahoma experiment, we followed the strategy described by Dong and Ochsner (2018). From the average driving speed during data collection (∼50 km/h), an average measurement interval of ∼800 m was derived. This was used to generate an ideal route with 800 m spacing between the end, start and turning points of the transect driven on 7 August 2015. Next, the neutron measurements within different radii from the generated location were averaged for each transect driven. For a more detailed explanation on the averaging strategy, we refer to Dong and Ochsner (2018). Gibson and Franz (2018) and Finkenbiner et al. (2019) applied a similar aggregation strategy, but extended it by inverse distance weighting of the averaged neutron measurements. We did not test the potential benefits of this interpolation method as our primary focus was to establish an analytical approach for soil moisture uncertainty assessment. However, we suggest that the effects of different interpolation methods should be investigated in a separate study.

RESULTS AND DISCUSSION

Expected Accuracy—Analytical vs. Monte Carlo Approach

Figure 2 shows the standard deviation of soil moisture as a function of soil moisture for synthetic neutron count rates using the Fendt site characteristics and N_0 values of 500, 1,000, 2,000, and 5,000 cts, respectively. It is important to note that the presented results are site-specific and depend on soil bulk density, θ_{off} and s. As expected, the uncertainty in soil moisture estimation increased with increasing soil moisture (Bogena et al., 2013). An increase in N_0 (i.e., more aggregation or more efficient detectors) and therefore an increase in the count rate N led to substantially lower errors in soil moisture estimation (**Figure 2**).

In addition, four error estimation methods are compared in **Figure 2**, namely the Monte Carlo approach and the Taylor expansions of 1st, 2nd, and 3rd order. We found that the analytical expressions for measurement uncertainty underestimated the standard deviation for high soil moisture content (> ∼0.3 m^3/m^3) when the 1st and 2nd order Taylor expansions were used. For N_0 values larger than 1,000, the 3rd order approximation matched the results of the Monte Carlo analysis very well. For low N_0, the 3rd order approximation still deviated from the Monte Carlo simulations (**Figure 2**) with high water content (i.e., low neutron counts). This can be explained by the increasing steepness of Equation 3 toward the asymptote present at a

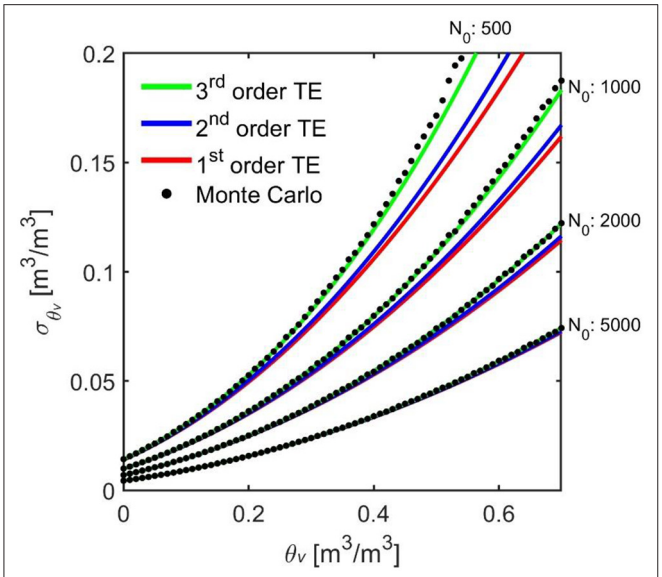

FIGURE 2 | Standard deviation of soil moisture from raw neutron counts (σ_{θ_v} [m^3/m^3]) as a function of soil moisture (θ_v [m^3/m^3]) using $N_0 = 500$, 1,000, 2,000, and 5,000 cts with Fendt site conditions and soil properties ($\varrho_{bd} =$ 1.028 g/m^3, $\theta_{off} = 0.072$ g/g and $s = 0.6136$). The standard deviations were obtained from a Monte Carlo approach and Taylor expansions (TE) of 1st, 2nd, and 3rd polynomial order with Equations 8, 9, and 11.

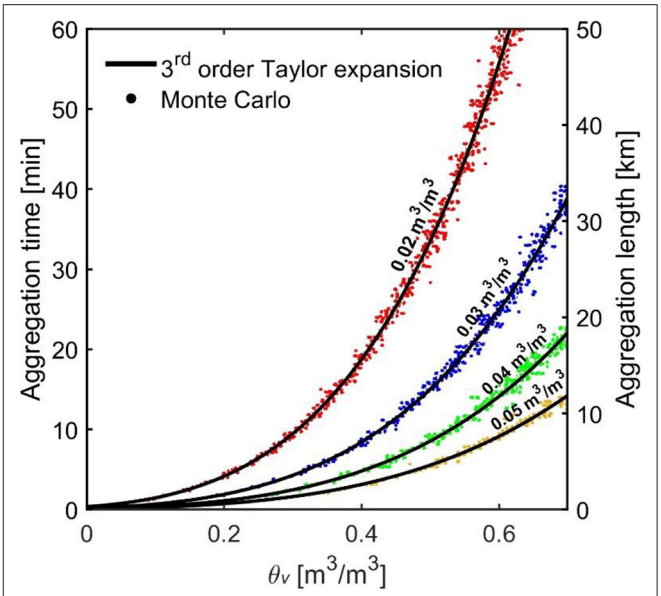

FIGURE 3 | Aggregation time/aggregation length with 50 km/h traveling speed required to obtain soil moisture estimates (θ_v [m^3/m^3]) with 0.02, 0.03, 0.04 and 0.05 m^3/m^3 measurement uncertainty expressed as standard deviation from raw neutron counts (σ_{θ_v} [m^3/m^3]) as function of soil moisture. The standard deviation was obtained from a Monte Carlo approach and a Taylor expansion approach of 3rd polynomial order with Equations 8, 9 and 11 and the presented estimates are valid for neutron measurements with the Jülich CRN rover and Fendt site conditions ($N_0 = 753$ cts/min, $\varrho_{bd} = 1.028$ g/m^3, $\theta_{off} = 0.072$ g/g and $s = 0.6136$). The aggregation length can be converted linearly to other aggregations lengths and corresponding traveling speeds with Equation 12 (e.g., for 100 km/h multiply tick marks with 2, for 10 km/h divide the tick marks by 5, and for 5 km/h divide tick marks by 10).

neutron count rate of $a_1 N_0$. Overall, we found only minor differences between Monte Carlo simulations and the 3rd order Taylor expansion to estimate measurement accuracy of soil moisture due to uncertainty of neutron count rates. Therefore, the 3rd order approximation was used in the remainder of this study.

Figure 2 clearly shows that higher count rates will result in lower soil moisture uncertainty. For this reason, aggregation periods of 12 or 24 h are often used with stationary probes and multiple CRN rover measurements along the same track are averaged. **Figure 3** shows the aggregation time required to obtain soil moisture estimates of a specified measurement uncertainty with the Jülich CRN rover and Fendt site conditions. The aggregation time was obtained using the Monte Carlo approach and the 3rd order Taylor expansion approach. In addition, the aggregation time was converted to aggregation length using Equation 12. For soil moisture contents below 0.4 m^3/m^3, an aggregation time of 10 min is necessary to achieve a measurement uncertainty below 0.03 m^3/m^3 with the Jülich CRN rover and Fendt site conditions. Correspondingly, this measurement uncertainty can be achieved with increasing spatial aggregation depending on the driving speed. For instance, aggregation lengths of ∼1, ∼2, ∼10, and ∼20 km are needed for driving speeds of 5, 10, 50, and 100 km/h, respectively (**Figure 3**).

It is important to note that the measurement uncertainty presented in **Figures 2**, **3** only considered uncertainty in neutron count rate, and thus does not include other sources of uncertainty in CRN soil moisture estimates, such as the uncertainty in soil bulk density (Avery et al., 2016; Baroni et al., 2018). **Figure 2** suggests that a soil moisture of 0.3 m^3/m^3 is associated with an uncertainty of 0.056 m^3/m^3 for $N_0 = 1{,}000$ cts due to uncertain neutron counts. An uncertainty of 20% in bulk density would add an additional uncertainty of 0.06 m^3/m^3 according to Equation 13. Thus, the combined uncertainty due to uncertain soil bulk density and raw neutron counts would be 0.116 m^3/m^3. It is clear that above a minimum threshold of raw neutron counts, the greatest absolute uncertainty in volumetric soil moisture estimates using CRNS technology can be attributed to soil bulk density (Avery et al., 2016). The framework presented here can be used to determine such a minimum threshold for a particular site, which is shown exemplary in **Figure 4** for the Fendt site. For this, we obtained the uncertainty in soil moisture estimation with fixed neutron count rates N for different values of N_0 using Equations 10 and 11. If we assume a 20% uncertainty in soil bulk density and a soil moisture range from 0.2 to 0.4 m^3/m^3, the uncertainties in soil bulk density and raw neutron counts are approximately equal, when there are 500 cts/unit area. For a soil moisture of 0.4 m^3/m^3 the combined uncertainties (Equation 13) from 20% uncertainty in soil bulk density and 1,000 cts/unit area is ∼0.13 m^3/m^3. As we lack estimates of the uncertainty in bulk density for the case studies presented here, we focus on the uncertainty from raw neutron counts in the remainder of this manuscript.

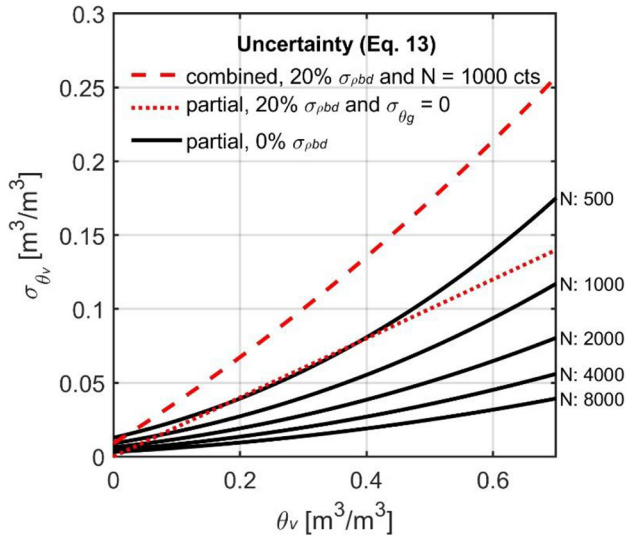

FIGURE 4 | Standard deviation from raw neutron counts (σ_{θ_v} [m^3/m^3]) as a function of soil moisture (θ_v [m^3/m^3]) using fixed N = 500, 1,000, 2,000, 4,000 and 8,000 cts and variable N_0s representative for soil moistures between 0 and 0.7 m^3/m^3 at the Fendt site (ϱ_{bd} = 1.028 g/m^3, θ_{off} = 0.072 g/g and s = 0.6136) obtained with Equation 11. For comparison the standard deviation from soil bulk density ($\sigma_{\varrho bd}$) in units of soil moisture as a function of soil moisture, assuming 20% uncertainty in bulk density, and the combined uncertainty from soil bulk density and raw neutron counts in units of soil moisture as a function of soil moisture, assuming N = 1,000 and 20% uncertainty in bulk density (Equation 13), is shown.

Experiment a (Fendt Site)

The measurements at the Fendt site (experiment A) were acquired to illustrate the accuracy of the 3rd order approximation to estimate measurement uncertainty of actual CRN roving measurements. The minimum, average and maximum count rates were 402, 606, and 810 cts/min, respectively, before correction (N). After correction, we observed a distinct reduction in neutron count rates, which is mostly attributed to the atmospheric pressure correction (responsible for an average reduction of ∼35%). It is important to note that the large reduction due to the pressure correction occurred because we normalized to standard pressure (1023.25 hPa). The use of a different reference value (e.g., the average pressure during the measurement campaign) would reduce this effect. Minimum, average and maximum count rates after correction (N_{cor}) were 246, 372, and 504 cts/min, respectively. The measurement transect showed a distinct gradient in epithermal neutron count rates, with increasing environmental water content toward the east and corresponding decreasing epithermal neutron count rates (**Figure 5A**). The gradient in neutron counts was dominated by the road at the western end and the small stream at the eastern end of the transect (**Figures 5A,B**). These additional influences were considered during calibration and validation by adding artificial measurement points along the road and the stream (see **Figure 5B**). It is perhaps possible to correct neutron counts for the road influence with the approach from Schrön et al. (2018b), but this was not tested here because this correction would not have influenced the error estimation because it is based on raw neutron counts. To our knowledge, there is currently no correction approach for nearby water bodies available. Here, we assumed homogeneous soil moisture equivalent values of 0.07 m^3/m^3 for the road (Schrön et al., 2018b) and 1.0 m^3/m^3 for the stream, respectively, and the density of the artificially added points to consider roads and water bodies corresponded to the *in-situ* measurements.

To guide the visual analysis of the results, we divided the measurement transect into 10 sections. The expected and measured uncertainty of N with increasing aggregation is shown in **Figure 5C**. Both showed very similar behavior with increasing aggregation in most sections. Exceptions were sections 5 and 9, where the measured standard deviation of the counts was lower than expected. **Figure 5D** shows the standard deviation of measured soil moisture calculated with Equations 3 and 4 and the expected standard deviation calculated with Equations 10 and 11 (3rd order Taylor expansion) as a function of spatial aggregation. With the exception of sections 5, 9 and 10, all sections showed good agreement between the expected and measured uncertainty of soil moisture. Generally, the standard deviation of measured soil moisture was relatively high (>0.05 m^3/m^3) even after aggregation. This can be explained by the relatively short maximum aggregation time per section, which varied between 1.5 and 2.5 min. Such short aggregation times lead to a high measurement uncertainty as shown in **Figure 3**. To achieve a measurement accuracy of 0.05 m^3/m^3 at a soil moisture content of 0.60 m^3/m^3 (e.g., section 10), it would be required to aggregate for more than 10 min (cf. **Figure 3**). To achieve the same measurement accuracy for a soil moisture of 0.3 m^3/m^3 (e.g., section 1), an aggregation time of 2.5 min would have been sufficient.

Figure 5E shows the CRN rover derived soil moisture with increasing aggregation time as well as the mean reference *in-situ* soil moisture of each section. In most sections, the mean reference soil moisture fell within the range of the standard deviation of soil moisture. We found the largest deviations between the reference *in-situ* soil moisture and CRN rover derived soil moisture in sections 5 and 10 (**Figure 5E**). A possible explanation is that within these two sections the environmental moisture conditions were not constant as assumed in the analysis approach. This is consistent with earlier results of Schrön et al. (2018a), who found that small differences in position can significantly influence soil moisture estimates from CRN probes in complex environments.

Experiment B (Selhausen Site)

The measurements from the Selhausen experiment were used to compare different aggregation scales and strategies. Minimum, average and maximum count rates were 450, 654, and 888 cts/min, respectively, before correction (N). After correction, we observed a moderate reduction in neutron count rates and the incoming neutron correction had the greatest influence (responsible for an average reduction of ∼10%). Minimum, average and maximum count rates after correction (N_{cor}) were 408, 588, and 798 cts/min, respectively.

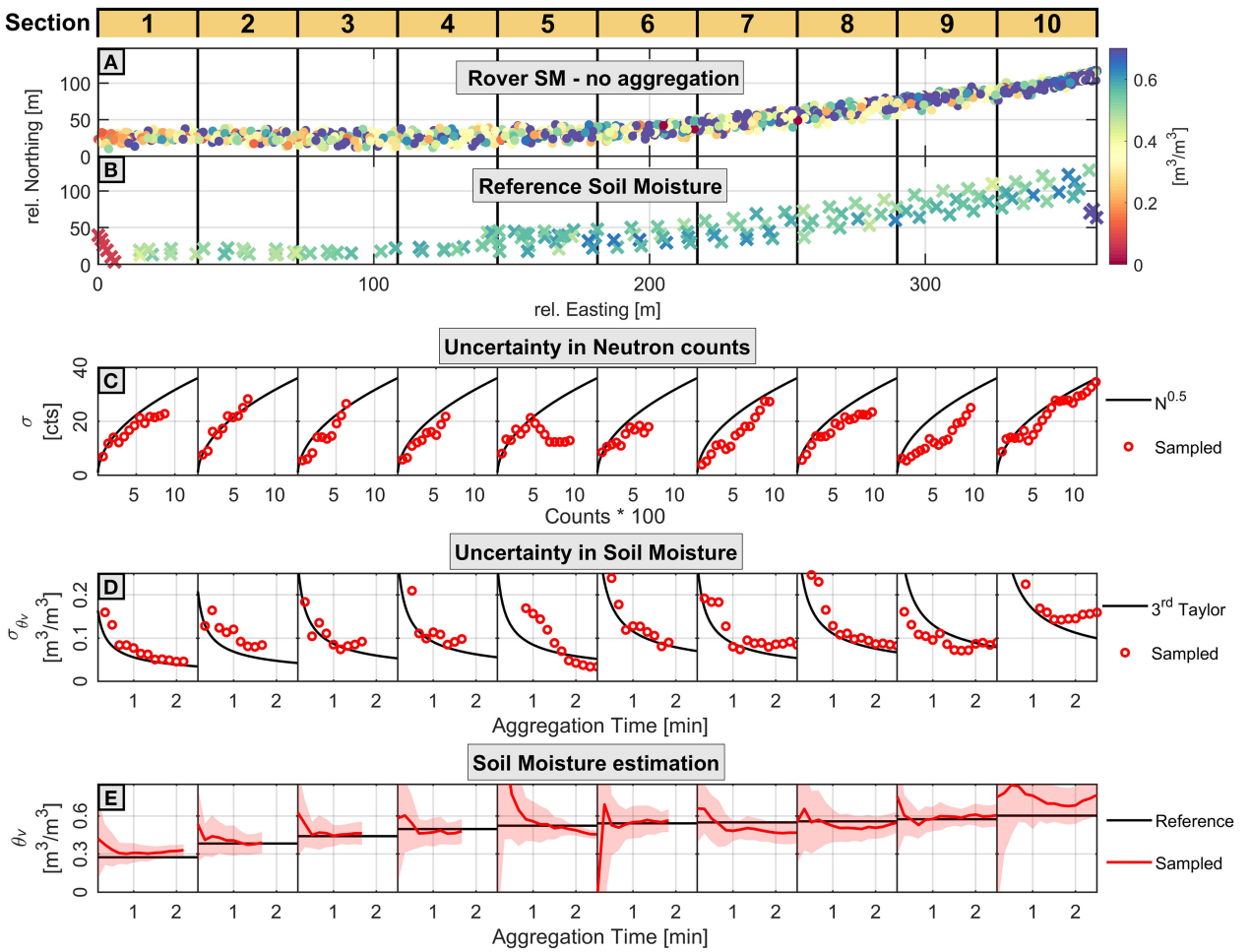

FIGURE 5 | Overview of the results from the Fendt experiment for each of the ten analyzed sections. **(A)** CRN rover soil moisture without aggregation. **(B)** *In-situ* reference soil moisture. The relative coordinates in panels a and b were calculated from UTM coordinates. **(C)** Expected standard deviation of raw neutron counts (σ). **(D)** 3rd order approximation of standard deviation of soil moisture from raw neutron counts (σ_{θ_v}) in comparison to measured standard deviation with the CRN rover. **(E)** Soil moisture (θ_v) estimated with the CRN rover in comparison with mean reference soil moisture content for each section. Red area indicates ± one measured standard deviation of the mean.

The estimated soil moisture was very low (< 0.15 m^3/m^3, **Figure 6**) due to the extended drought period before and during the campaign. The soil moisture estimates of the CRN rover showed low values in the northeast and high values in the southwest, which reflects differences in soil texture (Rudolph et al., 2015; Brogi et al., 2019; **Figure 6**). Reference soil moisture measurements were even lower (< 0.1 m^3/m^3) than the soil moisture estimates from CRN roving.

A correction for the effect of biomass on the soil moisture estimates was attempted using two approaches: (1) a linear regression between N_0 and *in-situ* measured biomass (e.g., Baatz et al., 2015), and (2) the thermal-to-epithermal neutron ratio method (Tian et al., 2016; Jakobi et al., 2018). Both correction methods did not result in substantial improvements of the soil moisture estimates. We also attempted to remove road effects on the measured neutron count rate using the approach of Schrön et al. (2018b). However, this also did not result in an improvement, which was perhaps related to the dry conditions. Soil moisture content was lower than or equal to the soil moisture equivalents of different road types (grassy pathways, dirt roads, and asphalt), which is unusual and was not considered in the development of the correction approach (Schrön et al., 2018b).

Aggregation clearly improved the accuracy of soil moisture estimates as indicated by the lower RMSE, irrespective of aggregation strategy (**Figure 6**). Only minor differences were found for the aggregation approaches both in the case of three and nine measurements. In the case of the aggregation of nine measurements, the most pronounced differences occurred near crossroads, or for closely separated tracks (**Figure 7**). If only three measurements were aggregated, the differences were more variable due to the high measurement uncertainty, but they occurred in the same locations for both cases. A drawback of the nearest neighbor aggregation approach is that the processing algorithm potentially also takes measurements into account that

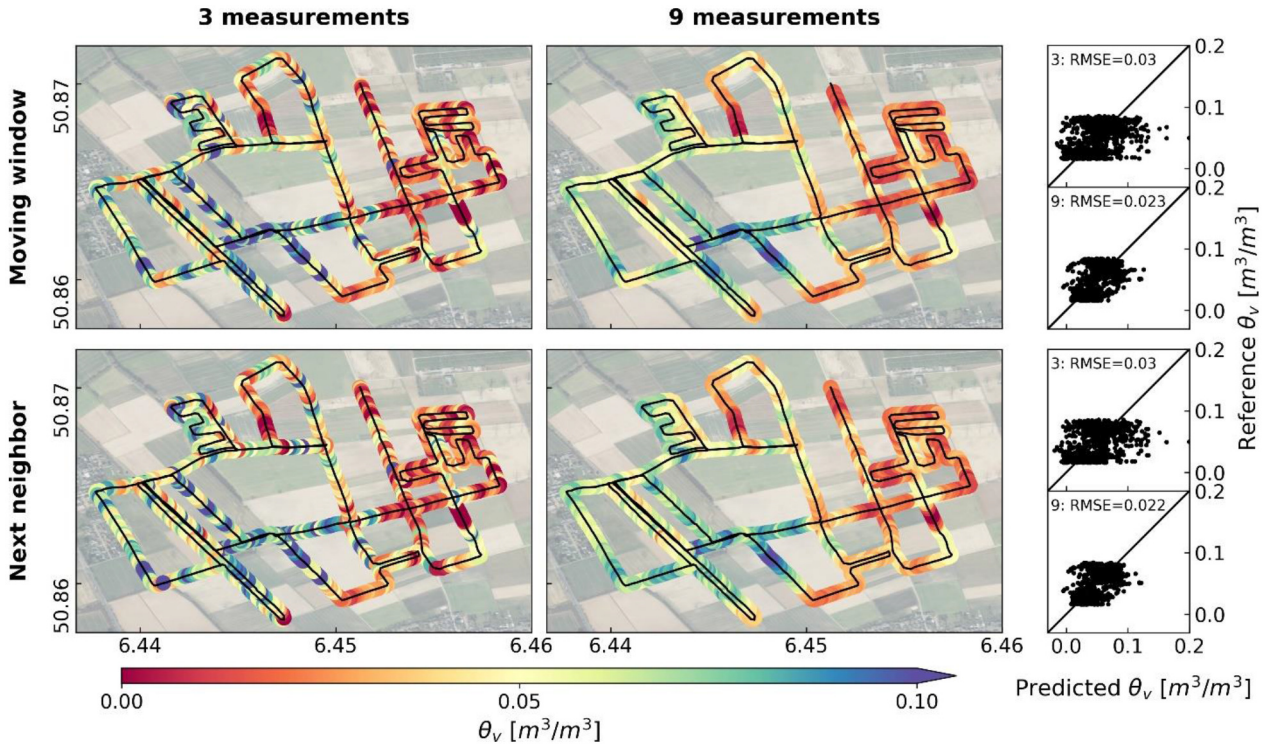

FIGURE 6 | Comparison of four aggregation strategies with the Jülich CRN rover at the Selhausen site with data measured on 11 July 2018. Top panels: moving window aggregation for three and nine following measurements, respectively. Bottom panels: nearest neighbor aggregation with the nearest two and eight neighbors, respectively. The scatter plots show the reference soil moisture (θ_v) measurements (horizontally averaged according to Schrön et al., 2017) as a function of the predicted soil moisture from the CRN rover. Base maps: ESRI World Imagery and Contributors.

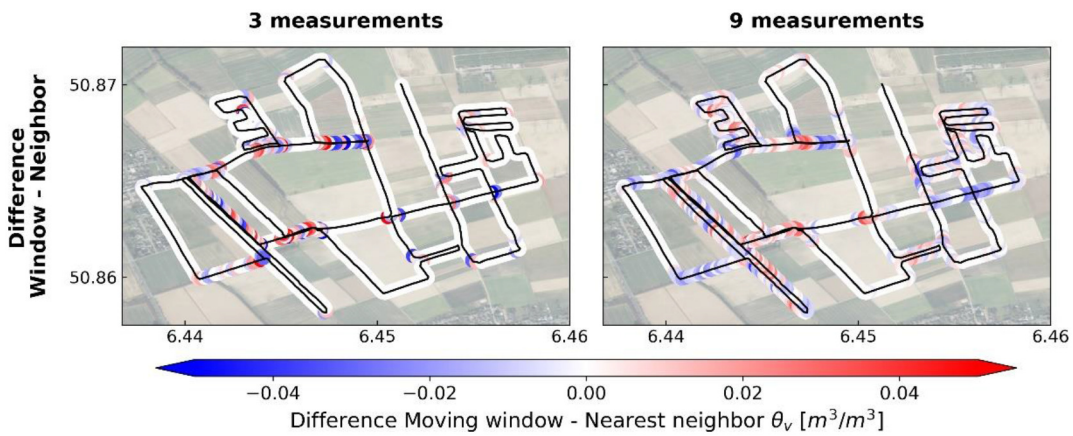

FIGURE 7 | Difference in soil moisture (θ_v) between moving window and nearest neighbor aggregation strategies for three and nine aggregated measurements. Base maps: ESRI World Imagery and Contributors.

were taken on parallel roads, even though they may have different water contents (cf. **Figure 7**).

At first sight, the results from this experiment looked satisfying because of the relatively low reported RMSEs. However, the expected soil moisture estimation uncertainty using Selhausen site conditions (**Figure 8**) were similar to the overall uncertainty as expressed by the RMSE when only 3 measurements were used (0.032 m^3/m^3). This is undesirable and suggests the need for more aggregation. When nine measurements were aggregated, the average uncertainty due to uncertain neutron measurements decreased to 0.017 m^3/m^3 irrespective of aggregation strategy. Also, the patterns of soil

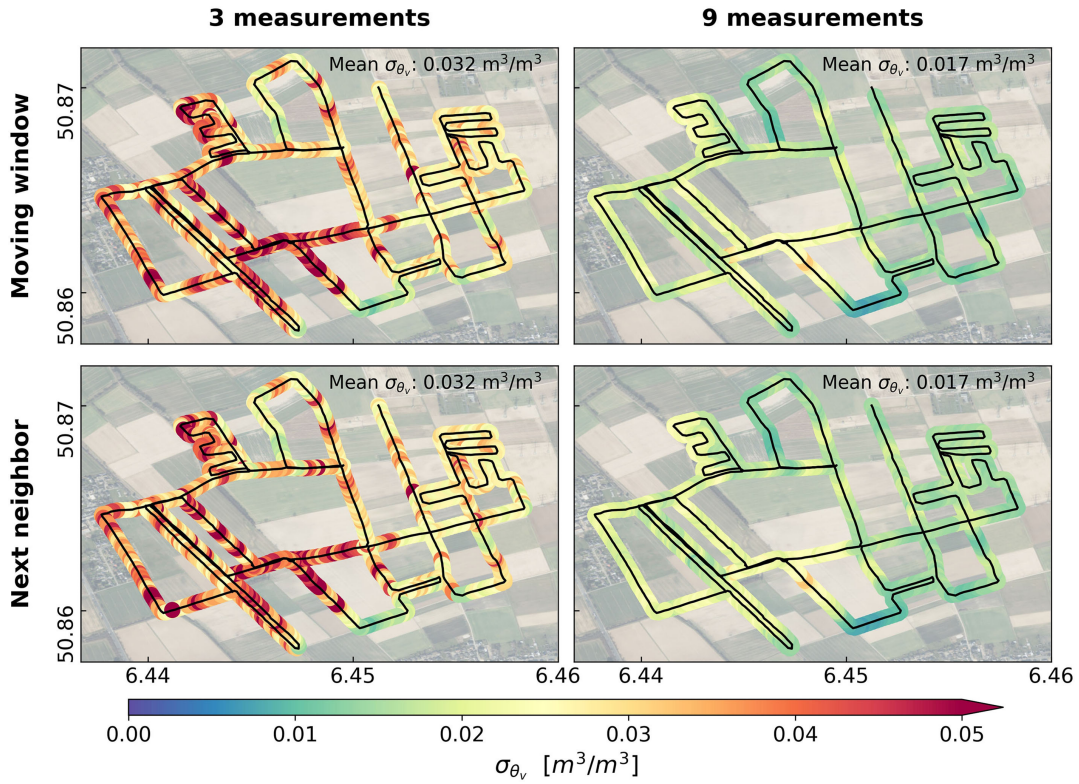

FIGURE 8 | Comparison of soil moisture uncertainty from neutron counts (σ_{θ_v}) estimation with four aggregation strategies with the Jülich CRN rover at the Selhausen site with data measured on 11 July 2018. Top panels: moving window aggregation for three and nine following measurements, respectively. Bottom panels: nearest neighbor aggregation with the nearest two and eight neighbors, respectively. Base maps: ESRI World Imagery and Contributors.

moisture uncertainty distribution varied minimally between the aggregation strategies (**Figure 8**).

This measurement campaign illustrates the required compromise between aggregation time and spatial resolution that is sometimes necessary for CRN rover measurements. In order to achieve lower uncertainty, the driving speed would have to be much lower. However, the vehicle did not allow lower driving speeds. Alternatively, one can increase the aggregation scale, with the drawback of less spatial resolution of the resulting soil moisture map. However, this led only to a slight reduction in RMSE (e.g., aggregation of 36 measurements led to a RMSE of 0.018 m^3/m^3). Since further aggregation only had a minor influence on the RMSE, we attribute the remaining part of the RMSE to other influences. Important additional sources of error were the spatial variability in bulk density, the heterogeneous vegetation, roads of different size and nature, as well as the inconsistency between *in-situ* and CRN rover measurements (both in time and depth).

Experiment C (Oklahoma Site)

Figure 9 provides an overview of the data from Dong and Ochsner (2018) with 800, 1,600, and 2,400 m aggregation length for soil moisture content, expected standard deviation as well as the relative standard deviation ($\frac{\sigma_{\theta_v}}{\theta_v}$). Using the original aggregation to 800 m, the mean soil moisture was 0.19 m^3/m^3 and the estimated mean standard deviation for all CRN rover measurements was 0.039 m^3/m^3, which is still below the error benchmark of 0.04 m^3/m^3 defined for the soil moisture active passive (SMAP) satellite mission (Chan et al., 2014). However, both soil moisture and the estimated standard deviation were spatially and temporally variable (**Figure 9**, upper and middle panel). As expected, the soil moisture and standard deviation of soil moisture showed a very similar pattern (**Figure 9**, upper and middle panel), while the relative standard deviation showed a different pattern (**Figure 9**, lower panel). There were two reason for this difference. First, some high relative standard deviation values were related to locations with only a few measurements within one pixel, which appear as red stripes across most measurement days in the lower panel of **Figure 9**. Second, measurement days with low soil moisture content and relatively low standard deviation nevertheless showed high relative errors. This is in line with the high relative uncertainty we found for the Selhausen site (Experiment B). Measurement days with high soil moisture and relatively high standard deviation nevertheless showed lower relative errors (**Figure 9**, compare driest and wettest measurement date). With increasing aggregation length, sharp transitions in soil moisture estimates of neighboring pixels are reduced (**Figure 9**, top panel) and both the absolute (**Figure 9**,

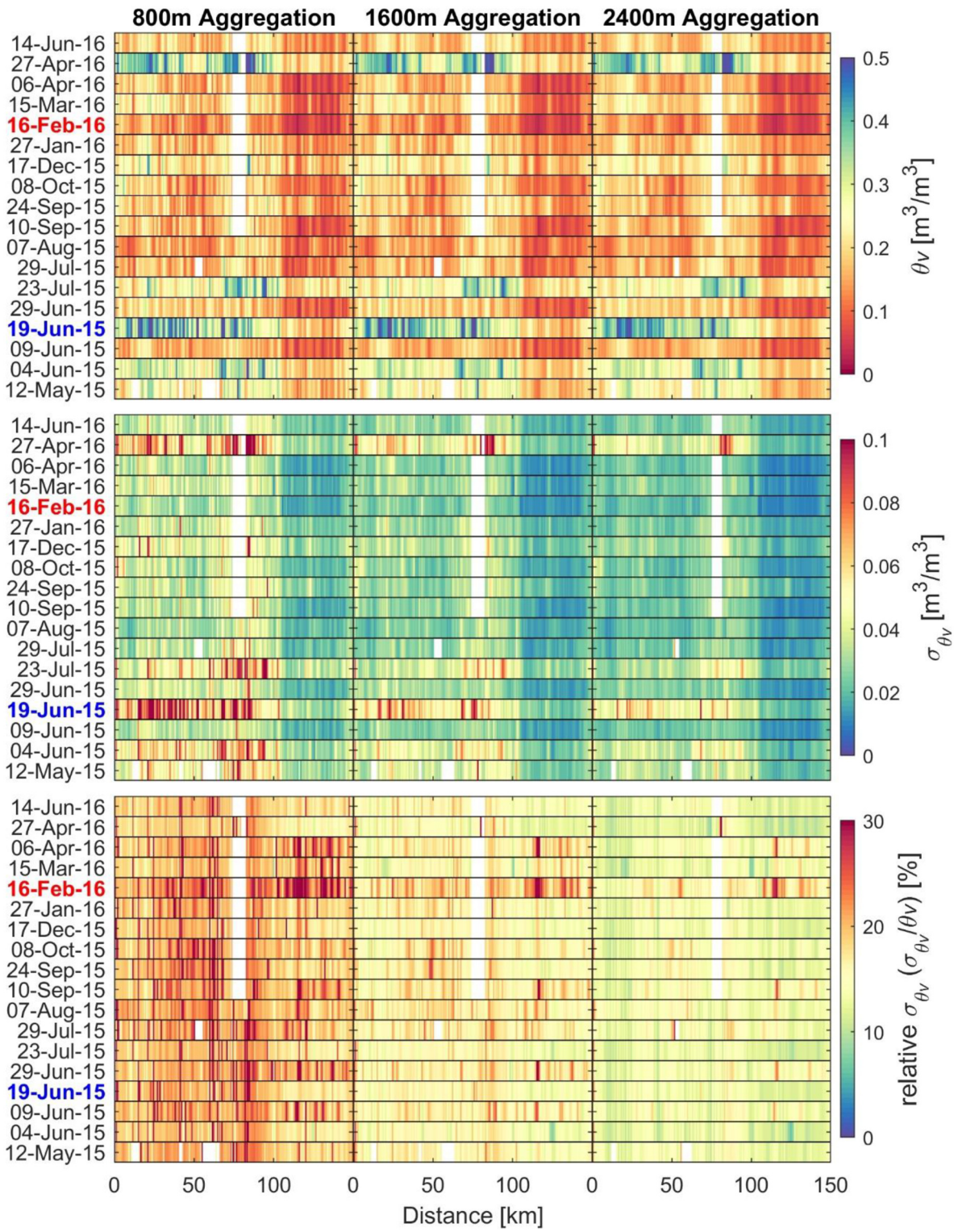

FIGURE 9 | Soil moisture (θ_v), uncertainty of soil moisture from neutron counts (σ_{θ_v}) approximated using a 3rd order Taylor expansion approach and relative standard deviation ($\frac{\sigma_{\theta_v}}{\theta_v}$) using 800, 1,600, and 2,400 m aggregation along the measurement transects in Oklahoma. White patches are areas not covered during a measurement date due to road closures (Dong and Ochsner, 2018). Blue and red dates indicate the wettest and driest measurement dates, respectively.

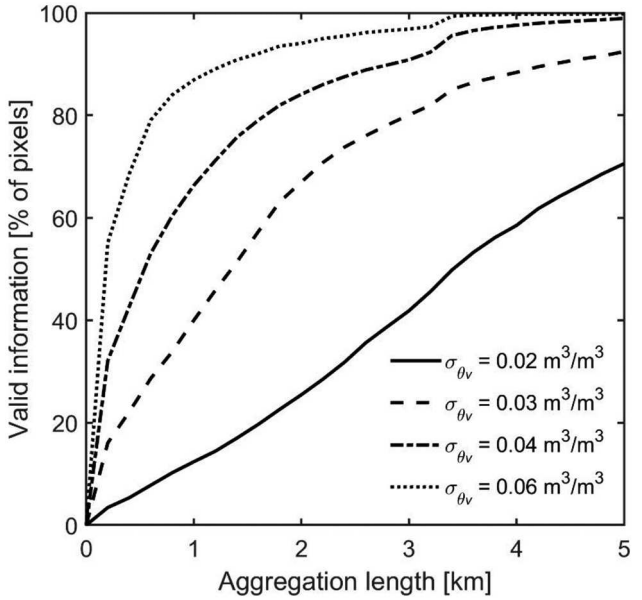

FIGURE 10 | Percentage of pixels with soil moisture uncertainty from neutron counts (σ_{θ_v}) ≤ 0.02, 0.03, 0.04, and 0.06 m^3/m^3 standard deviation as a function of aggregation length.

middle panel) and relative standard deviation of soil moisture (**Figure 9**, lower panel) are reduced.

To evaluate the trade-off between aggregation length and expected standard deviation for the Oklahoma CRN rover data, we determined the proportion of pixels with an expected measurement uncertainty below 0.02, 0.03, 0.04, and 0.06 m^3/m^3 for different aggregation lengths (**Figure 10**). With increasing aggregation lengths, the number of pixels with valid information increased and this increase became stronger with increasing uncertainty thresholds. Less than 40% of the pixels had a measurement uncertainty below 0.03 m^3/m^3 for the original aggregation length of 800 m solely due to the neutron count uncertainty. This is consistent with the analysis of Dong and Ochsner (2018), who estimated the average measurement uncertainty for 800 m aggregation length as 0.03 g/g, which corresponds to ∼0.044 m^3/m^3. Only at locations with low soil moisture content (< ∼0.14 m^3/m^3), the expected measurement uncertainty was lower than 0.02 m^3/m^3. If all CRN rover locations were required to have a measurement uncertainty below 0.04 m^3/m^3, an aggregation length of more than 5 km would be necessary. However, already with 2,400 m aggregation length, the measurement uncertainty in the drier part of the measurement transect was lower than this (**Figure 9**, top and middle panel: km 110–150).

Although we cannot recommend a universal aggregation length, we believe that the presented uncertainty approximation approach can serve as a tool for assessing the best possible compromise between measurement accuracy and spatial resolution. It should be noted that it is not possible to determine the uncertainty without taking into account site conditions and rover specifications and that the presented uncertainties are best possible estimates as other sources of uncertainty have not yet been taken into account. In general, the aggregation length should be carefully tailored to the needs of users, the capabilities of the CRN rover and the site conditions. In addition to the uncertainty in the neutron count rate, further uncertainties in the soil moisture estimation with the dataset from Dong and Ochsner (2018) are worthwhile mentioning. First, the influence of vegetation on soil moisture estimates was not considered. Promising approaches for removing these influences are the use of airborne (e.g., Fersch et al., 2018) or satellite (e.g., Avery et al., 2016) derived biomass estimates. Second, the influence of roads was not considered, which most likely resulted in underestimation of soil moisture content in most measurement locations (Schrön et al., 2018b). Third, the derivation of lattice water (θ_{off}) and soil bulk density from uncertain soil maps, such as the SSURGO database, will introduce uncertainty in soil moisture estimation. However, this has been demonstrated in several other studies (e.g., Avery et al., 2016; McJannet et al., 2017) and is challenging to overcome. Fourth, soil organic carbon is an additional hydrogen pool in soils that should be considered for accurate soil moisture estimation (Franz et al., 2013). Regarding the influence of some of those environmental factors and their uncertainty, the reader is referred to Baroni et al. (2018).

CONCLUSION AND OUTLOOK

In this study, we quantified the uncertainty in soil moisture estimation with cosmic ray neutron measurements with an easy to use 3rd order Taylor expansion approach. The performance was evaluated using Monte Carlo simulations and experimentally determined measurement uncertainty and we found good agreement. Because of the typically short aggregation time and thus a low amount of neutron counts, soil moisture estimates obtained with cosmic ray neutron rover measurements are typically more uncertain than those obtained using stationary measurements. The proposed approach to approximate measurement uncertainty in soil moisture estimates has great potential for the planning and evaluation of rover experiments. It was shown that such uncertainty estimates can be used to find a suitable trade-off between measurement accuracy, aggregation, and the associated spatial resolution of the resulting soil moisture products.

The approach can also be used to design surveys with the cosmic ray neutron rover according to given accuracy requirements. We applied our error estimation approach to three cosmic ray neutron rover experiments and the major findings were:

- Measured and expected uncertainty matched well even with short aggregation periods.
- Uncertainty in soil moisture estimation from uncertainty in cosmic ray neutron counts can be reduced to only a fraction of the total measurement uncertainty if appropriate aggregation is used.

- The aggregation length of an experiment needs to be carefully selected based on the needs of the user, taken into account the site characteristics, and the cosmic ray neutron rover specifications.

DATA AVAILABILITY STATEMENT

The datasets generated for this study are available on request to the corresponding author.

AUTHOR CONTRIBUTIONS

JJ: rover data sampling and data processing, writing the manuscript, editing the manuscript, experimental design. JH and HB: supervision, reference data sampling, editing the manuscript, experimental design. MS: editing the manuscript, CRNS teaching. JF: reference data sampling, prepratory work, experimental design. CB: prepratory work, sample processing, editing the manuscript. HV: supervision.

FUNDING

This research was funded by the Deutsche Forschungsgemeinschaft (DFG, German Research Foundation)—project 357874777 of the research unit FOR 2694 Cosmic Sense. It also received supported from the MOSES (Modular Observation Solutions for Earth Systems) project funded by the Helmholtz-Gemeinschaft, which provided funding for the Jülich CRN rover. We also acknowledge the NMDB database funded by EU-FP7.

ACKNOWLEDGMENTS

We thank Jingnuo Dong and Tyson Ochsner for making their dataset publicly available and for updating it for this work. Carsten Montzka, Bernd Schilling, Daniel Dolfus, and Ansgar Weuthen are thanked for supporting the reference measurements at the Selhausen test site and Benjamin Fersch is thanked for the organization of the measurement campaign at the Fendt test site. Furthermore, we thank the two reviewers for their constructive feedback and suggestions.

REFERENCES

Andreasen, M., Jensen, K. H., Desilets, D., Franz, T., Zreda, M., Bogena, H. R., et al. (2017). Status and perspectives of the cosmic-ray neutron method for soil moisture estimation and other environmental science applications. *Vadose Zone J.* 16:4079. doi: 10.2136/vzj2017.04.0086

Avery, W. A., Finkbeiner, C., Franz, T. E., Wang, T., Nguy-Robertson, A. L., Suyker, A., et al. (2016). Incorporation of globally available datasets into the roving cosmic-ray neutron probe method for estimating field-scale soil water content. *Hydrol. Earth Syst. Sci.* 20, 3859–3872. doi: 10.5194/hess-20-3859-2016

Baatz, R., Bogena, H. R., Hendricks Franssen, H.-J., Huisman, J. A., Qu, W., Montzka, C., et al. (2014). Calibration of a catchment scale cosmic-ray probe network: a comparison of three parametrization methods. *J. Hydrol.* 516, 231–244. doi: 10.1016/j.jhydrol.2014.02.026

Baatz, R., Bogena, H. R., Hendricks Franssen, H-J., Huisman, J. A., Montzka, C., and Vereecken, H. (2015). An empirical vegetation correction for soil water content quantification using cosmic ray probes. *Water Resour. Res.* 51, 2030–2046. doi: 10.1002/2014WR016443

Baroni, G., Scheiffele, L. M., Schrön, M., Ingwersen, J., and Oswald, S. E. (2018). Uncertainty, sensitivity and improvements in soil moisture estimation with cosmic-ray neutron sensing. *J. Hydrol.* 564, 873–887. doi: 10.1016/j.jhydrol.2018.07.053

Bogena, H., Kunkel, R., Krüger, E., Zacharias, S., Pütz, T., Schwank, M., et al. (2012). TERENO — long-term monitoring network for terrestrial research. *Hydrol. Wasserb.* 56, 138–143.

Bogena, H. R., Huisman, J. A., Baatz, R., Hendricks Franssen, H-J., and Vereecken, H. (2013). Accuracy of the cosmic-ray soil water content probe in humid forest ecosystems: the worst case scenario. *Water Resour. Res.* 49, 5778–5791. doi: 10.1002/wrcr.20463

Bogena, H. R., Huisman, J. A., Hübner, C., Kusche, J., Jonard, F., Vey, S., et al. (2015). Emerging methods for non-invasive sensing of soil moisture dynamics from field to catchment scale: a review. *WIREs Water* 2, 635–647. doi: 10.1002/wat2.1097

Bogena, H. R., Montzka, C., Huisman, J. A., Graf, A., Schmidt, M., Stockinger, M., et al. (2018). The TERENO-Rur hydrological observatory: a multiscale multi-compartment research platform for the advancement of hydrological science. *Vadose Zone J.* 17, 1–22. doi: 10.2136/vzj2018.03.0055

Brakensiek, D. L., and Rawls, W. J. (1994). Soil containing rock fragments: effects on infiltration. *Catena* 23, 99–110. doi: 10.1016/0341-8162(94)90056-6

Brogi, C., Huisman, J. A., Herbst, M., Weihermüller, L., Klosterhalfen, A., Montzka, C., et al. (2020). Simulation of spatial variability in crop leaf area index and yield using agroecosystem modeling and geophysics-based quantitative soil information. *Vadose Zone J.* 19:e20009. doi: 10.1002/vzj2.20009

Brogi, C., Huisman, J. A., Pätzold, S., von Hebel, C., Weihermüller, L., Kaufmann, M. S., et al. (2019). Large-scale soil mapping using multi-configuration EMI and supervised image classification. *Geoderma* 335, 133–148. doi: 10.1016/j.geoderma.2018.08.001

Chan, S., Njoku, E. G., and Colliander, A. (2014). *Soil Moisture Active Passive (SMAP), Algorithm Theoretical Basis Document, Level 1C Radiometer Data Product, Revision A, 20 pp, Jet Propulsion Laboratory*. Pasadena, CA: California Institute of Technology.

Chrisman, B., and Zreda, M. (2013). Quantifying mesoscale soil moisture with the cosmic-ray rover. *Hydrol. Earth Syst. Sci.* 17, 5097–5108. doi: 10.5194/hess-17-5097-2013

Desilets, D., and Zreda, M. (2001). On scaling cosmogenic nuclide production rates for altitude and latitude using cosmic-ray measurements. *Earth Planet. Sci. Lett.* 193, 213–225. doi: 10.1016/S0012-821X(01)00477-0

Desilets, D., and Zreda, M. (2003). Spatial and temporal distribution of secondary cosmic-ray nucleon intensities and applications to *in situ* cosmogenic dating. *Earth Planet. Sci. Lett.* 206, 21–42. doi: 10.1016/S0012-821X(02)01088-9

Desilets, D., Zreda, M., and Ferré, T. P. A. (2010). Nature's neutron probe: land surface hydrology at an elusive scale with cosmic rays. *Water Resour. Res.* 46:W11505. doi: 10.1029/2009WR008726

Dong, J., and Ochsner, T. E. (2018). Soil texture often exerts a stronger influence than precipitation on mesoscale soil moisture patterns. *Water Resour. Res.* 54, 2199–2211. doi: 10.1002/2017WR021692

Dong, J., Ochsner, T. E., Zreda, M., Cosh, M. H., and Zou, C. B. (2014). Calibration and validation of the COSMOS rover for surface soil moisture measurement. *Vadose Zone J.* 13, 1–8. doi: 10.2136/vzj2013.08.0148

Ehlers, W., Köpke, U., Hesse, F., and Böhm, W. (1983). Penetration resistance and root growth of oats in tilled and untilled loess soil. *Soil Tillage Res.* 3, 261–275. doi: 10.1016/0167-1987(83)90027-2

Fentanes, J. P., Badiee, A., Duckett, T., Evans, J., Pearson, S., and Cielniak, G. (2019). Kriging-based robotic exploration for soil moisture mapping using a cosmic-ray sensor. *J. Field Robot.* 37, 122–136. doi: 10.1002/rob.21914

Fersch, B., Jagdhuber, T., Schrön, M., Völksch, I., and Jäger, M. (2018). Synergies for soil moisture retrieval across scales from airborne polarimetric SAR, cosmic ray neutron roving, and an *in situ* sensor network. *Water Resour. Res.* 54, 9364–9383. doi: 10.1029/2018WR023337

Finkenbiner, C. E., Franz, T. E., Gibson, J., Heeren, D. M., and Luck, J. (2019). Integration of hydrogeophysical datasets and empirical orthogonal

functions for improved irrigation water management. *Precis. Agric.* 20, 78–100. doi: 10.1007/s11119-018-9582-5

Flint, A. L., and Childs, S. (1984). Physical properties of rock fragments and their effect on available water in skeletal soils. *Erosion Prod. Soils Contain. Rock Frag.* 13, 91–103. doi: 10.2136/sssaspecpub13.c10

Franz, T. E., Wang, T., Avery, W., Finkenbiner, C., and Brocca, L. (2015). Combined analysis of soil moisture measurements from roving and fixed cosmic ray neutron probes for multiscale real-time monitoring. *Geophys. Res. Lett.* 42, 3389–3396. doi: 10.1002/2015GL063963

Franz, T. E., Zreda, M., Rosolem, R., and Ferre, T. P. A. (2012). Field validation of a cosmic-ray neutron sensor using a distributed sensor network. *Vadose Zone J.* 11:vzj2012.0046. doi: 10.2136/vzj2012.0046

Franz, T. E., Zreda, M., Rosolem, R., Hornbuckle, B. K., Irvin, S. L., Adams, H., et al. (2013). Ecosystem-scale measurements of biomass water using cosmic ray neutrons. *Geophys. Res. Lett.* 40, 3929–3933. doi: 10.1002/grl.50791

Fu, J., Gasche, R., Wang, N., Lu, H., Butterbach-Bahl, K., and Kiese, R. (2017). Impacts of climate and management on water balance and nitrogen leaching from montane grassland soils of S-Germany. *Environ. Pollut.* 229, 119–131. doi: 10.1016/j.envpol.2017.05.071

Gibson, J., and Franz, T. E. (2018). Spatial prediction of near surface soil water retention functions using hydrogeophysics and empirical orthogonal functions. *J. Hydrol.* 561, 372–383. doi: 10.1016/j.jhydrol.2018.03.046

Gugerli, R., Salzmann, N., Huss, M., and Desilets, D. (2019). Continuous and autonomous snow water equivalent measurements by a cosmic ray sensor on an alpine glacier. *Cryosphere* 13, 3413–3434. doi: 10.5194/tc-13-3413-2019

Jakobi, J., Huisman, J. A., Vereecken, H., Diekkrüger, B., and Bogena, H. R. (2018). Cosmic ray neutron sensing for simultaneous soil water content and biomass quantification in drought conditions. *Water Resour. Res.* 54, 7383–7402. doi: 10.1029/2018WR022692

Kiese, R., Fersch, B., Bassler, C., Brosy, C., Butterbach-Bahl, K., Chwala, C., et al. (2018). The TERENO-preAlpine observatory: integrating meteorological, hydrological and biogeochemical measurements and modelling. *Vadose Zone J.* 17:180060. doi: 10.2136/vzj2018.03.0060

Köhli, M., Schrön, M., and Schmidt, U. (2018). Response functions for detectors in cosmic ray neutron sensing. *Nucl. Instrum. Methods Phys. Res. B.* 902, 184–189. doi: 10.1016/j.nima.2018.06.052

Köhli, M., Schrön, M., Zreda, M., Schmidt, U., Dietrich, P., and Zacharias, S. (2015). Footprint characteristics revised for field-scale soil moisture monitoring with cosmic-ray neutrons. *Water Resour. Res.* 51, 5772–5790. doi: 10.1002/2015WR017169

Korres, W., Reichenau, T. G., Fiener, P., Koyama, C. N., Bogena, H. R., Cornelissen, T., et al. (2015). Spatio-temporal soil moisture patterns—a meta-analysis using plot to catchment scale data. *J. Hydrol.* 520, 326–341. doi: 10.1016/j.jhydrol.2014.11.042

McJannet, D., Hawdon, A., Baker, B., Renzullo, L., and Searle, R. (2017). Multiscale soil moisture estimates using static and roving cosmic-ray soil moisture sensors. *Hydrol. Earth Syst. Sci.* 21, 6049–6067. doi: 10.5194/hess-21-6049-2017

Mekid, S., and Vaja, D. (2008). Propagation of uncertainty: expressions of second and third order uncertainty with third and fourth moments. *Measurements* 41, 600–609. doi: 10.1016/j.measurement.2007.07.004

Reichenau, T. G., Korres, W., Montzka, C., Fiener, P., Wilken, F., Stadler, A., et al. (2016). Spatial heterogeneity of Leaf Area Index (LAI) and its temporal course on arable land: combining field measurements, remote sensing and simulation in a Comprehensive Data Analysis Approach (CDAA). *PLoS ONE* 11:e0158451. doi: 10.1371/journal.pone.0158451

Robinson, D. A., Campbell, C. S., Hopmans, J. W., Hornbuckle, B. K., Jones, S. B., Knight, R., et al. (2008). Soil moisture measurement for ecological and hydrological watershed-scale observatories: a review. *Vadose Zone J.* 7:358–389. doi: 10.2136/vzj2007.0143

Rosolem, R., Shuttleworth, W. J., Zreda, M., Franz, T. E., Zeng, X., and Kurc, S. A. (2013). The effect of atmospheric water vapor on the cosmic-ray soil moisture signal. *J. Hydrometeorol.* 14, 1659–1671. doi: 10.1175/JHM-D-12-0120.1

Rudolph, S., van der Kruk, J., von Hebel, C., Ali, M., Herbst, M., Montzka, C., et al. (2015). Linking satellite derived LAI patterns with subsoil heterogeneity using large-scale ground-based electromagnetic induction measurements. *Geoderma* 241-242, 262–271. doi: 10.1016/j.geoderma.2014.11.015

Schrön, M. (2017). *Cosmic-ray Neutron Sensing and Its Applications to Soil and Land Surface Hydrology — on Neutron Physics, Method Development, and Soil Moisture Estimation Across Scales* (Ph.D. dissertation). University of Potsdam. pp. 224.

Schrön, M., Köhli, M., Scheiffele, L., Iwema, J., Bogena, H. R., Lv, L., et al. (2017). Improving calibration and validation of cosmic-ray neutron sensors in the light of spatial sensitivity — theory and evidence. *Hydrol. Earth Syst. Sci.* 21, 5009–5030. doi: 10.5194/hess-21-5009-2017

Schrön, M., Rosolem, R., Köhli, M., Piussi, L., Schröter, I., Iwema, J., et al. (2018b). Cosmic-ray neutron rover surveys of field soil moisture and the influence of roads. *Water Resour. Res.* 54, 6441–6459. doi: 10.1029/2017WR021719

Schrön, M., Zacharias, S., Womack, G., Köhli, M., Desilets, D., Oswald, S. E., et al. (2018a). Intercomparison of cosmic-ray neutron sensors and water balance monitoring in an urban environment. *Geosc. Instrum. Method Data Syst.* 7, 83–89. doi: 10.5194/gi-7-83-2018

Tian, Z. C., Li, Z. Z., Liu, G., Li, B. G., and Ren, T. S. (2016). Soil water content determination with cosmic-ray neutron sensor: correcting aboveground hydrogen effects with thermal/fast neutron ratio. *J. Hydrol.* 540, 923–933. doi: 10.1016/j.jhydrol.2016.07.004

Unger, P. W., and Jones, O. R. (1998). Long-term tillage and cropping systems affect bulk density and penetration resistance of soil cropped to dryland wheat and grain sorghum. *Soil Tillage Res.* 45, 39–57. doi: 10.1016/S0167-1987(97)00068-8

Vather, T., Everson, C., Mengistu, M., and Franz., T. (2019). Cosmic ray neutrons provide an innovative technique for estimating intermediate scale soil moisture. *S. Afr. J. Sci.* 114, 7–8. doi: 10.17159/sajs.2018/20170422

Vereecken, H., Huisman, J. A., Bogena, H., Vanderborght, J., Vrugt, J. A., and Hopmans, J. W. (2008). On the value of soil moisture measurements in vadose zone hydrology: a review. *Water Resour. Res.* 44:W00D06. doi: 10.1029/2008WR006829

Vereecken, H., Huisman, J. A., Hendricks Franssen, H. J., Brüggemann, N., Bogena, H. R., Kollet, S., et al. (2015). Soil hydrology: recent methodological advances, challenges, and perspectives. *Water Resour. Res.* 51, 2616–2633. doi: 10.1002/2014WR016852

Weihermüller, L., Huisman, J. A., Lambot, S., Herbst, M., and Vereecken, H. (2007). Mapping the spatial variation of soil water content at the field scale with different ground penetrating radar techniques. *J. Hydrol.* 340, 205–216. doi: 10.1016/j.jhydrol.2007.04.013

Wolf, B., Chwala, C., Fersch, B., Garvelmann, J., Junkermann, W., Zeeman, M. J., et al. (2016). The ScaleX campaign: scale-crossing land-surface and boundary layer processes in the TERENO-preAlpine observatory. *Bull. Am. Meteorol. Soc.* 98, 1217–1234. doi: 10.1175/BAMS-D-15-00277.1

Zacharias, S., Bogena, H. R., Samaniego, L., Mauder, M., Fuss, R., Puetz, T., et al. (2011). A network of terrestrial environmental observatories in Germany. *Vadose Zone J.* 10, 955–973. doi: 10.2136/vzj2010.0139

Zreda, M., Desilets, D., Ferré, T. P. A., and Scott, R. L. (2008). Measuring soil moisture content non-invasively at intermediate spatial scale using cosmic-ray neutrons. *Geophys. Res. Lett.* 35:L21402. doi: 10.1029/2008GL035655

Zreda, M., Shuttleworth, W. J., Zeng, X., Zweck, C., Desilets, D., Franz, T. E., et al. (2012). COSMOS: the COsmic-ray soil moisture observing system. *Hydrol. Earth Syst. Sci.* 16, 4079–4099. doi: 10.5194/hess-16-4079-2012

Conflict of Interest: The authors declare that the research was conducted in the absence of any commercial or financial relationships that could be construed as a potential conflict of interest.

frontiers in Water

CORRECTION
published: 26 November 2020
doi: 10.3389/frwa.2020.604482

Corrigendum: Error Estimation for Soil Moisture Measurements With Cosmic Ray Neutron Sensing and Implications for Rover Surveys

Jannis Jakobi[1], Johan A. Huisman[1], Martin Schrön[2], Justus Fiedler[1], Cosimo Brogi[1], Harry Vereecken[1] and Heye R. Bogena[1]*

[1] Agrosphere Institute (IBG-3), Forschungszentrum Jülich GmbH, Jülich, Germany, [2] Department of Monitoring and Exploration Technologies, Helmholtz-Zentrum für Umweltforschung GmbH-UFZ, Leipzig, Germany

Keywords: cosmic ray neutron sensing, error propagation, aggregation, cosmic ray rover, uncertainty

A Corrigendum on

Error Estimation for Soil Moisture Measurements With Cosmic Ray Neutron Sensing and Implications for Rover Surveys

by Jakobi, J., Huisman, J. A., Schrön, M., Fiedler, J., Brogi, C., Vereecken, H., et al. (2020). Front. Water 2:10. doi: 10.3389/frwa.2020.00010

In the original article, there was an error in the simplification of Equations (8) and (9) to Equation (10). A correction has been made to Equation (10):

$$\sigma_{\theta_g}(N) = \sigma_N \frac{a_0 N_0}{(N_{cor} - a_1 N_0)^4} \sqrt{(N_{cor} - a_1 N_0)^4 + 8\sigma_N{}^2 (N_{cor} - a_1 N_0)^2 + 15\sigma_N{}^4} \qquad (10)$$

In the original article, there were mistakes in **Figures 5** and **8** as published. The analytical uncertainty estimates were derived wrongly. The corrected **Figures 5** and **8** appear below.

The corrected **Figure 5** requires update of the description in the text. A correction has been made to the Results and Discussion section, Experiment A (Fendt site), paragraph 2:

"[…] With the exception of sections 5, 9 and 10, all sections showed good agreement between the expected and measured uncertainty of soil moisture. […]"

The corrected **Figure 8** requires update of the description in the text. A correction has been made to the Results and Discussion section, Experiment B (Selhausen site), paragraph 5:

"[…] However, the expected soil moisture estimation uncertainty using Selhausen site conditions (**Figure 8**) were similar to the overall uncertainty as expressed by the RMSE when only 3 measurements were used (0.032 m^3/m^3). This is undesirable and suggests the need for more aggregation. When nine measurements were aggregated, the average uncertainty due to uncertain neutron measurements decreased to 0.017 m^3/m^3 irrespective of aggregation strategy. […]"

The authors apologize for these errors and state that this does not change the scientific conclusions of the article in any way. The original article has been updated.

OPEN ACCESS

Edited by:
Jianzhi Dong, United States Department of Agriculture, United States

Reviewed by:
Trenton Franz, University of Nebraska-Lincoln, United States

****Correspondence:***
Jannis Jakobi
j.jakobi@fz-juelich.de

Specialty section:
This article was submitted to Water and Hydrocomplexity, a section of the journal Frontiers in Water

Received: *09 September 2020*
Accepted: *22 October 2020*
Published: *26 November 2020*

Citation:
Jakobi J, Huisman JA, Schrön M, Fiedler J, Brogi C, Vereecken H and Bogena HR (2020) Corrigendum: Error Estimation for Soil Moisture Measurements With Cosmic Ray Neutron Sensing and Implications for Rover Surveys. Front. Water 2:604482. doi: 10.3389/frwa.2020.604482

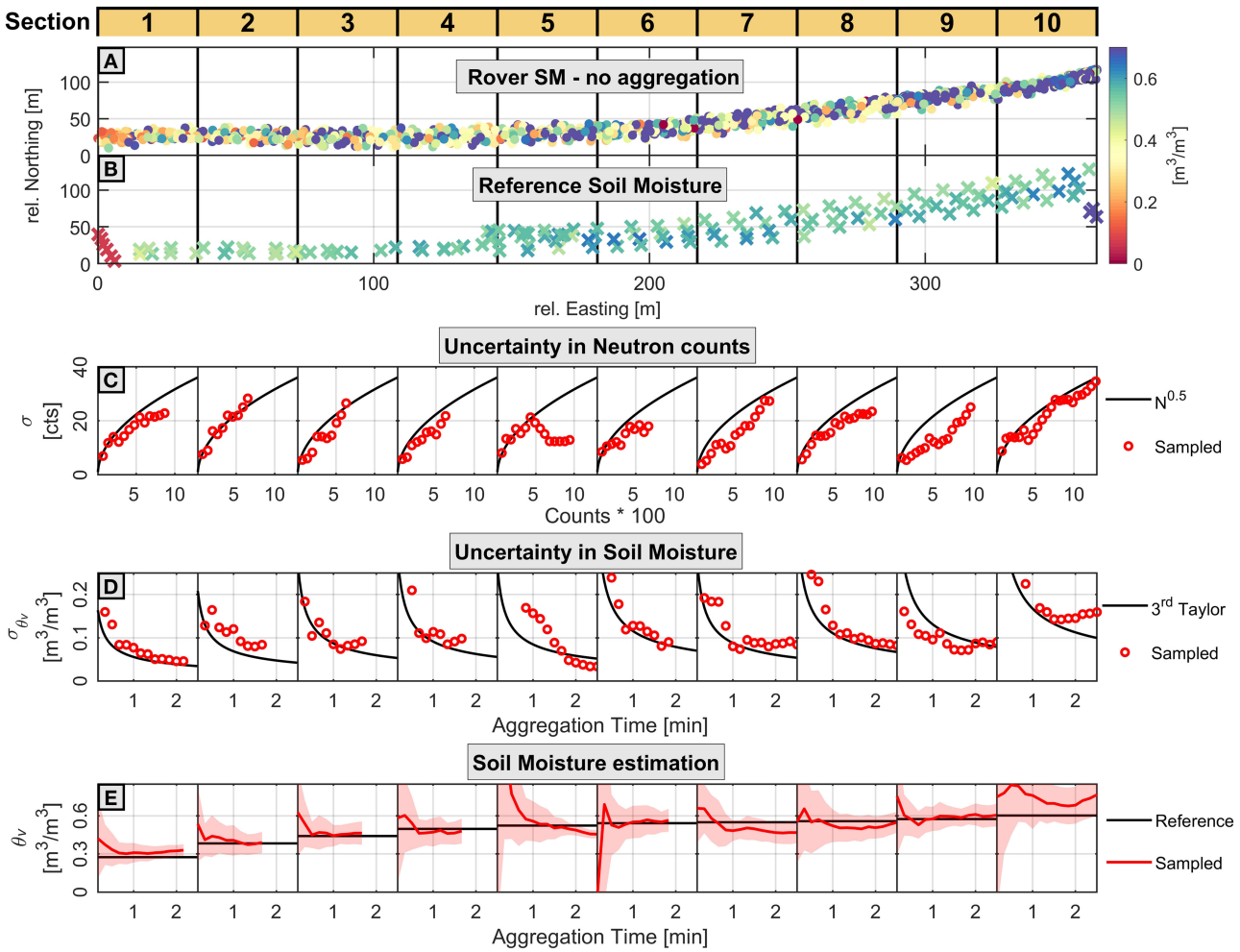

FIGURE 5 | Overview of the results from the Fendt experiment for each of the ten analyzed sections. **(A)** CRN rover soil moisture without aggregation. **(B)** *In-situ* reference soil moisture. The relative coordinates in panels a and b were calculated from UTM coordinates. **(C)** Expected standard deviation of raw neutron counts (σ). **(D)** 3rd order approximation of standard deviation of soil moisture from raw neutron counts (σ_{θ_v}) in comparison to measured standard deviation with the CRN rover. **(E)** Soil moisture (θ_v) estimated with the CRN rover in comparison with mean reference soil moisture content for each section. Red area indicates ± one measured standard deviation of the mean.

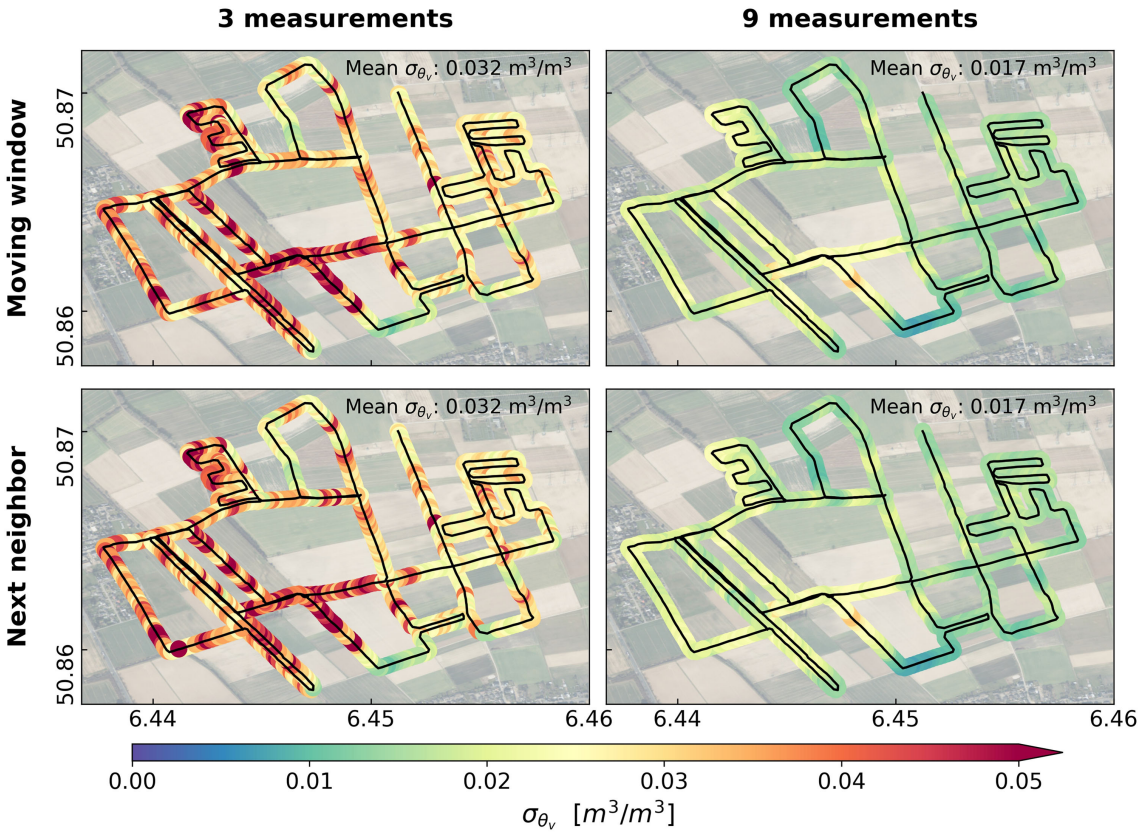

FIGURE 8 | Comparison of soil moisture uncertainty from neutron counts (σ_{θ_v}) estimation with four aggregation strategies with the Jülich CRN rover at the Selhausen site with data measured on 11 July 2018. Top panels: moving window aggregation for three and nine following measurements, respectively. Bottom panels: nearest neighbor aggregation with the nearest two and eight neighbors, respectively. Base maps: ESRI World Imagery and Contributors.

frontiers in Water

ORIGINAL RESEARCH
published: 04 August 2020
doi: 10.3389/frwa.2020.00019

Monitoring of Snowpack Dynamics With Cosmic-Ray Neutron Probes: A Comparison of Four Conversion Methods

Heye R. Bogena[1], Frank Herrmann[1], Jannis Jakobi[1], Cosimo Brogi[1], Andreas Ilias[2], Johan Alexander Huisman[1], Andreas Panagopoulos[2] and Vassilios Pisinaras[2]*

[1] Agrosphere IBG-3, Forschungszentrum Jülich GmbH, Jülich, Germany, [2] Soil and Water Resources Institute, Hellenic Agricultural Organization "DEMETER", Thessaloniki, Greece

Common snow monitoring instruments based on hydrostatic pressure such as snow pillows are often influenced by various disturbing effects, which result in a reduced quality of the snow cover and snow water equivalent estimates. Such disturbing effects include energy transport into the snowpack, wind fields, and variations of snow properties within the snowpack (e.g., ice layers). Recently, it has been shown that Cosmic-Ray Neutron Probes (CRNP) are a promising technique to monitor snow pack development. CRNP can provide larger support and need lower maintenance compared to conventional sensors. These instruments are sensitive to the intensity of epithermal neutrons that are produced in the soil by cosmic radiation and are widely used to determine soil moisture in the upper decimeters of the ground. The application of CRNP for snow monitoring is based on the principle that snow water moderates the epithermal neutron intensity, which can be directly related to the snow water equivalent (SWE) of the snow pack. In this study, long-term CRNP measurements in the Pinios Hydrologic Observatory (PHO), Greece, were used to test different methods for converting neutron count rates to snow pack characteristics: (i) linear regression, (ii) standard N_0-calibration function, (iii) a physically-based calibration approach, and (iv) thermal to epithermal neutron ratio. For this, a sonic sensor located near the CRNP was used to compare CRNP-derived snow pack dynamics with snow depth measurements. We found that the above-ground CRNP is well-suited for measurement of field scale SWE, which is in agreement with findings of other studies. The analysis of the accuracy of the four conversion methods showed that all methods were able to determine the mass of the snow pack during the snow events reasonably well. The N_0-calibration function and the physically-based calibration function performed best and the thermal to epithermal neutron ratio performed worst. Furthermore, we found that SWE determination with above-ground CRNP can be affected by other influences (e.g., heavy rainfall). Nevertheless, CRNP-based SWE determination is a potential alternative to established method like snow depth-based SWE methods, as it provides SWE estimate for a much larger scales (12–18 ha).

Keywords: cosmic-ray neutron probe, snow pack monitoring, snow water equivalent, snow depth, conversion methods, Pinios Hydrologic Observatory

OPEN ACCESS

Edited by:
Shaomin Liu,
Beijing Normal University, China

Reviewed by:
Trenton Franz,
University of Nebraska-Lincoln, United States
Hongyi Li,
Northwest Institute of Eco-Environment and Resources (CAS), China

****Correspondence:***
Heye R. Bogena
h.bogena@fz-juelich.de

Specialty section:
This article was submitted to Water and Hydrocomplexity, a section of the journal Frontiers in Water

Received: *20 March 2020*
Accepted: *25 June 2020*
Published: *04 August 2020*

Citation:
Bogena HR, Herrmann F, Jakobi J, Brogi C, Ilias A, Huisman JA, Panagopoulos A and Pisinaras V (2020) Monitoring of Snowpack Dynamics With Cosmic-Ray Neutron Probes: A Comparison of Four Conversion Methods. Front. Water 2:19. doi: 10.3389/frwa.2020.00019

INTRODUCTION

Snow accumulation dynamics are an important indicator of climate change development as it can be used to investigate modifications in precipitation patterns as well as the occurrence of increasingly strong snowmelt events that are caused by rising global temperatures (Kripalani and Kulkarni, 1999; Earman et al., 2006). A recent study showed that snow accumulation is dramatically decreasing over Europe (Fontrodona Bach et al., 2018), which has strong implications for the availability of freshwater (Earman et al., 2006; Akyurek et al., 2011). Unfortunately, data on snow dynamics are still rare because they are difficult to collect and generally distributed over rather inhomogeneous data bases (Kripalani and Kulkarni, 1999; Sun et al., 2004; Deems et al., 2013). Monitoring of snow water equivalent (SWE) in mountainous environments is particularly challenging because snow distribution is strongly and non-linearly related to topographic features such as slope and aspect (Pimentel et al., 2015). Therefore, more information on snow accumulation and melting is needed in climate research, especially for mountainous regions (Fontrodona Bach et al., 2018).

Various devices measuring temporal dynamics of SWE are available, all of which have their strengths and limitations (Pirazzini et al., 2018). Commonly, these devices are based on the measurement of the mass or of the pressure of the overlying snow (e.g., snow cushions and snow scales). Therefore, they are sometimes not well-suited for mountainous regions since they require a large and flat surface for installation (Kinar and Pomeroy, 2015). More sophisticated devices include sub-snow GPSs and ground-penetrating radar (GPR) (Koch et al., 2019). The first method uses two GPS antennas placed below and above the snowpack. Since the GPS signal is affected by the snow cover, the difference between the signals received by the two instruments can be used to quantify SWE. However, the strength of the GPS signal may be limited in mountainous regions depending on slope and location (Koch et al., 2019). In the case of GPR, upward-facing systems are placed below the snowpack to obtain information about snow stratigraphy (Heilig et al., 2009) and snow depth (Schmid et al., 2014). With this technique, the penetration depth strongly depends on the measurement frequency of the GPR system. Generally, high frequency instruments result in higher resolution but are also affected by higher attenuation, thus resulting in reduced depth of penetration. It has long been recognized that airborne gamma radiation surveys with low-flying airplanes can be used to determine snow water equivalent (Peck et al., 1971; Lundberg et al., 2010; Kinar and Pomeroy, 2015). However, high costs and low repeat frequencies hamper the use of airborne techniques. More recently, aboveground gamma-ray scintillators have been suggested to continuously monitor snow pack development (Choquette et al., 2013). A detailed list of instruments for measuring snow properties and their strengths and limitations can be found in Pirazzini et al. (2018).

In the past decade, the Cosmic-Ray Neutron Probe (CRNP) method has emerged as a promising method to non-invasively monitor soil moisture. This method is based on cosmic background radiation and uses the inverse relationship between hydrogen content and cosmic-ray neutron intensity near the soil surface (Zreda et al., 2012). Worldwide, ∼200 stationary CRNP have been installed since the introduction of the method in 2008 (Bogena et al., 2015; Andreasen et al., 2017a). Neutrons are sensitive to all sources of hydrogen at the land surface. Therefore, the CRNP method has the potential to measure not only soil moisture but SWE as well. This can be achieved, for example, with a CRNP placed below the snow cover (Kodama et al., 1979; Kodama, 1980; Gugerli et al., 2019). The buried CRNP records the intensity of downward-directed secondary cosmic radiation that penetrates the snow pack, thus providing a response area of up to a few square meters. Alternatively, the CRNP can be placed a few meters above the snow surface (Desilets et al., 2010; Sigouin and Si, 2016; Desilets, 2017; Schattan et al., 2017). As soon as the snowpack is formed, this becomes the dominant control on neutron intensity. Even in the case of small amounts of snow, the concentrated hydrogen layer effectively absorbs fast neutrons reflected from the ground (Desilets et al., 2010). For example, 1 cm of SWE can reduce the neutron count rate by ∼10% depending on the soil moisture under the snow cover (Andreasen et al., 2017b). A CRNP placed above the snow cover is influenced by snow up to more than 150 m away from the sensor (Zweck et al., 2013), thus enabling the characterization of larger scale and heterogeneous snow cover dynamics (Desilets et al., 2010).

Several studies already showed the potential of CRNP for snow pack monitoring. For example, a time series of SWE derived from fast neutron intensity corresponded well to snow measurements obtained within the detector footprint and to nearby snow depth measurements (Sigouin and Si, 2016). In a subsequent study, Schattan et al. (2017) determined non-linear regression functions to link both snow depth and SWE to fast neutron intensity. As in the case of all SWE monitoring methods, the CRNP technique has its limitations as well. First, the CRNP method cannot differentiate SWE dynamics from soil moisture dynamics. Second, there is a limited range of SWE that can be detected with the CRNP method. Based on neutron transport modeling, Desilets (2017) suggested that the upper limit should be about 100–150 mm SWE. For an alpine site with high neutron counts rates (>5,000 counts per hour), Schattan et al. (2017) found empirical evidence that the fast neutron intensity measured above the snow cover still shows snow-induced signals up to 600 mm SWE. However, the uncertainty of the CRNP measurements of snow height and SWE increased strongly with increasing snow cover, such that acceptable uncertainty was achieved up to 300 mm SWE only. According to Schattan et al. (2019), the footprint of the CRNP is anisotropic and affected by the spatial distribution of liquid water and snow as well as by the topography of the nearby mountains. Nevertheless, they found that the CRNP is able to accurately estimate SWE without prior knowledge about snow density profiles or other spatial anomalies when the snow cover is closed.

The studies mentioned above converted neutron intensity measurements to SWE with different approaches, including empirical linear regression functions (Sigouin and Si, 2016), a recalibrated version of the standard N_0-calibration function

(Schattan et al., 2017) and a more physically based approach by Desilets (2017). However, to date, there is no consensus on which method is best suited to convert neutron intensity data into SWE. In addition, these studies applied the conversion methods mostly to single snow events and not continuously over a period of several years.

The aim of this paper is to evaluate the accuracy of the CRNP method for measuring SWE dynamics at a test site situated in the Pinios Hydrologic Observatory (PHO)—central Greece. To this end, four different methods to convert neutron count rates to snow pack dynamics are tested based on a long-term time series of CRNP measurements (∼3 years).

PINIOS HYDROLOGIC OBSERVATORY - THE CS3 TEST SITE

The experimental test site CS3 investigated in this study is part of the PHO, which covers an area of ∼45 km² and is located at the eastern boundary of the Pinios River Basin in the municipality of Agia, Greece (**Figure 1**). The Pinios river basin is one of the most productive agricultural areas in the country and irrigation practices are responsible for more than 80% of the total fresh water consumption, leading to overuse of groundwater (Pisinaras et al., 2018). The mountain ranges framing the basin are responsible for the majority of groundwater recharge of the aquifer systems (Panagopoulos et al., 2015). Therefore, an accurate assessment of precipitation as rainfall and snow is important for efficient and sustainable water management, in particular with regard to the impacts of climate change (Panagopoulos et al., 2016). In order to support these efforts, the mGROWA model (Herrmann et al., 2015) has recently been applied in the Pinios river basin (Panagopoulos et al., 2018). First analyses of simulation results and associated uncertainties revealed a lack of continuously available climatic data including snowpack data for model calibration purposes, which was the main motivation to establish the Pinios Hydrologic Observatory (Pisinaras et al., 2018).

The CS3 test site was established in April 2017 at an elevation of 1,031 m (**Figure 2**) on a south-facing slope that ranges between 5° and 25°. The soil was classified as a lithic leptosol with varying rock content depending on the slope inclination and occasionally bare rock outcrops. Approximately 90% of the site is covered by medium to high Mediterranean scrubland (Phrygana) and 10% by grass and herbs. The CS3 site is characterized by Mediterranean climate with dry and hot summers, and precipitation concentrated in winter. Due to the high altitude, significant amounts of winter precipitation occur as snow even though snow cover often exists only for a few days.

The CS3 test site is equipped with a fully autonomous climate station. A heated weighing precipitation gauge (Pluvio², OTT Hydromet GmbH, Germany) was used to perform high precision monitoring of both liquid and solid precipitation. This system features an automated heating device that reliably keeps the orifice rim free of snow and ice during freezing temperatures. Other instruments of the climate station that were used in this study are: (i) an ultrasonic sensor (USH-8, Sommer GmbH & Co KG, Austria) mounted on a pole at 3 m height to observe snow depth, (ii) a weather multi-sensor (WXT520, Vaisala Oyj, Finland) measuring air temperature, wind speed and direction, atmospheric pressure, and relative air humidity, and (iii) a net radiometer (NR Lite2 net, Kipp & Zonen B.V., The Netherlands) measuring net radiation.

The soil moisture observation system established at CS3 comprises three wireless *in-situ* soil moisture stations (SoilNet, Forschungszentrum Jülich, Germany; Bogena et al., 2010) and one CRNP (CRS-2000/B, Hydroinnova LLC, Albuquerque, United States). Each SoilNet station consists of six SMT100 soil moisture/temperature sensors (Truebner GmbH, Germany), which are calibrated according to Bogena et al. (2017) and installed in pairs at 5, 20, and 50 cm depth. The SoilNet data are recorded and transmitted at 15-min intervals, while the CRNP records hourly neutron counts. The CRNP probe is equipped with two detector tubes that are filled with $^{10}BF_3$ enriched gas to obtain high neutron absorption cross sections. When neutrons enter the detector tube, the detector gas absorbs part of the neutrons and generates electrical currents that are counted by a pulse module (Zreda et al., 2012). The thermal detector of the CRS 2000/B probe is sensitive to neutrons with a maximum energy of ∼0.025 eV, whereas the moderated detector measures neutrons within the energy range from ∼0.2 eV to 100 keV. The CRNP and one of the SoilNet stations are installed a few meters away from the climate station on a grassy clearing within a fence (**Figure 2**), whereas the other two SoilNet stations measure soil moisture beneath the surrounding scrubs (**Figure 1**). The quality-checked time series data measured by all the above mentioned sensors is publicly available via a sensor observation service at https://deos-id.org:8000/20.500.11952/DEOS/PHO.

METHODS

Neutron Intensity Correction

The ground level neutron intensity is affected by variations in barometric pressure, solar activity (incoming cosmic radiation), and atmospheric water vapor (Zreda et al., 2012). These unwanted fluctuations are addressed by applying a correction factor *F(t)*:

$$N_{cor} = N_{raw} \cdot F(t) \tag{1}$$

where N_{cor} is the corrected moderated neutron intensity in counts per hour (cph), and N_{raw} is the raw neutron intensity in cph. The correction factor *F(t)* can be decomposed into individual correction factors for barometric pressure (f_{bar}), solar activity (f_{sol}), and atmospheric humidity (f_{hum}). The total correction factor is then (Andreasen et al., 2017b):

$$F(t) = f_{bar} \cdot f_{sol} \cdot f_{hum} \tag{2}$$

Local measurements of atmospheric pressure and humidity were used to determine f_{bar} and f_{hum} whereas data from the neutron

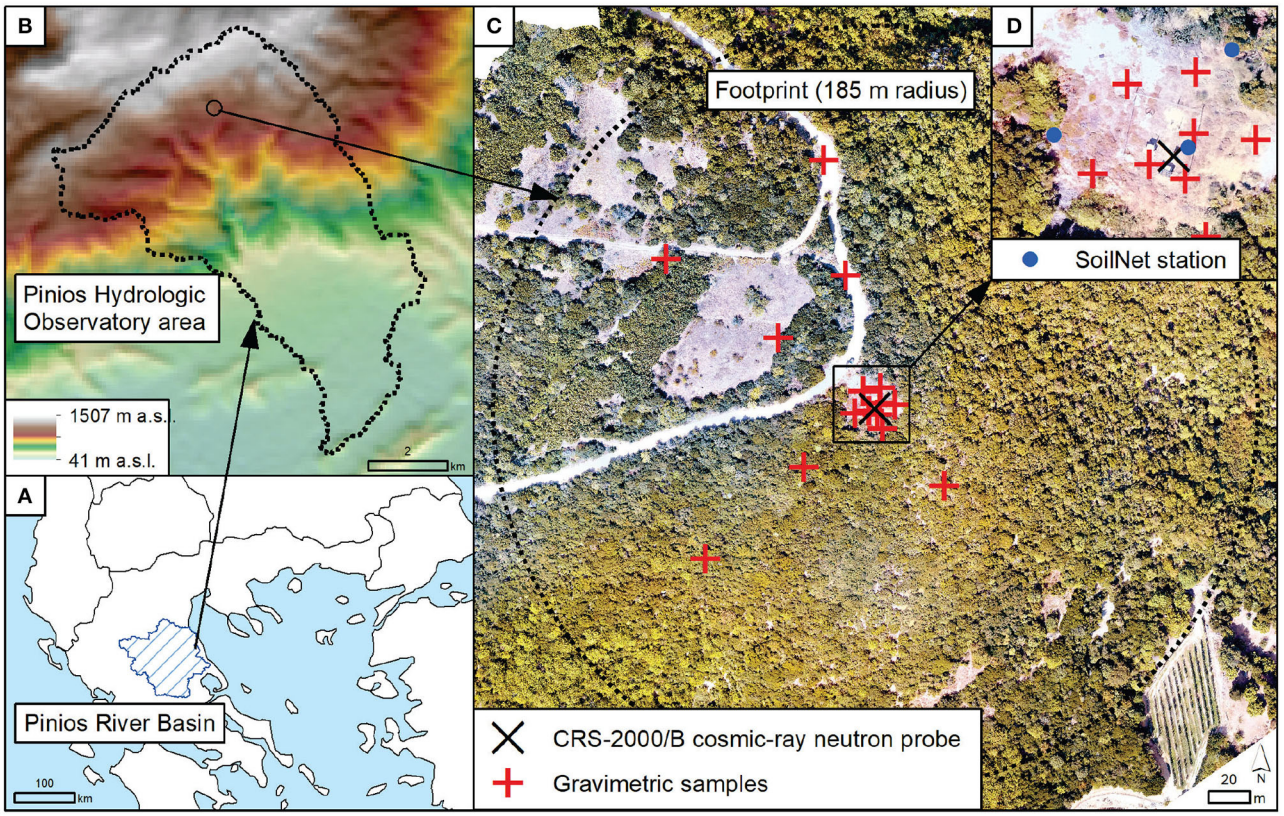

FIGURE 1 | Overview of the study area showing: **(A)** the extension of the Pinios River Basin, **(B)** the extension and topography of the Pinios Hydrologic Observatory, **(C)** a drone image of the CS3 test site and the footprint area of the CRNP with the locations of the gravimetric samples, and **(D)** the locations of the SoilNet stations.

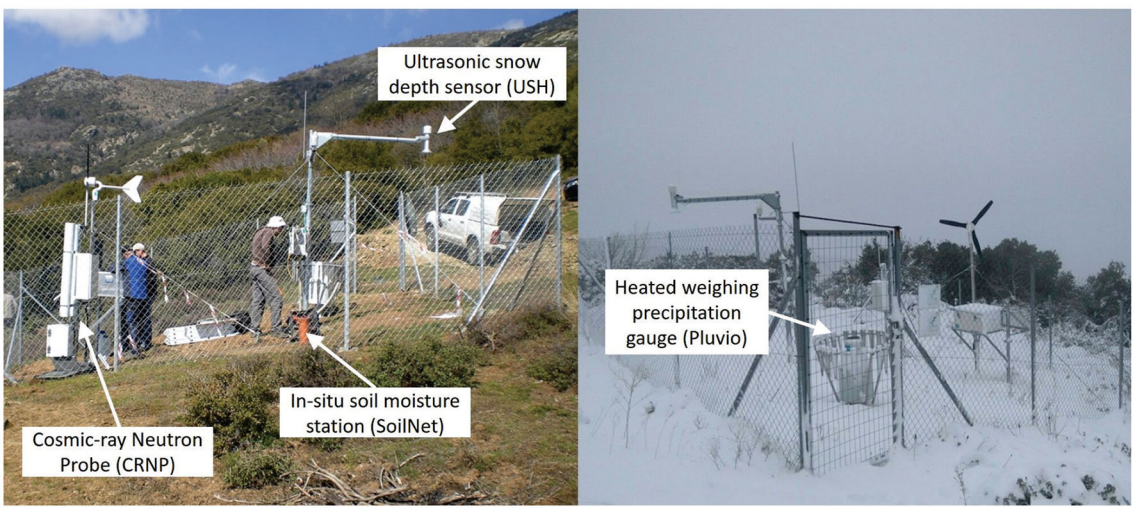

FIGURE 2 | The CS3 test site during installation in spring 2017 **(Left)** and in the winter period on November 30, 2018 **(Right)**.

monitor at the Jungfraujoch were used to determine f_{sol} (Zreda et al., 2012). The aim of these correction factors is to normalize the neutron counting rate to a number of reference conditions: the barometric reference pressure, the reference humidity, and the solar reference activity level. Following Zreda et al. (2008) and Bogena et al. (2013), a 24 h running average was applied to reduce the inherent noise of the hourly readings and reduce measurement uncertainty.

Conversion of Cosmic-Ray Neutrons to Soil Moisture

The corrected neutron intensity was converted to soil moisture using the standard N_0-calibration function proposed by Desilets et al. (2010):

$$\theta = \varrho_{bd}\left[a_0\left(\frac{N_{cor}}{N_0} - a_1\right)^{-1} - a_2 - \theta_{off}\right] \quad (3)$$

where θ is the volumetric soil water content (m^3/m^3), ϱ_{bd} is the dry bulk density (g/cm^3), N_0 is the moderated neutron intensity over dry soil that needs to be calibrated using reference *in-situ* soil moisture data, and α_i are fitting parameters ($\alpha_0 = 0.0808$, $\alpha_1 = 0.372$, and $\alpha_2 = 0.115$). Hydrogen stored in lattice water and organic matter was converted into gravimetric soil moisture equivalent (θ_{off}) (g/g) according to Franz et al., 2012.

In-situ Soil Moisture and Snow Sampling

Neutrons originating closer to the neutron detector have a greater influence on the CRNP measurements (Zreda et al., 2008). Therefore, gravimetric samples collected within the CRNP footprint following sampling schemes suggested by Schrön et al. (2017) were used to calibrate the CRNP probe. Schrön et al. (2017) proposed that the calibration should be based on volumetric soil samples taken at 18 locations and at different radial distances from the neutron detector depending on the site wetness (i.e. 2–10, 25–65 and 85–160 m) and in 5 cm increments up to a depth of 30 cm. In this study, a total of 90 gravimetric soil samples were collected at 16 locations (from 0 to 30 cm depth in 5 cm increments) within the footprint of the CRNP at two dates. The irregular distribution of the sample locations shown in **Figure 1** is due to the steep topography and challenging accessibility of the study area, especially in the eastern part of the CRNP footprint. Each sampling location was given equal weight for the calculation of the area-average volumetric soil moisture. Water content of the soil samples was determined by oven drying (24 h at 105°C), and used to calibrate the CRNP with respect to soil moisture measurements (see section Soil Moisture Derived From Epithermal Neutron Intensity).

Moreover, an *in-situ* SWE sampling was conducted at January 7, 2020 during snowmelt conditions. At this time, it was estimated that roughly ∼40% of the footprint area was covered with a heterogeneous snow cover in response to the small-scale spatial interplay of vegetation, snowdrift, and variations of melting rates. In an attempt to obtain a more rigorous estimate of the geometry of the snow patches, daily satellite images with a resolution of 3 m (Planet Lab Germany GmbH, Berlin, Germany) were acquired for the 8th and 9th of January (not shown). However, the estimation of snow distribution from satellite data was not possible due to: (i) the image resolution of 3 m which was not able to capture the geometry of small meter-scale snow patches, (ii) the early acquisition time of the images (i.e., 7 a.m.) which reduced illumination, and (iii) the presence of scrubland vegetation which covered the underlying snow. In the SWE sampling campaign, samples were collected at the same locations as during soil sampling in case these were covered with snow. Measured snow depth varied between 6 and 20 cm with an average of 10.83 cm. The corresponding SWE was estimated by weighing the molten snow, which resulted in a SWE range between 11 and 45 mm with an average of 21.63 mm (see also **Figure 5**). However, in view of the fact that the ground was not completely covered with snow, these values should be considered with caution.

Determination of Snow Water Equivalent Using Cosmic-Ray Neutrons

In this study, we investigate three different approaches to convert measured epithermal neutron intensities to SWE: a linear regression function, the standard N_0-calibration function, and a more physically-based model proposed by Desilets (2017). In addition, the thermal to epithermal neutron ratio was considered for SWE estimation.

Linear Regression Function

The linear regression function approach proposed by Sigouin and Si (2016) is based on the assumption that the corrected neutron intensities are linearly related to the SWE surrounding the CRNP. In their study, such a linear regression provided accurate estimates of average SWE within the CRNP footprint. However, Sigouin and Si (2016) found differences in intercepts when using different calibration data sets. Furthermore, overestimation of SWE was observed in the presence of considerable snowmelt as well as increased soil moisture in the first centimeters of soil. However, they found that substantial melt and soil moisture increases were necessary before SWE overestimation occurred, and they also noted that this effect can be well-isolated when continuous measurements of soil moisture are available.

Standard N_0-Calibration Function

Schattan et al. (2017) related *in-situ* measurements of SWE to epithermal neutron intensity using the standard N_0-calibration originally developed for relating neutron counts to soil moisture (Equation 3, Desilets et al., 2010). To this end, the coefficients α_0, α_1, and α_2 were recalibrated in addition to N_0 using continuous point-scale SWE measurements from an automatic weather station as well as several spatially distributed SWE maps obtained with terrestrial laser scanning. It was found that the sensitivity of this approach decreased with increasing SWE with a depth limit of ∼300 mm (Schattan et al., 2017). N_0 corresponds to the neutron intensity for dry soil, i.e., without water and snow cover. Therefore, the N_0 value resulting from the soil moisture calibration should not need to be recalibrated for the SWE application. Therefore, we only calibrated the coefficients α_0, α_1, and α_2 in this study. An advantage of fixing N_0 is the lower degree of freedom in calibration, which makes it easier to transfer the calibration function to other locations.

Physically-Based Calibration Function (Desilets, 2017)

With increasing snow cover, the neutron count rate reaches a constant value for an infinite snow depth (N_{snow}) and does not drop to zero. Assuming that the neutron attenuation by water (Λ)

is linear, the dependence of neutrons on SWE can be formulated as a first order differential equation (Desilets, 2017):

$$\frac{dN}{dSWE} = -\frac{N - N_{snow}}{\Lambda} \tag{4}$$

After integration, this results in Desilets (2017):

$$N - N_{snow} = exp\left(-\frac{SWE}{\Lambda}\right)\exp(C) \tag{5}$$

where C is an integration constant. Assuming that the neutron count rate in the absence of snow cover (SWE = 0) is controlled by the soil water content ($N = N_{SWC}$), C is given by Desilets (2017):

$$C = \ln\left(N_{SWC} - N_{snow}\right) \tag{6}$$

The combination of Equations (5) and (6) results in the following expression for SWE as a function of N:

$$SWE = -\Lambda \ln\left(\frac{N - N_{snow}}{N_{SWC} - N_{snow}}\right) \tag{7}$$

Using neutron modeling, Desilets (2017) found an approximate value of $\Lambda = 4.8$ cm. Furthermore, Desilets (2017) suggested that N_{snow} could be calculated from N_0 using:

$$N_{snow} = 0.24 \cdot N_0 \tag{8}$$

Thermal to Epithermal Neutron Ratio

The incoming cosmic radiation is dominated by fast neutrons that are moderated to epithermal neutrons (>1 eV) and thermal neutrons (<1 eV) as they travel and interact with air nuclei, vegetation, and soil (Zreda et al., 2012; Köhli et al., 2015). Andreasen et al. (2016) demonstrated the different physical response of thermal and epithermal neutrons and found that the moderation of epithermal neutrons is high in the soil and low in the air. They also observed that the decrease in thermal neutron intensity is proportional to the height above the ground surface (i.e., the source of thermal neutrons). Desilets et al. (2010) suggested that the neutron energy spectrum might also contain information on the spatial pattern of land surface water. Subsequently, the thermal to epithermal neutron ratio was used to determine aboveground biomass (e.g., Tian et al., 2016; Jakobi et al., 2018). Here, we explore whether the neutron ratio can also be used to predict SWE.

Neutron Signal Separation

For the simultaneous estimation of several variables exclusively from neutron intensity measurements, the time- and space-dependent effects on the measured neutron intensity need to be separated. For this, several studies identified benefits of combining measurements of bare and moderated neutron detectors (Desilets et al., 2010; Tian et al., 2016; Andreasen et al., 2017b; Jakobi et al., 2018). For instance, the ratio between thermal and fast neutrons can be used to distinguish snow events from rain events as shown by Desilets et al. (2010). In their study, it was also shown that snow events are typically characterized by a rapid increase in thermal neutron intensity with the first 1–3 cm of snow followed by a rapid decrease, whereas epithermal neutron intensity decreases monotonically with increasing snow depth. This finding is in accordance with results from neutron modeling of snow cover effects (Zweck et al., 2013). Desilets et al. (2010) also found that changes in the spatial distribution of the snow cover produced a hysteresis loop in the thermal and epithermal neutron intensity.

RESULTS

Precipitation and Neutron Data

Figure 3 shows the continuous measurements of temperature as well as liquid and solid precipitation at the CS3 site from April 3, 2017 to January 13, 2020. The average air temperature during this period was 12.8°C and ranged from −9.6°C to 35.1°C. The total precipitation was 3,187 mm, of which 330 mm occurred during freezing conditions indicating snowfall. In total, 11 snow events that produced a measurable snow cover occurred during the study period (gray areas in **Figure 3**). During the snow events from January 12, 2018 to January 19, 2018, the operation of the climate station was interrupted several times due to problems with the power supply.

During the investigated period, the average uncorrected epithermal and thermal neutron intensities were 2,946 and 1,457 cph, respectively. These relatively high values are due to the high elevation of the CS3 site (1,031 m) and the increase in cosmic radiation with altitude (Andreasen et al., 2017a). The measurement uncertainty in neutron counts follows Poisson counting statistics. Therefore, the expected standard deviation for a count rate of N is $N^{0.5}$ (Zreda et al., 2012). As a consequence, the high elevation of the test site approximately doubled the sensitivity of the neutron detectors compared to identical detectors at sea level. **Figure 3** shows the epithermal intensity corrected for atmospheric pressure, air humidity, and solar activity and the thermal neutron intensity corrected for atmospheric pressure and air humidity. Due to these corrections, the average epithermal and thermal neutron intensities were reduced to 1,201 and 651 cph, respectively. Generally, snow events led to a significant reduction of both epithermal and thermal neutron intensity, although a stronger reduction was apparent in the case of epithermal neutrons. Consequently, the neutron ratio increased during snow cover periods.

To obtain a better understanding of the interdependency of snow cover, soil moisture, and neutron intensities at different energy levels, a single snow event was investigated in detail. **Figure 4** shows the temporal evolution of the most pronounced snowpack during the investigated period that lasted from December 31, 2018 to January 23, 2019. Several snowfall events in the beginning of this period resulted in a total SWE of 109.2 mm with a snow depth of more than 600 mm (**Figure 4B**).

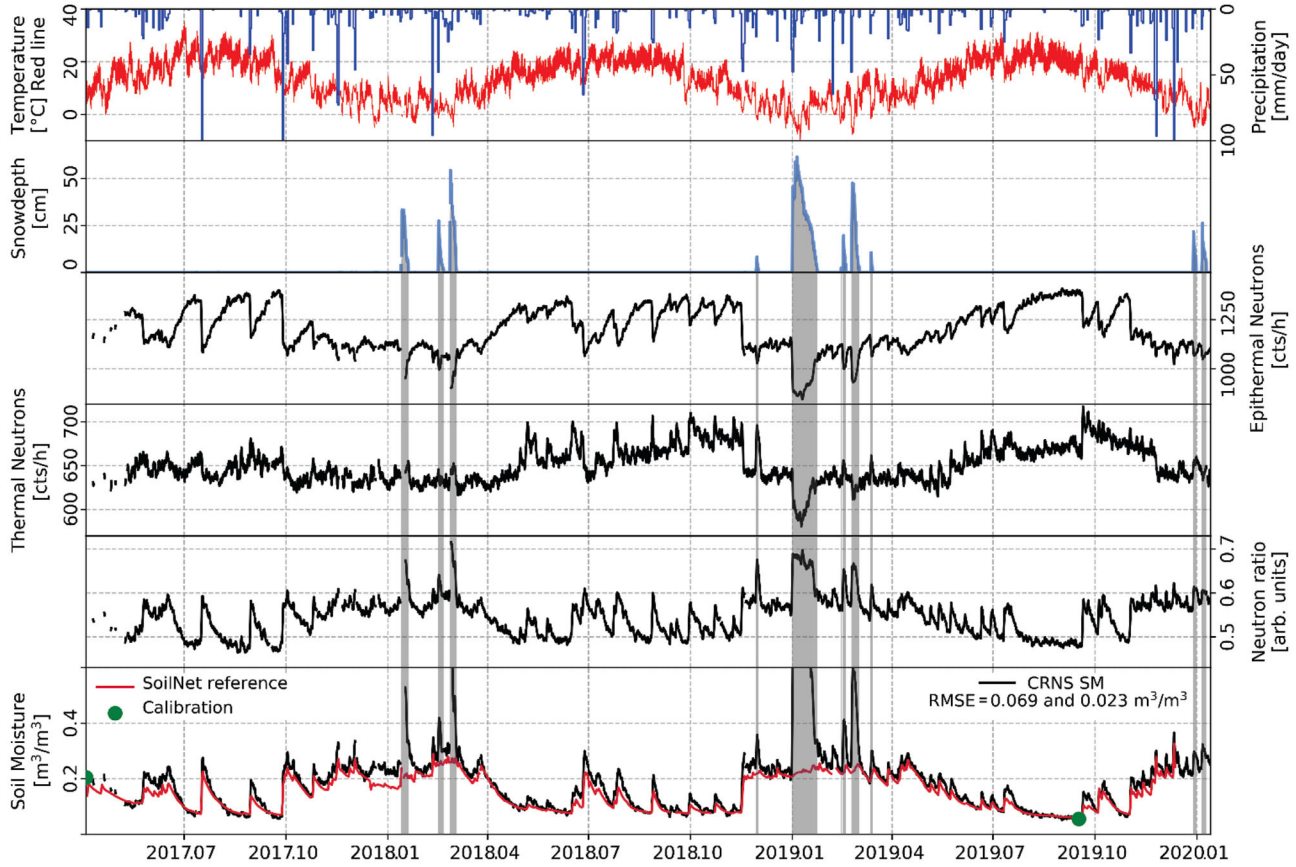

FIGURE 3 | Precipitation, air temperature, snow depth, epithermal neutron and thermal neutron intensity, neutron ratio, vertically and horizontally weighted average *in-situ* soil moisture (SoilNet), and calibrated CRNP soil moisture from April 3, 2017 to January 13, 2020. The vertically and horizontally weighted average soil moisture from the two calibration campaigns are shown with green dots. The RMSE between soil moisture obtained from CRNP and SoilNet for the whole period and excluding snow events are also shown.

The steep increase in snow depth during the first snowfall event had a strong impact on the neutron signals, especially on the epithermal neutron intensity and the neutron ratio (**Figure 4C**). After January 6, 2019, the snow depth decreased steadily due to continuous changes in snowpack density, snowmelt, and evaposublimation (Herrero and Polo, 2016). Soil temperature at 5 cm depth was above 0°C during the whole period (data not shown). This led to a continuous low-rate melting at the interface between soil and snowpack, which explains the slowly increasing soil moisture obtained with the *in-situ* soil moisture sensors (**Figure 4B**). In the middle and toward the end of the investigated period, liquid precipitation occurred during non-freezing conditions leading to fast soil moisture responses (**Figure 4B**). Correspondingly, the epithermal neutron intensity decreased and the neutron ratio increased. Warmer conditions with air temperatures above 8°C during daytime led to intense snow melt between January 17 and 21, 2020. During melt, the liquid water storage capacity of the snowpack was exceeded, and this resulted in significant downward percolation as indicated by consecutive peaks in the *in-situ* soil moisture measurements. The accelerated snowmelt is reflected in a pronounced increase in epithermal neutron intensity and a corresponding decrease in the neutron ratio. In contrast, measured snow depth (point based measurements) did not show an accelerated decline. This discrepancy is attributed to the spatial heterogeneity of the snowpack in the footprint of the CRNP.

Soil Moisture Derived From Epithermal Neutron Intensity

In this study, we used the *in-situ* thermogravimetric reference data from the two calibration campaigns for the conversion of measured epithermal neutron intensity to soil moisture. This was achieved by calibrating the N_0 parameter of Equation (3) as suggested by Zreda et al. (2012). For this, we considered an average bulk density of 1.21 g/cm^3 and a soil water equivalent of 0.058 mm for soil organic matter and lattice water together. This resulted in an estimated N_0 of 1,889 cph. **Figure 3** shows the soil moisture derived from epithermal neutron intensity compared to the weighted mean soil moisture measured by the three SoilNet stations and using the horizontal and vertical weighing approaches proposed by Schrön et al. (2017). The

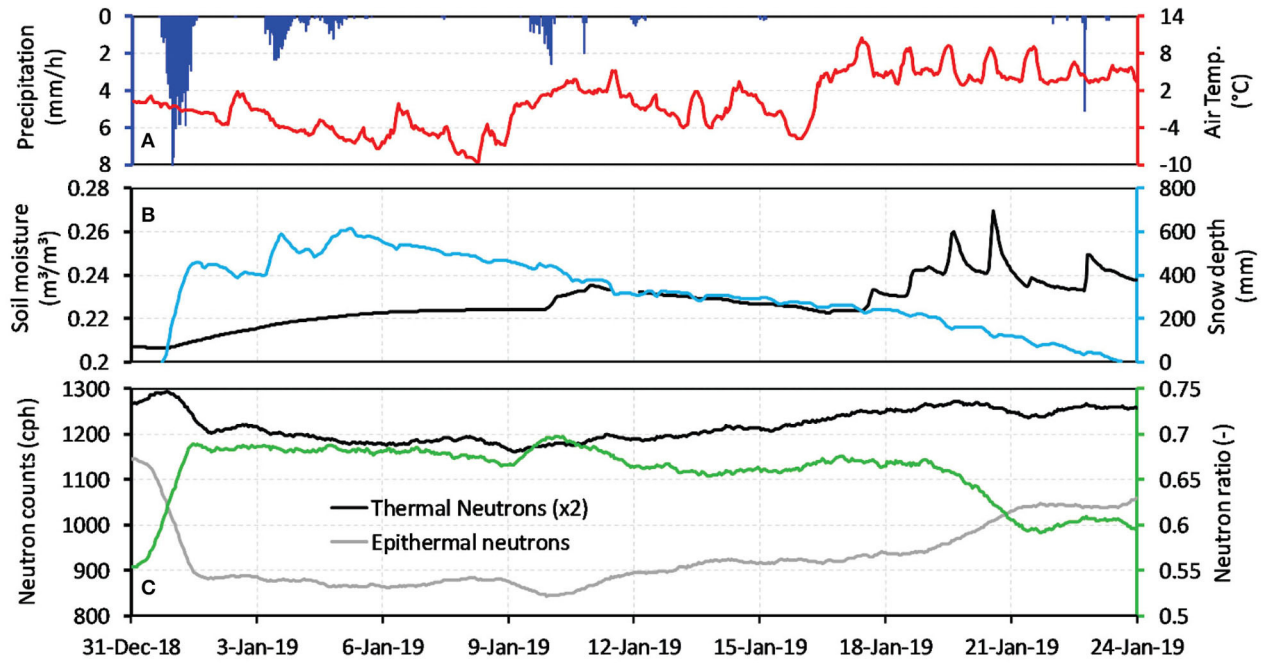

FIGURE 4 | Time series of: **(A)** precipitation and air temperature, **(B)** snow depth and vertically and horizontally weighted *in-situ* soil moisture measured with SoilNet, and **(C)** epithermal and thermal neutron count rates (24-h moving averages) and the neutron ratio. Note that the thermal neutron intensity is multiplied by two for illustrative purposes.

CRNP and measured soil moisture time series correspond well, except for the expected mismatches in periods where a snow cover is present. In these periods, the CRNP method strongly overestimated soil moisture due to the strong attenuation of epithermal neutrons by the snow cover. The root-mean-square error (RMSE) between the soil moisture obtained from CRNP and the *in-situ* measurements is relatively high (RMSE = 0.069 m^3/m^3). However, the RMSE decreased to 0.023 m^3/m^3 when the snow events were excluded, which is well within the range reported by other studies (e.g., Franz et al., 2012; Baatz et al., 2014, 2015; Iwema et al., 2015).

Relationship Between SWE and Snow Depth

The available snow depth measurements were converted to snow water equivalent (SWE) in order to perform a comparison with the estimates obtained with CRNP. Here, we used an empirical linear relationship to predict SWE from snow depth. Shook and Gray (1994) previously reported the following linear relationship:

$$SWE = 2.39 \cdot D + 2.05 \quad (9)$$

where D is snow depth (cm) and SWE is given in millimeters. **Figure 5** shows the measured SWE obtained from the heated precipitation gauge, i.e., the accumulated precipitation readings, and the snow depth measurements. Based on our measurements, we found the following relationship:

$$SWE = 1.6182 \cdot D \quad (10)$$

It can be seen that the linear function reported by Shook and Gray (1994) considerably overestimated SWE for our site, which is not surprising given the wide range of snow properties. The data from the SWE calibration campaign confirm the correctness of the site-specific regression function (**Figure 5**). Therefore, this regression is used in the following to derive dynamic changes in SWE from snow depth measurements obtained from the ultrasonic sensor.

Unfortunately, regular *in-situ* snow measurements during the winter periods were not possible at the site due to its remote location in a mountain range with limited accessibility during snow events. In addition, remote sensing data also did not provide reliable snow information for the test site (see section *in-situ* Soil Moisture and Snow Sampling). Therefore, we used the Pluvio precipitation gauge instead, because the heating of the gauging rim prevents the blocking of snow and thus ensures reliable SWE measurements. In a similar study, Boudala et al. (2014) compared snow measurements of the Pluvio with *in-situ* measurements and found that it underestimated the snow amount by only about 4%. Clearly, the use of an empirical relationship between SWE and snow depth implies that the snow density is relatively constant. This assumption may have led to an uncertainty in the estimated SWE data, as the snow density may have varied within and between snow events. Due to the long time series of 3 years and the large number of events during this

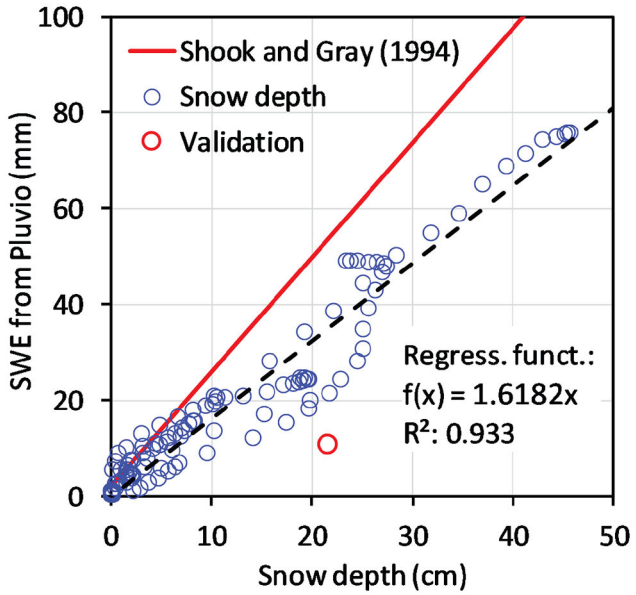

FIGURE 5 | SWE regression function derived from snow water equivalent (SWE) measured by the heated precipitation gauge (Pluvio), i.e., the accumulated precipitation readings, and the snow depth measured by the ultrasonic snow depth sensor. Results from the SWE validation campaign are also presented. In addition, the linear regression function proposed by Shook and Gray (1994) is shown.

period, different snow conditions were taken into account in this study. Nevertheless, we found a good agreement between CRNP and the snow height measurements suggesting that changes in snow density were not particularly strong, likely due to the relatively short duration of individual snow events (mostly < 1 week). For these reasons, we believe that our validation approach is reliable enough to compare different snow conversion methods for CRNP.

Snow Water Equivalent Derived From Epithermal Neutron Intensity

Regression Analysis

We selected nine snow events with different amounts of snowfall that occurred during the study period (**Figure 6**). From these nine events, *in-situ* SWE values were determined from the precipitation measurements as described in section Relationship Between SWE and Snow Depth. For this analysis, only SWE values that occurred during the build-up phase of the snowpack were selected in order to exclude any possible influence of snowmelt, density changes in the snowpack, or evaposublimation (red circles in **Figure 6**).

Figure 7A shows the relationship between the selected SWE observations (see **Figure 6**) and the epithermal neutron intensity measurements, and the fitted linear regression model. The coefficient of determination for the fitted model shows that ∼95% of the SWE variability can be explained, which indicates that epithermal neutron intensity is an excellent predictor for SWE (RMSE = 7.48 mm). This is also confirmed by the close relationship between all SWE estimates derived from snow depth and CRNP measurements (**Figure 7B**), which resulted in an R^2 of 0.852 and a RMSE of 8.22 mm.

In contrast, the relationship between SWE and neutron ratio is not as good as in the case of epithermal neutron intensity (**Figures 7C,D**), as indicated by the lower R^2 (0.82) and the higher RMSE (13.7 mm). This finding indicates that the neutron ratio is more sensitive to other influences than snow and thus a less robust predictor for SWE. Another explanation for this poorer performance could be the different measuring footprints for thermal and epithermal neutrons. Whereas, the footprint for epithermal neutrons ranges from 12 to 18 ha, the footprint for thermal neutrons covers a much smaller area. Preliminary neutron transport simulations indicate that thermal neutrons have a footprint with a radius of ∼35 m at average ambient conditions (Markus Köhli, personal communication). Thus, the neutron ratio may be more strongly affected by spatial heterogeneity of the snow cover than the epithermal neutron intensity. This may explain the larger scatter between SWE derived from snow depth and neutron ratio shown in **Figure 7D** ($R^2 = 0.53$, RMSE = 18.6 mm). This discrepancy in footprint size represents an even bigger challenge in mountainous areas due the higher spatial variability of snow covers in such environments (Schattan et al., 2019).

We also tested whether a multiple linear regression using both E and T/E leads to a better prediction of SWE from neutron counts. We found that the regression parameter for NR is significant at a 5% confidence level (p-value = 0.0354). However, multiple linear regression using E and NR was only minimally better compared to linear regression using E in terms of R^2 (0.953 vs. 0.946). In addition, the multiple regression function showed a lower transferability compared to the simple regression function. Therefore, we decided to not consider multiple linear regression using E and NR as an option for converting neutron counts into SWE in this study.

N_0-Calibration Function

As suggested by Schattan et al. (2017), we recalibrated the coefficients of the standard N_0 calibration function using the selected SWE observations presented in **Figure 6**. N_0 was fixed to the value found in the soil moisture calibration (1,889 cph). This resulted in $\alpha_0 = 144.861$, $\alpha_1 = 0$, and $\alpha_2 = 243.172$. Interestingly, the α_1 parameter was zero and thus could be omitted. The corresponding calibration curve is presented in **Figure 8A**. Similar to the case of the linear regression function, the N_0-function fits the calibration data well ($R^2 = 0.95$, RMSE = 7.45). The validation with all SWE values also showed good results ($R^2 = 0.762$, RMSE = 9.39). Thus, the performance of the N_0-calibration function was somewhat lower than that of the linear regression method for the validation measurements.

Physically-Based Calibration Function

Figure 9 presents the application of the physical-based calibration function proposed by Desilets (2017) using the selected SWE values shown in **Figure 6**. As suggested by Desilets (2017), we used a value of 4.8 cm for the attenuation length (Λ). We calibrated the remaining two parameters ($N_{SNOW} = 824.37$

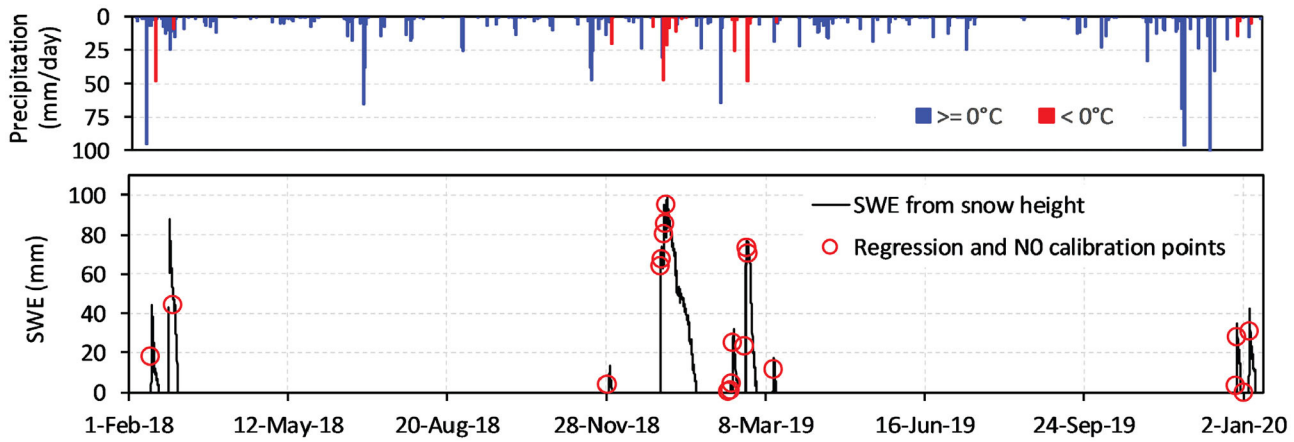

FIGURE 6 | Time series of precipitation and snow water equivalent derived from Equation (10), and the 20 snow depth observations selected for determining the relationship between SWE and CRNP measurements.

and $N_{SWC} = 1133.69$). As the summary statistics show, the quality of calibration with the Desilets function is very similar to the epithermal neutron linear regression function and the N_0 calibration function ($R^2 = 0.916$, RMSE = 9.89). However, the validation statistics ($R^2 = 0.81$, RMSE = 7.98, **Figure 9B**) indicate that the physically based model was better able to reproduce all SWE values than the other conversion methods.

Using neutron transport simulations, Desilets (2017) suggested that the value for N_{SNOW} should be 24% of the value of N_0 calibrated using *in-situ* soil moisture reference data. The parameter N_{SNOW} represents a condition in which the snow completely absorbs all epithermal neutrons generated in the soil below the snow cover. Thus, the detected epithermal neutrons above the snow cover are assumed to be generated within the snow cover only. In this study, we fitted the value of N_{SNOW} and found that N_{SNOW} was 43.6% of N_0. This may indicate that other sources of epithermal neutrons exist at the CS3 test site. The most likely candidate producing epithermal neutrons is high Mediterranean scrubland vegetation. Furthermore, due to the mountainous location with steep slopes, part of the ground in the footprint of the CRNP was not covered with snow and may thus have increased the amount of epithermal neutrons.

Comparison of SWE Methods

In this section, we investigate how well the four SWE conversion methods compare with the SWE derived from snow level measurements during the single snow event presented in section Precipitation and Neutron Data (**Figure 4**). In addition, it was investigated how well the conversion methods are able to indicate the onset and ending of snow events. To this end, the SWE conversion methods are applied continuously (i.e., for periods with and without snow coverage) for the three considered winter periods (2017/18, 2018/19, and 2019/20).

Event Scale

In order to explore how the different methods to estimate SWE from CRNP measurements are able to reproduce the SWE dynamics during a snow cover event, we now investigate a single snow event that took place during winter 2018/19 in more detail (**Figure 10**, see also **Figure 4**). In addition, we consider an event-based calibration of the conversion methods that is solely based on SWE data of this snow event. For this, only the first 6 days of SWE data were used to exclude any possible influence of rainfall, snowmelt, density changes in the snowpack, or evaposublimation.

Figure 10 shows that the SWE dynamics derived from epithermal neutron intensity and the neutron ratio using the linear regression functions described above compared well with SWE derived from snow level measurements for the first 10 days prior to a strong rainfall event. The additional meteoric water increased the soil moisture content as indicated by the *in-situ* measurements (see also **Figure 4**), which may explain the SWE overestimation after the rainfall event (**Figure 10B**). The bias in the SWE estimates obtained from the neutron ratio regression function is more pronounced than the bias in the SWE estimates obtained from the epithermal neutron regression function. This indicates that the thermal and epithermal neutrons are differently affected by the thawing processes in the second half of the snow period. In addition, effects of the different footprint sizes of the epithermal and thermal neutron detectors have to be taken into consideration (see section Regression Analysis). A calibration of both regression functions using the SWE data of this specific snow event resulted in a marginally better RMSE in the case of the epithermal neutron regression and a slightly worse RMSE in the case of the neutron ratio regression function (**Figures 10B,C**). The event-scale SWE predictions for the N_0-calibration function and the physically-based calibration function are presented in **Figures 10D,E**. Again, we also compared the global calibration with an event-based calibration. Both calibration functions were better able to reproduce the development of the snow pack than the linear regression functions with epithermal neutrons and the neutron ratio, as indicated by the calibration statistics. However, the SWE overestimation after the strong rainfall event on January 10, 2019 is more pronounced for these two

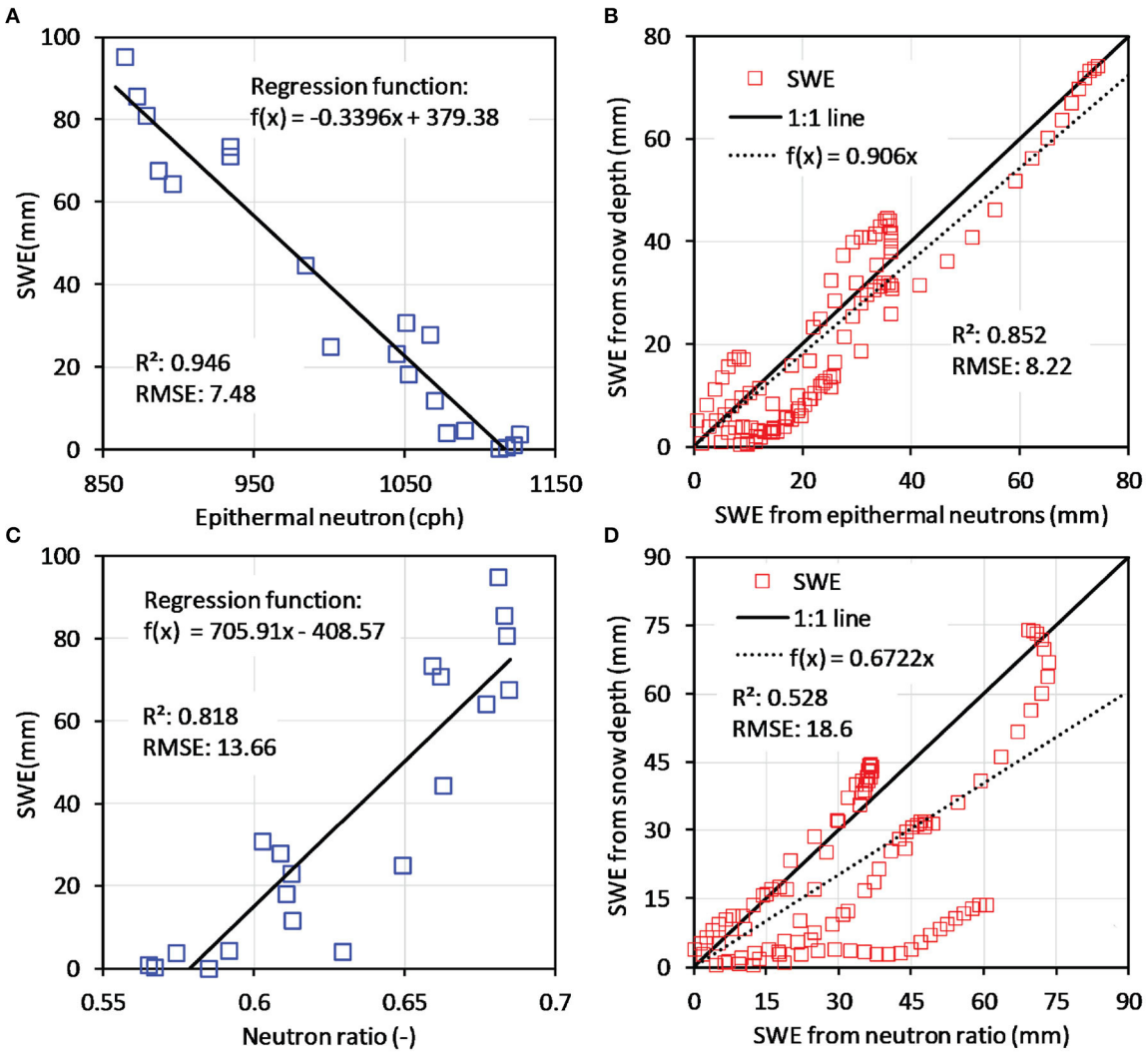

FIGURE 7 | (A) Relationship between SWE derived from 20 snow depth measurements (also shown in **Figure 6**) and corresponding epithermal neutron measurements; **(B)** validation of regression function to obtain SWE from epithermal neutron intensity using SWE from all snow depth measurements; **(C)** relationship between SWE derived from 20 snow depths and corresponding neutron ratios; **(D)** validation of regression function to obtain SWE from neutron ratio using SWE from all snow depth measurements.

approaches, especially in the case of the calibration function of Desilets (2017). This is related to the stronger non-linearity of these calibration functions. The event-based calibration reduced the SWE overestimation in case of the N_0-calibration function (**Figure 10D**). In contrast, the event-based calibration of the physically-based model did not significantly improve the match with SWE obtained from snow depth (**Figure 10E**).

Seasonal Scale

Figure 11 shows a comparison of the four CRNP-based methods to estimate SWE with the SWE derived from snow level measurements for the three winter seasons. The corresponding RMSE values for different periods are presented in **Table 1**. In most cases, all CRNP-based SWE conversion methods were able to determine the SWE during the snow events reasonably well (average RMSE of all methods = 7.69 mm) with the N_0-calibration function performing best and the NR regression function performing worst. The RMSE values obtained here are similar to those found in previous studies of Rasmussen et al. (2012) and Sigouin and Si (2016), who reported RMSE values between 5.1 and 8.8 mm between SWE estimated from snow depth and from CRNP measurements.

When comparing snow depth-derived SWE with CRNP-derived SWE for the entire winter period (**Figure 11**, **Table 1**), the average RMSE of all methods increased to 12.36 mm. This indicates that the CRNP-based SWE determination is affected by other influences such as rainfall. This effect is particularly pronounced during a heavy rainfall event in mid-December 2019, when all CRNP-based conversion methods erroneously indicate a snow event, possibly due to partial occurrence of

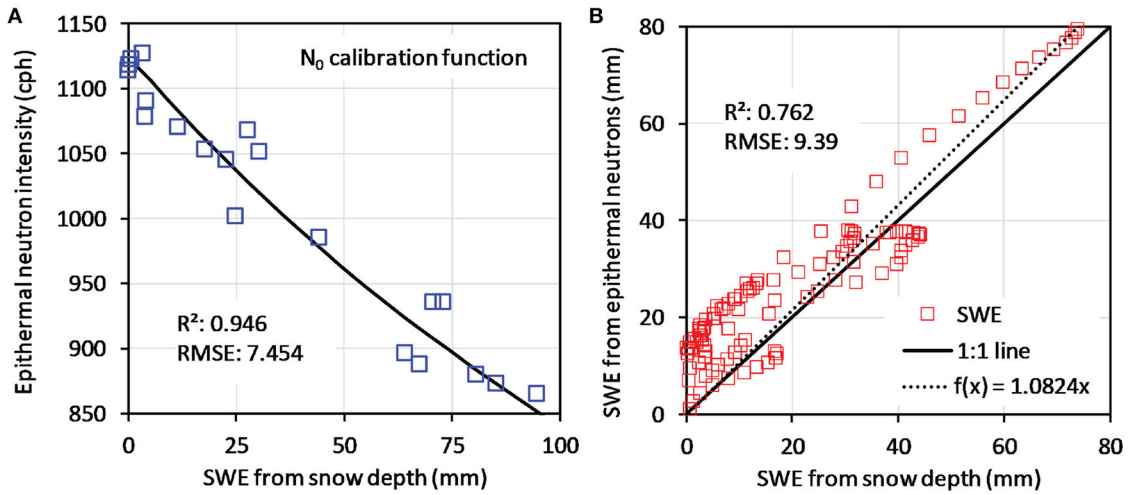

FIGURE 8 | (A) N_0-calibration function fitted to 20 selected SWE values obtained from snow level measurements using Equation (10); **(B)** validation of the N_0 calibration function using all SWE values.

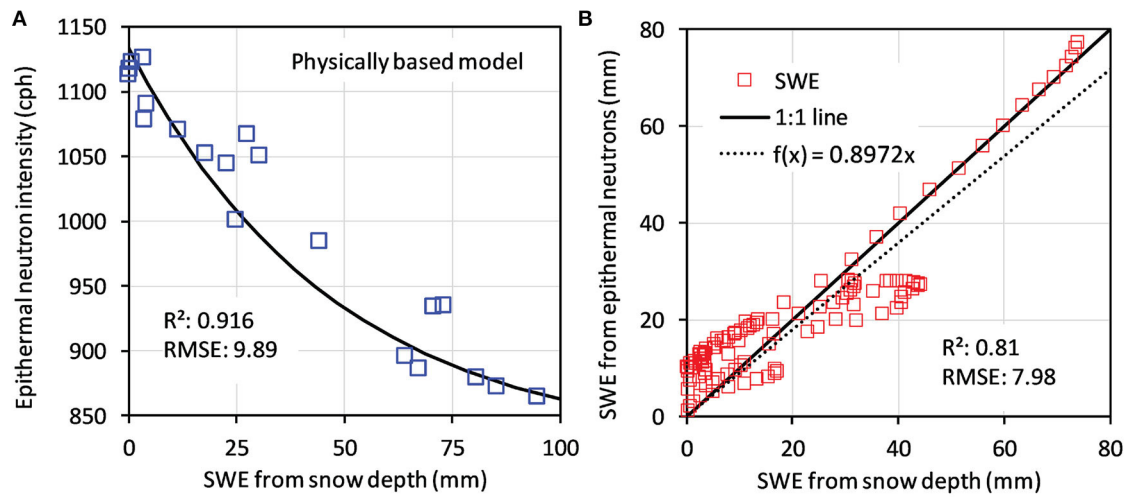

FIGURE 9 | (A) Physically-based model of Desilets (2017) fitted to 20 selected SWE values obtained from snow level measurements using Equation (10); **(B)** validation of the physically-based model using all SWE values.

ponding water. The error in the SWE estimates obtained for the entire monitoring period (including summers) is even higher as indicated by the high RMSE in **Table 1**. Therefore, it is currently not recommended to use CRNP measurements as a stand-alone method for SWE determination. It is essential to use supporting information (e.g., air temperature, snow level measurements) to independently determine periods with snow. Time-lapse snow photography could also be beneficial (Parajka et al., 2012) for this purpose.

Another reason for the observed discrepancy between SWE estimates obtained from CRNP and snow depth measurements is the difference in measurement scale. While the CRNP measurements cover 12–18 ha, snow depth is only a point measurement. The impact of this scale difference becomes apparent for a snow event from late December to beginning of January 2019 (**Figure 11**), in which all CRNP-based conversion methods indicate a longer snow cover period than the snow depth-based SWE. It is likely that the snow under the snow depth sensor melted faster due to the influence of direct solar radiation, while the snow cover in the shadow of the shrubbery vegetation remained longer, which is detected by the CRNP-based conversion methods.

CONCLUSIONS

In our study, we found that the above-ground CRNP is well-suited for measurement of field scale SWE, which is in agreement with findings of other studies (e.g., Desilets et al., 2010;

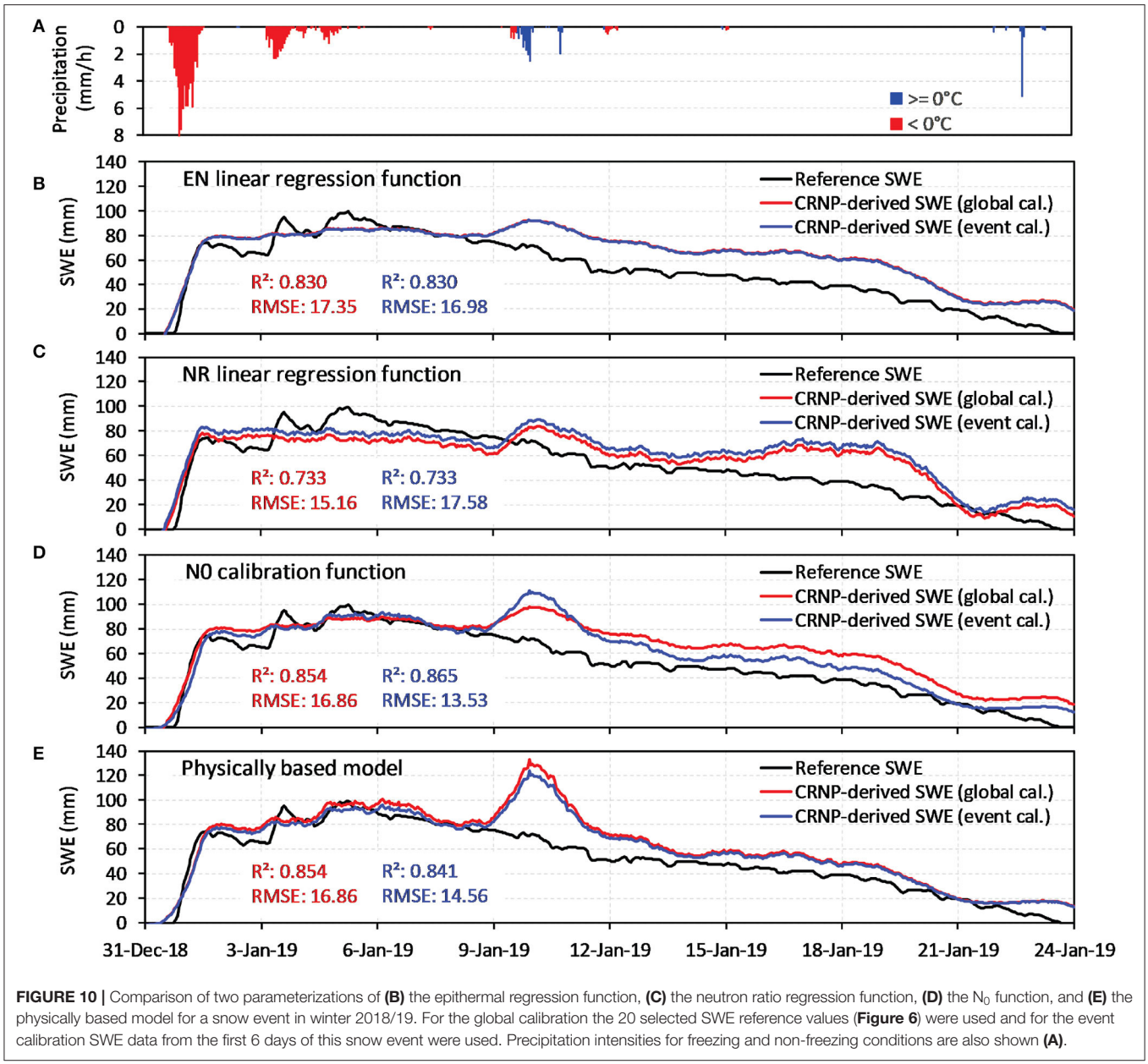

FIGURE 10 | Comparison of two parameterizations of **(B)** the epithermal regression function, **(C)** the neutron ratio regression function, **(D)** the N_0 function, and **(E)** the physically based model for a snow event in winter 2018/19. For the global calibration the 20 selected SWE reference values (**Figure 6**) were used and for the event calibration SWE data from the first 6 days of this snow event were used. Precipitation intensities for freezing and non-freezing conditions are also shown **(A)**.

Rasmussen et al., 2012; Sigouin and Si, 2016; Schattan et al., 2017). We also demonstrated that all four methods to obtain SWE from CRNP measurements were able to determine snow pack dynamics reasonably well, with the N_0-calibration function and the physically-based calibration function of Desilets (2017) performing best and the regression function using the neutron ratio performing worst. Furthermore, we showed that the above-ground CRNP can be used for continuous SWE determination. However, the CRNP-based SWE determination can be affected by other influences. Especially heavy rainfall can lead to erroneous indications of snow events due to the occurrence of ponding water. Nevertheless, CRNP-based SWE estimation is a potential alternative to established methods like snow depth-based SWE methods, as it provides SWE estimates for a much larger scale (12–18 ha). In view of the fact that the SWE methods based on snow depth measurement can also yield biased results (e.g., preferred snow cover melting due to the direct influence of solar radiation), we propose that the CRNP-based SWE estimation can lead to results that are more representative for larger areas and therefore better suited for regional studies.

According to Andreasen et al. (2017a), there are currently about 200 stationary CRNPs installed worldwide, often operated as regional networks in hydrological observatories (e.g., Bogena et al., 2018; Kiese et al., 2018; Liu et al., 2018) or in entire countries (Zreda et al., 2012; Hawdon et al., 2014; Evans et al., 2016). Some of the epithermal neutron time series of these CRNPs started already more than a decade ago. Therefore, we expect that the application of the presented SWE conversion methods

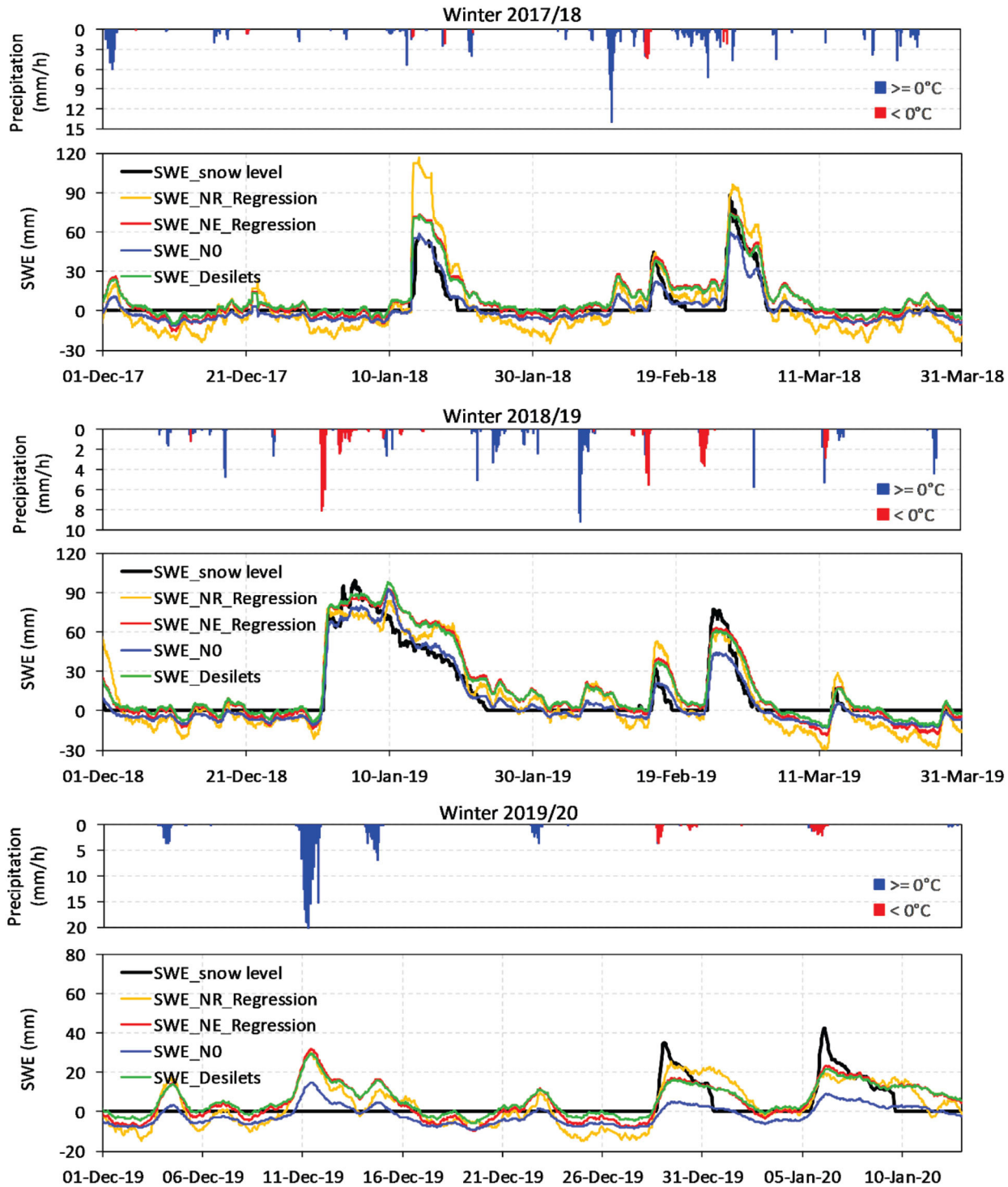

FIGURE 11 | Comparison of the four CRNP-based methods to estimate SWE with the SWE derived from snow level measurements for the winter seasons 2017/18, 2018/19, and 2019/20. Precipitation intensities for freezing and non-freezing conditions are also shown.

to available CRNP data will be very useful for the investigation of changes in snow precipitation patterns as well as of increasingly severe snowmelt events caused by rising global temperatures. Future research should seek to further improve the accuracy of the CRNP-based SWE estimates as well as the characterization of onsets and endings of snow cover events e.g., with use of neutron

TABLE 1 | RMSE calculated between snow depth-derived and CRNP-derived SWE for different periods indicating the quality of CRNP-based SWE estimation using different conversion methods.

SWE conversion method	RMSE (mm)		
	Whole period	Winter periods	Snow events
NE regression function	44.89	12.50	7.81
NR regression function	36.69	16.32	9.16
N_0 calibration function	19.87	8.92	6.37
Physically based model	15.44	9.89	7.42

The duration of the snow events were determined from the snow level measurements.

transport modeling (e.g., Andreasen et al., 2017b; Schattan et al., 2019), as well as measurements of neutrons at different and multiple energy ranges.

DATA AVAILABILITY STATEMENT

The datasets presented in this study can be found in online repositories. The names of the repository/repositories and accession number(s) can be found below: https://enoha.eu/ddp/.

AUTHOR CONTRIBUTIONS

HB developed the idea for this research. FH, AP, AI, and VP developed the experimental design of the research station and accomplished the field measurements. HB, JJ, CB, and JH accomplished the data analysis. HB and FH conceived and wrote a first draft of the manuscript. CB, JH, AP, AI, and VP commented on the draft, which was afterwards revised and submitted by HB. All authors contributed to the article and approved the submitted version.

FUNDING

The Pinios Hydrologic Observatory was supported by TERENO (TERrestrial Environmental Observatories) funded by the Helmholtz-Gemeinschaft, and by the Hellenic Agricultural Organisation - Soil and Water Resources Institute under the internal R&D infrastructure funds.

ACKNOWLEDGMENTS

This research was supported by the FOR 2694 project 'Cosmic Sense' funded by the Deutsche Forschungsgemeinschaft under the grant agreement no. 357874777 and the ATLAS project funded by the European Union's Horizon 2020 research and innovation programme under grant agreement no. 857125. We would like to thank the Municipality of Agia and especially Mr. Giannis Patsiavouras for facilitating our work in the Pinios Hydrologic Observatory. Bernd Schilling and Ansgar Weuthen are thanked for support with the installation and maintenance of measurement equipment. Incoming neutron data was obtained from the NMDB database (www.nmdb.eu). Most data presented in this study is freely available via the ENOHA (European Network of Hydrological Observatories) data portal (https://www.enoha.eu/).

REFERENCES

Akyurek, Z., Surer, S., and Beser, Ö. (2011). Investigation of the snow-cover dynamics in the Upper euphrates basin of Turkey using remotely sensed snow-cover products and hydrometeorological data. *Hydrol. Process.* 25, 3637–3648. doi: 10.1002/hyp.8090

Andreasen, M., Jensen, K. H., Desilets, D., Franz, T., Zreda, M., Bogena, H., et al. (2017a). Status and perspectives of the cosmic-ray neutron method for soil moisture estimation and other environmental science applications. *Vadose Zone J.* 16, 1–11. doi: 10.2136/vzj2017.04.0086

Andreasen, M., Jensen, K. H., Desilets, D., Zreda, M., Bogena, H., and Looms, M. C. (2017b). Cosmic-ray neutron transport at a forest field site: the sensitivity to various environmental conditions with focus on biomass and canopy interception. *Hydrol. Earth Syst. Sci.* 21, 1875–1894. doi: 10.5194/hess-21-1875-2017

Andreasen, M., Jensen, K. H., Zreda, M., Desilets, D., Bogena, H., and Looms, M. C. (2016). Modeling cosmic ray neutron field measurements. *Water Resour. Res.* 52, 6451–6471. doi: 10.1002/2015WR018236

Baatz, R., Bogena, H. R., Hendricks Franssen, H.-J., Huisman, J. A., Montzka, C., and Vereecken, H. (2015). An empirical vegetation correction for soil moisture content quantification using cosmic ray probes. *Water Resour. Res.* 51, 2030–2046. doi: 10.1002/2014WR016443

Baatz, R., Bogena, H. R., Hendricks Franssen, H. J., Huisman, J. A., Qu, W., Montzka, C., et al. (2014). Calibration of a catchment scale cosmic-ray probe network: a comparison of three parameterization methods. *J. Hydrol.* 516, 231–244. doi: 10.1016/j.jhydrol.2014.02.026

Bogena, H., Huisman, J. A., Schilling, B., Weuthen, A., and Vereecken, H. (2017). Effective calibration of low-cost soil water content sensors. *Sensors* 17:208. doi: 10.3390/s17010208

Bogena, H. R., Herbst, M., Huisman, J. A., Rosenbaum, U., Weuthen A., and Vereecken, H. (2010). Potential of wireless sensor networks for measuring soil water content variability. *Vadose Zone J.* 9, 1002–1013. doi: 10.2136/vzj2009.0173

Bogena, H. R., Huisman, J. A., Baatz, R., Hendricks Franssen, H.-J., and Vereecken, H. (2013). Accuracy of the cosmic-ray soil water content probe in humid forest ecosystems: the worst case scenario. *Water Resour. Res.* 49, 1–14. doi: 10.1002/wrcr.20463

Bogena, H. R., Huisman, J. A., Güntner, A., Hübner, C., Kusche, J., Jonard, F., et al. (2015). Emerging methods for noninvasive sensing of soil moisture dynamics from field to catchment scale: a review. *Wiley Interdiscip. Rev. Water* 2, 635–647. doi: 10.1002/wat2.1097

Bogena, H. R., Montzka, C., Huisman, J. A., Graf, A., Schmidt, M., Stockinger, M., et al. (2018). The rur hydrological observatory: a multiscale multi-compartment research platform for the advancement of hydrological science. *Vadose Zone J.* 17:180055. doi: 10.2136/vzj2018.03.0055

Boudala, F. S., Isaac, G. A., Rasmussen, R., Cober, S. G., and Scott, B. (2014). Comparisons of snowfall measurements in complex terrain made during the 2010 winter olympics in Vancouver. *Pure Appl. Geophys.* 171, 113–127. doi: 10.1007/s00024-012-0610-5

Choquette, Y., Ducharme, P., and Rogoza, J. (2013). "CS725, an accurate sensor for the snow water equivalent and soil moisture measurements," in *Proceedings of the International Snow Science Workshop* (Grenoble), 931–936.

Deems, J. S., Painter, T. H., and Finnegan, D. C. (2013). Lidar measurement of snow depth: a review. *J. Glaciol.* 59, 467–479. doi: 10.3189/2013JoG12J154

Desilets, D. (2017). *Calibrating a Non-invasive Cosmic Ray Soil Moisture Probe for Snow Water Equivalent*. Hydroinnova Technical Document, 17–01.

Desilets, D., Zreda, M., and Ferré, T. P. A. (2010). Nature's neutron probe: land surface hydrology at an elusive scale with cosmic rays. *Water Resour. Res.* 46:W11505. doi: 10.1029/2009WR008726

Earman, S., Campbell, A. R., Phillips, F. M., and Newman, B. D. (2006). Isotopic exchange between snow and atmospheric water vapor: estimation of the snowmelt component of groundwater recharge in the southwestern United States. *J. Geophys. Res.* 111:D09302. doi: 10.1029/2005JD006470

Evans, J. G., Ward, H. C., Blake, J. R., Hewitt, E. J., Morrison, R., Fry, M., et al. (2016). Soil water content in southern England derived from a cosmic ray soil moisture observing system: COSMOS-UK. *Hydrol. Process.* 30, 4987–4999. doi: 10.1002/hyp.10929

Fontrodona Bach, A., van der Schrier, G., Melsen, L. A., Klein Tank, A. M. G., and Teuling, A. J. (2018). Widespread and accelerated decrease of observed mean and extreme snow depth over Europe. *Geophys. Res. Lett.* 45, 312–312. doi: 10.1029/2018GL079799

Franz, T. E., Zreda, M., Rosolem, R., and Ferre, T. P. A. (2012). Field validation of a cosmic-ray neutron sensor using a distributed sensor network. *Vadose Zone J.* 11:vzj2012.0046. doi: 10.2136/vzj2012.0046

Gugerli, R., Salzmann, N., Huss, M., and Desilets, D. (2019). Continuous and autonomous snow water equivalent measurements by a cosmic ray sensor on an alpine glacier. *Cryosphere* 13, 3413–3434. doi: 10.5194/tc-13-3413-2019

Hawdon, A., McJannet, D., and Wallace, J. (2014). Calibration and correction procedures for cosmic-ray neutron soil moisture probes located across Australia. *Water Resour. Res.* 50, 5029–5043. doi: 10.1002/2013WR015138

Heilig, A., Schneebeli, M., and Eisen, O. (2009). Upward looking ground-penetrating radar for monitoring snowpack stratigraphy. *Cold Reg. Sci. Technol.* 59, 152–162. doi: 10.1016/j.coldregions.2009.07.008

Herrero, J., and Polo, M. J. (2016). Evaposublimation from the snow in the mediterranean mountains of sierra nevada (Spain). *Cryosphere* 10, 2981–2998. doi: 10.5194/tc-10-2981-2016

Herrmann, F., Keller, L., Kunkel, R., Vereecken, H., and Wendland, F. (2015). Determination of spatially differentiated water balance components including groundwater recharge on the Federal State level – a case study using the mGROWA model in North Rhine-Westphalia (Germany). *J. Hydrol. Reg. Stud.* 4, 294–312. doi: 10.1016/j.ejrh.2015.06.018

Iwema, J., Rosolem, R., Baatz, R., Wagener, T., and Bogena, H. R. (2015). Investigating temporal field sampling strategies for site-specific calibration of three soil moisture-neutron intensity parameterization methods. *Hydrol. Earth Syst. Sci.* 19, 3203–3216. doi: 10.5194/hess-19-3203-2015

Jakobi, J., Huisman, J. A., Vereecken, H., Diekkrüger, B., and Bogena, H. R. (2018). Cosmic-ray neutron sensing for simultaneous soil water content and biomass quantification in drought conditions. *Water Resour. Res.* 54, 7383–7402. doi: 10.1029/2018WR022692

Kiese, R., Fersch, B., Baessler, C., Brosy, C., Butterbach-Bahl, K., Chwala, C., et al. (2018). The TERENO pre-alpine observatory: integrating meteorological, hydrological and biogeochemical measurements and modeling. *Vadose Zone J.* 17:180060. doi: 10.2136/vzj2018.03.0060

Kinar, N. J., and Pomeroy, J. W. (2015). Measurement of the physical properties of the snowpack. *Rev. Geophys.* 53, 481–544. doi: 10.1002/2015RG000481

Koch, F., Henkel, P., Appel, F., Schmid, L., Bach, H., Lamm, M., et al. (2019). Retrieval of snow water equivalent, liquid water content, and snow height of dry and wet snow by combining GPS signal attenuation and time delay. *Water Resour. Res.* 55, 4465–4487. doi: 10.1029/2018WR024431

Kodama, M. (1980). Continuous monitoring of snow water equivalent using cosmic-ray neutrons. *Cold Reg. Sci. Technol.* 3, 295–303. doi: 10.1016/0165-232X(80)90036-1

Kodama, M., Nakai, K., Kawasaki, S., and Wada, M. (1979). An application of cosmic-ray neutron measurements to the determination of the snow-water equivalent. *J. Hydrol.* 41, 85–92. doi: 10.1016/0022-1694(79)90107-0

Köhli, M., Schrön, M., Zreda, M., Schmidt, U., Dietrich, P., and Zacharias, S. (2015). Footprint characteristics revised for field-scale soil moisture monitoring with cosmic-ray neutrons. *Water Resour. Res.* 51, 5772–5790. doi: 10.1002/2015WR017169

Kripalani, R. H., and Kulkarni, A. (1999). Climatology and variability of historical soviet snow depth data: some new perspectives in snow–Indian monsoon teleconnections. *Clim. Dyn.* 15, 475–489. doi: 10.1007/s003820050294

Liu, S., Li, X., Xu, Z., Che, T., Xiao, Q., Ma, M., et al. (2018). The heihe integrated observatory network: a basin-scale land surface processes observatory in China. *Vadose Zone J.* 17:180072. doi: 10.2136/vzj2018.04.0072

Lundberg, A., Granlund, N., and Gustafsson, D. (2010). Towards automated "Ground truth" snow measurements - a review of operational and new measurement methods for Sweden, Norway, and Finland. *Hydrol. Process.* 24, 1955–1970. doi: 10.1002/hyp.7658

Panagopoulos, A., Arampatzis, G., Kuhr, P., Kunkel, R., Tziritis, E., and Wendland, F. (2015). Area-differentiated modeling of water balance in pinios basin, central Greece. *Global NEST J.* 17, 221–235. doi: 10.30955/gnj.001402

Panagopoulos, A., Arampatzis, G., Tziritis, E., Pisinaras, V., Herrmann, F., Kunkel, R., et al. (2016). Assessment of climate change impact in the hydrological regime of river Pinios Basin, central Greece. *Desalin. Water Treat.* 57, 2256–2267. doi: 10.1080/19443994.2014.984926

Panagopoulos, A., Herrmann, F., Pisinaras, V., and Wendland, F. (2018). Impact of climate change on irrigation need and groundwater resources in pinios basin. *Proceedings* 2:659. doi: 10.3390/proceedings2110659

Parajka, J., Haas, P., Kirnbauer, R., Jansa, J., and Blöschl, G. (2012). Potential of time-lapse photography of snow for hydrological purposes at the small catchment scale. *Hydrol. Process.* 26, 3327–3337. doi: 10.1002/hyp.8389

Peck, E. L., Bissell, V. C., Jones, E. B., and Burge, D. L. (1971). Evaluation of snow water equivalent by airborne measurement of passive terrestrial gamma radiation. *Water Resour. Res.* 7, 1151–1159. doi: 10.1029/WR007i005p01151

Pimentel, R., Herrero, J., Zeng, Y., Su, Z., and Polo, M. J. (2015). Study of snow dynamics at subgrid scale in semiarid environments combining terrestrial photography and data assimilation techniques. *J. Hydrometeor.* 16, 563–578. doi: 10.1175/JHM-D-14-0046.1

Pirazzini, R., Leppänen, L., Picard, G., Lopez-moreno, J. I., Marty, C., Macelloni, G., et al. (2018). European *in-situ* snow measurements: practices and purposes. *Sensors* 18:2016. doi: 10.3390/s18072016

Pisinaras, V., Panagopoulos, A., Herrmann, F., Bogena, H. R., Doulgeris, C., Ilias, A., et al. (2018). Hydrologic and geochemical research at pinios hydrologic observatory - initial results. *Vadose Zone J.* 17, 1–16. doi: 10.2136/vzj2018.05.0102

Rasmussen, R., Baker, B., Kochendorfer, J., Meyers, T., Landolt, S., Fischer, A. P., et al. (2012). How well are we measuring snow: the NOAA/FAA/NCAR winter precipitation test bed. *Bull. Am. Meteorol. Soc.* 93, 811–829. doi: 10.1175/BAMS-D-11-00052.1

Schattan, P., Baroni, G., Oswald, S. E., Schober, J., Fey, C., Kormann, C., et al. (2017). Continuous monitoring of snowpack dynamics in alpine terrain by aboveground neutron sensing. *Water Resour. Res.* 53, 3615–3634. doi: 10.1002/2016WR020234

Schattan, P., Köhli, M., Schrön, M., Baroni, G., and Oswald, S. E. (2019). Sensing area-average snow water equivalent with cosmic-ray neutrons: the influence of fractional snow cover. *Water Resour. Res.* 55, 10796–10812. doi: 10.1029/2019WR025647

Schmid, L., Heilig, A., Mitterer, C., Schweizer, J., Maurer, H., Okorn, R., et al. (2014). Continuous snowpack monitoring using upward-looking ground-penetrating radar technology. *J. Glaciol.* 60, 509–525. doi: 10.3189/2014JoG13J084

Schrön, M., Köhli, M., Scheiffele, L., Iwema, J., Bogena, H. R., Lv, L., et al. (2017). Spatial sensitivity of cosmic-ray neutron sensors applied to improve calibration and validation. *Hydrol. Earth Syst. Sci.* 21, 5009–5030. doi: 10.5194/hess-21-5009-2017

Shook, K., and Gray, D. M. (1994). "Determining the snow water equivalent of shallow prairie snowcovers," in *Proceedings of the 51st Eastern Snow Conference* (Dearborn, MI), 89–95.

Sigouin, M. J. P., and Si, B. C. (2016). Calibration of a non-invasive cosmic-ray probe for wide area snow water equivalent measurement. *Cryosphere* 10, 1181–1190. doi: 10.5194/tc-10-1181-2016

Sun, C., Walker, J. P., and Houser, P. R. (2004). A methodology for snow data assimilation in a land surface model. *J. Geophys. Res.* 109:D08108. doi: 10.1029/2003JD003765

Tian, Z. C., Li, Z. Z., Liu, G., Li, B. G., and Ren, T. S. (2016). Soil water content determination with cosmic-ray neutron sensor: correcting aboveground hydrogen effects with thermal/fast neutron ratio. *J. Hydrol.* 540, 923–933. doi: 10.1016/j.jhydrol.2016.07.004

Zreda, M., Desilets, D., Ferre, T. P. A., and Scott, R. L. (2008). Measuring soil moisture content non-invasively at intermediate spatial scale using cosmic-ray neutrons. *Geophys. Res. Lett.* 35:L21402. doi: 10.1029/2008GL035655

Zreda, M., Shuttleworth, W. J., Zeng, X., Zweck, C., Desilets, D., Franz, T., and Rosolem, R. (2012). COSMOS: the cosmic-ray soil moisture observing system. *Hydrol. Earth Syst. Sci.* 16, 4079–4099. doi: 10.5194/hess-16-4079-2012

Zweck, C., Zreda, M., and Desilets, D. (2013). Snow shielding factors for cosmogenic nuclide dating inferred from monte carlo neutron transport simulations. *Earth Planet. Sci. Lett.* 379, 64–71. doi: 10.1016/j.epsl.2013.07.023

Conflict of Interest: HB, FH, JJ, CB, and JH were employed by the company Forschungszentrum Jülich GmbH.

The remaining authors declare that the research was conducted in the absence of any commercial or financial relationships that could be construed as a potential conflict of interest.

frontiers in Water

ORIGINAL RESEARCH
published: 02 September 2020
doi: 10.3389/frwa.2020.00026

Integrating Invasive and Non-invasive Monitoring Sensors to Detect Field-Scale Soil Hydrological Behavior

Paolo Nasta[1], *Heye R. Bogena*[2], *Benedetto Sica*[3], *Ansgar Weuthen*[2], *Harry Vereecken*[2] *and Nunzio Romano*[1,3]*

[1] Department of Agricultural Sciences, AFBE Division, University of Naples Federico II, Naples, Italy, [2] Agrosphere Institute, Forschungszentrum Jülich GmbH, Jülich, Germany, [3] The Interdepartmental Center for Environmental Research (C.I.R.AM.), University of Naples Federico II, Naples, Italy

In recent decades, while great emphasis has been given to the monitoring of point-scale soil moisture patterns and field-scale integrated soil moisture, the measurement of matric potential has attracted little attention. Information on the soil matric potential is available in point-scale measurements but is still missing at field-scale. This state variable is necessary to understand hydrological fluxes and to determine the soil water retention function (WRF) for field-scale applications. In this study, we combine data from cosmic-ray neutron probes (CRNP, non-invasive proximal soil moisture sensors) and SoilNet wireless sensor networks (invasive ground-based soil moisture and matric potential sensors) installed in two sub-catchments with contrasting land-use (agroforestry vs. near-natural forest) to derive a field-scale WRF. We investigate the hypothesis that both sensor types provide effective measurements that are representative for the entire sub-catchment, as well as the drawbacks of integrating the different measurement scales of the sensor types (i.e., spatial-mean of distributed point-scale data vs. an integrated field-scale measurement). We found discrepancies in the data of the two sensor types related to the effects of the time-varying vertical measurement footprint of the CRNP, which induces a scale mismatch between CRNP-based soil moisture (referring mostly to near-surface depths) and the spatially averaged soil matric potential data measured at soil depths of 0.15 and 0.30 m. To remove the offsets, we opted to use the soil moisture index (SMI) based on the estimation of field capacity and wilting point, retrieved from the knowledge of the field-scale WRF. We found that the bimodality of SMI calculated with SoilNet-based soil moisture induced by Mediterranean rainfall seasonal behavior is not well-captured by CRNP-based soil moisture, except in a particularly dry year like 2017. The contrasts in SMI values between the two test sites were associated with differences in the spatial variability of soil moisture patterns explained by soil texture or terrain characteristics. We argue that field-scale WRFs are useful for the analysis of hydrological processes at the sub-catchment (field) scale and the application of distributed models.

Keywords: cosmic-ray neutron probe (CRNP), wireless sensor network (WSN), Mediterranean seasonality, machine-learning technique, partial-least squares regression (PLSR), water retention function, soil matric potential

OPEN ACCESS

Edited by:
Shaomin Liu,
Beijing Normal University, China

Reviewed by:
Kuai Fang,
Pennsylvania State University (PSU), United States
Rene Orth,
Max Planck Institute for Biogeochemistry, Germany

***Correspondence:**
Nunzio Romano
nunzio.romano@unina.it

Specialty section:
This article was submitted to Water and Hydrocomplexity, a section of the journal Frontiers in Water

Received: *26 January 2020*
Accepted: *22 July 2020*
Published: *02 September 2020*

Citation:
Nasta P, Bogena HR, Sica B, Weuthen A, Vereecken H and Romano N (2020) Integrating Invasive and Non-invasive Monitoring Sensors to Detect Field-Scale Soil Hydrological Behavior. Front. Water 2:26. doi: 10.3389/frwa.2020.00026

HIGHLIGHTS

- Coupling two types of sensing systems allows effective identification of field-scale soil hydrological responses of sites with different characteristics.
- Our results suggest the presence of a scale mismatch in the cosmic-ray probe's vertical footprint.
- Data from CRNP are unable to capture the effects of the bimodal precipitation regime of the Mediterranean climate.

INTRODUCTION

Soil moisture (θ) is an important state variable in environmental systems and can be inferred from ground-based devices, proximal sensors, and remote-sensing platforms enabling observations to be performed across different spatial and temporal scales. Satellite systems are non-invasive measurement methods, with a spatial resolution ranging from about 10^1 m (e.g., Sentinel-1) to 10^3 m (e.g., SMAP, SMOS), which roughly determine near-surface soil moisture when canopy disturbance is not significant, but are unable to provide information in the entire soil rooting zone (Brocca et al., 2017). Direct measurement based on the thermogravimetric technique (Topp and Ferré, 2002), can operationally provide reliable data in sparse locations and is commonly used during sporadic field campaigns. This technique enables the soil water content distribution within the root zone to be measured occasionally and is destructive, time-consuming, expensive, and therefore unfeasible for large-scale applications (Entin et al., 2000; Romano, 2014). Unattended and automated *in-situ* monitoring networks for monitoring soil moisture are designed to overcome most of these drawbacks and comprise invasive ground-based instrumentation or non-invasive proximal sensors. The former include point-scale sensors installed in multiple positions and soil depths, thus providing localized information about soil moisture dynamics in a field. The latter consist of stationary "passive" cosmic-ray neutron probes (CRNPs) that monitor areal soil moisture over a footprint of hundreds of meters in diameter and of several decimeters of soil depth (Ochsner et al., 2013; Vereecken et al., 2015; Babaeian et al., 2019). The issue of coupling root-zone sensor networks and CRNP-based observations has been investigated only recently (e.g., Franz et al., 2012; Peterson et al., 2016; Nguyen et al., 2019). Other proximal sensors are the thermal or spectral cameras carried by unmanned aerial systems (UASs), although this relatively recent sensing technique can provide only sporadic measurements of soil moisture patterns.

At the field scale, soil moisture strongly depends on the local dynamics of the hydrological processes and therefore varies considerably in space and time. Soil moisture is greatly affected by complex and interwoven time-variant (e.g., climate, vegetation) and (mostly) time-invariant (e.g., topography, soil characteristics) factors. Especially in croplands, a variety of human activities and management practices induce changes in soil physical and hydraulic properties that have quite direct repercussions on the spatial-temporal evolutions of soil moisture (Hébrard et al., 2006; Price et al., 2010; Jonard et al., 2013). Grayson et al. (1997) identified the controls exerted by local (such as soil properties, vegetation, etc.) and non-local (such as terrain attributes) characteristics on soil moisture patterns: the former exerts a major influence under drier-than-normal soil conditions, when vertical water fluxes, such as evapotranspiration and infiltration, become the dominating hydrological processes; the latter, instead, is linked more to lateral fluxes and has a greater influence when wetter-than-normal conditions establish in the soil (Orth and Destouni, 2018).

Over the last two decades, monitoring of soil moisture has entered a stage of unprecedented growth, mainly because it plays an important role in controlling the exchange of water and energy between land and atmosphere and partly because it is increasingly employed to validate distributed hydrological models of different complexity over different spatial scales (Orth and Seneviratne, 2015; Nasta et al., 2019). Nevertheless, another fundamental state variable is the soil matric potential (ψ) that enables the total potential gradient to be determined, and hence the water fluxes in the soil domain. Low-cost sensors provide point-scale measurements of soil matric potential that can be coupled to sensors that indirectly measure soil moisture. Data pairs of ψ and θ provide the point-scale water retention function $\theta(\psi)$ (WRF) that is a necessary input soil characteristic to solve a Richards-based distributed hydrological model, but also represents valuable information to parameterize a bucket-type hydrological model. Knowledge of the field-scale WRF allows the estimation of the soil moisture values at the conditions of "field capacity" and "permanent wilting." These two points are commonly employed for the purpose of irrigation scheduling.

In an ideal situation, large scale distributed modeling of hydrological processes should rely on measurements of both field-scale soil moisture and matric potential values. While field-scale soil moisture can be provided by non-invasive proximal sensors (e.g., CRNPs), to our knowledge there is still a lack of sensing techniques enabling field-scale soil matric potentials to be monitored.

To offer a step forward, a major goal of this study is to explore the feasibility of assessing field-scale soil hydrological behavior of two experimental fields by coupling the measurements provided by non-invasive and invasive sensors. The area-average soil moisture monitored by CRNP is integrated with the spatial-mean of the point-scale soil moisture and soil matric potential values measured by a network of multiple low-cost sensors (SoilNet) installed in two sub-catchments of the Alento observatory with different physiographic characteristics. The results section is organized into four sub-sections. The first part concerns the correspondence between the vertical measuring soil volume of the CRNP (i.e., the CRNP's support depth) and the relative positions of the SoilNet sensors below the soil surface (section Assessing the CRNP Vertical Footprint at MFC2 and GOR1). The second part of the results is devoted to identifying the field-scale soil water retention functions at the two experimental sites (section Field-Scale Soil Water Retention Characteristics). The paper then proceeds by analyzing

the temporal variability of CRNP-based and SoilNet-based soil moisture data by questioning their ability to respond to the typical rainfall seasonality of the Mediterranean climate (section Temporal Variability of the Soil Moisture Index). Finally, we quantify the spatial variability of soil moisture data explained by more easily retrievable information, such as soil texture and terrain features (section Spatial Variability of Soil Moisture). To remove the offset between CRNP-based and SoilNet-based soil moisture data and the impact of physiographic characteristics on the soil moisture temporal variability, we employed the soil moisture index (SMI) that is a transformation of soil moisture data by referring to the soil moisture values at the conditions of "field capacity" and "permanent wilting" retrieved from the field-scale WRF. The obtained results are firstly discussed to shed some more light on the estimation of a field-scale WRF (section Drawbacks in Setting Up the Field-Scale Water Retention Function) while critically evaluating the drawback associated with the identification of the field capacity and permanent wilting soil moisture values (section Shortcomings Related to the Calculation of the Soil Moisture Index). Then, we explore whether, and to what extent, non-invasive datasets obtained from the stationary CRNPs can be assumed as representative of areal soil moisture values whose spatial variations can be explained, in turn, by easily retrievable controlling factors, such as the soil textural classes and terrain attributes (section Explaining the Spatial Variability of Soil Moisture Data).

DATA COLLECTION AND ANALYSIS AT THE STUDY SITES

Site Descriptions and Monitoring Devices

The Alento River Catchment (ARC) is located in the region of Campania in southern Italy (Nasta et al., 2020a) (**Figure 1**) and forms part of the TERENO (TERrestrial ENvironmental Observatories) long-term ecosystem infrastructure network (Bogena et al., 2012). For the purposes of the present study, we selected two sub-catchments, namely MFC2 and GOR1, located in the Upper Alento River Catchment (UARC), which is a hilly upper part of ARC, with a drainage area of ∼102 km^2 and delimited downstream by the Piano della Rocca earthen dam (Nasta et al., 2017). The climate and environmental characteristics of these two experimental sub-catchments are described in Romano et al. (2018). MFC2 is located near the village of Monteforte Cilento on the south-facing hillslope of UARC, and has a drainage area of ∼8.0 hectares (**Figure 1a**). This site is representative of the cropland zone of UARC with a co-existence of relatively sparse horticultural crops, olive, walnut, and cherry trees. MFC2 exhibits a typical V-shaped topography to form an ephemeral creek in the valley-bottom; hence it has a classic signature from a hydrological viewpoint. GOR1 is the other experimental sub-catchment located near the village of Gorga, on the north-facing hillslope of UARC (**Figure 1b**). It has a drainage area of ∼22.8 hectares and is representative of the woodland zone of UARC, characterized by chestnut and oak trees with brushwood made up of ferns and brambles growing during summer. This forested site is on average steeper than MFC2 and has a bedrock mainly consisting of turbidite sandstones, with medium permeability and mantled by a regolith zone of sand-silt mixtures.

In 2016 and at each of the above-mentioned experimental sites, a SoilNet wireless sensor network (Forschungszentrum Jülich, Germany) was installed comprising twenty end-devices connected to sensors positioned at the soil depths of 0.15 and 0.30 m. At each soil depth, the apparent soil dielectric permittivity (which is used to estimate θ through an empirical calibration relation), soil temperature, and soil electrical conductivity are measured by the GS3 capacitance sensors (METER Group, Inc., Pullman, WA, USA), whereas the soil matric pressure potential, ψ, is determined by the MPS-6 sensor (METER Group, Inc., Pullman, WA, USA). Note that the MPS-6 sensor can measure ψ values only in the range from -90 hPa (i.e., a matric suction head of about 0.92×10^0 m of H_2O) to -10^6 hPa (i.e., a matric suction head of about 1.02×10^4 m of H_2O) and is, therefore, unable to provide measurements when the soils are near saturation. The SoilNet data are transmitted wirelessly to a local gateway and then via Global System for Mobile Communications (GSM) modem to a central data server in near-real time (Bogena et al., 2010). The SoilNet end-devices were installed around a stationary cosmic-ray neutron probe (CRS2000/B by Hydroinnova LLC, Albuquerque, USA) by covering the experimental sub-catchments as much as possible for future application and validation of hydrological models (**Figures 1a,b**). The CRNP is a particle detector that measures the neutron intensity in the well-mixed neutron pool above the land surface, which is mainly determined by the amount of hydrogen atoms in the soil. The resulting inverse relationship between soil moisture and neutron intensity is described by the equation proposed by Desilets et al. (2010), where an empirical parameter requires site-specific calibration. The soil volume probed by the CRNP (i.e., in terms of radial footprint and penetration depth) is still a matter of debate, as new theories, additional data, and further interpretations are constantly being added (Köhli et al., 2015). According to Schrön et al. (2017), the CRNP provides indirect measurements of soil moisture over a circular footprint with an effective radius ranging from ∼150 to 210 m (i.e., from about 7 to 14 hectares) depending on various factors, e.g., soil moisture, atmospheric pressure, air humidity, vegetation biomass, etc. The CRNP is hyper-sensitive to soil moisture within the immediate vicinity and the sensitivity to soil moisture decreases non-linearly with radial distance (Schrön et al., 2017). The CRNP is most sensitive to soil moisture in the upper soil horizon, and this sensitivity decreases exponentially to a penetration depth of about 0.3–0.8 m depending on the soil moisture content. Therefore, we used the weighting procedure proposed from Schrön et al. (2017) to calculate appropriate mean values of our point-scale soil moisture measurements with the GS3 capacitance sensors installed at soil depths of 0.15 m and 0.30 m for comparisons with our CRNP-based soil moisture measurements.

One automatic weather station is located near MFC2, at 400 m a.s.l., and another near GOR1, at 711 m a.s.l. (**Figure 1**). Both weather stations are equipped with the same types of sensors for

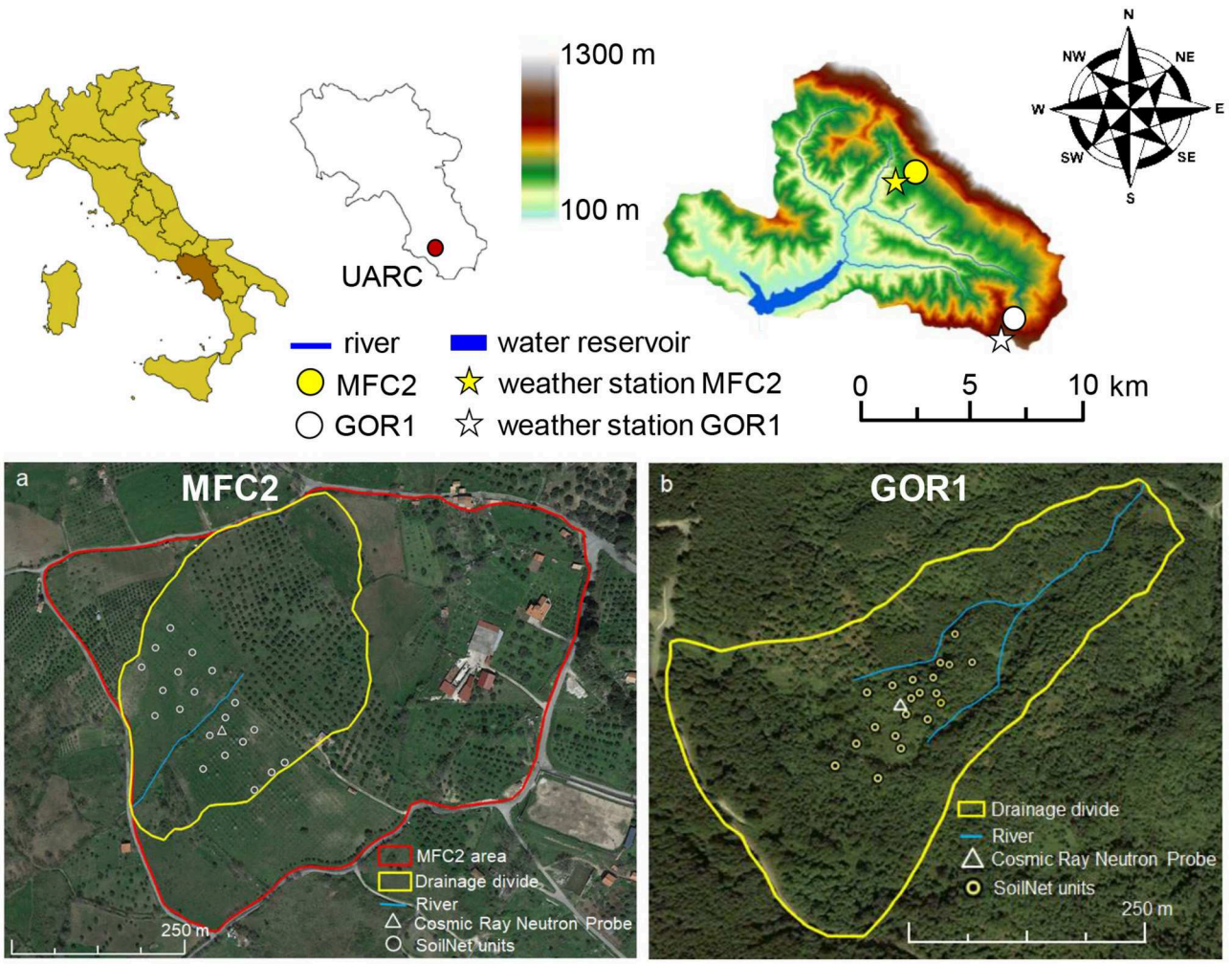

FIGURE 1 | Geographical location and 5-m Digital Elevation Model (DEM) of the Upper Alento River Catchment (UARC) in Campania (southern Italy), with the two experimental sites (MFC2 and GOR1) and corresponding weather stations displayed in the upper plots. The artificial water reservoir is delimited by the Piano della Rocca earthen dam. The layouts of the 20 end-devices of the SoilNet wireless sensor network and Cosmic Ray Neutron Probe are displayed on the satellite image (on the bottom plots) at MFC2 (plot **a**) GOR1 (plot **b**).

measuring the following variables at hourly time-steps: rainfall (R), air temperature, air relative humidity, wind speed, and direction, and net solar radiation using four-component net radiation sensors (NR01 net radiometer, Hukseflux Thermal Sensors, The Netherlands). According to World Meteorological Organization (WMO) standards, wind speed and air temperature are measured at a height of 3.0 m, whereas solar radiation is measured with the sensors positioned at a height of 2.0 m above the soil surface. Reference evapotranspiration (ET_0) was calculated by using the Penman-Monteith equation according to the protocol proposed by Allen et al. (1998).

At each position of the SoilNet end-devices, disturbed soil samples were collected at the two sensing depths for the laboratory determination of the soil particle-size distribution (PSD). Undisturbed soil cores (steel cylinder of 0.072 m inner diameter and 0.070 m height) were also collected at the soil depth of 0.15 m (vertical sampling at a soil depth of 0.115–0.185 m) of each measuring position to determine oven-dry soil bulk density (ρ_b).

Table 1 lists the descriptive statistics of United States Department of Agriculture (USDA) soil particle classes (sand, silt, and clay contents expressed in percentages) at the two soil depths (0.15 and 0.30 m) as well as the oven-dry soil bulk density and soil porosity at a soil depth of 0.15 m for the 20 SoilNet units in both MFC2 and GOR1 (see also **Tables A1, A2** in the **Appendix** reporting measurements of soil physical properties at each location). The individual triplet of sand-silt-clay percent is inserted in the USDA soil textural triangle of **Figure 2**, showing that the MFC2 cropland site is dominated by the clay and silty-clay-loam textural classes, whereas the predominant soil textural class of the GOR1 woodland site is loamy.

TABLE 1 | Descriptive statistics of sand, silt, and clay contents (in percent) at the two sampled soil depths (0.15 and 0.30 m) and oven-dry soil bulk density (ρ_b) with corresponding soil porosity at the soil depth of 0.15 m in the 20 SoilNet units for both MFC2 and GOR1 sub-catchments.

			Sand %	Silt %	Clay %	ρ_b g cm^{-3}	Soil porosity m^3 m^{-3}
MFC2	$z = 0.15$ m	Mean	20.8	40.4	38.8	1.29	0.51
		Std. Dev.	8.4	7.6	6.8	0.11	0.04
		CV (%)	40.1	18.9	17.6	8.4	7.9
		Min	10.5	22.1	23.5	1.00	0.46
		Max	41.8	51.3	52.8	1.43	0.62
	$z = 0.30$ m	Mean	22.3	40.7	37.1		
		Std. Dev.	9.7	8.5	8.7		
		CV (%)	43.4	21.0	23.6		
		Min	10.6	15.6	14.2		
		Max	50.6	51.2	51.5		
GOR1	$z = 0.15$ m	Mean	40.7	37.8	21.5	1.18	0.55
		Std. Dev.	7.2	6.4	3.5	0.30	0.11
		CV (%)	17.7	16.8	16.1	25.3	25.3
		Min	31.5	24.9	16.5	0.71	0.39
		Max	56.1	49.8	27.8	1.63	0.73
	$z = 0.30$ m	Mean	40.6	37.1	22.3		
		Std. Dev.	8.2	6.1	4.4		
		CV (%)	20.2	16.4	19.9		
		Min	28.4	25.5	14.3		
		Max	55.9	44.7	28.6		

At MFC2 and GOR1, the mean and standard deviation values of the textural particles are virtually the same for both sensing soil depths. Therefore, the shallow soil layer of both sites can be considered quite uniform in terms of soil properties. However, the mean sand content at MFC2 is almost half that at GOR1, thus offering a first glimpse of the diversity between the two experimental sites. Mean oven-dry soil bulk density (ρ_b) values measured at the soil depth of 0.15 m are also virtually the same at both MFC2 and GOR1, but the spatial variability of ρ_b is slightly higher in the forested site. Mean soil porosity is computed from the knowledge of ρ_b, assuming the soil particle density always equal to 2.65 g cm^{-3}.

Table 2 reports the descriptive statistics of the following terrain attributes: elevation (ζ), slope tangent, surface curvature (κ), aspect (in degrees), and upslope contributing area (A_c). The elevation of the forest site is almost twice that of the agricultural site. The high steepness at GOR1 induces a wide range of elevation (almost 100 m) of the SoilNet end-device positions, whilst MFC2 has gentle slopes and hence a very narrow elevation range (about 20 m). The two sites have similar curvature, but different slope aspect as described above.

Calibration Procedure for Invasive and Non-invasive Soil Moisture Sensors

A calibration step is necessary for ensuring good accuracy and precision when estimating point-scale and field-scale soil moisture values from the soil dielectric properties measured by capacitance sensors (Bogena et al., 2017; Gasch et al., 2017; Domínguez-Niño et al., 2019) and from neutron counts measured by CRNP (Franz et al., 2013; Baroni et al., 2018), respectively. Calibration of the CRNP requires simultaneous measurements of soil moisture using the thermogravimetric method and neutron intensity measured by the CRNP to estimate the area-wide soil moisture, θ_{CRNP}. We followed the calibration protocol suggested by Heidbüchel et al. (2016) and conducted three field campaigns to cover both wet and dry climate conditions to account for local climate seasonality. Soil sampling was carried out using a stainless steel core sampler with a plastic liner inside, with a length of 0.30 m and an inner diameter of 0.05 m. The soil samples were collected in 18 positions around the CRNP (six locations along radial distances of 1.0, 10.0, and 110.0 m). Each plastic liner was then cut into six pieces (each of 0.05 m length) to measure the oven-dry soil bulk density and soil-water content with the thermogravimetric method. Therefore, for each experimental sub-catchment, a total of 108 undisturbed soil cores were collected in each field campaign. The annex to this paper provides the Excel file employed for the calculations of the calibration procedure (Heidbüchel et al., 2016).

For calibrating the GS3 capacitance sensors, we carried out five field campaigns to collect undisturbed soil cores with the same core sampler used for calibrating the CRNP. The soil samples were collected over the twenty positions of the SoilNet end-devices. After soil sampling, we cut each core into six sub-cores (each of 0.05 m in length) to measure the soil moisture value by the thermogravimetric method and also the particle-size distribution. For calibration purposes, only the two sub-cores relating to the soil depths of 0.15 and 0.30 m were considered. To convert the apparent soil dielectric permittivity, ε_a, into the GS3-based soil moisture, θ_{GS3}, we used the relation proposed by the METER company (Ferrarezi et al., 2020):

$$\theta_{GS3} = 5.89 \cdot 10^{-6}\varepsilon_a^3 - 7.62 \cdot 10^{-4}\varepsilon_a^2 + 3.67 \cdot 10^{-2}\varepsilon_a - 7.53 \cdot 10^{-2}, \quad (1)$$

which was validated with the soil moisture values determined in our laboratory with the thermogravimetric method (not shown in this paper).

Two MPS-6 sensors were tested and calibrated in the laboratory using a pressure plate apparatus in a way similar to that described by Malazian et al. (2011). Finally, the empirical equation was used to compensate for the temperature effect on soil matric potential measured by the MPS-6 sensor (see Equation (3) in Walthert and Schleppi, 2018).

For both sub-catchments, the monitoring program started in spring 2016. Daily (indicated by the subscript d) values of rainfall, R_d, and reference evapotranspiration, $ET_{0,d}$, together with the soil moisture content time series are shown in **Figure 3** for MFC2 and in **Figure 4** for GOR1.

The presence of sporadic sensor malfunctioning of the GS3 sensors appears in these graphs due to the abrupt voltage drops of some batteries. Unfortunately, the CRNP at GOR1 (from June 2018 to January 2019) and at MFC2 (from April 2019 to July 2019) experienced a fault because of the modem interruption. The CRNP measurements, θ_{CRNP}, were affected

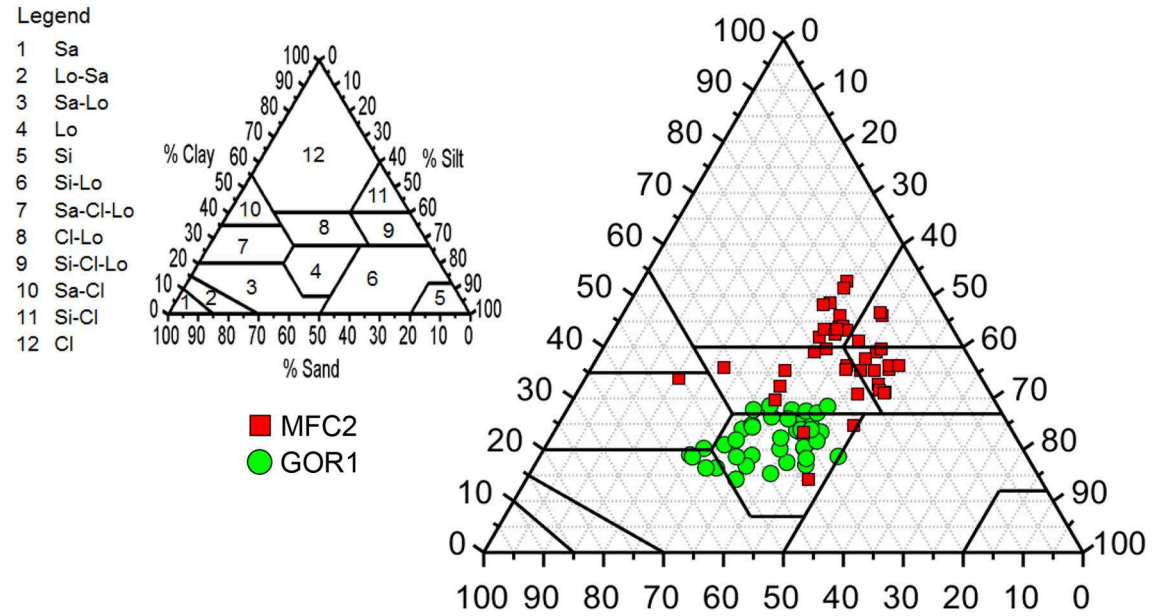

FIGURE 2 | USDA soil textural classes (Sa = sand; Lo = loam; Si = silt; Cl = clay) of the 20 soil samples collected at each of the two soil depths (0.15 and 0.30 m) at MFC2 (red squares) and GOR1 (green circles).

TABLE 2 | Descriptive statistics of terrain attributes, namely elevation (ζ, above mean sea level), tangent of slope [tg(*slope*)], tangential curvature (κ), aspect, and upslope contributing area (A_c) for the 20 SoilNet units in both MFC2 and GOR1 sub-catchments.

		Terrain attributes				
		ζ m	tg(slope) -	κ m^{-1}	Aspect Degrees	A_c %
MFC2	Mean	427.9	0.16	−0.15	247.5	23.5
	Std. Dev.	6.2	0.06	0.38	30.6	17.5
	CV (%)	1.4	37.4	252.1	12.4	74.7
	Min	417.5	0.05	−1.17	173.8	2.0
	Max	436.4	0.35	0.32	287.3	79.0
GOR1	Mean	701.3	0.33	−0.15	49.6	85.8
	Std. Dev.	23.0	0.16	0.56	68.8	164.4
	CV (%)	3.3	47.8	363.8	138.8	191.7
	Min	668.0	0.14	−1.39	14.4	1.0
	Max	759.6	0.85	0.70	335.4	666.0

by episodic spikes during the rainy season probably because of water ponding, low air temperature on the soil surface, or water being retained by leaf interception. Therefore, such values were removed from the data analysis.

Table 3 reports the descriptive statistics of SoilNet-based (θ_{GS3}) and CRNP-based (θ_{CRNP}) soil moisture, rainfall (R_a), cumulative reference potential evapotranspiration ($ET_{0,a}$) depths on an annual (indicated by subscript a) basis over the years 2017, 2018, and 2019. It is worth noting that the year 2017 was characterized by a notable meteorological drought, with R_a being about <41.5% in 2018 and <33.2% in 2019 for the cropland area and <31.4% in 2018 and <8.5% in 2019 for the forested area. During these 3 years, the mean annual rainfall in GOR1 was constantly and noticeably less than in MFC2, whereas the mean annual potential evapotranspiration $ET_{0,a}$ in GOR1 was only slightly less than in MFC2.

Data Analysis for Assessing Temporal Variability of the Soil Moisture Index

The soil moisture index (SMI_j) at time j provides a rough quantification of soil wetness and was computed in this study according to Hunt et al. (2009):

$$SMI_j = -5 + 10\frac{(\theta_j - \theta_{WP})}{(\theta_{FC} - \theta_{WP})} \quad (2)$$

where θ_j is soil moisture content at time j, θ_{FC} is soil moisture at the condition of "field capacity" in the soil profile, and θ_{WP} is soil moisture when on average a plant wilts permanently, being unable to recover its turgor. Note that the difference θ_{FC}-θ_{WP} is commonly defined as the Plant Available Soil Water Holding Capacity (Romano and Santini, 2002). SMI takes on negative and positive values indicating the presence of soil conditions from relatively dry to driest ($-5 \leq SMI < 0$) or from relatively wet to wettest ($0 \leq SMI \leq +5$). The values $SMI = -5$ correspond to the soil moisture content at "permanent wilting," whereas $SMI = +5$ is indicative of the soil moisture content at "field capacity" (Hunt et al., 2009).

The permanent wilting point (θ_{WP}) is commonly computed from the knowledge of the soil WRF, $\theta(\psi)$, as θ at the matric pressure potential $\psi = -15{,}300$ hPa [i.e., 15 bars; Romano and Santini (2002)], and this criterion is employed in the present study. Instead, the condition of "field capacity" in a soil profile

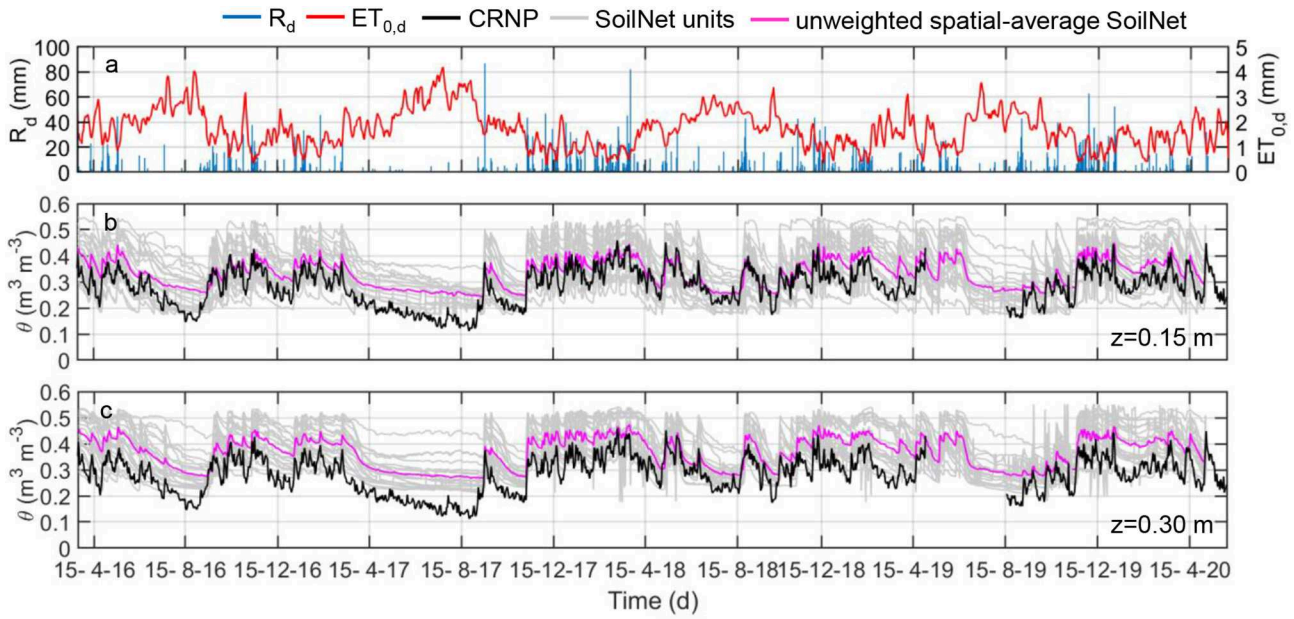

FIGURE 3 | Daily values of **(a)** rainfall, R_d (blue bars), reference evapotranspiration, $ET_{0,d}$ (red line), **(b)** SoilNet-based soil moisture contents (gray lines) at 0.15 m soil depth at the 20 locations and their unweighted spatial-mean (magenta line) and CRNP-based soil moisture (black line) and **(c)** SoilNet-based soil moisture contents (gray lines) at 0.30 m soil depth at the 20 locations and their unweighted spatial-mean (magenta line) and CRNP-based soil moisture (black line) at MFC2.

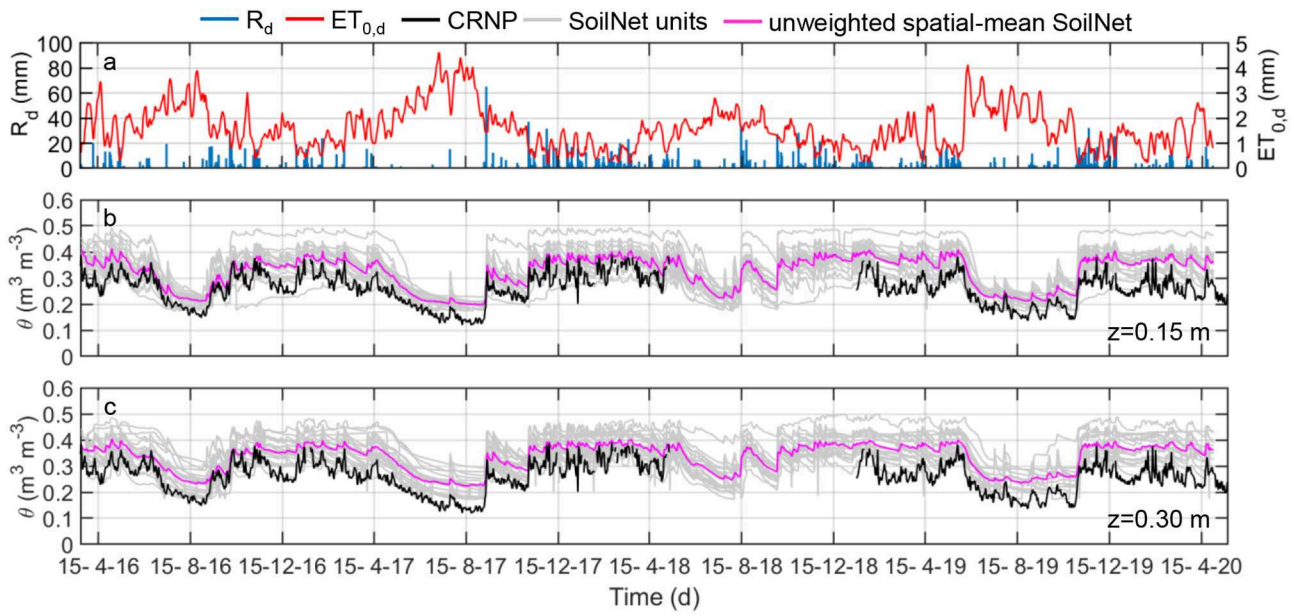

FIGURE 4 | Daily values of **(a)** rainfall, R_d (blue bars), reference potential evapotranspiration, $ET_{0,d}$ (red line), **(b)** SoilNet-based soil moisture contents (gray lines) at 0.15 m soil depth at the 20 locations and their unweighted spatial-mean (blue line) and CRNP-based soil moisture (black line) and **(c)** SoilNet-based soil moisture contents (gray lines) at 0.30 m soil depth at the 20 locations and their unweighted spatial-mean (blue line) and CRNP-based soil moisture (black line) at GOR1 site.

does not have a clear and shared definition and is still subjected to slightly different meanings. Actually, the soil moisture content at "field capacity," θ_{FC}, is a process-dependent parameter that can be defined as the average soil moisture measured in the entire soil profile when the water flux at its lower boundary becomes virtually nil during a drainage process starting with the initial condition of full saturation and with evaporation prevented at the upper boundary of soil surface (Romano and

TABLE 3 | Rainfall (R_a) and reference potential evapotranspiration ($ET_{0,a}$) depths on an annual basis with corresponding spatio-temporal-mean of SoilNet-based soil moisture (θ_{GS3}) at soil depths of 0.15 and 0.30 m and time-averaged CRNP-based soil moisture (θ_{CRNP}) at MFC2 and GOR1 in 2017, 2018, and 2019.

Site	Soil depth	Year	Units	2017	2018	2019
MFC2		R_a	mm	865.8	1481.6	1296.7
		$ET_{0,a}$	mm	710.9	596.7	579.3
	$z = 0.15$ m	θ_{GS3}	$m^3\ m^{-3}$	0.313	0.344	0.345
	$z = 0.30$ m	θ_{GS3}	$m^3\ m^{-3}$	0.338	0.380	0.367
		θ_{CRNP}	$m^3\ m^{-3}$	0.236	0.316	0.286
GOR1		R_a	mm	599.6	874.8	655.8
		$ET_{0,a}$	mm	686.5	466.2	549.7
	$z = 0.15$ m	θ_{GS3}	$m^3\ m^{-3}$	0.305	0.340	0.322
	$z = 0.30$ m	θ_{GS3}	$m^3\ m^{-3}$	0.323	0.350	0.331
		θ_{CRNP}	$m^3\ m^{-3}$	0.245	0.335	0.244

Santini, 2002; Nasta and Romano, 2016). This parameter is considered a critical threshold of soil water-holding capacity and commonly employed in bucketing-type models to control hydrological processes, such as overland flow and drainage below the root zone of a uniform soil profile (Romano et al., 2011). The value of θ_{FC} should be obtained using a specifically designed *in-situ* drainage experiment, but can be conveniently retrieved also through numerical simulations, especially in the case of layered soil profiles that are the rule rather than an exception in the real world (Nasta and Romano, 2016). Under simplified assumptions and in the case of a uniform soil profile, the value of θ_{FC} can instead be roughly estimated from the knowledge of the soil WRF using a static criterion that assumes, on average, that θ_{FC} is equal to the soil-water content at the matric pressure potential of −330 hPa. Allowing for the effect of soil texture on the "field capacity" value, Romano and Santini (2002) suggested setting a soil matric pressure potential of ∼-100 hPa for coarse soils and −500 hPa for fine soils. The matric pressure value of −330 hPa should be mostly used in the cases of medium-textured soils (Romano et al., 2011).

Given the simplified picture of soil condition offered by the SMI, in this study we estimated the θ_{FC} value through the analytical equation proposed by Assouline and Or (2014) that computes the soil matric potential at "field capacity" (ψ_{FC}) as follows:

$$\psi_{FC} = \frac{1}{\alpha_{vG}} \left(\frac{n_{vG} - 1}{n_{vG}} \right)^{\left(\frac{1-2\,n_{vG}}{n_{vG}}\right)}, \tag{3}$$

and hence determines the soil moisture content at field capacity as follows:

$$\theta_{FC} = \theta_r + (\theta_s - \theta_r) \left[1 + (\alpha_{vG} |\psi_{FC}|)^{n_{vG}} \right]^{\left(\frac{1-n_{vG}}{n_{vG}}\right)}, \tag{4}$$

where α_{vG} (hPa^{-1}) and n_{vG} (–) are the two shape parameters featuring in van Genuchten (1980) analytical soil-water retention relationship $\theta(\psi)$:

$$\theta(\psi) = \theta_r + \frac{\theta_s - \theta_r}{(1 + |\alpha_{vG}\psi|^{n_{vG}})^{m_{vG}}}, \tag{5}$$

with the condition $m_{vG} = 1–1/n_{vG}$. We use the acronym "vG" as a subscript to refer to the above parameters. The θ_s ($m^3\ m^{-3}$) and θ_r ($m^3\ m^{-3}$) parameters are the saturated and residual soil water contents, respectively. While θ_s has a clear physical meaning and is measured with laboratory or field tests, θ_r is often set at zero or assumed as an additional unknown parameter to be estimated by the fitting procedure together with the other two unknown parameters α_{vG} and n_{vG}. By substituting Equation (3) into Equation (4), the knowledge of θ_s, θ_r, and n_{vG}, allows to determine θ_{FC} through the following closed-form expression:

$$\theta_{FC} = \theta_r + (\theta_s - \theta_r) \left\{ 1 + \left[\frac{n_{vG} - 1}{n_{vG}} \right]^{(1 - 2n_{vG})} \right\}^{\left(\frac{1-n_{vG}}{n_{vG}}\right)}. \tag{6}$$

To test whether the SMI distributions are unimodal or bimodal, in this study we refer to the empirical method that evaluates a bimodality coefficient, termed BC (Pfister et al., 2013), which ranges between 0 and 1 and is computed as follows:

$$BC = \frac{m_3^2 + 1}{m_4 + 3\left[(n-1)^2 / (n-2)(n-3)\right]}, \tag{7}$$

where n is the sample size, m_3 is the skewness and m_4 is kurtosis of the distribution. To avoid sample bias, the skewness and kurtosis values are calculated as follows:

$$m_3 = \frac{\sqrt{n(n-1)}}{n-2} \left\{ \frac{1/n \sum_{i=1}^{n} (x_i - \overline{x})^3}{\left[\sqrt{1/n \sum_{i=1}^{n} (x_i - \overline{x})^2} \right]^3} \right\}, \tag{8}$$

$$m_4 = \frac{n-1}{(n-2)(n-3)} \left\{ (n+1) \frac{1/n \sum_{i=1}^{n} (x_i - \overline{x})^4}{\left[1/n \sum_{i=1}^{n} (x_i - \overline{x})^2\right]^2} - 3(n-1) \right\}, \tag{9}$$

where $\overline{x}$ is the arithmetic mean of the set of data. A bimodal distribution is characterized by high skewness, low kurtosis, or both. Specifically, if BC is >0.555 (BC > 0.555), then the hypothesis that the data follow a bimodal distribution cannot be rejected (Kang and Noh, 2019).

Data Analysis for Assessing Spatial Variability of Soil Moisture Data

The partial least-squares regression (PLSR) model is used to reveal the factor explaining the spatial variance of daily soil moisture data. As discussed in (Romano and Chirico, 2004) and Nasta et al. (2018b), most soil moisture variations are cross-correlated with soil physical properties, such as the percentages of sand, silt, and clay contents (see **Table 1** and **Tables A1**, **A2**), as well as terrain attributes, such as elevation above mean sea level, slope aspect, slope gradient, tangential

curvature, and upslope contributing area (see **Table 2**). The PLSR model generates new predictor variables (components) as combinations of the original predictors and finds combinations of the predictors that have a large covariance with the soil moisture data. The predictive ability of PLSR is expressed in terms of the coefficient of determination and root mean squared error (RMSE) which, respectively, evaluate the scatter of the data points around the fitted regression curve and the bias between observed and modeled soil moisture values. PLSR also provides the percent of variance explained by the components, distinguishing between soil textural characteristics and topographic attributes.

RESULTS

Assessing the CRNP Vertical Footprint

In this study, we investigated the vertical footprint of the CRNP in the two experimental areas (MFC2 and GOR1). Among the variety of weighting procedures provided in the literature, we opted to use the equal (unweighted) spatial-mean and a reliable physically-based weighted spatial-mean of point-scale soil moisture measurements (Schrön et al., 2017). The first step is to compare the CRNP-based soil moisture with the unweighted soil moisture spatial-mean, as depicted in **Figures 3**, **4**. We also computed the physically-based weighted spatial-mean of the SoilNet-based soil moisture data as recommended by Schrön et al. (2017) by using the MATLAB script provided by these authors. The comparisons between the CRNP-based soil moisture and all the unweighted or weighted spatial-mean SoilNet-based soil moisture are depicted in the scatter plots of **Figure 5** for both the MFC2 and GOR1 sites. Although RMSE takes on very similar values for the four cases considered, the Schrön et al. (2017) weighted procedure seems to provide a slightly better correlation than the unweighted one especially at the higher soil moisture contents, as evident from the fact that the scatter cloud tends to be closer to the identity line as θ increases. This situation is more pronounced for MFC2 than GOR1. It is also worth noting that the scatter cloud increasingly diverges from the identity line when soil moisture values decrease. Overall, the impact of employing a weighting procedure for our case studies seems to provide only a scant improvement. This situation can be explained if one considers that, allowing for the limited number of available devices, the positioning of the sensor nodes was primarily designed to detect the spatial patterns of the soil hydrological variables as well as possible and not for comparison purposes between the two sensing systems (i.e., a relatively low number of SoilNet end-devices is located in the direct vicinity of the CRNP). That said, in the following we assumed that both vertical and radial weights also apply to obtain the averaged soil matric potential values.

Because the soil moisture values observed by the two sensing systems show different means and ranges of variation, the comparison among the time series is more robust when these data are standardized using the Z-scores, which can take on positive or negative values (for example, positive values indicate that the data are above the arithmetic mean). As evident from a perusal of **Figure 6**, both unweighted and weighted time series of θ_{GS3} overlap almost perfectly over the CRNP-based soil moisture time series. Nevertheless, the CRNP data show significantly higher temporal variability, thus indicating a stronger response to climate forcing. This feature reflects the higher sensitivity of the CRNP to near-surface soil moisture due to the decreasing sensitivity with soil depth (Schrön et al., 2017).

Field-Scale Soil Water Retention Characteristics

The simultaneous availability of soil moisture, $\theta_{GS3,j}$, and matric pressure head, ψ_j, values, at the same time, j, and soil depth, z, from the wireless sensor networks, allows us to identify the SoilNet-based soil water retention functions (WRFs) at the two sites. The WRFs of **Figures 7A,B**, shown for the two sensing depths of 0.15 and 0.30 m, were determined by coupling the daily unweighted values of the spatial-mean of $\theta_{GS3,j}$and $\log_{10}$-transformed ψ_j. Because the MPS-6 sensor is unable to measure matric pressures $>$-90 hPa, data pairs $|\psi_j|$-$\theta_{GS3,j}$ are not available in the near-saturated region of the WRF. Consequently, we set the saturated soil water content, θ_s, as 90% of the spatial-mean soil porosity obtained from the direct measurements of ρ_b (see **Table 1**). **Figures 7A,B** also show van Genuchten's water retention relations whose unknown parameters α_{vG} and n_{vG} were obtained by non-linear regression, while setting θ_r at zero. All parameters, including the prescribed (θ_s), optimized (α_{vG}, n_{vG}), and those derived from the knowledge of the WRFs (θ_{FC}, θ_{WP}) are reported for each site in **Table 4** with the corresponding RMSE values. Overall, the two SoilNet-based WRFs belonging to the MFC2 and GOR1 sites (solid black line for GOR1 and dashed black line for MFC2) are characterized by different shapes, with the solid curve of GOR1 showing a shape typical for medium- or coarser-textured soils, with a quite rapid decrease in soil moisture contents in the wet region of the diagram. The dashed curve for MFC2 desaturates with a smooth decay which certainly reflects the typical behavior of finer-textured soils.

According to our method and as depicted in **Figure 7C**, an "effective" (field-scale) soil WRF over the CRNP footprint can be suitably obtained by coupling, for the same time j, the areal-based soil moisture ($\theta_{CRNP,j}$) contents with the weighted spatial-mean matric pressure potential (ψ_j) values. The weights applied to ψ_j-values were obtained through the weighting procedure recommended by Schrön et al. (2017).

In all the soil water retention curves of **Figure 7**, the black circles identify the soil moisture contents at "field capacity," as computed by Equation (6), and the black squares identify the soil moisture contents at "permanent wilting," corresponding to $|\psi| = 1.50 \times 10^4$ hPa. The picture provided by the $\theta_{CRNP}(|\psi|)$ retention curves of **Figure 7C** allows us to frame in a new perspective the potential of using the areal soil moisture contents offered by a CRNP, and also gives us some preliminary indications on possible drawbacks related to a scale

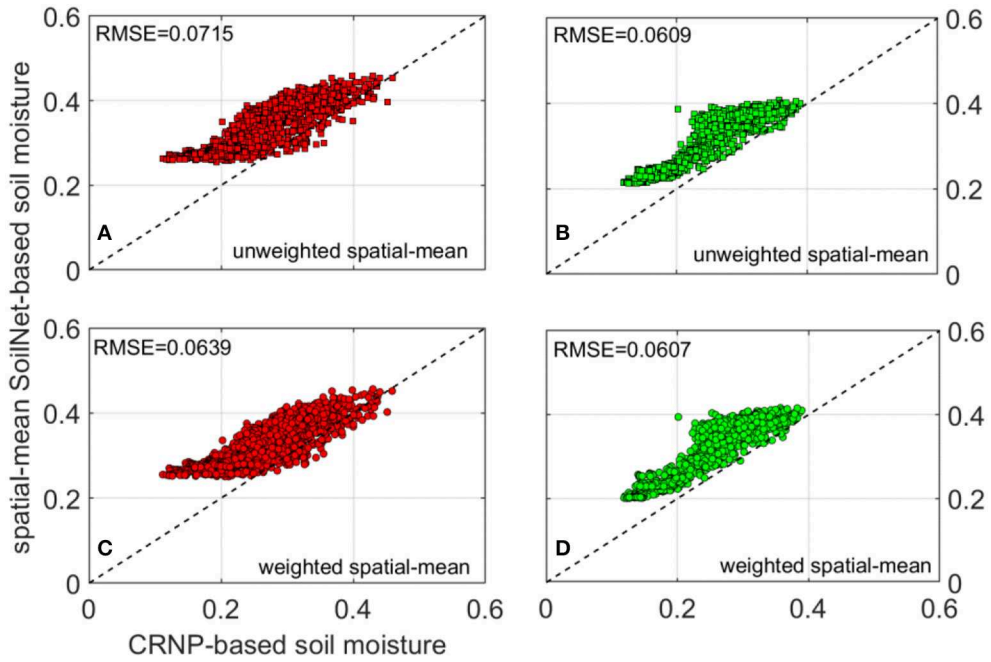

FIGURE 5 | Relation between CRNP-based soil moisture and unweighted spatial-mean of SoilNet-based soil moisture at **(A)** MFC2; **(B)** GOR1; relation between CRNP-based soil moisture and weighted spatial-mean of SoilNet-based soil moisture at **(C)** MFC2; **(D)** GOR1. Dashed black line depicts the 1:1 identity line. RMSE values are reported in each subplot.

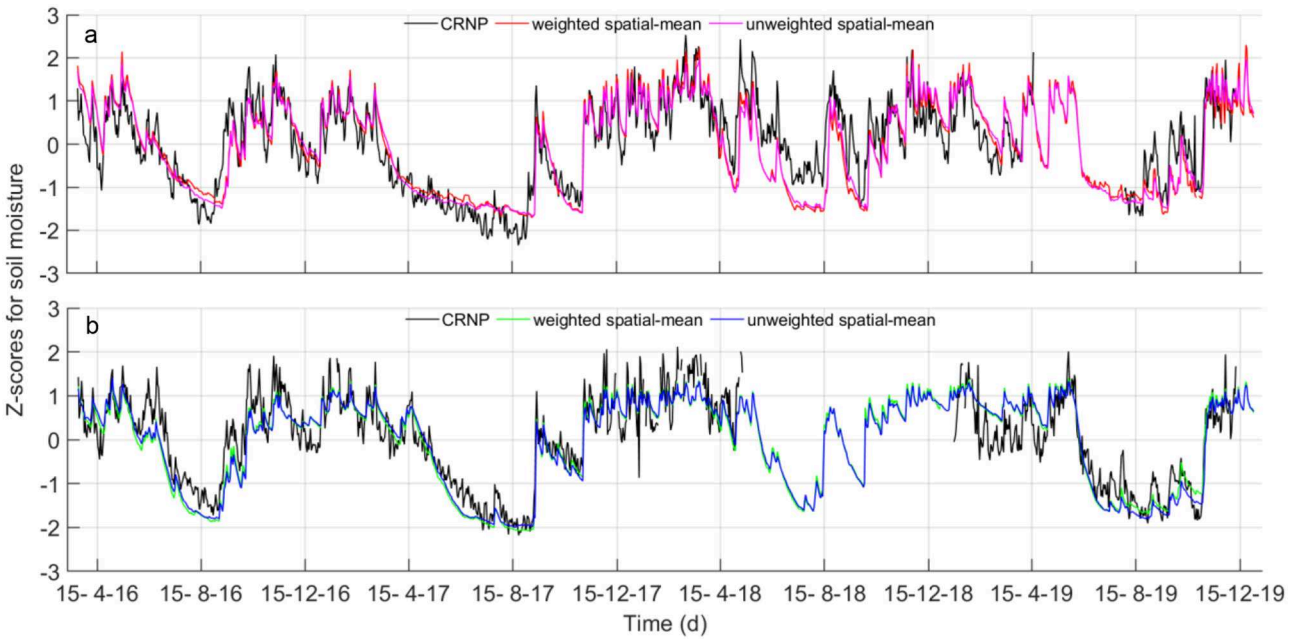

FIGURE 6 | Daily values of *Z*-scores of unweighted spatial-mean SoilNet-based soil moisture contents, weighted spatial-mean and CRNP-based soil moisture (black line) in **(a)** MFC2; and **(b)** GOR1.

mismatch between the areal θ and the point-scale ψ data. For both MFC2 and GOR1 sites, the observed scatter of the retention points (see RMSE values in **Table 4**) is likely due to the different spatial scales associated with the CRNP-based soil moisture contents and the point-measured matric potential pressure values.

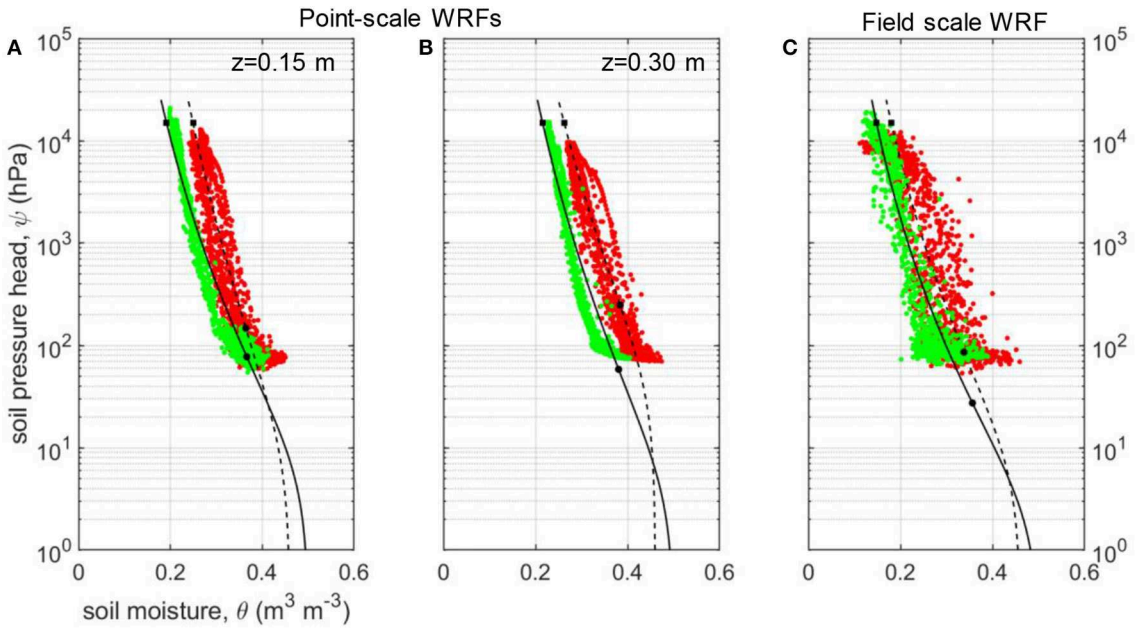

FIGURE 7 | Soil-water retention functions obtained by relating daily values of **(A)** SoilNet data pairs at $z = 0.15$ m; **(B)** SoilNet data pairs at $z = 0.30$ m; **(C)** CRNP-based soil moisture ($\theta_{CRNP,j}$) and spatial-mean SoilNet-based soil matric potential (absolute value $|\psi_j|$) at MFC2 (red circles) and GOR1 (green circles). Dashed black (MFC2) and solid black (GOR1) lines represent the soil-water retention curves fitted using van Genuchten's parametric relation. Black circles and black squares denote the θ_{FC} and θ_{WP} values at the conditions of "field capacity" and "permanent wilting," respectively.

TABLE 4 | Parameters feauturing in the vG-WRF at MFC2 and GOR1 referring to point-scale SoilNet based WRF at soil depths of 0.15 and 0.30 m and field-scale WRF.

		MFC2			GOR1		
		$z = 0.15$ m $z = 0.30$ m			$z = 0.15$ m $z = 0.30$ m		
		Point-scale		Field-scale	Point-scale		Field-scale
θ_s	$m^3\ m^{-3}$	0.46	0.46	0.46	0.50	0.50	0.50
α_{vG}	cm^{-1}	0.108	0.024	0.135	0.149	0.228	0.374
n_{vG}	-	1.08	1.09	1.12	1.13	1.12	1.14
θ_{FC}	$m^3\ m^{-3}$	0.364	0.384	0.338	0.366	0.380	0.356
θ_{WP}	$m^3\ m^{-3}$	0.249	0.262	0.180	0.192	0.215	0.147
RMSE	$m^3\ m^{-3}$	0.0196	0.0172	0.0365	0.0166	0.0142	0.0288

Temporal Variability of the Soil Moisture Index

The soil moisture index (SMI) is a transformation of soil moisture data and was employed in this study to remove (i) the offset between CRNP-based and SoilNet-based soil moisture observed in **Figures 3**–**5**, and (ii) the impact of time-invariant environmental controls, such as the soil textural characteristics and topographical features, on the soil moisture temporal variability (Mittelbach and Seneviratne, 2012). The SMI is computed by using the soil moisture contents at "field capacity" (θ_{FC}) and "permanent wilting" (θ_{WP}) as determined in section Field-Scale Soil Water Retention Characteristics and reported in **Table 4** (see also the plots in **Figure 7**) following the procedure described in section Data Analysis for Assessing Temporal Variability of the Soil Moisture Index.

Based on the results shown by Romano et al. (2018) regarding the soil moisture distributions, we further processed our datasets by analyzing the histograms of daily SMI values (SMI_d) that are depicted in **Figure 8**. The individual graphs of this figure enable us to suitably compare the hydrological responses of the cropland (red bars) and woodland (green bars) areas. The SMI_d values mostly fluctuate around the zero value with the occurrence of wetter-than-normal conditions induced by rainfall surplus and drier-than-normal conditions determined by rainfall deficits. Note that the period from March to September 2017 was characterized by an exceptionally long dry spell. For almost all months over the investigated 4-year period, the rainfall at MFC2 exceeded that at GOR1, which is reflected in the amount of water present in the soil.

The graphs of **Figure 8** show that the histograms of SMI_d computed from the θ_{GS3} data, at the two soil depths of 0.15 and 0.30 m, are characterized by an evident bimodal shape and this visual evidence is also quantified by the bimodal coefficient BC, which always takes on values >0.555. In contrast, the histograms of SMI_d obtained from the θ_{CRNP} data follow a more Gaussian-like unimodal distribution, as indicated by BC values lower than 0.555. A perusal of these plots provides a useful indication of the soil hydrological behavior of these two experimental sites. Inspection of **Figures 3**, **4** highlights that

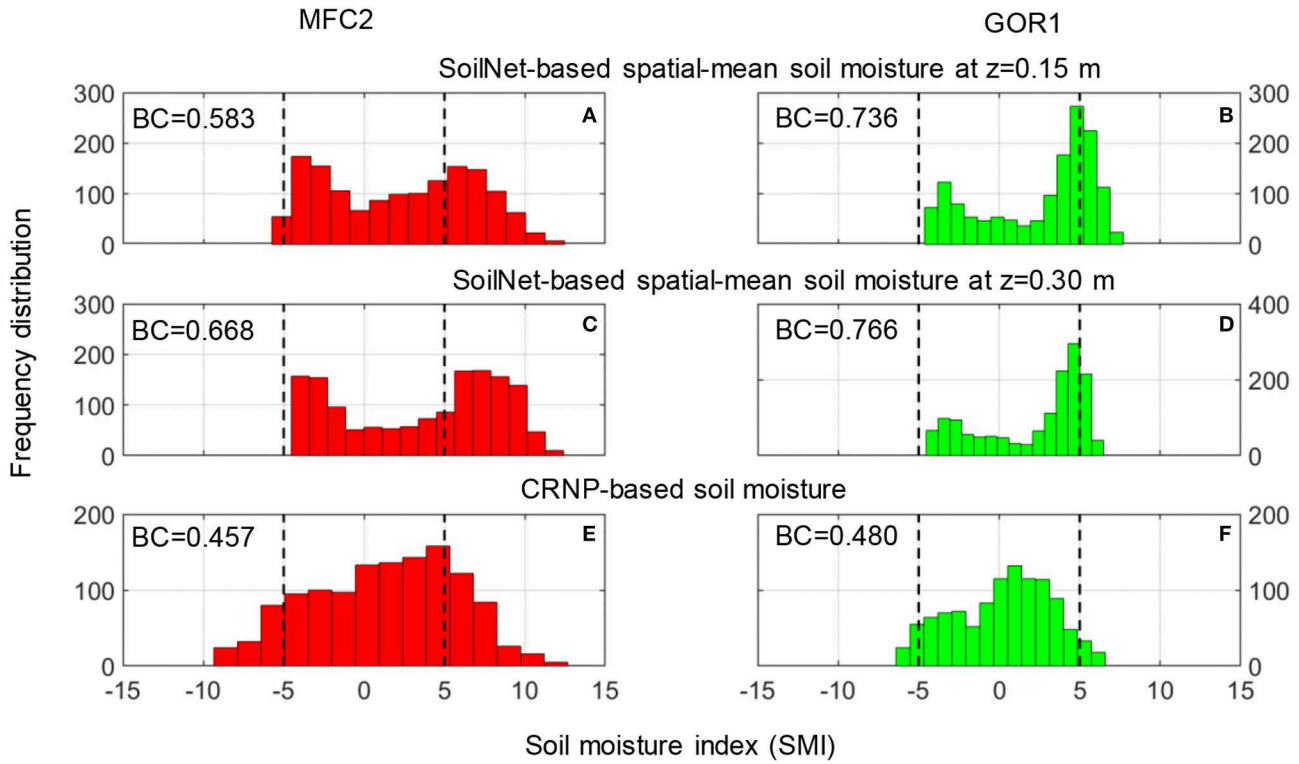

FIGURE 8 | Frequency distributions of daily values of SMI (SMI_d) calculated using SoilNet-based soil moisture spatial-mean at $z = 0.15$ m at **(A)** MFC2 and **(B)** GOR1, and $z = 0.30$ m at **(C)** MFC2 and **(D)** GOR1, and CRNP-based soil moisture at **(E)** MFC2 and **(F)** GOR1. Each subplot reports the bimodality coefficient (BC).

the soil moisture time series measured by the GS3 sensors show the presence of persistent wet and dry conditions that are interrupted by sharp wetting pulses and smooth soil desaturation. The two observed long-term plateaus induce the bimodal shape of the corresponding distribution of SoilNet-based SMI_d values that reflect the typical rainfall seasonality of the Mediterranean climate (Vilasa et al., 2017). By contrast, CRNP-based soil moisture data show a constant decrease during desaturation in the growing season and sharp wetting-drying pulses during the rainy season. This temporal variability is typical of the near-surface soil moisture dynamics and is reflected in the unimodal frequency distribution of CRNP-based SMI_d values in **Figure 8**. Nevertheless, a further step is to verify whether these patterns hold within a year-by-year analysis given the remarkable variability of annual rainfall sums reported in **Table 3**. **Figures 9**, **10** report the frequency distributions of SMI_d values calculated by using SoilNet-based soil moisture at $z = 0.15$ m and CRNP-based soil moisture for each year at MFC2 and GOR1, respectively. Interestingly, CRNP-based soil moisture is able to capture bimodality only in 2017 (characterized by a long drought) in MFC2 (BC = 0.57). Extremely wet conditions recorded in 2018 induce a unimodal normal distribution in CRNP-based SMI_d values in MFC2. Unfortunately, a similar situation could not be explored in GOR1 due to a large amount of missing data at this site.

Spatial Variability of Soil Moisture

This section illustrates the spatial variability of SoilNet-based soil moisture explained by easily-available environmental variables such as soil textural classes and terrain features. **Figure 11** illustrates the CRNP-based SMI_d values against the spatial-standard deviation of $\theta_{GS3,j}$ values measured at the soil depth of 0.15 m in both MFC2 and GOR1. The spatial variability of soil moisture data is related to SMI_d values with a somewhat concave downward shape that is more pronounced for the forested site. This shape is similar to that reported by, for example, Teuling and Troch (2005), Famiglietti et al. (2008), and Rosenbaum et al. (2012), although different patterns of this relationship have been reported elsewhere (Mittelbach and Seneviratne, 2012). Because of the larger spatial variability of soil properties in the cropland site, one immediately notices the larger scatter of the points for MFC2 (**Figures 11A,B**) with respect to GOR1 (**Figures 11C,D**) in the central range of the catchment's spatially averaged soil moisture measured by the CRNP. This may explain the large scatter observed in the field-scale WRF belonging to MFC2 (**Figure 7C**). Further insights are gained by evaluating the role exerted by easily-retrievable local and non-local factors, comprising the five topographical attributes (elevation, aspect, slope, tangential curvature, upslope contributing area) and the three soil textural classes (percentages of sand, silt, and clay content), to help describe the spatial organization of the observed soil moisture datasets. However,

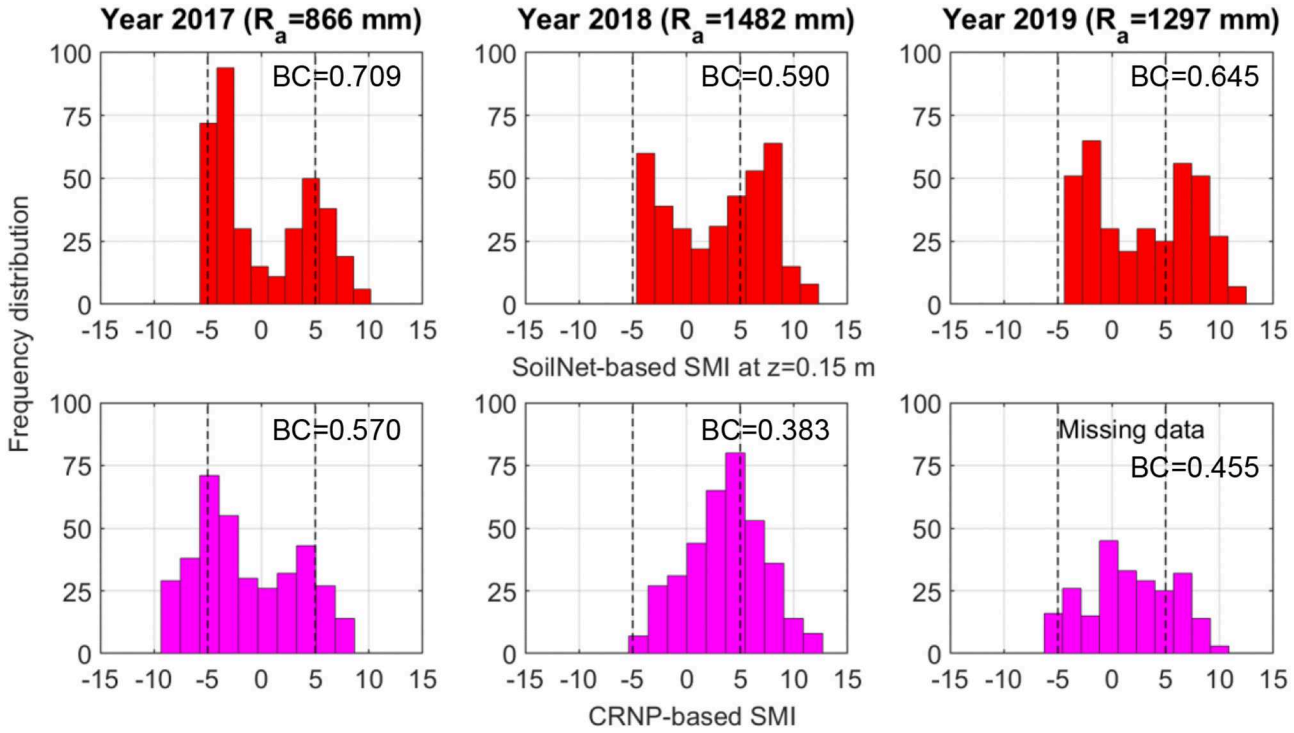

FIGURE 9 | Frequency distributions of daily values of SMI (SMI_d) calculated using SoilNet-based soil moisture at $z = 0.15$ m (red bars) and CRNP-based soil moisture (magenta bars) at MFC2 in 2017, 2018, and 2019. Each subplot reports the bimodality coefficient (BC).

apart from a few general comments, we caution the reader that the impact of vegetation was neglected in this study due to a lack of direct robust measurements.

The variability explained by the soil terrain attributes (top panels, **Figure 11A** for MFC2 and **Figure 11C** for GOR1) and textural characteristics (bottom panels, **Figure 11B** for MFC2 and **Figure 11D** for GOR1) is quantified by using the PLSR method (described in section Data Analysis for Assessing Spatial Variability of Soil Moisture Data) and represented by the color bar on the right side of the plots in **Figure 11**. It is worth noting that, on average, the terrain attributes explain almost 50% of soil moisture spatial variability in the case of the cropland site (i.e., MFC2), under both wet and dry conditions. In the forested site (i.e., GOR1), the considered terrain attributes explain on average about 40% of soil moisture spatial variability. Nonetheless, this percentage of explained variability increases significantly under wet conditions (bluish colors in **Figure 11C**) and decreases considerably under dry conditions (reddish colors in **Figure 11C**). **Figures 11B,D** show that soil texture has a scant ability to explain the spatial organization of soil moisture data in both sites at the soil depth of 0.15 m.

The five terrain attributes (elevation, aspect, slope, tangential curvature, upslope contributing area) explain most near-surface soil moisture variability in both sites. Interesting aspects emerge if we iteratively repeat the PLSR exercise by removing one terrain attribute at a time: aspect-induced variability of soil moisture plays a major role in both experimental sites; the second-ranked topographic attribute is elevation for MFC2, and upslope contributing area for GOR1.

DISCUSSION

Drawbacks in Setting Up the Field-Scale Water Retention Function

In this study, we proposed to construct an "effective" (field-scale) soil WRF by coupling the areal-based soil moisture ($\theta_{CRNP,j}$) contents with the weighted spatial-mean matric pressure potential (ψ_j) values with weights obtained through the weighting procedure recommended by Schrön et al. (2017). On the one hand, a persistent offset occurs between the spatial-mean θ_{GS3} and θ_{CRNP} (see **Figures 3**, **4**) mostly to be attributed to calibration effects; on the other, we observed a relatively large scatter among the water retention data pairs of **Figure 7** which may be attributed to several drawbacks. Enhancing the calibration procedure for the CRNPs is certainly to be considered a priority and more field campaigns would probably be required under extremely dry or wet conditions. However, the onset of a sort of scale mismatch represents another important issue which, however, can be tempered by installing some MPS-6 sensors at depths much closer to the soil surface and over more locations, especially near the CRNP (within a radial distance of 5 m). The biomass of dense understory vegetation during

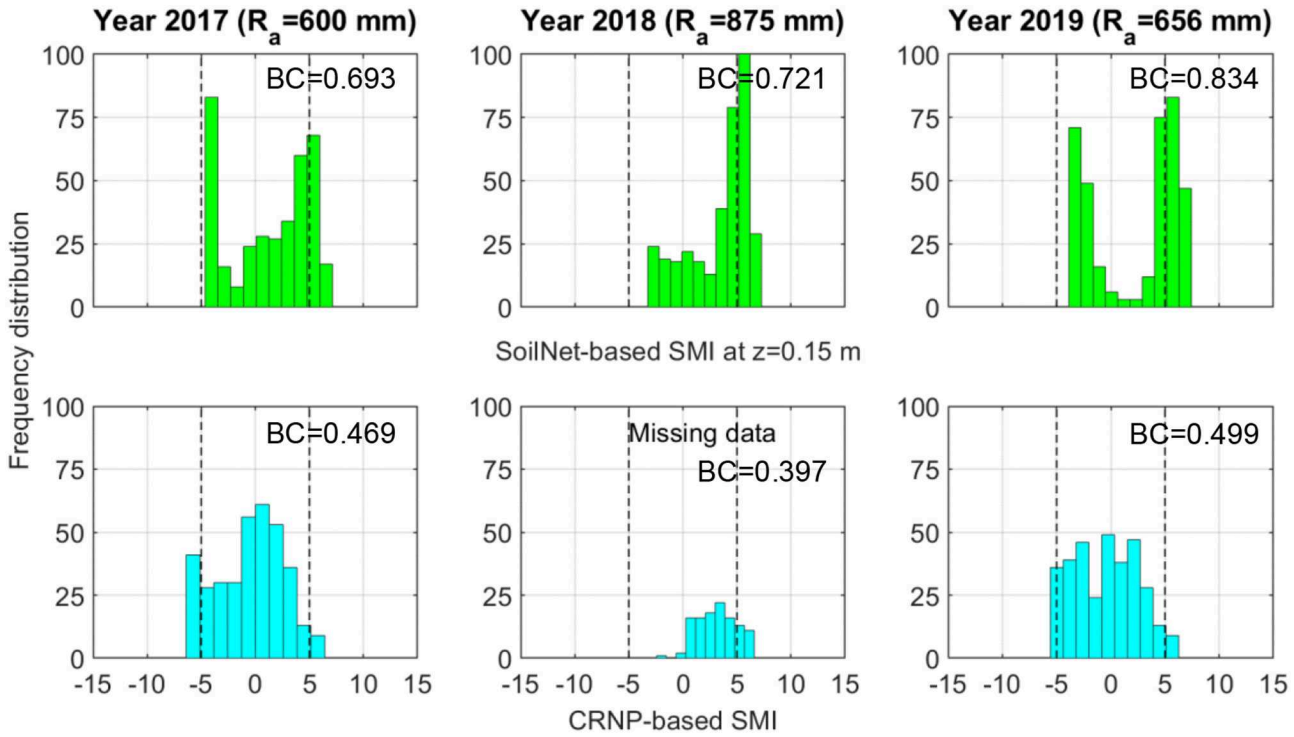

FIGURE 10 | Frequency distributions of daily values of SMI (SMI_d) calculated with SoilNet-based soil moisture at $z = 0.15$ m (green bars) and CRNP-based soil moisture (cyan bars) at MFC2 in 2017, 2018, and 2019. Each subplot reports the bimodality coefficient (BC).

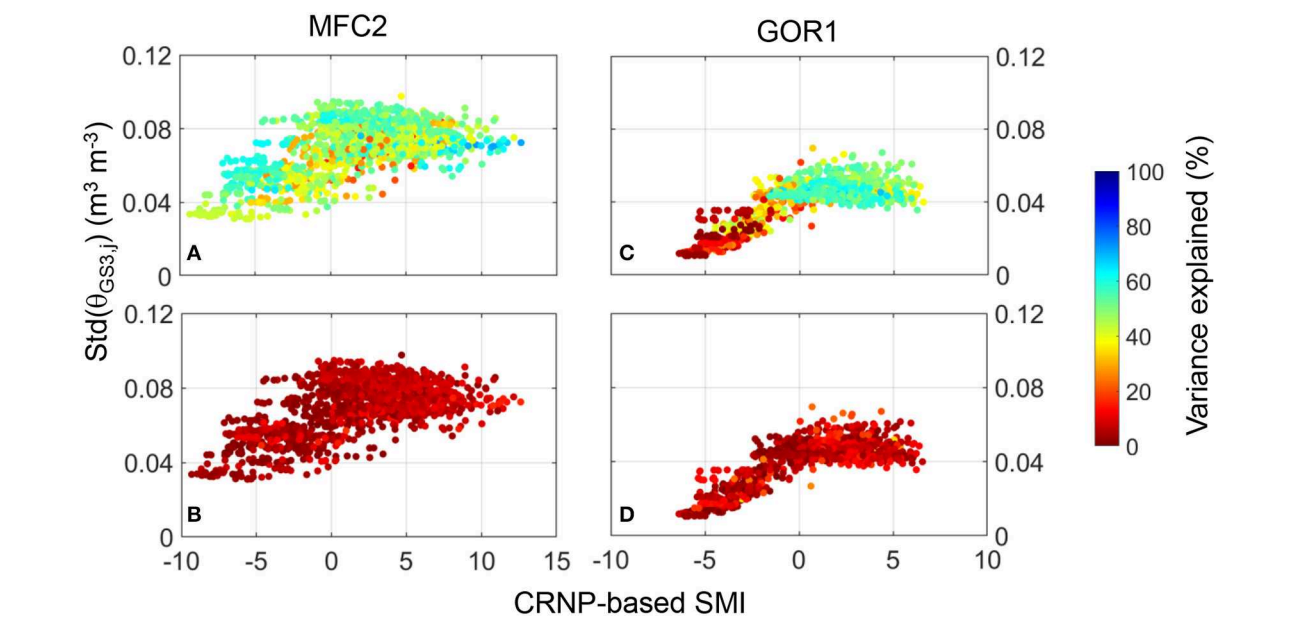

FIGURE 11 | Scatter plots of CRNP-based SMI-values against spatial standard-deviation of SoilNet-based soil moisture, Std($\theta_{GS3,j}$), at 0.15 m soil depth and time j for the two experimental sites. The various shades of the colored circles indicate the amount (in percent) of spatial variance explained: **(A)** by terrain attributes at MFC2; **(B)** by soil texture at MFC2; **(C)** by terrain attributes at GOR1; **(D)** by soil texture at GOR1.

the summer season may have influenced the neutron counts determined by the CRNP (Baatz et al., 2015; Jakobi et al., 2018), and the corresponding impact on soil moisture estimates needs more attention in the near future.

To some extent, we used the SMI values to remove the effect of sensor calibration on both the offset and impact of environmental conditions between the two experimental sites. An analysis of the time series of SMI_d values highlights the different behavior between the CRNP-based and SoilNet-based soil moisture contents. The SMI from the sensor networks at soil depths of 0.15 and 0.30 m was able to reflect the impact of Mediterranean rainfall seasonality (Nasta et al., 2020b), although the possibility of having additional capacitance sensors installed at a shallower soil depth would have helped us to better compare our two sensing systems (Franz et al., 2012).

Shortcomings Related to the Calculation of the Soil Moisture Index

In this study, we assumed that the soil moisture index (SMI) can give a useful picture of the soil hydrological behavior of zones with quite different physiographic characteristics, such as our MFC2 and GOR1 experimental sites. Yet the calculation of SMI values requires knowledge of soil moisture contents at field capacity and permanent wilting which, in turn, should be at least retrieved from the soil WRF. If an analytical $\theta(\psi)$ relation cannot be obtained from direct measurements, one can resort to a pedotransfer function (PTF) (van Looy et al., 2017) and then compute the values of θ_{FC} and θ_{WP} for example by following the static approaches proposed by Assouline and Or (2014) or Reynolds (2018). Alternatively, Guber et al. (2006) reported a list of PTFs to directly estimate the soil moisture contents at the prescribed matric suction pressure $|\psi|$ of 330 hPa (field capacity) and 15,300 hPa (wilting point).

Another question concerns the lack of direct measurement of the soil moisture content at full saturation, θ_s. We assumed θ_s as 90% of the spatial-mean soil porosity, which was calculated from the spatial-mean soil bulk density as suggested by Pollacco et al. (2013). To better support non-invasive measurement methods, such as cosmic-ray neutron sensing, we will shortly carry out field campaigns to measure θ_s at both experimental sub-catchments.

The observed area-wide θ_{CRNP} values are on average lower than θ_{GS3} values (see **Table 3**). The sensitivity of the CRNP exponentially decreases with depth, with most information on θ_{CRNP} being concentrated in the first 0.05 m of soil depth, which is not covered by the SoilNet sensors. The differences between SoilNet-based and CRNP-based soil moisture data can definitely affect the determination of the WRF, hence yielding different θ_{FC} and θ_{WP} values and consequently different SMI-values (**Table 4**). In MFC2 the SoilNet-based WRFs lead to field capacity and wilting point values other than those obtained by the CRNP-based WRF ($\theta_{FC} = 0.338$ m^3 m^{-3} and $\theta_{WP} = 0.180$ m^3 m^{-3}). Similarly, at GOR1 the SoilNet-based WRFs lead to field capacity and wilting point values different from those obtained by the CRNP-based WRF ($\theta_{FC} = 0.356$ m^3 m^{-3} and $\theta_{WP} = 0.147$ m^3 m^{-3}).

SMI was computed over a period of time (from 2016 to 2019) which may be considered as short for drawing sound conclusions. Therefore, this paper presented only some preliminary results of an ongoing long-term monitoring program underway in the Upper Alento River Catchment. As more data become available, a subsequent paper will explore the relationships between long-term time-series of SMI and climate-based standardized indices, such as the Standardized Precipitation Index (SPI) or Standardized Precipitation-Evapotranspiration Index (SPEI), obtaining robust correlations between meteorological and agricultural/hydrological droughts (Mozny et al., 2012; Martínez-Fernández et al., 2015; Barker et al., 2016). Capturing such relationships is of paramount importance in the decision-making process applied to the management of water resources.

Explaining the Spatial Variability of Soil Moisture Data

Assessing the spatial variability of soil moisture, even over relatively small areas, is challenging and commonly obtained using a large number of sensors sparsely deployed in the uppermost soil layer of a study area and along the soil profiles. This task is prohibitively expensive and laborious, and therefore motivated the present investigation, i.e., to explore whether, and to what extent, non-invasive soil moisture datasets obtained from stationary CRNPs can be assumed as representative of areal values whose spatial variations can be explained, in turn, by easily retrievable controlling factors, such as the soil textural classes and terrain attributes. The practical implication of this outcome concerns, for example, either physically-based or statistically-based downscaling methods enabling high-resolution spatial maps of near-surface soil moisture (at meter grid-size) to be estimated from the cosmic-ray areal measurements (i.e., at hectometer grid-size) (Qu et al., 2015; Nasta et al., 2018a).

An increase in spatial variability of soil moisture as its spatial-mean increases was reported in several studies (Martínez-Fernández and Ceballos, 2003; Molina et al., 2014), but increasing spatial variability with decreasing spatial-mean soil moisture was observed by others (e.g., Famiglietti et al., 2008). Most of the investigations reported in the literature have detected a concave downward shape for the relationship that links the spatial soil moisture variability and the spatial-mean soil moisture (e.g., Rosenbaum et al., 2012; Fatichi et al., 2015) as we also found at GOR1 for the soil depth of 0.15 m.

By exploiting the results from the PLSR method, **Figure 11** shows the spatial variance of soil moisture explained by terrain attributes and soil texture. In MFC2, almost 50% of the observed spatial variance of topsoil soil moisture (i.e., that measured at the soil depth of 0.15 m) is explained by non-local controls (terrain attributes); soil texture is instead able to explain only 5% of the total variance.

In the forested site (GOR1), the spatial variance of soil moisture data explained by easily-available soil and terrain factors increases when moving from dry to wet conditions. The maximum amount explained reaches 92% in the wet season. Beaudette et al. (2013) reported that terrain attributes were able to consistently account for 30–70% of the total

variance of soil moisture at 0.10 m soil depth, and 10–40% at the soil depths of 0.30 and 0.50 m. Wilson et al. (2004) were able to explain a small component (<30%) of the soil moisture spatial variability in six experimental sites using terrain attributes.

CONCLUDING REMARKS

This study explores the feasibility of assessing the soil hydrological behavior of two experimental fields by integrating the area-average soil moisture monitored by CRNP and the spatial-mean of the point-scale soil moisture and soil matric potential values measured by a network of multiple low-cost sensors (SoilNet). An in-depth understanding of the hydrological behavior of a field helps improve the application of suitable hydrological models to run numerical simulations. Nonetheless, the measurement of field-scale near-surface soil moisture is sometimes not sufficient to calibrate and validate hydrological models which, in turn, require the knowledge of the soil water retention function. In the present study, we have proposed a technique for obtaining a field-scale soil water retention function as an alternative to laboratory-based methods that are time-consuming, expensive, and rather unfeasible for large-scale applications. However, some drawbacks need to be considered and better understood at least before a proximal sensor for monitoring soil matric potential comes out in the future. The scale mismatch affecting the scatter in the field-scale WRF can be reduced only at the cost of installing a large number of MPS-6 sensors, especially in the near-surface positions. Yet this would increase costs and might become unpractical. Improving calibration procedures can help reduce the offset between CRNP-based soil moisture and weighted spatial-mean SoilNet-based soil moisture as demonstrated by the strong agreement of their *Z*-scores. The CRNP is not able to capture the bimodal distribution reflected by the SoilNet-based soil moisture data, except in a very dry year like 2017. Last but not least, the large scatter observed in the field-scale WRF in MFC2 can also be induced by the large spatial variability of soil moisture which, in turn, is largely explained by terrain attributes. If the CRNP-based soil moisture is assumed to be representative of areal values, the practical implication of this outcome opens room for using topography-based downscaling methods enabling high-resolution spatial maps of near-surface soil moisture.

DATA AVAILABILITY STATEMENT

The datasets generated for this study are available on request to the corresponding author.

AUTHOR CONTRIBUTIONS

NR and PN made the conception and design of this study. All the authors participate in the analysis and interpretation of data.

FUNDING

The TERENO infrastructure was funded by the Helmholtz Association and the Federal Ministry of Education and Research of Germany. Maintenance activities, data collection, and other equipment are resourced by the University of Naples Federico II and partly supported by MiUR-PRIN Project WATer mixing in the critical ZONe: observations and predictions under environmental changes—WATZON (grant 2017SL7ABC) and the iAQUEDUCT project funded within the Water JPI 2018 Joint Call on Closing the Water Cycle Gap–Sustainable Management of Water Resources.

ACKNOWLEDGMENTS

We are grateful to the landowners of MFC2 and GOR1 for having allowed the installation of the sensor networks.

SUPPLEMENTARY MATERIAL

The Supplementary Material for this article can be found online at: https://www.frontiersin.org/articles/10.3389/frwa.2020.00026/full#supplementary-material

REFERENCES

Allen, R. G., Pereira, L. S., Raes, D., and Smith, M. (1998). *Crop Evapotranspiration: Guidelines for Computing Crop Water Requirements*. Rome: Food and Agriculture Organization of the United Nations.

Assouline, S., and Or, D. (2014). The concept of field capacity revisited: defining intrinsic static and dynamic criteria for soil internal drainage dynamics. *Water Resour. Res.* 50, 4787–4802. doi: 10.1002/2014WR015475

Baatz, R., Bogena, H. R., Hendricks Franssen, H.-J., Huisman, J. A., Montzka, C., and Vereecken, H. (2015). An empirical vegetation correction for soil water content quantification using cosmic ray probes. *Water Resour. Res.* 51, 2030–2046. doi: 10.1002/2014WR016443

Babaeian, E., Sadeghi, M., Jones, S. B., Montzka, C., Vereecken, H., and Tuller, M. (2019). Ground, proximal, and satellite remote sensing of soil moisture. *Rev. Geophys.* 57, 530–616. doi: 10.1029/2018RG000618

Barker, L. J., Hannaford, J., Chiverton, A., and Svensson, C. (2016). From meteorological to hydrological drought using standardised indicators. *Hydrol. Earth Syst. Sci.* 20, 2483–2505. doi: 10.5194/hess-20-2483-2016

Baroni, G., Scheiffele, L. M., Schrön, M., Ingwersen, J., and Oswald, S. E. (2018). Uncertainty, sensitivity and improvements in soil moisture estimation with cosmic-ray neutron sensing. *J. Hydrol.* 564, 873–887. doi: 10.1016/j.jhydrol.2018.07.053

Beaudette, D. E., Dahlgren, R. A., and O'Geen, A. T. (2013). Terrain-shape indeces for modeling soil moisture dynamics. *Soil Sci. Soc. Am. J.* 77, 1696–1710. doi: 10.2136/sssaj2013.02.0048

Bogena, H. R., Herbst, M., Huisman, J. A., Rosenbaum, U., Weuthen, A., and Vereecken, H. (2010). Potential of wireless sensor networks for measuring soil water content variability. *Vadose Zone J.* 9, 1002–1013. doi: 10.2136/vzj2009.0173

Bogena, H. R., Huisman, J. A., Schilling, B., Weuthen, A., and Vereecken, H. (2017). Effective calibration of low-cost soil water content sensors. *Sensors* 17:208. doi: 10.3390/s17010208

Bogena, H. R., Kunkel, R., Krüger, E., Zacharias, S., Pütz, T., Schwank, M., et al. (2012). TERENO–long-term monitoring network for terrestrial research. *Hydrol. Wasserbewirtsch.* 56, 138–143.

Brocca, L., Ciabatta, L., Massari, C., Camici, S., and Tarpanelli, A. (2017). Soil moisture for hydrological applications: open questions and new opportunities. *Water* 9:140. doi: 10.3390/w9020140

Desilets, D., Zreda, M., and Ferré, T. (2010). Nature's neutron probe: land surface hydrology at an elusive scale with cosmic rays. *Water Resour. Res*. 46:W11505. doi: 10.1029/2009WR008726

Domínguez-Niño, J. M., Bogena, H. R., Huisman, J. A., Schilling, B., and Casadesús, J. (2019). On the accuracy of factory-calibrated low-cost soil water content sensors. *Sensors* 19:3101. doi: 10.3390/s19143101

Entin, J. K., Robock, A., Vinnikov, K. Y., Hollinger, S. E., Liu, S., and Namkhai, A. (2000). Temporal and spatial scales of observed soil moisture variations in the extratropics. *J. Geophys. Res.* 105, 11865–11877. doi: 10.1029/2000JD 900051

Famiglietti, J. S., Ryu, D. R., Berg, A. A., Rodell, M., and Jackson, T. J. (2008). Field observations of soil moisture variability across scales. *Water Resour. Res.* 44:W01423. doi: 10.1029/2006WR005804

Fatichi, S., Katul, G. G., Ivanov, V. Y., Pappas, C., Paschalis, A., Consolo, A., et al. (2015). Abiotic and biotic controls of soil moisture spatiotemporal variability and the occurrence of hysteresis. *Water Resour. Res*. 51, 3505–3524. doi: 10.1002/2014WR016102

Ferrarezi, R. S., Nogueira, T. A. R., and Zepeda, S. G. C. (2020). Performance of soil moisture sensors in Florida sandy soils. *Water* 12:358. doi: 10.3390/w12020358

Franz, T. E., Zreda, M., Rosolem, R., and Ferre, T. P. A. (2012). Field validation of a cosmic-ray neutron sensor using a distributed sensor network. *Vadose Zone J.* 11:vzj2012.0046. doi: 10.2136/vzj2012.0046

Franz, T. E., Zreda, M., Rosolem, R., and Ferre, T. P. A. (2013). A universal calibration function for determination of soil moisture with cosmic-ray neutrons. *Hydrol. Earth Syst. Sci*. 17, 453–460. doi: 10.5194/hess-17-453-2013

Gasch, C. K., Brown, D. J., Brooks, E. S., Yourek, M., Poggio, M., Cobos, D. R., et al. (2017). A pragmatic, automated approach for retroactive calibration of soil moisture sensors using a two-step, soil-specific correction. *Comput. Electron. Agric*. 137, 29–40. doi: 10.1016/j.compag.2017.03.018

Grayson, R. B., Western, A. W., Chiew, F. H. S., and Blöschl, G. (1997). Preferred states in spatial soil moisture patterns: local and nonlocal controls. *Water Resour. Res.* 33, 2897–2908. doi: 10.1029/97WR02174

Guber, A. K., Pachepsky, Y. A., van Genuchten, M. T., Rawls, W. J., Šimunek, J., Jacques, D., et al. (2006). Field-scale water flow simulations using ensembles of pedotransfer functions for soil water retention. *Vadose Zone J.* 5, 234–247. doi: 10.2136/vzj2005.0111

Hébrard, O., Voltz, M., Andrieux, P., and Moussa, R. (2006). Spatio-temporal distribution of soil surface moisture in a heterogeneously farmed mediterranean catchment. *J. Hydrol.* 329, 110–121. doi: 10.1016/j.jhydrol.2006.02.012

Heidbüchel, I., Güntner, A., and Blume, T. (2016). Use of cosmic-ray neutron sensors for soil moisture monitoring in forests. *Hydrol. Earth Syst. Sci*. 20, 1269–1288. doi: 10.5194/hess-20-1269-2016

Hunt, E. D., Hubbard, K. G., Wilhite, D. A., Arkebauer, T. J., and Dutcher, A. L. (2009). The development and evaluation of a soil moisture index. *Int. J. Climatol*. 29, 747–759. doi: 10.1002/joc.1749

Jakobi, J., Huisman, J. A., Vereecken, H., Diekkrüger, B., and Bogena, H. R. (2018). Cosmic-ray neutron sensing for simultaneous soil water content and biomass quantification in drought conditions. *Water Resour. Res*. 54, 7383–7402. doi: 10.1029/2018WR022692

Jonard, F., Mahmoudzadeh, M., Roisin, C., Weihermüller, L., André, F., Minet, J., et al. (2013). Characterization of tillage effects on the spatial variation of soil properties using ground-penetrating radar and electromagnetic induction. *Geoderma* 207–208, 310–322. doi: 10.1016/j.geoderma.2013.05.024

Kang, Y.-J., and Noh, Y. (2019). Development of hartigan's dip statistic with bimodality coefficient toassess multimodality of distributions. *Math. Probl. Eng.* 2019:4819475. doi: 10.1155/2019/4819475

Köhli, M., Schrön, M., Zreda, M., Schmidt, U., Dietrich, P., and Zacharias, S. (2015). Footprint characteristics revised for field-scale soil moisture monitoring with cosmic-ray neutrons. *Water Resour. Res*. 51, 5772–5790. doi: 10.1002/2015WR017169

Malazian, A., Hartsough, P., Kamai, T., Campbell, G. S., Cobos, D. R., and Hopmans, J. W. (2011). Evaluation of MPS-1 soil water potential sensor. *J. Hydrol*. 402, 126–134. doi: 10.1016/j.jhydrol.2011.03.006

Martínez-Fernández, J., and Ceballos, A. (2003). Temporal stability of soil moisture in a large-field experiment in Spain. *Soil Sci. Soc. Am. J*. 67, 1647–1656. doi: 10.2136/sssaj2003.1647

Martínez-Fernández, J., González-Zamora, A., Sánchez, N., and Gamuzzio, A. (2015). A soil water based index as a suitable agricultural drought indicator. *J. Hydrol*. 522, 265–273. doi: 10.1016/j.jhydrol.2014.12.051

Mittelbach, H., and Seneviratne, S. I. (2012). A new perspective on the spatio-temporal variability of soil moisture: temporal dynamics versus time-invariant contributions. *Hydrol. Earth Syst. Sci*. 16, 2169–2179. doi: 10.5194/hess-16-2169-2012

Molina, A. J., Latron, J., Rubio, C. M., Gallart, F., and Llorens, P. (2014). Spatio-temporal variability of soil water content on the local scale in a mediterranean mountain area (Vallcebre, North Eastern Spain). How different spatio-temporal scales reflect mean soil water content. *J. Hydrol*. 516, 182–192. doi: 10.1016/j.jhydrol.2014.01.040

Mozny, M., Trnka, M., Zalud, Z., Hlavinka, P., Nekovar, J., Potop, V., et al. (2012). Use of a soil moisture network for drought monitoring in the Czech Republic. *Theor. Appl. Climatol*. 107, 99–111. doi: 10.1007/s00704-011-0460-6

Nasta, P., Allocca, C., Deidda, R., and Romano, N. (2020b). Impact of seasonal rainfall anomalies on catchment-scale water balance components. *Hydrol. Earth Syst. Sci*. 24, 1–17. doi: 10.5194/hess-24-3211-2020

Nasta, P., Boaga, J., Deiana, R., Cassiani, G., and Romano, N. (2019). Comparing ERT and scaling-based approaches to parameterize soil hydraulic properties for spatially distributed model applications. *Adv. Water Resour.* 126, 155–167. doi: 10.1016/j.advwatres.2019.02.014

Nasta, P., Palladino, M., Sica, B., Pizzolante, A., Trifuoggi, M., Toscanesi, M., et al. (2020a). Evaluating pedotransfer functions for predicting soil bulk density using hierarchical mapping information in Campania, Italy. *Geoderma Reg.* 21:e00267. doi: 10.1016/j.geodrs.2020.e00267

Nasta, P., Palladino, M., Ursino, N., Saracino, A., Sommella, A., and Romano, N. (2017). Assessing long-term impact of land use change on hydrologic ecosystem functions in a Mediterranean upland agro-forestry catchment. *Sci. Total Environ*. 605–606, 1070–1082. doi: 10.1016/j.scitotenv.2017.06.008

Nasta, P., Penna, D., Brocca, L., Zuecco, G., and Romano, N. (2018a). Downscaling near-surface soil moisture from field to plot scale: a comparative analysis under different environmental conditions. *J. Hydrol*. 557, 97–108. doi: 10.1016/j.jhydrol.2017.12.017

Nasta, P., and Romano, N. (2016). Use of a flux-based field capacity criterion to identify effective hydraulic parameters of layered soil profiles subjected to synthetic drainage experiments. *Water Resour. Res*. 52, 566–584. doi: 10.1002/2015WR016979

Nasta, P., Sica, B., Mazzitelli, C., Di Fiore, P., Lazzaro, U., Palladino, M., et al. (2018b). How effective is information on soil-landscape units for determining spatio-temporal variability of near-surface soil moisture? *J. Agric. Eng*. 49, 174–182. doi: 10.4081/jae.2018.822

Nguyen, H. H., Jeong, J., and Choi, M. (2019). Extension of cosmic-ray neutron probe measurement depth for improving field scale root-zone soil moisture estimation by coupling with representative *in-situ* sensors. *J. Hydrol*. 571, 679–696. doi: 10.1016/j.jhydrol.2019.02.018

Ochsner, T. E., Cosh, M., Cuenca, R., Dorigo, W., Draper, C., Hagimoto, Y., et al. (2013). State of the art in large-scale soil moisture monitoring. *Soil Sci. Soc. Am. J*. 77, 1888–1919. doi: 10.2136/sssaj2013.03.0093

Orth, R., and Destouni, G. (2018). Drought reduces blue-water fluxes more strongly than green-water fluxes in Europe. *Nature Commun.* 9:3602. doi: 10.1038/s41467-018-06013-7

Orth, R., and Seneviratne, S. I. (2015). Introduction of a simple-model-based land surface dataset for Europe. *Environ. Res. Lett*. 10:044012. doi: 10.1088/1748-9326/10/4/044012

Peterson, A. M., Helgason, W. D., and Ireson, A. M. (2016). Estimating field-scale root zone soil moisture using the cosmic-ray neutron probe. *Hydrol. Earth Syst. Sci.* 20, 1373–1385. doi: 10.5194/hess-20-1373-2016

Pfister, R., Schwarz, K. A., Janczyk, M., Dale, R., and Freeman, J. (2013). Good things peak in pairs: a note on the bimodality coefficient. *Front. Psychol.* 4:700. doi: 10.3389/fpsyg.2013.00700

Pollacco, J. A. P., Nasta, P., Soria-Ugalde, J. M., Angulo-Jaramillo, R., Lassabatere, L., Mohanty, B. P., et al. (2013). Reduction of feasible parameter space of the inverted soil hydraulic parameters sets for Kosugi model. *Soil Sci.* 178, 267–280. doi: 10.1097/SS.0b013e3182a2da21

Price, K., Jackson, C. R., and Parker, A. J. (2010). Variation of surficial soil hydraulic properties across land uses in the southern Blue Ridge Mountains, North Carolina, USA. *J. Hydrol.* 383, 256–268. doi: 10.1016/j.jhydrol.2009.12.041

Qu, W., Bogena, H. R., Huisman, J. A., Vanderborght, J., Schuh, M., Priesack, E., et al. (2015). Predicting subgrid variability of soil water content from basic soil information. *Geophys. Res. Lett.* 42, 789–796. doi: 10.1002/2014GL062496

Reynolds, W. D. (2018). An analytic description of field capacity and its application in crop production. *Geoderma* 326, 56–67. doi: 10.1016/j.geoderma.2018.04.007

Romano, N. (2014). Soil moisture at local scale: measurements and simulations. *J. Hydrol.* 516, 6–20. doi: 10.1016/j.jhydrol.2014.01.026

Romano, N., and Chirico, G. B. (2004). "The role of terrain analysis in using and developing pedotransfer functions," in *Development of Pedotransfer Functions in Soil Hydrology*, eds Y. A. Pachepsky and W. J. Rawls (Amsterdam: Elsevier Science B.V.), 273–294. doi: 10.1016/S0166-2481(04)30016-4

Romano, N., Nasta, P., Bogena, H. R., De Vita, P., Stellato, L., and Vereecken, H. (2018). Monitoring hydrological processes for land and water resources management in a mediterranean ecosystem: the Alento river catchment observatory. *Vadose Zone J.* 17:180042. doi: 10.2136/vzj2018.03.0042

Romano, N., Palladino, M., and Chirico, G. B. (2011). Parameterization of a bucket model for soil-vegetation-atmosphere modeling under seasonal climatic regimes. *Hydrol. Earth Syst. Sci.* 15, 3877–3893. doi: 10.5194/hess-15-3877-2011

Romano, N., and Santini, A. (2002). "Water retention and storage: field," in *Methods of Soil Analysis, Part 4, Physical Methods*, eds J. H. Dane and G. C. Topp (Madison, WI: Soil Science Society of America), 721–738.

Rosenbaum, U., Bogena, H. R., Herbst, M., Huisman, J. A., Peterson, T. J., Weuthen, A., et al. (2012). Seasonal and event dynamics of spatial soil moisture patterns at the small catchment scale. *Water Resour. Res.* 48:W10544. doi: 10.1029/2011WR011518

Schrön, M., Köhli, M., Scheiffele, L., Iwema, J., Bogena, H. R., Lv, L., et al. (2017). Spatial sensitivity of cosmic-ray neutron sensors applied to improve calibration and validation. *Hydrol. Earth Syst. Sci.* 21, 5009–5030. doi: 10.5194/hess-21-5009-2017

Teuling, A. J., and Troch, P. A. (2005). Improved understanding of soil moisture variability dynamics. *Geophys. Res. Lett.* 32:L05404. doi: 10.1029/2004GL021935

Topp, G. C., and Ferré, P. A. (2002). "Thermogravimetric using convective oven-drying," in *Methods of Soil Analysis, Part 4, Physical Methods*, eds J. H. Dane and G. C. Topp (Madison, WI: Soil Science Society of America), 422–424.

van Genuchten, M. T. (1980). A closed form equation for predicting the hydraulic conductivity of unsaturated soils. *Soil Sci. Soc. Am. J.* 44, 892–898. doi: 10.2136/sssaj1980.03615995004400050002x

van Looy, K., Bouma, J., Herbst, M., Koestel, J., Minasny, B., Mishra, U., et al. (2017). Pedotransfer functions in Earth system science: challenges and perspectives. *Rev. Geophys.* 55, 1199–1256. doi: 10.1002/2017RG000581

Vereecken, H., Huisman, J. A., Hendricks Franssen, H.-J., Brüggemann, N., Bogena, H. R., Kollet, S., et al. (2015). Soil hydrology: recent methodological advances, challenges, and perspectives. *Water Resour. Res.* 51, 2616–2633. doi: 10.1002/2014WR016852

Vilasa, L., Miralles, D. G., de Jeu, R. A. M., and Dolman, A. J. (2017). Global soil moisture bimodality in satellite observations and climate models. *J. Geophys. Res. Atmos.* 122, 4299–4311. doi: 10.1002/2016JD026099

Walthert, L., and Schleppi, P. (2018). Equations to compensate for the temperature effect on readings from dielectric decagon MPS-2 and MPS-6 water potential sensors in soils. *J. Plant Nutr. Soil Sci.* 181, 749–759. doi: 10.1002/jpln.201700620

Wilson, D. J., Western, A. W., and Grayson, R. B. (2004). Identifying and quantifying sources of variability in temporal and spatial soil moisture observations. *Water Resour. Res.* 40:W02507. doi: 10.1029/2003WR002306

Conflict of Interest: The authors declare that the research was conducted in the absence of any commercial or financial relationships that could be construed as a potential conflict of interest.

frontiers in Water

ORIGINAL RESEARCH
published: 17 September 2020
doi: 10.3389/frwa.2020.00016

Large-Scale Boron-Lined Neutron Detection Systems as a ^{3}He Alternative for Cosmic Ray Neutron Sensing

Jannis Weimar[1]*, *Markus Köhli*[1,2], *Christian Budach*[3] and *Ulrich Schmidt*[1]

[1] Physikalisches Institut, Heidelberg University, Heidelberg, Germany, [2] Physikalisches Institut, University of Bonn, Bonn, Germany, [3] Institute of Environmental Science and Geography, University of Potsdam, Potsdam, Germany

Cosmic-Ray neutron sensors are widely used to determine soil moisture on the hectare scale. Precise measurements, especially in the case of mobile application, demand for neutron detectors with high counting rates and high signal-to-noise ratios. For a long time Cosmic Ray Neutron Sensing (CRNS) instruments have relied on ^{3}He as an efficient neutron converter. Its ongoing scarcity demands for technological solutions using alternative converters, which are ^{6}Li and ^{10}B. Recent developments lead to a modular neutron detector consisting of several ^{10}B-lined proportional counter tubes, which feature high counting rates via its large surface area. The modularity allows for individual shieldings of different segments within the detector featuring the capability of gaining spectral information about the detected neutrons. This opens the possibility for active signal correction, especially useful when applied to mobile measurements, where the influence of constantly changing near-field to the overall signal should be corrected. Furthermore, the signal-to-noise ratio could be increased by combining pulse height and pulse length spectra to discriminate between neutrons and other environmental radiation. This novel detector therefore combines high-selective counting electronics with large-scale instrumentation technology.

Keywords: CRNS, neutron, detector, soil moisture, readout electronics, boron-10, helium-3 alternative

OPEN ACCESS

Edited by:
Virginia Strati,
University of Ferrara, Italy

Reviewed by:
Trenton Franz,
University of Nebraska-Lincoln, United States
Luca Stevanato,
University of Padova, Italy

***Correspondence:**
Jannis Weimar
weimar@physi.uni-heidelberg.de

Specialty section:
This article was submitted to Water and Hydrocomplexity, a section of the journal Frontiers in Water

Received: *22 March 2020*
Accepted: *15 June 2020*
Published: *17 September 2020*

Citation:
Weimar J, Köhli M, Budach C and Schmidt U (2020) Large-Scale Boron-Lined Neutron Detection Systems as a ^{3}He Alternative for Cosmic Ray Neutron Sensing. Front. Water 2:16. doi: 10.3389/frwa.2020.00016

1. INTRODUCTION

The hydrological cycle and energy transfer at the land-atmosphere interface strongly depend on soil moisture. It is therefore a key variable in the effort to understand the Earth's climate system. However, soil moisture detection methods are either locally restricted to point measurements or large-area sensitive, satellite-based techniques with shallow depth resolution (Mohanty et al., 2017). In recent years Cosmic-Ray Neutron Sensing (CRNS) has become a prominent method for non-invasive soil moisture determination, although the basic principles are known for decades (Kodama et al., 1985; Zreda et al., 2008). It measures the environmental hydrogen content within a footprint of several hectares and penetration depths of up to 80 cm (Köhli et al., 2015), which enables CRNS to close the gap between large area and local measurements (Robinson et al., 2008). Further methods with larger support for soil moisture sensing include GNSS-R (Rodriguez-Alvarez et al., 2011) and gamma-ray spectroscopy (Strati et al., 2018). CRNS relies on the inverse relationship between the above-ground epithermal-to-fast

cosmic-ray neutron intensity N and the surrounding hydrogen, e.g., the volumetric water content θ (cm^3/cm^3). The originally proposed equation by Desilets et al. (2010)

$$\theta(N) = \rho_{bd} \left[\frac{a_0}{\left(\frac{N}{N_0} - a_1\right)} - a_2 \right] \quad (1)$$

included the fitted parameters a_i and was extended by the dry soil bulk density ρ_{bd} (Bogena et al., 2013). N has to be corrected for pressure, air humidity and incoming radiation variation with regard to one calibration value N_0, the intensity over dry soil at this reference point (Zreda et al., 2012). Advances in the CRNS technique within the last years have been achieved from theory as well as due to the broadening applications. Such efforts quantified different signal contributions like vegetation (Baatz et al., 2015), snow (Schattan et al., 2017), atmospheric water vapor (Rosolem et al., 2013), and local heterogeneities (Schrön et al., 2018). Extensive neutron transport simulation studies improved the understanding in the transport of ambient neutrons (Köhli et al., 2015; Andreasen et al., 2016). Mobile campaigns have also extended the spatial scale up to several km^2 and therefore could contribute to closing the measurement scale gap, especially relevant for small catchments (Schrön et al., 2018). Furthermore, CRNS has shown to be a prominent candidate for agricultural applications (Franz et al., 2016; Li et al., 2019), for validation of satellite based measurements (Montzka et al., 2017) and to improve hydrological modeling (Shuttleworth et al., 2013). The success of this technique (Andreasen et al., 2017) lead to a worldwide deployment of meanwhile more than 100 sensors.

The design of the neutron detector is essential for the performance of the method. Consequently, several studies examined the most common cosmic-ray neutron probe (CRNP) model. The probe comprises gaseous proportional counters with so-called converters, either ^3He or $^{10}BF_3$. Typically one counter is housed in a plastic moderator in order to focus its sensitivity to the epithermal-to-fast energy regime. In some models it is accompanied by another counter, which is left bare making it most sensitive to thermal neutrons. Furthermore, shielding material around the moderator blocks thermal neutrons and allows for better separation between the thermal and epithermal-to-fast signal (Desilets et al., 2010). Andreasen et al. (2016) elaborated first steps to compare the modeled and measured neutron flux using the Monte Carlo Code MCNPX (Waters et al., 2007). Köhli et al. (2018) extended the understanding of the detector response by calculating the exact energy sensitivity of common CRNPs with the URANOS package (Köhli et al., 2015). Their study revealed the similarity of the CRNPs to Bonner Spheres (Bramblett et al., 1960; Hertel and Davidson, 1985; Mares et al., 1991; Mares and Schraube, 1994) in terms of energy sensitivity. Beyond the standard probes recent developments also aim to introduce scintillation-based instruments (Stevanato et al., 2019). Besides the achievable count rate, the main difference between the two concepts lies in the detector energy response function and the background suppression. In contrast to the previous studies about the standard CRNP detector that were mostly descriptive, this work aims at unfolding the key challenges on a neutron detector dedicated to CRNS. It also introduces a new detection system especially designed for the needs of CRNS.

1.1. Motivation for a New CRNS Detection System

Neutron detectors applied in CRNS have to be improved in order to support a holistic progress of the method. In view of existing systems and the demands of CRNS on the neutron detector, four major challenges are identified:

1. **Count rate enhancement:** The neutron detector count rate directly relates to the time resolution by its statistical uncertainty. For typical systems and environmental conditions, neutron count rates have to be integrated over 4–12 h in order to achieve a statistical precision of a few percent. While this is sufficient for many hydrological processes, it renders the method incapable of capturing interception or irrigation. But most certainly, large integration times impede mobile measurements where the area to be covered in a certain time is primarily restricted by the detector's count rate.
2. **Higher signal-to-noise ratio (SNR):** The SNR describes the ratio between the detected neutrons that relate to the environmental hydrogen content (signal) to such which do not (noise). It determines the change in detected neutron count rate per hydrogen content change. With increasingly moist conditions, the sensitivity to hydrogen content changes decreases steadily until it eventually saturates due to the hyperbolic relationship to θ (see Equation 1). In close-to saturated conditions, i.e., humid forests (Bogena et al., 2013) and snow covered areas (Schattan et al., 2017), a high signal-to-noise ratio is critical for the assessment of water resources.
3. **Refinement of the energy sensitivity:** Some of the CRNPs come with two detectors, which feature peak sensitivities in the thermal and the epithermal energy regime, respectively. Recent studies tried to make use of spectral information (Baatz et al., 2015; Tian et al., 2016) by comparing the two signals. However, the moderated detector suffers from a thermal neutron contamination that constitutes up to 20% of its signal (Köhli et al., 2018). Moreover, preventing thermal neutron leakage is equivalently important for standard soil moisture sensing applications, since thermal neutrons exhibit a different and much smaller dependence on the environmental hydrogen content than epithermal-to-fast neutrons. Andreasen et al. (2016) and Desilets et al. (2010), therefore, already suggested to disentangle the signals to provide a higher contrast. The latter study also determined an appropriate moderator thickness of 25 mm through empirical studies. However, it might not be the ideal setup for any environmental condition and has not been further investigated by means of neutron modeling. Lastly, the spectral resolution can be extended by a modular multiple-counter detector system. Spectral information of higher energy neutrons can be used to actively correct for local effects (Schrön et al., 2018).
4. **Replacement of ^3He as an efficient neutron converter:** Until the 2000s neutron detection almost exclusively relied on the element ^3He as an efficient neutron converter. However,

the only substantial source of ^{3}He is the radioactive decay of tritium, which is extracted during the maintenance of thermonuclear weapons. As a consequence of the 9/11 attacks in 2001, most U.S. reserves of ^{3}He were spent for homeland security and the stockpile depleted (Shea and Morgan, 2010). Ever since a number of commercially available replacement technologies have been developed, but none of them focused their design on CRNS. Beyond ^{3}He, mostly $^{10}BF_3$ has been used as a neutron converter for CRNPs. However, it is less efficient and highly toxic which puts concerns on its use for CRNS.

2. METHODOLOGY AND THEORY

2.1. Monte Carlo Packages for Neutron Transport Simulation

A specific CRNS-tailored neutron detector design needs to take into account a large variety of environmental conditions typically found in the context of CRNS. This is achieved most efficiently by neutron transport simulations using Monte Carlo packages. The tools used in this study are MCNP 6.2 (Werner et al., 2018) and URANOS (Köhli et al., 2015).

MCNP 6: MCNP (**M**onte **C**arlo **N**-**P**article) is a general purpose software to simulate the propagation and interaction of a multitude of particles. Although originally developed in 1957 to investigate processes involving nuclear reactions, since the release of MCNPX (Waters et al., 2007) it has been also extended to simulate the propagation of particles in the Earth's atmosphere. Especially MCNPX was used in several studies to understand the CRNS signal (Desilets, 2012; Rosolem et al., 2013; Andreasen et al., 2016). With version 6 (Werner et al., 2018) the MCNPX branch was merged into the main development line featuring an optional cosmic-ray source (McKinney, 2013).

URANOS: The Monte Carlo code URANOS (**U**ltra **R**apid **N**eutron-**O**nly **S**imulation) was developed at the Physikalisches Institut, Heidelberg University, in collaboration with the UFZ Leipzig. This code has been specifically tailored to the needs of the CRNS method. It is based on a voxel engine and excludes any particles other than neutrons replacing them by effective models. Thereby, URANOS is a computationally efficient code that allows to simulate the large environmental setups typically found in the context of CRNS on standard desktop computers. It uses the validated near-ground cosmic-ray neutron spectrum by Sato (2016). The code was employed for CRNS footprint revision by Köhli et al. (2015) and Schrön et al. (2017), in roving (Schrön et al., 2018) and irrigation studies (Li et al., 2019) as well as understanding the signal for snow height measurements (Schattan et al., 2019). It also features special input options for conducting detector-related neutron transport studies (Köhli et al., 2018).

2.2. Neutrons in the Epithermal-to-Fast Energy Regime, a Proxy for Environmental Hydrogen Content

Cosmic-ray neutrons are generated via three different channels by high-energy primary cosmic-rays, typically protons, while they impinge on Earth. In one channel the interaction of primary cosmic-rays with nuclei in the outer Earth's atmosphere generate neutrons via a spallation process (Letaw and Normand, 1991). In a second channel even more neutrons are produced within the atmosphere as stable products of particle showers while at the same time the primary particles are slowed down or absorbed when propagating toward the Earth's surface (Pfotzer, 1936; Nesterenok, 2013). The soil likewise acts as a third channel. As high-energy neutrons and protons penetrate into the soil, they excite atomic nuclei triggering the emission of evaporation neutrons with energies of ≈ 1 MeV. The neutrons may cross the air-ground interface multiple times, while losing kinetic energy until being absorbed. These processes lead to the buildup of the typical energy spectrum above the ground as depicted in **Figure 1** by the light red and light blue curve. The magnitude of the spectrum, i.e., total neutron flux density, mainly depends on the altitude (Kowatari et al., 2005) whereas its shape is mostly dominated by the environmental hydrogen content (Zreda et al., 2012). The use of cosmic-ray neutrons as a proxy for changes in the hydrogen content, e.g., soil moisture, snow and vegetation, requires a precise knowledge about which neutrons are affected most by hydrogen and which are insensitive to it. Understanding the underlying processes which lead to the desired signal is therefore the fundamental prerequisite for any CRNS focused neutron detector design.

The hydrogen-sensitive region of the cosmic-ray neutron spectrum lies in the epithermal-to-fast range, see **Figure 1** dashed blue curve. Neutrons of such energies mainly interact with matter via elastic collisions in which the neutron changes its direction and loses kinetic energy, leading to constant deceleration. Hydrogen is the element that most efficiently moderates, i.e., slows down, neutrons down to thermal energies. That is because of the similar mass of neutrons and hydrogen accompanied with a large energy transfer per collision and a high collision probability. Furthermore, the abundance of hydrogen changes significantly in absolute numbers between dry and wet conditions. Hence, any change in environmental hydrogen content directly and predominantly affects the amount of epithermal-to-fast neutrons making them a suitable proxy for soil moisture, snow and other hydrogen bodies. No other element typically found in soil, vegetation, and in the air combines these criteria. **Figure 1** reveals that the maximum signal change is limited to a factor of ≈ 4.5. The hydrogen-sensitive domain ends when neutrons are in thermal equilibrium with the environment, i.e., on average no energy loss occurs at collision. Thermal neutrons show a different or more complex response to soil moisture. For wet conditions the soil efficiently slows down neutrons, it acts as a source for thermal neutrons, however, the overall neutron density is lower. For dry conditions the much higher epithermal intensity competes with the poor moderation capability of the soil in absence of hydrogen. For both cases, the thermal neutron flux is nearly identical. Below 10% soil moisture a maximum builds up for sufficiently high ambient flux and average moderation power. Monte Carlo simulations show that the thermal intensity change due to hydrogen for standard soils is more than a magnitude lower than that of epithermal neutrons, see **Figure 1** in this work and Figure 11 in Sato and Niita (2006). Moreover, some elements present in soil exhibit a high absorption probability for thermal neutrons. Hence, detailed knowledge of

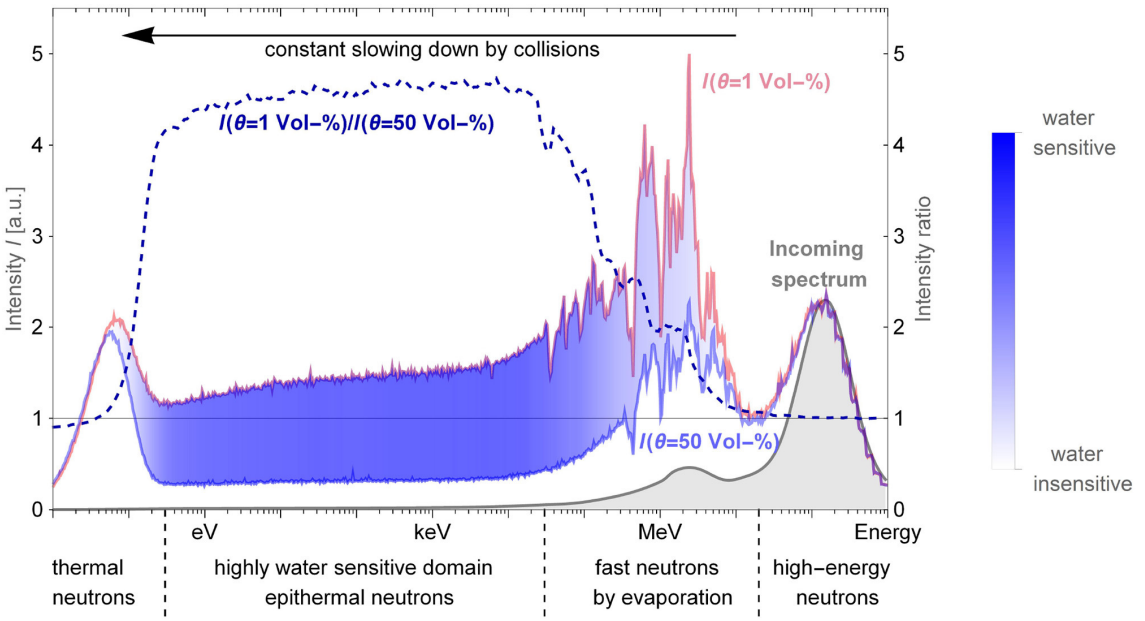

FIGURE 1 | Simulated cosmic-ray neutron spectrum with focus on the hydrogen-sensitive energy domain. The input spectrum, according to Sato (2015) (gray curve), is released in 450 m height and propagated toward the soil. Above-ground neutron intensities are shown for dry (light red) and moist conditions (light blue), both at an air humidity of 1 g/m^3. The intensity ratio between dry and moist (dashed blue curve and color-coded filling between the two spectra) reveals the hydrogen-sensitive domain. Neutrons with energies between 0.3 eV and 30 keV are most suitable as a proxy for the environmental hydrogen content. The simulations were carried out using the Monte Carlo Code MCNP 6.2 (Goorley et al., 2012) and cross section definitions from the ENDF/B-VIII.0 (Brown et al., 2018) data base.

the chemical composition of the soil is required when thermal intensity changes have to be interpreted correctly (Quinta-Ferreira et al., 2016). The evaporation peak represents the upper limit of the hydrogen-sensitive domain. Evaporation neutrons are equally sensitive to hydrogen content as epithermal neutrons, because elastic scattering processes dominate these energies as well. However, there is a significant production of evaporation neutrons in the atmosphere leading to a prominent peak in the incoming flux. As opposed to the epithermal energy regime, a large part of evaporation neutrons has not been in contact with the ground, i.e., was not influenced by soil moisture. Additionally, a few percent of the evaporation neutrons created in the soil do not interact with the latter before entering the air volume. This effect leads to a slow decline of hydrogen sensitivity from energies of 30 keV to 10 MeV. For energies above 10 MeV the intensity is purely made up of incoming neutrons and the sensitivity vanishes completely. Consequentially, a neutron detector design tailored for CRNS should aim at being most sensitive to neutrons with energies between 0.3 eV to 30 keV with lower sensitivity between 30 keV and 1 MeV, while being insensitive to neutrons with other energies.

3. COSMIC-RAY NEUTRON PROBE DESIGN CONSIDERATIONS

3.1. Uncertainties of Neutron Measurements

Precise measurements of environmental hydrogen content via cosmic-ray neutrons require low statistical uncertainty and a high signal-to-noise (SNR) ratio of deployed neutron detectors. From a physical point of view signal may be defined as the detected epithermal-to-fast neutrons that penetrated the soil and underwent at least one scattering event. Following that, noise includes epithermal-to-fast neutrons which did not enter the soil volume, neutrons with different energy and detections that were erroneously assigned to a neutron event. Additionally, it comprises those evaporation neutrons that were created in the soil but leave it without any interaction. From a principle point of view, however, neutrons which were in contact with soil and those which did not are not distinguishable. Even with directional-sensitive detectors, it is not possible to trace back the location of the soil contact. That is because neutrons scatter multiple times in the air changing their direction with each scatter event. The following discussion, nonetheless, focuses on the former definition of SNR as the above mentioned limitation does not hold for Monte Carlo studies where neutrons can be tracked. Additionally to the systematic uncertainty introduced by noise σ_{ns}, another uncertainty is introduced by counting statistics σ_{stat}. The total uncertainty on the neutron count therefore becomes:

$$\sigma_N^2 = \sigma_{stat}^2 + \sigma_{ns}^2 \tag{2}$$

The detection of neutrons obeys Poisson statistics, where the variance σ_{stat}^2 equals the expected value N, which is the number of detected neutron events. Assuming a constant neutron flux under constant environmental

conditions, the relative statistical uncertainty can be determined as:

$$\frac{\sigma_{\text{stat}}}{N} = \frac{1}{\sqrt{N}} \propto \frac{1}{\sqrt{t}}. \tag{3}$$

Hence, the statistical uncertainty can be reduced by prolonging the integration time of a single neutron measurement. Here, the propagation of the neutron measurement uncertainty onto the soil moisture retrieval is discussed briefly, before an appropriate strategy to build CRNS neutron detectors with low measurement uncertainty is discussed in more detail in the following sections. For simplicity, all hydrogen content is considered to be bound in soil moisture. The calculation still holds true if using the total water equivalent approaches like Franz et al. (2013) or Schattan et al. (2019). However, here the uncertainty analysis of specific further parameters such as air humidity or snow is neglected. Equation (1) can be used to estimate the uncertainty σ_θ:

$$\begin{aligned}\sigma_\theta &= \left|\frac{\delta\theta}{\delta N}\sigma_N\right| = \frac{a_0\rho_{\text{bd}}}{N_0\left(\frac{N}{N_0} - a_1\right)^2}\sigma_N = \ldots \\ &= \left(\frac{\theta}{\rho_{\text{bd}}} + a_2\right)^2 \frac{\sigma_N\rho_{\text{bd}}}{a_0 N_0}.\end{aligned} \tag{4}$$

The derivation can be found in the **Appendix**. It is important to note that σ_θ increases linearly with σ_N and quadratically with the hydrogen content. The ability to detect small hydrogen content variations in saturated environments is therefore strongly coupled to the measurement uncertainty of the neutron detector. Bogena et al. (2013) already discussed σ_θ with respect to the statistical uncertainty σ_{stat}. In the following sections the setup of gaseous neutron counters is described and each factor that may contribute to the noise is analyzed in view of detector design.

In the following the bare neutron detection device is referred to as neutron counter and the whole detection system including moderator, thermal shielding and electronics as neutron detector.

3.2. The Detection of Neutrons With Gaseous Proportional Counters

A proportional counter is a hermetically sealed cylinder with a thin wire in its center, see schematic setup in **Figure 2**. It is filled with a noble gas, which is ionized when charged particles propagate through the counter volume. Electrons and ions along this ionization track are separated when applying an electric field between the wire (cathode) and the cylinder barrel. The positive ions, therefore, drift to the cylinder wall and the electrons to the central wire. The electrons experience an increase in electric field strength reciprocal to the radius as they drift toward the wire due to the cylindrical shape of the counter. In the very vicinity of the wire, the electric field is strong enough to accelerate electrons beyond the ionization energy between two successive gas collisions and therefore start ionizing the gas. Secondary electrons created in that process ionize the gas further, which leads to a charge avalanche formation. The high voltage applied to the wire is chosen in such a way that this avalanche increases the

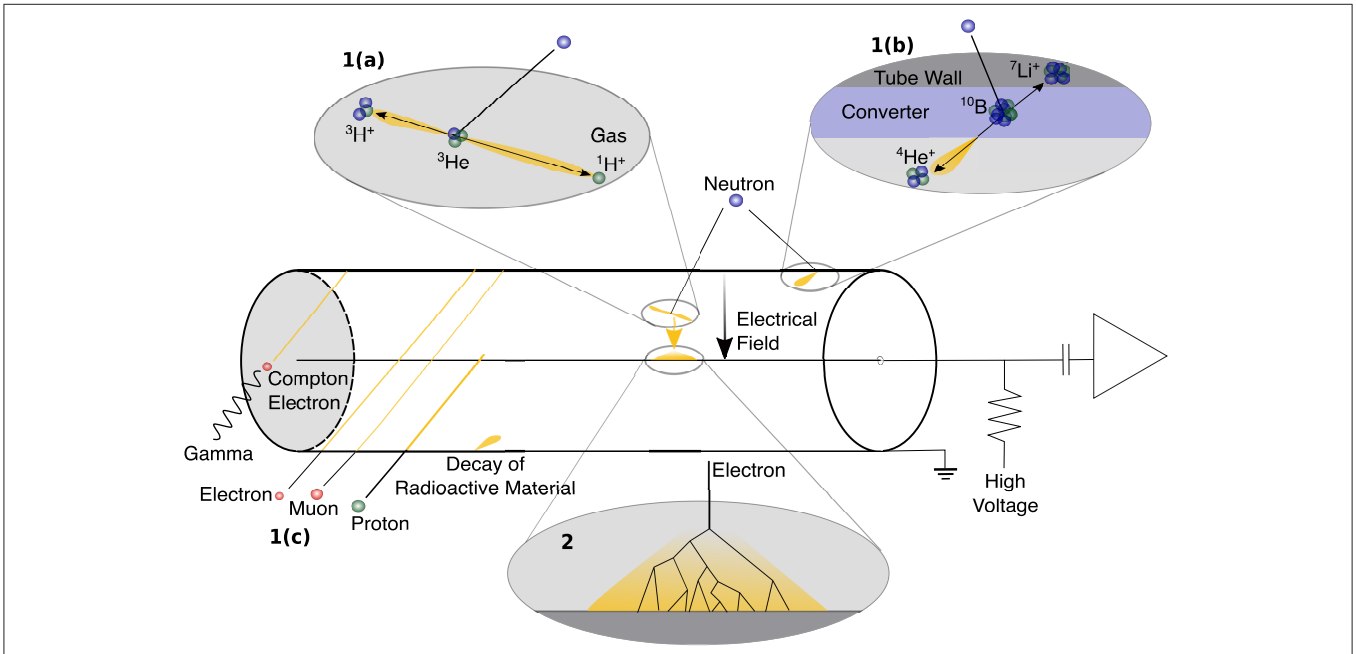

FIGURE 2 | Detection principle of a proportional counter. Neutron conversion into ionizing radiation takes place in either the gas phase (1a) or in solid material (1b). (1a) indicates the ^{3}He and (1b) the ^{10}B conversion processes. The fragments of the conversion process are emitted in opposite directions. The ionization trace is indicated in yellow. An electric field between the tube wall and the axial wire accelerates the generated electrons toward the wire. In the vicinity of the wire, the electron's kinetic energy reaches the gas ionization energy and charge multiplication takes place (2). The resulting pulse is then read out by charge sensitive amplifiers. 1(c) Indicates other types of radiation that may induce a signal. The thickness of the tracks indicate the ionization energy deposition (see section 3.2.1).

number of electrons by a constant gain factor. Hence the amount of electrons is proportional to the amount of primarily generated electrons by the track of the incident particle. The electrons collected at the wire form a charge pulse that can be read out by appropriate electronics. Neutrons are non-ionizing particles and, therefore, cannot be detected directly by means of gaseous detectors. Most proportional counters instead use specific elements to convert neutrons into detectable particles. Such converters absorb the neutron and immediately decay into fragments that carry the kinetic energy Q released in these reactions. The three most common converter elements (Chadwick et al., 2011) are

$$^{3}\mathrm{He} + \mathrm{n} \rightarrow {}^{3}\mathrm{H} + {}^{1}\mathrm{H} \qquad \text{with } Q = 0.764\,\mathrm{MeV},$$
$$^{10}\mathrm{B} + \mathrm{n} \rightarrow {}^{7}\mathrm{Li} + {}^{4}\mathrm{He} \qquad \text{with } Q = 2.31\ (93.6\%)\ /\ 2.79\ (6.4\%)\,\mathrm{MeV},$$
$$^{6}\mathrm{Li} + \mathrm{n} \rightarrow {}^{4}\mathrm{He} + {}^{3}\mathrm{H} \qquad \text{with } Q = 4.78\,\mathrm{MeV}.$$

The filling gas itself can act as a converter as ^{3}He and $^{10}BF_3$ or converters are applied as solid surfaces to the inside of the counter like ^{6}Li metal and boron carbide $^{10}B_4C$. The absorption probability for thermal neutrons of ^{10}B and ^{3}He are larger than that of ^{6}Li by about a factor of 4 and 5.5, respectively. Conversion is only efficient at low energies as the absorption probability decreases inverse proportional to the square root of the energy of the neutron. The charged reaction products are emitted isotropically in opposite directions. In the case of gaseous converters, the reaction products may deposit their complete kinetic energy Q inside the gas (see **Figure 2**, 1a). If any of the fragments hit the tube wall its remaining kinetic energy is missing in the ionization process. In the case of solid converters, some of the kinetic energy of the fragment is lost in the conversion layer itself (see **Figure 2**, 1b), and only one fragment can enter the gas volume. That restricts the thickness of the solid converters and thereby their absorption i.e., detection efficiency. With increasing layer thickness more neutrons are absorbed but less conversion products reach and ionize the gas volume. For solid boron and lithium metal layers, the maximum efficiency is approximately 7 and 24 %, respectively (Nelson et al., 2012; Köhli et al., 2016). The ^{6}Li conversion products have higher energies and are lighter than those of ^{10}B, thus allowing thicker conversion layers. Furthermore, ^{6}Li is currently only applied in combination with a Multi-Wire Proportional Chamber (MWPC) readout (Forsyth et al., 2017), which is a detector concept similar to proportional counters with a planar geometry (Nelson et al., 2012). The conversion layer thickness in a MWPC may be larger than for standard proportional counters as the conversion products from a metal sheet can be detected from both layer surfaces. No such limitations exist for gaseous converters and the efficiency is determined by the amount of converter gas or more precisely, the counter dimensions and the converter gas pressure. Proportional counters using solid converters are usually filled with P10 gas (90% argon and 10% CO_2). The range of the conversion products in the corresponding gas differs significantly ranging from few millimeters for ^{10}B to few centimeters for ^{6}Li and ^{3}He (Nelson et al., 2012; Langford et al., 2013; Köhli et al., 2016). That means their ionization traces are short and dense. Gas ionization by other particles, indicated in **Figure 2**, 1c, and their influence on the detector signal is discussed in the following section.

3.2.1. False Positive Detections—Neutron Counter Efficiency to Other Types of Radiation

One important source of detector noise are particles that generate a similar signature like neutrons inside the neutron counter and therefore may be mistaken for such (see **Figure 2**, 1c). Sources of ionizing particles include other cosmic rays, terrestrial radiation and weakly radioactive materials inside the detector itself. In particular, a similar signal compared to neutron conversion is triggered when particles are of the same kind as the conversion products. Such are mainly heavy and highly ionizing particles with short ranges of less than a few millimeters in solid materials (see section 3.2). If possible they should be shielded against by the housing of the counter. Only if for example generated in the innermost layer of the tube wall, they can enter and ionize the gas and contribute to the noise. Hence, only material with lowest intrinsic radioactivity should be used for the production of neutron counters. Even a comparably low abundance of radioisotopes may decrease the signal-to-noise ratio significantly due to the small flux of cosmic-ray neutrons. A key property of particles that penetrate the counter is the energy loss due to ionization per distance traveled $\mathrm{d}E/\mathrm{d}x$. As seen above, the conversion products feature a high $\mathrm{d}E/\mathrm{d}x$, are therefore short-ranged and deposit large amounts of energy by ionization. Cosmic-ray muons, although abundant, are weakly ionizing, i.e., have a small $\mathrm{d}E/\mathrm{d}x$, and because of the limited track length inside the counter, they trigger small signals in gaseous counters (Groom et al., 2001). Electrons, i.e., beta radiation, though less ionizing than the conversion products, can still deposit a significant amount of energy in the active counter volume. The significance of such contributions depends on the geometry of the system, which allows or prevents long track length for electrons. Gamma rays may also induce electron emissions via Compton scattering (Compton, 1923) and can, therefore, trigger similar ionization traces like beta radiation. Ionization by incident cosmic-ray protons may also lead to false positive detections. However, their overall flux is almost one magnitude lower as the cosmic-ray neutron flux (Sato, 2015) and mostly of too high energies to effectively ionize the gas. In summary, careful material selection can minimize intrinsic radioactive background that may induce false positive signals. The energy E and the energy loss per distance traveled $\mathrm{d}E/\mathrm{d}x$ can be used to discriminated between the conversion products and other ionizing particles.

3.2.2. Moderator Design Considerations

Neutron absorption, including the conversion process, is most efficient for low energy neutrons. Therefore, the energy dependent detection efficiency of a bare neutron counter lies in the thermal energy regime, see the black curve in **Figure 3**. In order to shift the neutron counter sensitivity to the hydrogen-sensitive energy domain, a hydrogen-rich casing,

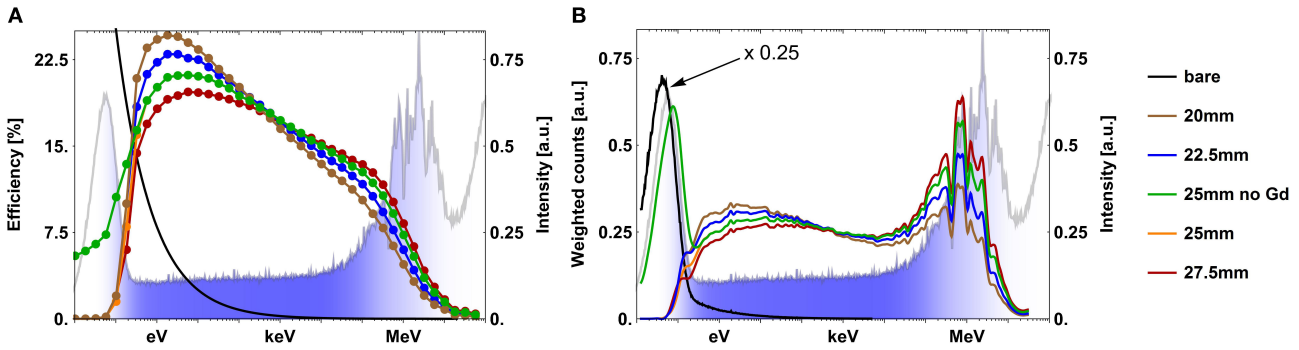

FIGURE 3 | (A) Response functions of a bare neutron counter and detectors with moderator thicknesses of 20–27.5 mm in steps of 2.5 mm. All models except for one of the 25 mm versions are equipped with a thermal shield. The thermal shield consists of a Gd_2O_3 layer with a thickness of 90 μm in order to provide a sufficiently high absorption cross section for the thermal peak. The chosen thickness reduces the spectral count rate for energies below 100 meV to approximately 1%. For this study the reference density for the high density polyethylene moderator was chosen to be 0.95 g/cm^3. The detector model is based on the ^{3}He Rover, introduced in Desilets et al. (2010) and analyzed by Köhli et al. (2018). In order to compare energy ranges a cosmic-ray neutron spectrum above the soil at 20% soil moisture and 15 g/m^3 air humidity simulated by MCNP (Goorley et al., 2012) is drawn. The dry soil consists to 75 % of SiO_2 and to 25 % of Al_2O_3 with a porosity of 50 %. The sensitivity to hydrogen according to **Figure 1** is shown by the shaded blue filling. **(B)** Weighting of this neutron spectrum with the response functions reveals the total count rate contribution of the different energy domains. The weighted count rate of the bare counter are decreased by a factor of 4.

called moderator, is mounted around the counter. It slows down epithermal neutrons in the same fashion as hydrogen contained in soil moisture. This necessary statistical deceleration comes with the drawback, that some neutrons are absorbed within the moderator material itself and some are reflected. Additionally, the environmental thermal neutron flux can partly leak into the moderator and increase the detector noise. This can be prevented by mounting a strongly absorbing material at the outside of the moderator case like cadmium, boron or gadolinium oxide (Gd_2O_3), further referred to as thermal shield. Due to the probabilistic nature of the deceleration sequence, the result is a rather broad energy sensitivity, called response function (see **Figure 3**, colored curves). The response function $R(E, \phi)$ describes the detection efficiency for an incoming neutron with energy E and incident angle ϕ. In general the response functions of neutron detectors typically used in CRNS resemble those of Bonner Spheres. For a more comprehensive study focused on standard CRNS detectors (see Köhli et al., 2018). **Figure 3A** shows the response functions of neutron counters with various moderator and thermal shield configurations. The standard CRNP configuration is shown in green. Multiplication with the cosmic-ray spectrum yields the spectral count rate (see **Figure 3B**), which, if integrated over all energies, leads to the total count rate. The relative thermal contribution of the signal of the standard CRNP is in particular large for moist soil. The reason for this observation is that the ratio between thermal and epithermal-to-fast neutrons increases with soil moisture, as the thermal intensity is not as sensitive to environmental hydrogen. However, as mentioned above the numbers shown here are subject to a high systematic uncertainty since the intensity of the thermal peak additionally depends on the soil chemistry. Following the signal definition in section 3.1 this thermal contamination of standard probes leads to a lower SNR as compared to shielded detectors (see **Figure 4A**). A high SNR is especially achieved for thin moderator configurations as the contamination of evaporation neutrons that did not penetrate the ground is relatively low, indicated in **Figure 3B**. However, excluding the evaporation regime is accompanied by a loss of signal as still a large part of such neutrons probed the soil. The signal normalized to the configuration of 27.5 mm moderator thickness and thermal shield is shown in **Figure 4B**. **Figures 4C,D** are also normalized with respect to the same configuration. **Figures 4A,B** reveal the competition between gain in signal quality by a higher SNR and by higher count rates, i.e., lower statistical uncertainty. Higher SNR leads to higher signal dynamics, i.e., relative count rate change per Vol-% soil moisture change, $\frac{\Delta N}{N}/\Delta\theta$, as depicted in **Figure 4C**. However, the statistical uncertainty needs to be sufficiently low in order to resolve these dynamics. Therefore, maximizing

$$\frac{\sqrt{S} \times \frac{\Delta N}{N}}{\Delta\theta} \tag{5}$$

is suggested as an optimization variable, where S is the signal. This product of statistical and dynamic range precision is shown in **Figure 4D**. It features maximum values for 20 and 22.5 mm moderator thicknesses in dry and moist conditions, respectively. As for dry conditions the signal dynamic is larger, it is concluded that a 22.5 mm moderator accompanied with a thermal shield shows the best overall performance. Yet, the difference to the 25 mm moderator and thermal shield combination as it was presented by Desilets et al. (2010) is marginal. In some use cases the thickness might be reduced further as for example in high altitude for close-to-saturation environments like alpine snow measurements. High altitudes come with the benefit of a high neutron flux and therefore low statistical uncertainty in shorter time frames. It might, thus, be beneficial to opt for a higher SNR with thinner moderators in order to maximize the

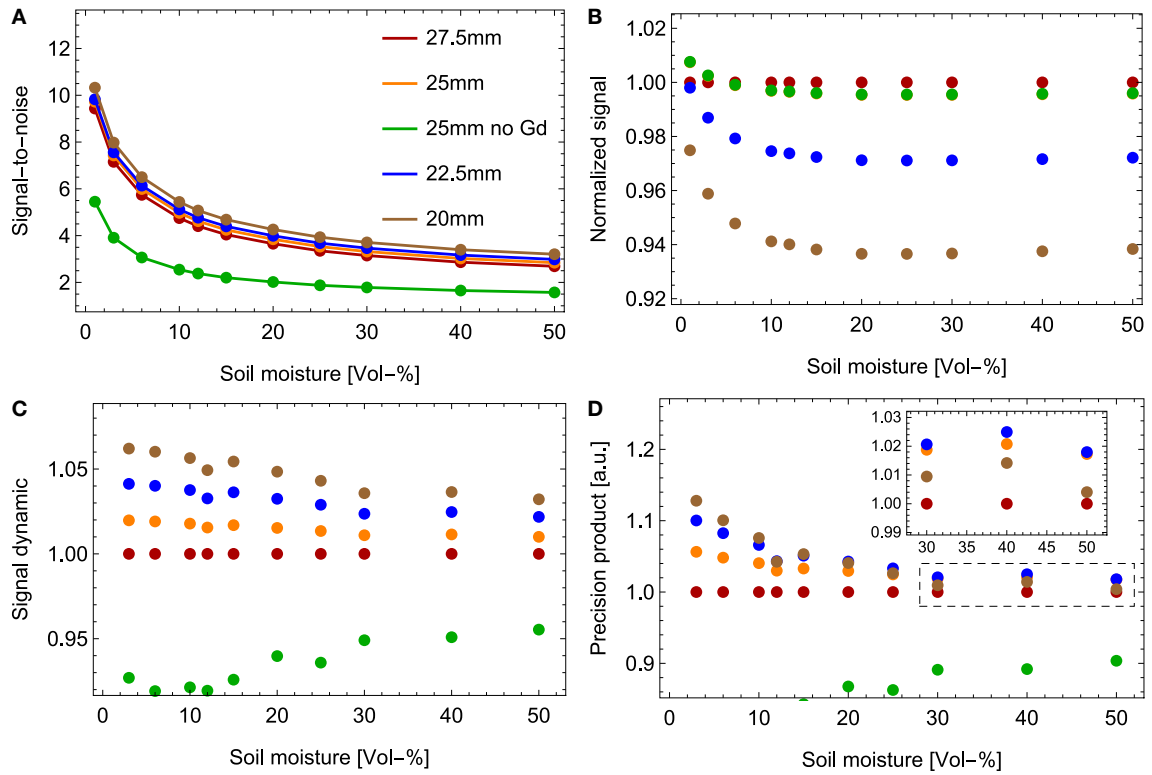

FIGURE 4 | Detector response to soil moisture dependent on the moderator thickness. All detector configurations feature a thermal shield except for "25 mm no Gd." **(A)** SNR according to the definition of section 3.1. **(B)** Signal count rates normalized to the detector setup with 27.5 mm moderator thickness and a thermal shield. **(C)** Dynamical range or signal contrast, normalized like **(B)**. **(D)** Suggested optimization procedure, maximizing the product of statistical, and contrast precision according to Equation (5).

overall precision. **Figure 4** shows the important role of thermal shielding as it significantly improves the dynamic range while keeping the signal count rate constant. If thermal neutrons are not efficiently shielded (5) shifts to thicker moderators and finally yields an optimum of 27.5–30 mm if no thermal shield is applied. The shape of the response functions is dominated by the moderator thickness but is also slightly influenced by the detector geometry and aspect ratio (Köhli et al., 2018). Hence, any detailed moderator optimization procedure should be adapted to the individual detector dimensions and might differ slightly from the above analysis.

3.2.3. Dimensional Considerations

The cosmic-ray neutron flux I_n at sea level integrated over all energies below 15 MeV is around 50–200 neutrons per second and m^2, depending on the magnetic cut-off rigidity and hydrogen pools (Goldhagen et al., 2004; Nesterenok, 2013; Sato, 2015). For most CRNS systems that ensues integration times on the order of hours in order to reduce the relative statistical uncertainty on the neutron count rate to a few per cents (Bogena et al., 2013; Schrön et al., 2018). Two parameters control the detector count rate. Firstly, the flux impinging on the neutron detector is proportional to its surface area A. Secondly, the detector magnitude of the response function $R(E, \phi)$, as discussed above, is a measure for the efficiency of the system. In total one yields

$$\begin{aligned} \text{count-rate [N/s]} &= \text{flux through detector [N/s]} \\ &\times \text{ detection efficiency } (E, \phi) \text{ [\%]} \\ &= A \text{ [m}^2\text{]} \times R(E, \phi) \text{ [\%]} \times I_n(E) \text{ [N/(s m}^2\text{)]}. \end{aligned} \tag{6}$$

Surface area and energy response function anticorrelate in the count rate optimization process at a fixed amount of converter material (see **Figure 5**). An optimal compromise between the two in particular depends on the efficiency and dimensions of the neutron counter. Monte Carlo simulations reveal that a thermalized neutron entering the inside of the moderator casing transits the latter on average 3 times due to backscattering at the inner surface. It may, therefore, traverse the neutron counter inside the moderator several times. The smaller the counter compared to the volume enclosed by the moderator the lower the probability to hit the tube. However, for highly efficient counters multiple traverses or large path lengths through the counter contribute less and less to the detection efficiency due to the exponential absorption law. For neutron counters with high efficiencies, it is advantageous to have a slightly bigger moderator

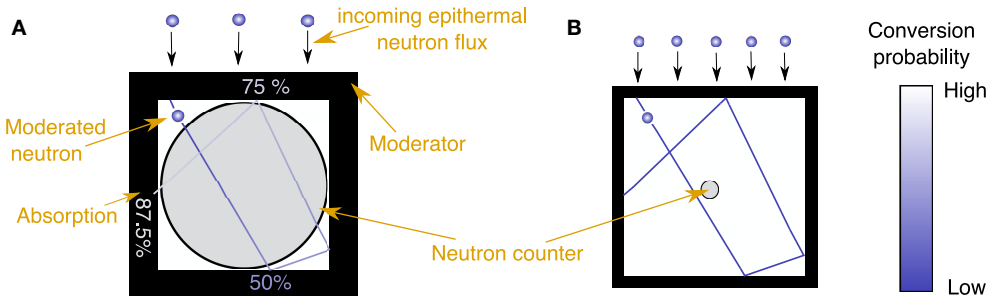

FIGURE 5 | Schematic drawing of the interplay between surface area and response function. The cross sections through two combinations of a rectangular moderator and cylindrical neutron counter at thermal efficiency of 50% are shown. Both figures are not to scale. A typical neutron track after thermalization through the inside of the moderator is shown in blue with the color saturation indicating the absorption probability by the converter material. **(A)** Maximizes the response function but features the smallest surface area possible, while **(B)** has a large surface area compared to the neutron counter dimension. Configuration **(B)** therefore has a large neutron flux impinging the moderator but a low response function because of the lower probability for a counter transect.

casing, hence a larger surface area in exchange for a lower traverse probability (see **Figure 5**). The optimum moderator size for a specific counter can be calculated individually using Monte Carlo simulations. As the neutron converter usually makes up for most of the production costs, it is instructive to optimize the detector design for a certain amount of converter. In the ideal case, the converter is evenly spread throughout the inside of the moderator as opposed to a highly efficient but infinitely small counter with the same amount of converter. In the context of CRNS, a cost-efficient detector design, therefore, is large in size while less efficient to maximize the use of its converter.

4. LARGE-AREA BORON-LINED NEUTRON DETECTORS FOR CRNS

The CRNP design considerations introduced above have led to a CRNS-tailored neutron detector development. This study introduces the first dedicated approach, a large-area boron-lined neutron detector. It makes use of a multitude of boron-lined proportional counters. The B_4C converter layer (96% enrichment of ^{10}B) has a thickness of up to 1.5 µm that is sputter-deposited on high purity copper foils. It is filled with a gas mixture of 90% argon and 10% CO_2. The efficiency of a single counter for thermal neutrons amounts to roughly 10% (Piscitelli, 2013; Modzel et al., 2014). Another 3% are absorbed but not detected as the conversion products do not reach the gas or their ionization signature is below the detection limit. The foil is embedded at the inner wall of a hermetically sealed aluminum tube with an inner diameter of 54 mm and a length of 1,250 mm. Aluminum is chosen for its low absorption probability for neutrons compared to other materials as for example stainless steel. The gold plated tungsten wire in the center has a diameter of 25 µm and requires a high voltage of 1,200 V. Stationary detectors are equipped with up to five counter tubes and a mobile detection system is composed of four rows with eight counters each as indicated in **Table 1**. Each row is subdivided into two base units with four neutron counters each. The detector tubes are surrounded by a modular moderator of 25–35 mm thickness and a removable thermal neutron shield made of Gd_2O_3. Further moderator sheet inlays between the base units allow for modular shielding and a specific energy response function adjustment. The counters of a base unit and those of a stationary detector are connected to one pulse analyzing and digitizing readout electronics module. The readout electronics assigns individual timestamps to each detected event with a temporal resolution of one millisecond. Such information may be used to study the "ship effect" and allows for corrections of occasional spikes in the count rate (Kouzes et al., 2008; Aguayo et al., 2013). A data logger collects the pulse information of the frontend electronics and records temperature, relative humidity and air pressure. The data is stored locally on a SD card and can be transmitted remotely via GSM or LTE. GNSS connectivity enables location tracking for mobile measurements but also updates the real time clock of the data logger ensuring stable timing over long periods. **Table 1** shows that the boron-lined detection systems feature a large surface area compared to other systems resulting in a high neutron flux throughput. The neutron counters inside the large moderator housing take up a substantial part of the inner moderator volume. Therefore, moderated neutrons are likely to traverse multiple boron-lined conversion layers, resulting in a moderate response function, which is two times lower than that of a ^{3}He-based CRS-1000 detector. However, due to the larger surface a pseudo efficiency that is approximately five times higher than that of the CRS-1000 detector is achieved (Köhli et al., 2018). An optional thermal shield reduces the count-rate by 10–20%, depending on the environmental conditions, but significantly improves the signal-to-noise ratio (see also section 3.2.2).

4.1. Modularity: Scientific Use Cases for Adapted Energy Response Functions

The mobile detection system setup (see **Figure 6** and **Table 1**), allows for moderator sheet inlays between rows of counter tubes. Information about the neutron spectrum can be retrieved by comparing the count rates of the differently moderated rows, similarly to the use of Bonner Spheres. The inset of **Figure 7** shows a simple configuration of 25 mm moderator sheet inlays between three counter rows, with a 25 mm moderator at each side and 10 mm at the top and bottom as well as a thermal

TABLE 1 | Key properties of the mobile and stationary detection system presented in this study and the commonly used CRS-1000.

Detection system	Dimensions [cm^3]	Neutron counter	Pseudo efficiency
CRS-1000	40 × 10 × 10	1 (^{3}He)	3.0 ± 0.2
Stationary (StX-140-5)	140 × 32 × 35	5	15.8 ± 1.2
Mobile	145 × 120 × 80	8 × 4	88 ± 5

Dimensions refer to the size of the moderator casing and the pseudo efficiency follows the definition by Köhli et al. (2018). It directly relates to the count rate of the system and was calculated using the Monte Carlo code URANOS.

FIGURE 6 | Setup of the large-area boron-lined detector for mobile measurements. Six base units are shown, assembled in two rows with two units each and two units on top of the back row. Each base unit is equipped with moderator sheets on three sides.

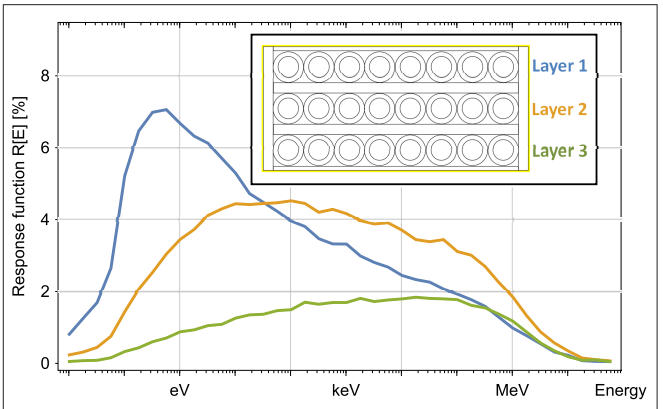

FIGURE 7 | Example for response function adaptation of the mobile unit that may be used for active signal correction of the near-field. Further layers increase the number of energy bands and allows to move toward characteristics of Bonner Sphere spectrometers. However, this calculation is valid for single side irradiation only.

shield (yellow outline). The upper and middle row feature highest sensitivity in the lower and upper energy part of the hydrogen-sensitive domain. The lower row's sensitivity peaks at energies between 10 keV and 1 MeV. Comparing the count rates yields information about the intensity changes of evaporation neutrons. These are mainly affected by the near field and, thus, may help to investigate the "road effect" (Schrön et al., 2018). Moreover, a configuration with rows that are especially sensitive in the thermal energy regime along with rows that show a standard response function may help in biomass focused studies (Baatz et al., 2015). The fourth counter row of the mobile unit may be added to any of the other three rows in order to increase the count rate for this specific energy domain. In principle, all four rows can be moderated differently.

4.2. Noise Reduction and Particle Discrimination by Pulse Shape Analysis

The key feature of any proportional counter is to precisely measure the charge generated in the ionization process by the incoming particle (see section 3.2). A well-adapted analog amplifier stage generates pulses with heights proportional to the energy deposition in the counter. It can therefore discriminate between the dense tracks from the neutron conversion process and weak ionization processes. Energy discrimination can effectively suppress muons as such deposit only low amounts of energy in the counter. However, some electrons and gamma rays that induce electrons can deposit significant amounts of energy in the gas if their track length is large enough. Long ionization traces lead to large differences in the arrival of the primary electrons close to the counter wall and those close to the wire. In general, the projected axial ionization path directly relates to the rise time of the charge pulse. As opposed to electrons, the rise time generated by the ^{10}B conversion is very short due to the short-ranged and dense ionization processes (see section 3.2). Pulse rise time is therefore another tool for particle discrimination as was shown by Izumi and Murata (1971) and Langford et al. (2013). As an upgrade to the commonly used pulse height discrimination, we use two-dimensional information about pulse height and length, which is shown in **Figures 8**, **9**. With the pulse length representing the rise time convoluted by the exponential decay of the amplifier electronics, displayed in **Figure 8b**. When exposing a boron-lined counter with 1 bar counting gas pressure to a radioactive gamma, beta and neutron source its efficiency to the various particle species can be determined. As suspected, neutrons and electrons populate different but also overlapping regions in the pulse length and height plot (**Figure 8c**), due to their different ionization characteristics, E and dE/dx. An event cluster that exclusively contains neutrons depicted in blue can be separated by the orange cluster populated by a mix of particle species. In both, the pulse height and pulse length spectrum, these clusters overlap and may not be distinguished completely. Only a combination of the two quantities provides a clear separation. However, a substantial amount of neutron events are contained in the orange cluster that makes up one third of all events. Therefore, a loss in count rate cannot be entirely avoided.

The most efficient scheme to reduce the contamination of weakly ionizing particles, however, is to reduce the gas pressure inside the counter tube. Thereby, the ionization per track length dE/dx and so the total energy deposition is reduced. By reducing

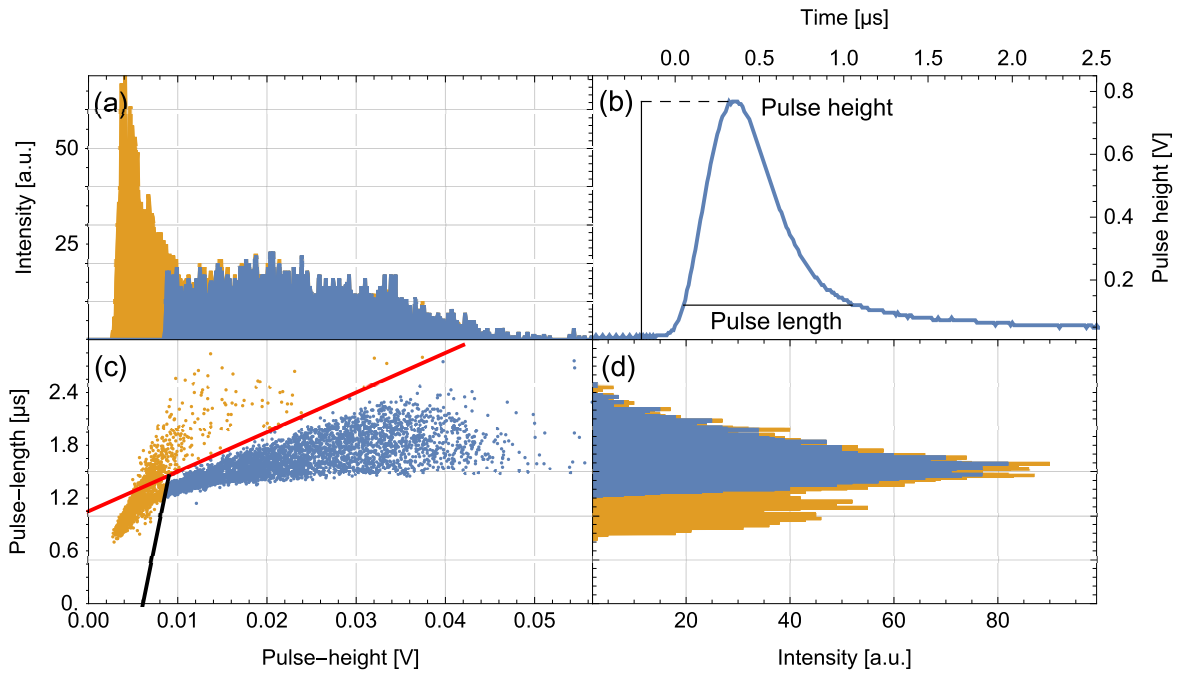

FIGURE 8 | Pulse shape analysis for a boron-lined detector at a counting gas pressure of 1 bar. **(a)** Shows the pulse height spectrum of 6,200 detected events. **(b)** Displays a pulse generated by the readout electronics corresponding to a neutron event and indicates how pulse height and length are determined. Pulse length corresponds to the time interval during which the pulse exceeds a certain threshold voltage level. The scatter plot **(c)** depicts the two-dimensional pulse data of the detected events. **(d)** Shows the event pulse length data as a histogram. **(a,d)** Are the projections of **(c)** to the pulse height and length axis, respectively. The blue events could be identified as neutrons whereas the orange cluster contains both electrons and neutrons. These regions can be separated by appropriate thresholds depicted by the red and black line in **(c)**.

the gas pressure to 250 mbar, the efficiency for electrons emitted by a radioactive strontium source was measured to be as low as 10^{-9}. The gamma sensitivity is on the same order of magnitude as the gamma rays ionize the gas indirectly by kick-off electrons. The heavy and highly ionizing conversion products of ^{10}B still deposit the same amount of energy inside the gas, because their track length is still smaller than the radius of the counter tube. The resulting pulse height spectrum (**Figure 9a**) resembles the theoretical spectrum (**Figure 9b**) simulated by URANOS and convoluted with a Gaussian distribution function of 2% full width at half maximum (FWHM). The convolution is used to simulate the effects of the detector energy resolution. The events in **Figure 9b** with energies E, 1.47 MeV$< E <$1.78 MeV correspond to the ^{10}B decay channel with a probability of 6% (see section 3.2). Particles with higher energies amount to two percent of all events under typical conditions. These alpha particles can easily be discriminated against via their pulse height. This event rate is also extrapolated to the boron conversion energy range, shown in **Figures 9a,b** to estimate the background noise by radioisotopes to be 0.74 $\pm$ 0.06 mHz, i.e., 64 $\pm$ 5 events per day. The main reason for this low intrinsic radioactivity is the 50 µm thick, high purity SE-Cu foil inside the boron-lined neutron counter as it has an intrinsic activity that was measured to be as low as (1.05 $\pm$ 0.1) events/(s m^2) in the energy region between 2.6 and 5 MeV. The copper foil also acts as a barrier between the aluminum housing of the counter and the gas filling. It effectively shields alpha and heavier particles from entering and ionizing the gas. Further contamination can arise from the decay of radon-222 gas, which accumulates on every surface. However, with typical decay energies above 5 MeV it can be easily discriminated against. The hardware discrimination threshold to lower energies is set to be $\approx$ 100 keV. This lower threshold cuts $\approx$ 6% of the total ^{10}B pulse height spectrum. The low electron efficiency mentioned above could also be confirmed with the Penelope Monte Carlo package (Salvat, 2015) simulating the electron transport and ionization trace inside the counter. The largest energy deposition for 250 mbar amounted to $\approx$ 50 keV, even for maximum track lengths through the counter volume and thus lies with a large margin below the hardware threshold.

The same readout electronics is used to record neutrons with a 2 $\times$ 12 inch proportional counter filled with 1.5 bar ^{3}He (GE Energy, 2005). This neutron counter is deployed in the widely used CRS-1000 standard CRNP by Hydroinnova LLC (Desilets, 2013). **Figure 10A** displays the pulse length and height scatter plot of the ^{3}He counter. The pulse height spectrum shown in **Figure 10B** resembles that given by the manufacturer (GE Energy, 2005). The background noise of the ^{3}He counter was extrapolated using the high energy alpha background similar to above and was estimated to be as low as 0.12 $\pm$ 0.04 mHz. This measured background noise has the same order of magnitude as the values reported by other studies (Hashemi-Nezhad and Peak, 1998; Debicki et al., 2011). The data series shown in this section were recorded at the Physikalisches Institut,

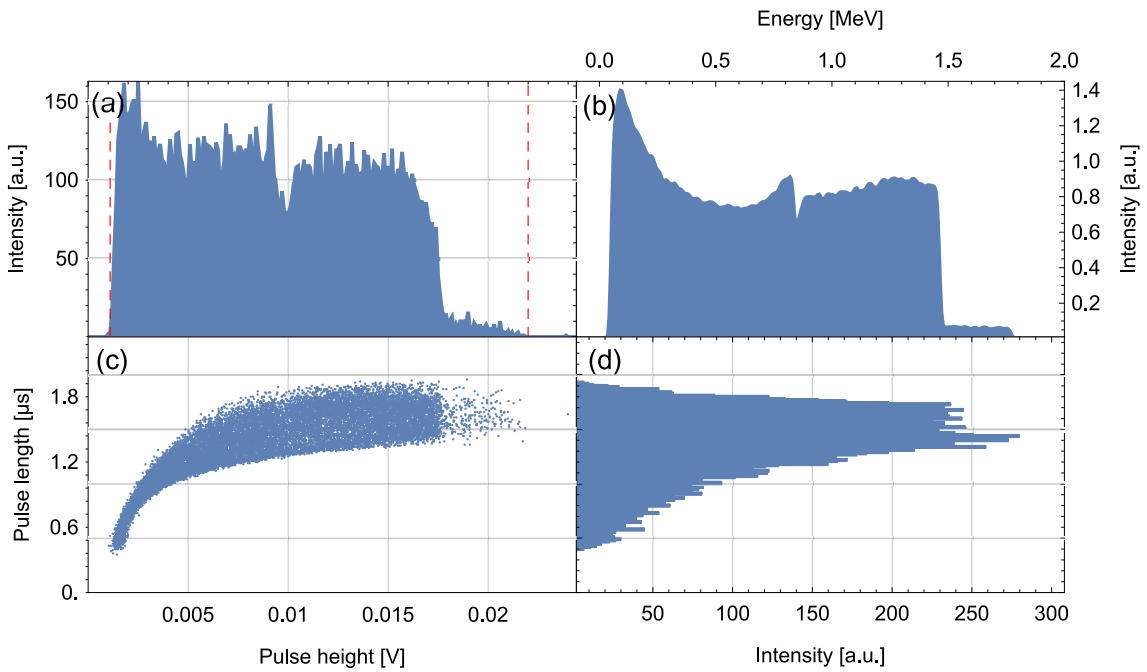

FIGURE 9 | Pulse shape analysis for a boron-lined detector at a counting gas pressure of 250 mbar. A total of ≈ 18,000 events are recorded. **(a)** Shows the pulse height spectrum and **(b)** a reference pulse height spectrum simulated by the URANOS Monte Carlo tool for a 1.44 µm thick boron layer. The first red line in **(a)** shows the hardware threshold discrimination to lower energies. The second red line symbolizes the upper threshold as it is set for detecting cosmic-ray neutrons for soil moisture measurements. In this setup, higher energy particles were also recorded in order to estimate the total background noise. **(c)** Shows the two-dimensional pulse shape data and the event pulse lengths are plotted as a histogram in **(d)**.

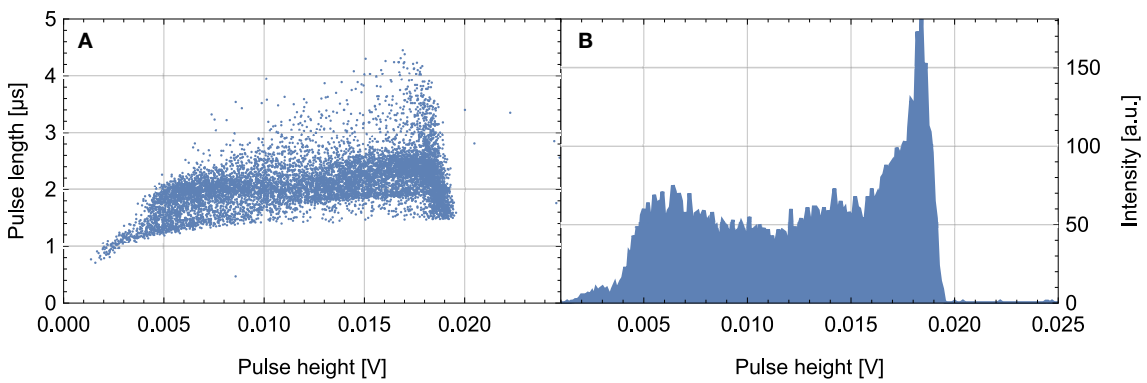

FIGURE 10 | Pulse shape analysis for a ^{3}He proportional counter. **(A)** Shows the pulse length and height plot and **(B)** the projected pulse height spectrum.

Heidelberg, Germany with the recently developed new frontend readout electronics.

4.3. Field Data

Four stationary detectors are deployed at the ATB Marquardt test site along with eight other cosmic-ray neutron sensors, operated by the University of Potsdam (see **Figure 11**). The test site is located close to Potsdam, Germany and has a cut-off rigidity r_c of 2.93 GV (Desorgher, 2004). The soil is composed of loamy sand and the biomass distribution is very heterogeneous. Total annual precipitation amounts to approximately 500 mm. The sensors are located in a small area such that their footprints overlap. **Figure 12** shows the neutron count rates of one boron-lined stationary detector with five neutron counter tubes with 1 bar counting gas pressure and a CRS-1000 and CRS-2000/B neutron detector in its vicinity. For comparison, all three detectors shown are equipped with a moderator of 25 mm thickness but without thermal neutron shields. The boron-lined stationary detector shows a similar response to precipitation events and pressure variations.

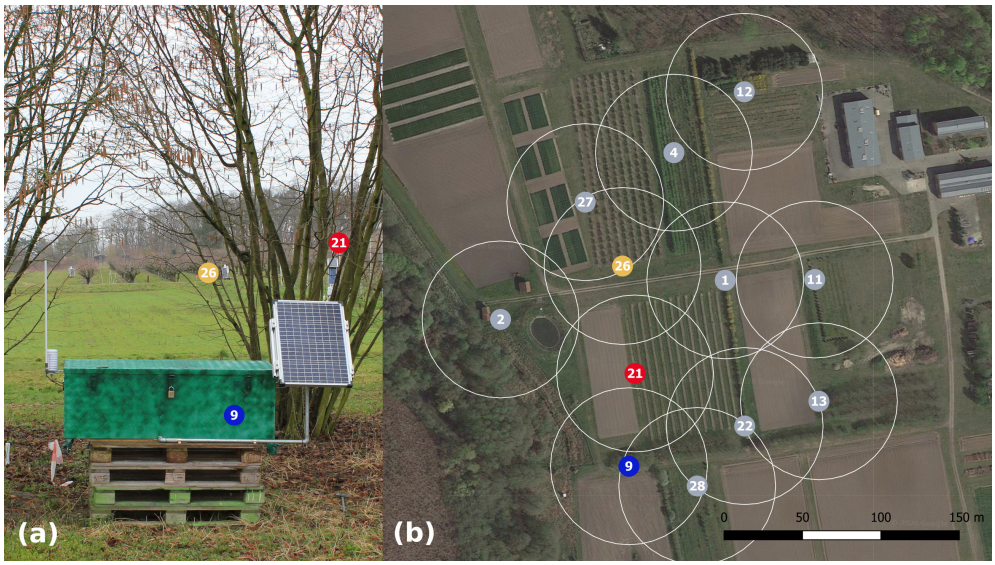

FIGURE 11 | Installation at the Marquardt test site of the Leibniz Institute for Agricultural Engineering and Bioeconomy with CRNPs compared in **Figure 12**. **(a)** Preliminary setup of sensor 9 in its camouflage box with external solar panel and GSM antenna. **(b)** Bird's eye view of the site. The neutron detectors are located with overlapping footprints (50 m radius, white circles). Background image, map data: Google imagery.

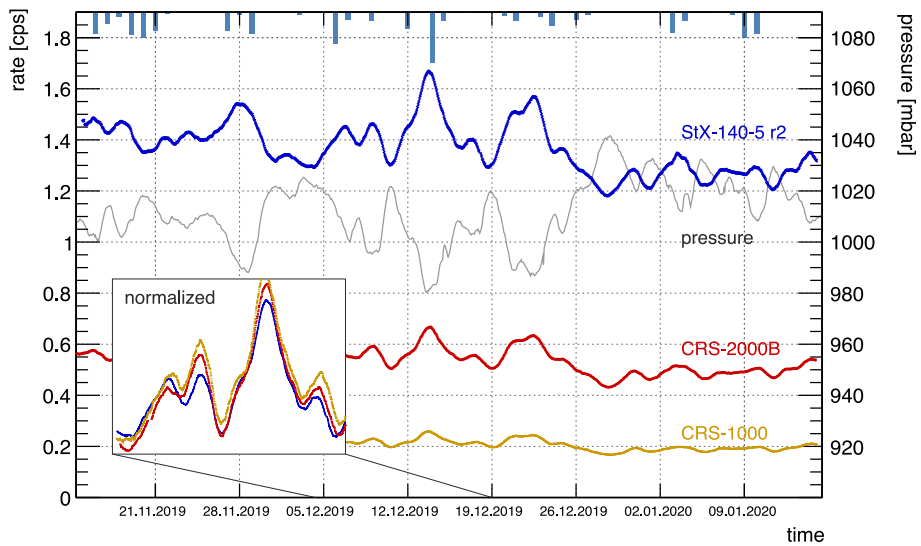

FIGURE 12 | Comparison of different CR probes installed at the Marquardt site (ATB Potsdam). The time series show raw data from the probes, which are tagged using the same color code as in **Figure 11**. The integration time of the probes was set to 20 min, however, a moving average of ±6 h has been applied to the neutron count time series. As a result the count rate errors are in the order of the plotted line width, yet, the averaging leads to an error of the given time scale. Rainfall with a maximum of 8 mm is indicated at the top, however the uncorrected rate changes are mainly due to atmospheric pressure changes plotted in gray. The inset shows 2 weeks of data with all probes scaled to each other.

5. CONCLUSION

This study examined critical properties of neutron detectors designed for Cosmic Ray Neutron Sensing and introduced a large-scale detector setup tested *in situ* at an experimental field site. Extensive Monte Carlo studies using both URANOS and MCNP 6.2 were conducted and detector design implementations suggested. The ideal moderator thickness was found to be a compromise between count rate enhancement and avoiding contamination of neutrons that do not carry information about the environmental hydrogen content. The typical value of 25 mm accompanied with a thermal neutron shield firstly introduced by Desilets et al. (2010) was confirmed to be appropriate for a universal detector approach. However, slightly better results were

obtained for 22.5 mm. For some settings a thinner moderator and thermal shield combination were identified to increase the neutron measurement precision. In general, the importance of a thermal shield was demonstrated, as it significantly increases the detector's signal-to-noise ratio. If no thermal shield is applied the optimum moderator thickness is slightly larger, lying between 27.5 and 30 mm. The measurement precision may be further increased by adapting the spatial dimensions of the moderator housing and thereby increasing the count rate. Changing the dimensions alters both the response functions magnitude and the total neutron flux impinging the detector surface with opposed effects on the count rate. Here, the ideal configuration strongly depends on the neutron counter's thermal sensitivity. Overall, high count rates are found to be achieved for large detector systems with large neutron counters. At last, the signal induced by non-neutron radiation and its influence on the overall signal quality was discussed. A novel detection system based on these design considerations was presented. It combines a moderate detection efficiency with a large surface area and achieves count rates that are higher by multiple times than usual systems. An appropriate selection of materials minimizes the relevant intrinsic background of radioisotopes to < 70 events per day per neutron counter. The readout electronics combines pulse height and length analysis to suppress the detection of non-neutron particles. It was shown that a reduction of the counter gas pressure to 250 mbar leads to a reduced efficiency to beta and gamma radiation of about 10^{-9}. Neutron events are recorded with a time resolution of milliseconds that allows for studying the "ship effect." The large-area detector is composed of several neutron counters. This modularity allows for adaptable response functions of the different counter tubes. Spectral information can then be retrieved and used for signal correction or biomass investigations.

The benefits for the standard soil moisture retrieval are two-fold. Firstly, a high signal-to-noise ratio increases the relative change in neutron detection rate per hydrogen content change. Secondly, high count rates lower the relative statistical uncertainty and the neutron detection rate can be resolved more precisely. Hence, the high signal-to-noise ratio and high count rates of the large-scale boron-lined detector lead to precise soil moisture measurements in short time frames.

DATA AVAILABILITY STATEMENT

The datasets presented in this article are not readily available because, the data presented is partly owned by other research institutes. Requests to access the datasets should be directed to weimar@physi.uni-heidelberg.de.

AUTHOR CONTRIBUTIONS

JW, MK, and US elaborated the introduced detector design with their research group at the Physics Institute Heidelberg, Heidelberg University. JW and MK contributed with neutron transport simulations and all three authors mentioned above contributed equally to the neutron counter and readout electronics design. CB deployed and maintained the sensors in the field and advised on how to transfer theoretical considerations onto a field applicable neutron detector system. All authors contributed to the article and approved the submitted version.

FUNDING

The project large-scale and high-resolution mapping of soil moisture on field and catchment scales—boosted by cosmic-ray neutrons was funded within the DFG research group Cosmic Sense FOR 2694. During the writing of this article JW was on a scientific exchange with alpS GmbH in Innsbruck, Austria funded by the DAAD program One-Year Grants for Doctoral Candidates.

ACKNOWLEDGMENTS

JW acknowledges Martin Schrön, UFZ Leipzig, Till Francke, and Sascha Oswald, both University of Potsdam, for their support during field campaigns and valuable comments on the applicability of some design considerations. The author also appreciates the fruitful discussions with Paul Schattan on this article's structure. MK acknowledges Heinrich Wilsenach, IKTP Dresden, for supporting background measurements. This work was supported by the ATB Marquardt where the stationary detectors were deployed. We acknowledge financial support by the Baden-Württemberg Ministry of Science, Research and the Arts and by Ruprecht-Karls-Universität Heidelberg.

REFERENCES

Aguayo, E., Kouzes, R., and Siciliano, E. (2013). *Ship Effect Neutron Measurements and Impacts on Low-Background Experiments*. Technical Report PNNL-22953, Pacific Northwest National Laboratory, Richland, WA.

Andreasen, M., Jensen, H. K., Zreda, M., Desilets, D., Bogena, H., and Looms, C. (2016). Modeling cosmic ray neutron field measurements. *Water Resour. Res.* 52, 6451–6471. doi: 10.1002/2015WR018236

Andreasen, M., Jensen, K., Desilets, D., Franz, T., Zreda, M., Bogena, H., et al. (2017). Status and perspectives on the cosmic-ray neutron method for soil moisture estimation and other environmental science applications. *Vadose Zone J.* 16, 1–11. doi: 10.2136/vzj2017.04.0086

Baatz, R., Bogena, H., Hendricks-Franssen, H.-J., Huisman, J., Montzka, C., and Vereecken, H. (2015). An empirical vegetation correction for soil water content quantification using cosmic ray probes. *Water Resour. Res.* 51, 2030–2046. doi: 10.1002/2014WR016443

Bogena, H., Huisman, J., Baatz, R., Hendricks-Franssen, H.-J., and Vereecken, H. (2013). Accuracy of the cosmic-ray soil water content probe in humid forest ecosystems: the worst case scenario. *Water Resour. Res.* 49, 5778–5791. doi: 10.1002/wrcr.20463

Bramblett, R., Ewing, R., and Bonner, T. (1960). A new type of neutron spectrometer. *Nucl. Instrum. Methods* 9, 1–12. doi: 10.1016/0029-554X(60)90043-4

Brown, D., Chadwick, M., Capote, R., Kahler, A., Trkov, A., Herman, M., et al. (2018). ENDF/B-VIII.0: the 8th major release of the nuclear reaction

data library with CIELO-project cross sections, new standards and thermal scattering data. *Nucl. Data Sheets* 148, 1–142. doi: 10.1016/j.nds.2018.02.001

Chadwick, M., Herman, M., Obložinský, P., Dunn, M., Danon, Y., Kahler, A., et al. (2011). ENDF/B-VII.1 nuclear data for science and technology: cross sections, covariances, fission product yields and decay data. *Nucl. Data Sheets* 112, 2887–2996. doi: 10.1016/j.nds.2011.11.002

Compton, A. (1923). A quantum theory of the scattering of x-rays by light elements. *Phys. Rev*. 21:483. doi: 10.1103/PhysRev.21.483

Debicki, Z., Jedrzejczak, K., Karczmarczyk, J., Kasztelan, M., Lewandowski, R., Orzechowski, J., et al. (2011). Helium counters for low neutron flux measurements. *Astrophys. Space Sci. Trans*. 7, 511–514. doi: 10.5194/astra-7-511-2011

Desilets, D. (2012). Probe background, technology, calibration, MCNP.

Desilets, D. (2013). *CRS1000 and CRS1000/B User's Guide*. Albuquerque, NM: Hydroinnova.

Desilets, D., Zreda, M., and Ferré, T. (2010). Nature's neutron probe: land surface hydrology at an elusive scale with cosmic rays. *Water Resour. Res*. 46:W11505. doi: 10.1029/2009WR008726

Desorgher, L. (2004). *The Magnetocosmics Code*. Technical report. Available online at: http://cosray.unibe.ch/laurent/magnetoscosmics

Forsyth, A., Teal, T., and Inglis, A. (2017). "Silverside neutron detector performance," in *2017 IEEE International Symposium on Technologies for Homeland Security (HST)* (Waltham, MA), 1–7. doi: 10.1109/THS.2017.7943461

Franz, T., Wahbi, A., Vreugdenhil, M., Weltin, G., Heng, L., Oismueller, M., et al. (2016). Using cosmic-ray neutron probes to monitor landscape scale soil water content in mixed land use agricultural systems. *Appl. Environ. Soil Sci*. 2016:4323742. doi: 10.1155/2016/4323742

Franz, T., Zreda, M., Rosolem, R., Hornbuckle, B., Irvin, S., Adams, H., et al. (2013). Ecosystem-scale measurements of biomass water using cosmic ray neutrons. *Geophys. Res. Lett*. 40, 3929–3933. doi: 10.1002/grl.50791

GE Energy (2005). *Reuter Stokes 3-He Neutron Detectors for Homeland Security Radiation Portal Monitors*. Twinsburg, OH: GE Energy.

Goldhagen, P., Clem, J., and Wilson, J. (2004). The energy spectrum of cosmic-ray induced neutrons measured on an airplane over a wide range of altitude and latitude. *Radiat. Protect. Dosimet*. 110, 387–392. doi: 10.1093/rpd/nch216

Goorley, T., James, M., Booth, T., Brown, F., Bull, J., Cox, L., et al. (2012). Initial MCNP6 release overview. *Nucl. Technol*. 180, 298–315. doi: 10.13182/NT11-135

Groom, D., Mokhov, N., and Striganov, S. (2001). Muon stopping power and range tables 10 MeV-100 TeV. *Atom. Data Nucl. Data Tables* 78, 183–356. doi: 10.1006/adnd.2001.0861

Hashemi-Nezhad, S., and Peak, L. (1998). Limitation on the response of ^{3}He counters due to intrinsic alpha emission. *Nucl. Instrum. Methods Phys. Res. Sect. A* 416, 100–108. doi: 10.1016/S0168-9002(98)00565-8

Hertel, N., and Davidson, J. (1985). The response of Bonner Spheres to neutrons from thermal energies to 17.3 MeV. *Nucl. Instrum. Methods Phys. Res. A* 238, 509–516. doi: 10.1016/0168-9002(85)90494-2

Izumi, S., and Murata, Y. (1971). Pulse risetime analysis of a ^{3}He proportional counter. *Nucl. Instrum. Methods* 94, 141–145. doi: 10.1016/0029-554X(71)90351-X

Kodama, M., Kudo, S., and Kosuge, T. (1985). Application of atmospheric neutrons to soil moisture measurement. *Soil Sci*. 140, 237–242. doi: 10.1097/00010694-198510000-00001

Köhli, M., Allmendinger, F., Häußler, W., Schröder, T., Klein, M., Meven, M., et al. (2016). Efficiency and spatial resolution of the CASCADE thermal neutron detector. *Nucl. Instrum. Methods Phys. Res. Sect. A* 828, 242–249. doi: 10.1016/j.nima.2016.05.014

Köhli, M., Schrön, M., and Schmidt, U. (2018). Response functions for detectors in cosmic ray neutron sensing. *Nucl. Instrum. Methods Phys. Res. Sect. A* 902, 184–189. doi: 10.1016/j.nima.2018.06.052

Köhli, M., Schrön, M., Zreda, M., Schmidt, U., Dietrich, P., and Zacharias, S. (2015). Footprint characteristics revised for field-scale soil moisture monitoring with cosmic-ray neutrons. *Water Resour. Res*. 51, 5772–5790. doi: 10.1002/2015WR017169

Kouzes, R., Ely, J., Seifert, A., Siciliano, E., Weier, D., Windsor, L., et al. (2008). Cosmic-ray-induced ship-effect neutron measurements and implications for cargo scanning at borders. *Nucl. Instrum. Methods Phys. Res. Sect. A* 587, 89–100. doi: 10.1016/j.nima.2007.12.031

Kowatari, M., Nagaoka, K., Satoh, S., Ohta, Y., Abukawa, J., Tachimori, S., et al. (2005). Evaluation of the altitude variation of the cosmic-ray induced environmental neutrons in the Mt. Fuji Area. *J. Nucl. Sci. Technol*. 42, 495–502. doi: 10.1080/18811248.2004.9726416

Langford, T., Bass, C., Beise, E., Breuer, H., Erwin, D., Heimbach, C., et al. (2013). Event identification in ^{3}He proportional counters using risetime discrimination. *Nucl. Instrum. Methods Phys. Res. Sect. A* 717, 51–57. doi: 10.1016/j.nima.2013.03.062

Letaw, J., and Normand, E. (1991). Guidelines for predicting single-event upsets in neutron environments (RAM devices). *IEEE Trans. Nucl. Sci*. 38, 1500–1506. doi: 10.1109/23.124138

Li, D., Schrön, M., Köhli, M., Bogena, H., Weimar, J., Jiménez Bello, M., et al. (2019). Can drip irrigation be scheduled with cosmic-ray neutron sensing? *Vadose Zone J*. 18:190053. doi: 10.2136/vzj2019.05.0053

Mares, V., Schraube, G., and Schraube, H. (1991). Calculated neutron response of a Bonner Sphere Spectrometer with ^{3}He counter. *Nucl. Instrum. Methods Phys. Res. Sect. A* 307, 398–412. doi: 10.1016/0168-9002(91)90210-H

Mares, V., and Schraube, H. (1994). Evaluation of the response matrix of a Bonner Sphere Spectrometer with liI detector from thermal energy to 100 MeV. *Nucl. Instrum. Methods Phys. Res. Sect. A* 337, 461–473. doi: 10.1016/0168-9002(94)91116-9

McKinney, G. (2013). MCNP6 cosmic and terrestrial background particle fluxes. LA-UR-13-24293. Release 3.

Modzel, G., Henske, M., Houben, A., Klein, M., Köhli, M., Lennert, P., et al. (2014). Absolute efficiency measurements with the 10B based Jalousie detector. *Nucl Instrum Meth in Physics Research Section A*. 743, 90–95. doi: 10.1016/j.nima.2014.01.007

Mohanty, B., Cosh, M., Lakshmi, V., and Montzka, C. (2017). Soil moisture remote sensing: state-of-the-science. *Vadose Zone J*. 16, 1-9. doi: 10.2136/vzj2016.10.0105

Montzka, C., Bogena, H., Zreda, M., Monerris, A., Morrison, R., Muddu, S., et al. (2017). Validation of spaceborne and modelled surface soil moisture products with cosmic-ray neutron probes. *Remote Sens*. 9:103. doi: 10.3390/rs9020103

Nelson, K., Bellinger, S., Montag, B., Neihart, J., Riedel, T., Schmidt, A, J., et al. (2012). Investigation of a lithium foil multi-wire proportional counter for potential ^{3}He replacement. *Nucl. Instrum. Methods Phys. Res. Sect. A* 669, 79–84. doi: 10.1016/j.nima.2011.12.003

Nesterenok, A. (2013). Numerical calculations of cosmic ray cascade in the Earth's atmosphere - Results for nucleon spectra. *Nucl. Instrum. Methods Phys. Res. B* 295, 99–106. doi: 10.1016/j.nimb.2012.11.005

Pfotzer, G. (1936). Dreifachkoinzidenzen der ultrastrahlung aus vertikaler richtung in der stratosphäre. *Zeitsch. Phys*. 102, 41–58. doi: 10.1007/BF01336830

Piscitelli, F. (2013). *Boron-10 layers, Neutron Reflectometry and Thermal Neutron Gaseous Detectors*. Ph.D. thesis, Universitá degli Studi di Perugia, Perugia, Italy.

Quinta-Ferreira, M., Dias, J., and Alija, S. (2016). False low water content in road field compaction control using nuclear gauges: a case study. *Environ. Earth Sci*. 75:1114. doi: 10.1007/s12665-016-5901-1

Robinson, D., Campbell, C., Hopmans, J., Hornbuckle, B., Jones, S., Knight, R., et al. (2008). Soil moisture measurement for ecological and hydrological watershed-scale observatories: a review. *Vadose Zone J*. 7, 358–389. doi: 10.2136/vzj2007.0143

Rodriguez-Alvarez, N., Bosch-Lluis, X., Camps, A., Aguasca, A., Vall-Llossera, M., Valencia, E., et al. (2011). Review of crop growth and soil moisture monitoring from a ground-based instrument implementing the interference pattern GNSS-R technique. *Radio Sci*. 46,1–11. doi: 10.1029/2011RS004680

Rosolem, R., Shuttleworth, W., Zreda, M., Franz, T., Zeng, X., and Kurc, S. (2013). The effect of atmospheric water vapor on neutron count in the cosmic-ray soil moisture observing system. *J. Hydrometeorol*. 14, 1659–1671. doi: 10.1175/JHM-D-12-0120.1

Salvat, F. (2015). "The PENELOPE code system," in *Specific Features and Recent Improvements, Vol. 82*, ed EDP, Science (Barcelona: Elsevier), 98–109. doi: 10.1016/j.anucene.2014.08.007

Sato, T. (2015). Analytical model for estimating terrestrial cosmic ray fluxes nearly anytime and anywhere in the world: extension of PARMA/EXPACS. *PLoS ONE* 10:e144679. doi: 10.1371/journal.pone.0144679

Sato, T. (2016). Analytical model for estimating the zenith angle dependence of terrestrial cosmic ray fluxes. *PLoS ONE* 11:e160390. doi: 10.1371/journal.pone.0160390

Sato, T., and Niita, K. (2006). Analytical functions to predict cosmic-ray neutron spectra in the atmosphere. *Radiat. Res*. 166, 544–555. doi: 10.1667/RR0610.1

Schattan, P., Baroni, G., Oswald, S., Schöber, J., Fey, C., Kormann, C., et al. (2017). Continuous monitoring of snowpack dynamics in alpine terrain by aboveground neutron sensing. *Water Resour. Res*. 53, 3615–3634. doi: 10.1002/2016WR020234

Schattan, P., Köhli, M., Schrön, M., Baroni, G., and Oswald, S. (2019). Sensing area-average snow water equivalent with cosmic-ray neutrons: the influence of fractional snow cover. *Water Resour. Res*. 55, 10796–10812. doi: 10.1029/2019WR025647

Schrön, M., Köhli, M., Scheiffele, L., Iwema, J., Bogena, H., Lv, L., et al. (2017). Improving calibration and validation of cosmic-ray neutron sensors in the light of spatial sensitivity. *Hydrol. Earth Syst. Sci*. 21, 5009–5030. doi: 10.5194/hess-21-5009-2017

Schrön, M., Rosolem, R., Köhli, M., Piussi, L., Schröter, I., Iwema, J., et al. (2018). Cosmic-ray neutron rover surveys of field soil moisture and the influence of roads. *Water Resour. Res*. 54, 6441–6459. doi: 10.1029/2017WR021719

Shea, D., and Morgan, D. (2010). *The Helium-3 Shortage: Supply, Demand, and Options for Congress*. CRS Report for Congress. R41419. Congressional Research Service.

Shuttleworth, J., Rosolem, R., Zreda, M., and Franz, T. (2013). The COsmic-ray Soil Moisture Interaction Code (COSMIC) for use in data assimilation. *Hydrol. Earth Syst. Sci*. 17, 3205–3217. doi: 10.5194/hess-17-3205-2013

Stevanato, L., Baroni, G., Cohen, Y., Cristiano Lino, F., Gatto, S., Lunardon, M., et al. (2019). A novel cosmic-ray neutron sensor for soil moisture estimation over large areas. *Agriculture* 9:202. doi: 10.3390/agriculture 9090202

Strati, V., Albéri, M., Anconelli, S., Baldoncini, M., Bittelli, M., Bottardi, C., et al. (2018). Modelling soil water content in a tomato field: proximal gamma ray spectroscopy and soil-crop system models. *Agriculture* 8:60. doi: 10.3390/agriculture8040060

Tian, Z., Li, Z., Liu, G., Li, B., and Ren, T. (2016). Soil water content determination with cosmic-ray neutron sensor: correcting aboveground hydrogen effects with thermal/fast neutron ratio. *J. Hydrol*. 540, 923–933. doi: 10.1016/j.jhydrol.2016.07.004

Waters, L., McKinney, G., Durkee, J., Fensin, M., Hendricks, J., James, M., et al. (2007). The MCNPX Monte Carlo radiation transport code. *AIP Conf. Proc*. 896, 81–90. doi: 10.1063/1.2720459

Werner, C. J., Bull, J. S., Solomon, C. J., Brown, F. B., McKinney, G. W., Rising, M. E., et al. (2018). *MCNP Version 6.2 Release Notes*. Technical report, Los Alamos National Lab (LANL), Los Alamos, NM, United States.

Zreda, M., Desilets, D., Ferré, T., and Scott, R. (2008). Measuring soil moisture content non-invasively at intermediate spatial scale using cosmic-ray neutrons. *Geophys. Res. Lett*. 35:L21402. doi: 10.1029/2008GL035655

Zreda, M., Shuttleworth, W., Zeng, X., Zweck, C., Desilets, D., Franz, T., et al. (2012). COSMOS: The COsmic-ray Soil Moisture Observing System. *Hydrol. Earth Syst. Sci*. 16, 4079–4099. doi: 10.5194/hess-16-4079-2012

Conflict of Interest: JW and MK hold CEO positions at StyX Neutronica GmbH.

The remaining authors declare that the research was conducted in the absence of any commercial or financial relationships that could be construed as a potential conflict of interest.

APPENDIX

DETAILED CALCULUS OF SOIL MOISTURE UNCERTAINTY

This article aims at analyzing the most relevant neutron count uncertainty sources for gaseous neutron detectors tailored for CRNS. In section 3.1 it is indicated how this uncertainty propagates onto the uncertainty of soil moisture as this is the desired variable. Here the corresponding calculus is shown in more length. For the calculation we use Equation (1) and its inverse:

$$N(\theta) = N_0 \left[\frac{a_0}{\left(\frac{\theta}{\rho_{\mathrm{bd}}} + a_2 \right)} + a_1 \right] \tag{7}$$

We use simple uncertainty propagation and neglect the influence of other uncertainty sources on the soil moisture content:

$$\begin{aligned} \sigma_\theta &= \left| \frac{\partial \theta}{\partial N} \sigma_N \right| = \frac{\partial \left[\rho_{\mathrm{bd}} \left(\frac{a_0}{\left(\frac{N}{N_0} - a_1 \right)} - a_2 \right) \right]}{\partial N} \sigma_N \\ &= \sigma_N \frac{\partial}{\partial N} \left[\rho_{\mathrm{bd}} a_2 + \frac{\rho_{\mathrm{bd}} a_0}{\frac{N}{N_0} - a_1} \right] = \sigma_N \frac{\rho_{\mathrm{bd}} a_0}{N_0 \left(\frac{N}{N_0} - a_1 \right)^2} \end{aligned} \tag{8}$$

For simplicity we omitted the determination of the absolute value in the second step. Replacing N with Equation (7) to obtain σ_θ dependent on θ results in:

$$\sigma_\theta = \sigma_N \frac{\rho_{\mathrm{bd}} a_0}{N_0 \left(\frac{N_0 \left[\frac{a_0}{\left(\frac{\theta}{\rho_{\mathrm{bd}}} + a_2 \right)} + a_1 \right]}{N_0} - a_1 \right)^2} = \sigma_N \frac{\rho_{\mathrm{bd}} a_0}{N_0 \left(\frac{a_0}{\frac{\theta}{\rho_{\mathrm{bd}}} + a_2} \right)^2}$$

$$= \frac{\rho_{\mathrm{bd}} \sigma_N}{a_0 N_0} \left(\frac{\theta}{\rho_{\mathrm{bd}}} + a_2 \right)^2 \tag{9}$$

This result is presented in section 3.1.

ACCOUNT OF DETECTOR COSTS

Besides the benefits mentioned above boron-lined neutron detectors are likewise a cost-effective alternative to ^{3}He-based CRNPs. Boron-lined systems require enriched ^{10}B as the absorption cross section of the naturally more abundant ^{11}B is lower by three orders of magnitude. Contrary to helium-3 which is extracted from refurbished thermonuclear warheads, boron is widely used as a semiconductor dopant. For radiation hard applications it needs to be depleted in ^{10}B in order to make it more resilient against neutron-induced damages. ^{10}B enriched boron is therefore a by-product of the semiconductor industry. The price is subject to fluctuations that can be as high as 50% and by the time this article was written amounted to 1,500$ per 100 g. Enriched boron is sputter deposited as $^{10}B_4C$ with a thickness of 1.5 µm on a copper substrate. The current price of such a 96% enriched $^{10}B_4C$ coating amounts to approximately 2,500 $ per m^2 with the sputter deposition being the most substantial item in the cost budget. Absorption cross section comparison shows that 1 m^2 × 1.5 µm has the absorption, and thus neutron conversion, capability of approximately 5 barliters of ^{3}He. However, approximately 43% of the reaction products do not leave the boron layer and thus can not be detected, as indicated in section 3.2. Moreover some of the reaction products may not be distinguished from other radiation when depositing small amounts of energy in the counter's gas. This leads to a factor of 2.5 in neutron detection efficiency between 1 m^2 of ^{10}B to 1 barliter of ^{3}He, which for example can approximately be found in CRS-1000 counter tubes. In order to compare neutron count rates the total surface of the CRNP has to be taken into account (see section 3.2.2). The stationary detector introduced in section 4.3 incorporates a total of approximately 1 m^2 of 1.5 µm boron-lined copper substrate.

frontiers in Water

ORIGINAL RESEARCH
published: 17 November 2020
doi: 10.3389/frwa.2020.552508

Comparison of Soil Water Estimates From Cosmic-Ray Neutron and Capacity Sensors in a Semi-arid Pine Forest: Which Is Able to Better Assess the Role of Environmental Conditions and Thinning?

María González-Sanchis[1,2]*, *Juan M. García-Soro*[1,2], *Antonio J. Molina*[1,2], *Antonio L. Lidón*[1], *Inmaculada Bautista*[1], *Elie Rouzic*[3], *Heye R. Bogena*[4], *Harrie-JanHarrie Hendricks Franssen*[4] *and Antonio D. del Campo*[1,2]

[1] *Research Group in Forest Science and Technology (Re-ForeST), Research Institute of Water and Environmental Engineering (IIAMA), Universitat Politècnica de València, Valencia, Spain,* [2] *Environmental Hydraulics Department, Universitat Politècnica de València (UPV), Valencia, Spain,* [3] *École Nationale Supérieure de Techniques Avancées (ENSTA Paris), Paris, France,* [4] *Agrosphere Institute (Institute of Bio- and Geosciences), Forschungszentrum Jülich, Jülich, Germany*

OPEN ACCESS

Edited by:
Bhavna Arora, Lawrence Berkeley National Laboratory, United States

Reviewed by:
Tim Scheibe, Pacific Northwest National Laboratory (DOE), United States
Raghavendra Belur Jana, Skolkovo Institute of Science and Technology, Russia

***Correspondence:**
María González-Sanchis
macgonsa@gmail.com

Specialty section:
This article was submitted to Water and Hydrocomplexity, a section of the journal Frontiers in Water

Received: *16 April 2020*
Accepted: *29 September 2020*
Published: *17 November 2020*

Citation:
González-Sanchis M, García-Soro JM, Molina AJ, Lidón AL, Bautista I, Rouzic E, Bogena HR, Hendricks Franssen H-J and del Campo AD (2020) Comparison of Soil Water Estimates From Cosmic-Ray Neutron and Capacity Sensors in a Semi-arid Pine Forest: Which Is Able to Better Assess the Role of Environmental Conditions and Thinning? Front. Water 2:552508. doi: 10.3389/frwa.2020.552508

Water scarcity in semi-arid regions is expected to increase under climate change, which will significantly affect forest ecosystems by increasing fire risk, diminishing productivity and water provisioning. Eco-hydrological forest management is conceived here as an adequate strategy to buffer climate change effects and increase forest resilience. Under this context, soil moisture is a key variable to quantify the impacts of eco-hydrological forest management on forest-water relations. Cosmic-ray neutron and capacitance probes are two different techniques for measuring soil moisture, which differ greatly in the spatial scale of the measurement support (i.e., few centimeters vs. several hectares). This study compares the capability of both methodologies in assessing soil water dynamics as a key variable that reflects the effects of forest management in a semi-arid environment. To this end, two experimental plots were established in Sierra Calderona in the province of Valencia in Spain in a post-fire regeneration Aleppo pine forest with high tree density. One plot was thinned (T) and the other remained as control (C). Nine capacitance probes and one Cosmic Ray Neutron Probe (CRNP) were installed in each plot. First, the CRNP was calibrated and validated, and subsequently, the performance of both techniques was analyzed by comparing soil moisture and its relationship with environmental variables and stand transpiration. The validation results confirmed the general reliability of CRNP to obtain soil moisture under semi-arid conditions, with a Kling-Gupta efficiency coefficient (KGE) between 0.75 and 0.84, although this performance decreased significantly when dealing with extreme soil moisture (KGE: −0.06–0.02). A significant effect of forest biomass and litter layer was also observed on CRNP-derived soil moisture, which produced an overestimation of soil moisture. The performance of both methodologies was analyzed by partial correlations between soil moisture and environmental variables and transpiration, as well as by applying Boosted Regression Trees to reproduce tree transpiration with each

soil moisture measurement technique together with the environmental variables. Both methodologies were capable to reproduce tree transpiration affected by soil moisture, environmental variables and thinning, although CRNP always appeared as the most affected by atmospheric driving forces.

Keywords: forest hydrology, silviculture, capacitance sensors, cosmic-ray sensor, *Pinus halepensis*

INTRODUCTION

Semi-arid forests are water-controlled environments where water availability has direct and indirect effects on key processes such as weathering, decomposition, soil respiration, nitrogen mineralization, nutrient uptake, biomass production, and long–term carbon sequestration (Rodríguez-Iturbe and Porporato, 2007). This water dependence leads these forests to face abiotic and biotic threats (e.g., wildfires, insect outbreaks and severe drought events) that may decline their capability to persist in their current geographic ranges, and to colonize new habitats (Bell et al., 2014; Rehfeldt et al., 2014). During the 20th Century, their persistence has been dependent on favorable climatic and environmental conditions (Savage et al., 1996; Mast et al., 1999; Brown and Wu, 2005), which unfortunately, according to climate change projections, are going to be less frequent, increasing the ecosystem threats and therefore diminishing its regeneration capability (Coops et al., 2005; van Mantgem et al., 2009; Williams et al., 2013). Under this context, adaptive forest management is conceived as useful strategy that shapes forest-water relationships to improve the capability of these forests to face the effects of climate change (del Campo et al., 2017).

Soil moisture can be an accurate proxy of water availability in a semi-arid forest as it is an important water source for vegetation development, and one of the most important factors controlling hydrological processes (Castillo et al., 2003; Seeger et al., 2004). Changes of soil water may greatly affect tree species diversity and forest canopy structure. In turn, changes in vegetation, which are often pursued in forest management, typically lead to changes in soil moisture. Therefore, soil moisture is a key variable in quantifying the impact of forest management on the forest-water relationship (del Campo et al., 2019b). There are different measuring methods to obtain reliable estimates of soil moisture, depending on the required spatio-temporal accuracy, ranging from direct manual measurements to satellite-based sensors (Vereecken et al., 2008). Time domain reflectometry (TDR) and capacitance sensors have been extensively used at the local scale (Gardner et al., 1998; Seyfried and Murdock, 2001; Topp and Ferré, 2006). Both are invasive methods that require several measurement points to estimate representative spatial and temporal mean soil water contents (Molina et al., 2014). In natural ecosystems, the need for a large number of measurement points is typically greater because the heterogeneity of soil moisture is larger compared to arable land, due to the typically greater differences in topography and vegetation cover, the uneven input of litter and the less intensive mixing of the soil (Hawley et al., 1983; Flinn and Marks, 2007). Alternatively, soil moisture sensors with larger measurement support could be used that are able to better cover the local scale variability, e.g., non-invasive methods like remote sensing or geophysical methods (Lv et al., 2014; Bogena et al., 2015). Although their capabilities are improving constantly, satellite based remote sensing currently shows lower accuracy than geophysical methods at the field to catchment scale (Lv et al., 2014). Therefore, when measuring soil moisture in forests, CRNP could be a compromise solution between spatial heterogeneity, accuracy and functionality.

The CRNP is a novel, non-invasive technique to measure the areal-averaged soil moisture of an effective depth in the order of decimeters within a radial footprint on the order of several hectares (Zreda et al., 2008; Andreasen et al., 2017). The CRNP are detectors that measure the fast neutron intensity at ground level generated by cosmic radiation (Heidbüchel et al., 2016). The interaction of fast neutrons with hydrogen atoms, which are mainly present in soil moisture, lowers the intensity of fast neutrons detected by the CRNP. Therefore an inverse relationship between neutron intensity and soil moisture exists that can be exploited to monitor soil moisture dynamics at the field scale (Bogena et al., 2013). According to Schrön et al. (2017), the CRNP provides indirect measurements of soil moisture over a circular footprint with an effective radius ranging approximately from 150 to 210 m (i.e., from about 7 to 14 hectares) depending on various factors, e.g., soil moisture, atmospheric pressure, air humidity, vegetation biomass etc. The contribution of neutron counts decreases rapidly with separation distance from the CRNP (Zreda et al., 2012), and ∼50% of the cumulative fraction of neutron counts is contributed from distances <50 m (Schrön et al., 2017). The effective measurement depth strongly depends on soil water content (SWC), and decreases non-linearly from around 70–80 cm in dry soils to ∼12 cm in saturated soils (Zreda et al., 2012). The CRNP is most sensitive to soil moisture in the upper soil horizon, and this sensitivity decreases exponentially with depth (Schrön et al., 2017).

Measurements of soil moisture with CRNP have been reported in many studies (e.g., Bogena et al., 2013; Hawdon et al., 2014; Lv et al., 2014; McJannet et al., 2014; Rosolem et al., 2014; Heidbüchel et al., 2016; Jana et al., 2016; Schreiner-McGraw et al., 2016; Wang et al., 2018), and around 60% have been carried out in crop or grasslands, 30% in forests and 11% in mixed forest-grassland ecosystems. Only 22% of these studies have been carried out under dry climates, such as semi-arid, and only 4% correspond to dry forests. Thus, there appears to be a gap of CRNP usage in semi-arid forests that alternate between very wet and very dry conditions. This inter-annual variation may strongly affect the effective penetration depth of CRNP, which is a particular challenge for the adequate interpretation of CRNP-derived soil moisture information (Schrön et al., 2017).

This study aims to contribute to filling this experimental gap by means of a dual objective dealing with the comparison between CRNP and capacitance sensors in a semi-arid forest, given their different spatial representativeness for (indirectly) measuring soil moisture content. On the one hand, we aim to analyze how the derived soil moisture from both methodologies is correlated with the environmental variables of the study area. On the other hand, we pursue to study which sensor is better indicating a physiological response to thinning and can therefore be used as a proxy of water availability in managed and unmanaged forests. To achieve this dual objective, the following secondary objectives were assessed: (a) to calibrate and validate CRNP through common procedures; (b) to study the degree of correlation between soil moisture (measured by CRNP or capacitance sensors) with different environmental variables like vegetation transpiration, and (c) to compare the potential explanatory power of CRNP and capacitance sensors when addressing the role of thinning on stand transpiration. To this end, the present work takes advantage of an experimental context that already exists in a pine stand growing under semi-arid conditions, where several measurements in the soil-plant-atmosphere continuum are taken in order to understand the role of thinning on tree-water relations (del Campo et al., 2019b; González-Sanchis et al., 2019).

MATERIALS AND METHODS

Study Site and Forest Treatments

The study was carried out in a semi-arid forest with high tree density, located within the natural park of "La Sierra Calderona" (39°42"N, 0°27"W, altitude: 790 m asl) in the province of Valencia (Spain) (**Figure 1**). The existing vegetation is a young Aleppo pine stand with scattered shrubs (such as *Quercus coccifera*, *Juniperus oxycedrus*, and *Ulex parviflorus*) regenerated after a wildfire occurred in 1992. The climate is Mediterranean, characterized by high temporal rainfall variability and intense droughts (means of annual precipitation and potential evapotranspiration of 342 and 837 mm, respectively); with extreme dry years with cumulated precipitation lower than 150 mm. More information about vegetation, climate, soils and other bio-geographical traits is found in del Campo et al. (2018, 2019b) and González-Sanchis et al. (2019).

No forest management has been carried out since the 1992 wildfire, except for 2012 (between January and October) when a small portion of the forest was managed in the context of an experimental study and a contractor of the Forest Service executed juvenile thinning with shrub clearing. The thinning removed the trees with the smallest diameters and the double-stemmed trees (reduction of 74% of basal area or 94% of tree density) (**Table 1**), trying to achieve a relatively homogeneous forest cover distribution. The experimental design consisted of a representative control plot (C) with no thinning and a contiguous thinned plot (T), each of them having an area of 1,500 m^2. Both plots have similar slope (27.8 vs. 32.0%) and aspect (311° vs. 319° NW). More details about forest structure can be found in del Campo et al. (2018, 2019b) and González-Sanchis et al. (2019).

Measurements

Climatic Variables

Air temperature (T, °C) and relative humidity (RH, %) were measured (CS215, Campbell Sci., Decagon Devices, Pullman,

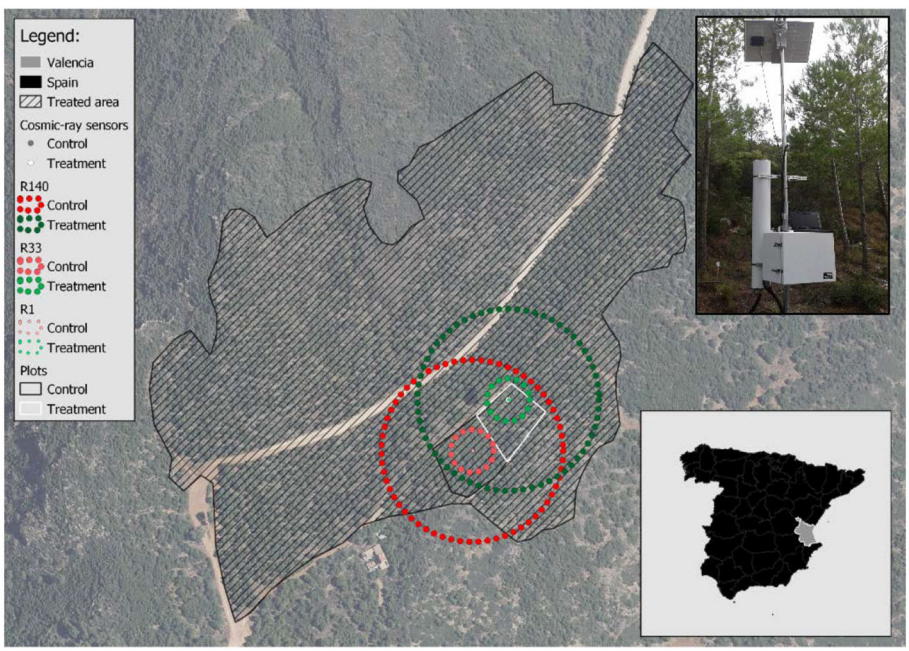

FIGURE 1 | The experimental site within the "Sierra Calderona" Natural Park (Valencia, Spain). The dashed area indicates the treated area in 2012. R1, R33, and R140 indicate soil samplings with radii of 1, 33, and 140 m, respectively. The control and treatment plots are indicated by black and white line, respectively. The picture in the upper right shows one of the CRNP probes.

TABLE 1 | Forest structure metrics (means and standard deviations) in control (C) and treatment (T) for the period between 2014 and 2019.

	T				C			
Year	DBH (cm)		DB (cm)		DBH (cm)		DB (cm)	
	Mean	SD	Mean	SD	Mean	SD	Mean	SD
2014	13.25	5.86	8.59	4.03	10.69	3.89	6.99	3.26
2015	14.09	5.82	9.24	4.09	11.05	4.16	7.71	3.10
2016	14.83	5.31	10.08	4.07	12.08	3.78	7.92	3.28
2017	15.63	5.16	10.78	4.12	12.66	3.84	8.47	3.28
2018	16.42	4.98	11.52	4.21	13.36	3.84	8.94	3.33
2019	17.21	4.85	12.26	4.31	14.06	3.86	9.41	3.39
mean	15.24	5.33	10.41	4.14	12.32	3.89	8.24	3.27

DBH, diameter at breast height; DB, basal diameter at 30 cm height. Tree density in T and C:705 and 11,300 tree ha^{-1}. N, 9 trees per plot.

WA, United States) in each experimental plot at two different heights, one at 2 m above the ground and the other at 6.5 m. Gross Precipitation (Pg, mm) was measured with a tipping-bucket (0.2 mm resolution) at 6 meters above the ground (7852, Davis Instruments Corp., Hayward, CA, United States). The net precipitation (Pn) has been calculated by the difference of Pg minus the canopy interception (It); the canopy interception was estimated to be 16.7 and 36.4% of Pg for T and C, respectively (del Campo et al., 2018). Wind speed (Ws, m s^{-1}) and direction (Wd, °) were obtained using an anemometer (Anemometers 7911, Davis Instruments Corp.), located on the same mast measuring T and RH at 6.5 m above the ground. The sensors were connected to a data-logging unit (CR1000, Campbell Sci., UT, United States) supplemented with two AM16/32B Multiplexers, two SDM-IO16 expansion modules, a solar panel and a 12 V battery. Data was stored every 10 min. Vapor pressure deficit (VPD, kPa) was calculated following standard Equations (1–3) based on T and RH:

$$VPsat = 6.108 \times exp((17.27 \times T)/(T + 273.3)) \quad (1)$$

$$VPair = VPsat \times RH \quad (2)$$

$$VPD = VPsat - VPair \quad (3)$$

Where T is air temperature (°C), VPsat is the air saturated vapor pressure (kPa), VPair is the air vapor pressure (kPa) and VPD is the vapor pressure deficit (kPa).

Soil Moisture

Soil moisture (θ, m^3 m^{-3}) was continuously measured every 10 min, or every 5 s when raining, by means of capacitive probes (EC-5, Decagon Devices Inc., Pullman, WA) connected to a CR1000 data-logger. The EC-5 sensors were installed by digging nine pits per experimental plot (systematically placed), organized into three groups following contour lines (del Campo et al., 2019b). In each group, one of the pits contained two sensors poked horizontally at depths of 15 and 30 cm into the unaltered upslope pit face, whereas in the other two pits one sensor was poked at 15 cm depth (12 EC-5 sensors per plot, 24 EC-5 sensors per experimental site). The pits were regularly placed on a grid of 10 × 10 m to get a good estimate of mean soil moisture (Molina et al., 2014). After installation, the pits were backfilled with the excavated soils and slightly compacted to achieve a similar bulk density as the original, unaltered soil. As already reported in del Campo et al. (2018), a soil-specific calibration was not possible due to the stoniness at the field site, hence we used the standard EC-5 calibration (for mineral soils) in all cases (Detty and McGuire, 2010). For the validation of the CRNP, we considered the weighted θ average for each experimental plot based on the number of probes for each soil depth.

Stand Transpiration

Tree sap flow velocity (Vs, cm h^{-1}) was measured every half hour by the heat ratio method (HRM) (Burgess et al., 2001). Eighteen home-made sap flow sensors were installed in 9 trees per plot [see González-Sanchis et al. (2019) for more details]. The sensors were installed on the upslope side at a height between 0.3 and 1 m. In addition, all sensors were connected to a data logger, a 12 V battery and a solar panel (CR1000, Campbell Sci., UT, United States). Sap flow (S_f) was obtained by calculating sapwood area (Sa, m^{-2}) and up-scaling sap flow velocity (Vs, cm h^{-1}) using the Excel macro provided by Berdanier et al. (2016). Subsequently, S_f was up-scaled to stand transpiration per plot (Tr, mm day^{-1}) by using the number of trees (De, tree m^{-2}) as scalar. We obtained a correction factor (cf) by regressing S_f on Sa ($R^2 >$ 91%) so that the S_f corresponding to the mean sampled tree was corrected to the mean plot tree (del Campo et al., 2019a).

Biomass Calculation at Plot Scale

Total biomass (Tb, kg m^{-2}) was calculated using the allometric Equations (4–8) proposed by Ruiz-Peinado et al. (2011) for *Pinus halepensis*:

$$B_s = 0.0139 \times d^2 \times h \quad (4)$$

$$B_{b7} = \left[3.926 \times \left(d - 27.5\right)\right] \times Z \quad (5)$$

$$B_{b7-2} = 0.00162 \times d^2 \times h \quad (6)$$

$$B_{b2+l} = 0.0844 \times d^2 - 0.0731 \times h^2 \quad (7)$$

$$B_b = 0.155 \times d^2 \quad (8)$$

where B_s is the stem biomass, B_{b7} is the biomass of thick branches (>7 cm of diameter), B_{b7-2} is the biomass of medium branches (between 7 and 2 cm), B_{b2+l} is the biomass of small branches (<2 cm) and leaves, and B_b is the root biomass. d is de tree diameter at 1.30 m, h is tree height in meters and Z is 0 when $d \leq 27.5$ cm, and 1 when $d \geq 27.5$ cm.

Finally, Tb was calculated by summing up the different biomass parts of all trees and dividing this value by the area of each experimental plot.

Cosmic-Ray Neutron Sensors

Two CRNP (CRS-1000, Hydroinnova LLC, Albuquerque, NM, United States) were installed at the study site, one in the thinned (T) plot in January 2017, and the other one in the control (C) plot in June 2019 (**Figure 1**). In summary, the CRNP counts fast neutrons that enter the detector tube as indication for the local fast neutron intensity. The neutron count rate is corrected by the atmospheric pressure (P_{atm}), the absolute water content in the air (Habs), the influence of the incoming neutrons (Inn) and finally, the influence of the amount of vegetation on these neutrons (fveg). For more details about CRNP see Bogena et al. (2013), Heidbüchel et al. (2016), and Zreda et al. (2008). This setup involved two different measurement periods for each experimental plot, January 1st 2017 to October 22th 2019 for the T plot, and June 17th 2019 to October 22th 2019 for the C plot. Therefore, CRNP data was simultaneously measured in both plots during a period of 4 months.

Sampling soil campaigns

The soil characterization at the experimental plots was carried out by collecting soil samples at four points in each plot, distributed along the slope and randomly selected in March 2013. At each point, a metal frame of 25 × 25 cm was used to collect separately the litter layer, the humified organic layer underneath and the top mineral soil layer from 0 to 5 cm. The deeper samples (from 5 to 20 cm and below 20 cm when possible) were taken with a 5 cm diameter helicoidal probe. Soil depth was highly variable from less of 20 cm to more than 70 cm. The samples were weighed, air dried and different fractions were separated by sieving through 2 mm mesh size. Air-dry soil humidity was determined in a subsample by drying at 105°C until constant weight. The larger fraction was separated (by hand) into stones, roots, leaf debris, woody debris and miscellaneous organic fraction. In the fine fraction, we determined soil pH in a 1:2.5 water suspension, inorganic carbonate content by the Bernard calcimeter method (MAPA, 1994), and total organic carbon (TOC) by the Walkey-Black method (Nelson and Sommers, 1982). The litter layer depth of C and T plots was measured at 9 points per plot, randomly distributed along the slope.

For CRNP calibration five soil samples were taken using different procedures. The first two sampling campaigns (T1 and T2) were carried out following the usual calibration procedure suggested by Bogena et al. (2013) which includes 18 extraction points distributed in 3 different circumferences (radius of 1, 33, and 140 m) whose center is CRNP, 6 extraction points per circumference (**Figure 2**). However, since the large volume of rock complicated the sampling procedure, during the rest of the sampling campaigns (T3, C1, and C2) the number of samples was reduced. This reduction was carried out attending to the significant differences between gravimetric humidity of samples from T1 and T2 campaigns. In these sense, sampling campaigns T3, C1, and C2 was carried out by sampling just in those extraction points were no significant differences between gravimetric humidity of T1 and T2 campaigns was observed (**Figure 2B**). As a result, sampling campaigns T3, C1, and C2 used 9 extraction points, while T1 and T2 collected samples at 18 points, both distributed within 3 sampling circumferences. At each sampling circumference, samples were collected in different orientations and depths. In T1 and T2, there were 18 extraction points in all directions (N, NE, NW, S, SE, and SW) and at all depths (0–5, 5–10, 10–15, 15–20, 20–25, 25–30), but for T3, C1, and C2, the direction was also reduced to N, SE, and SW (**Figure 2**).

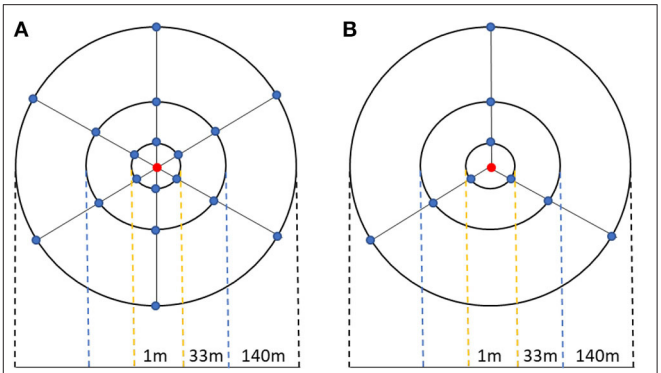

FIGURE 2 | Schematic representation of the soil-sampling campaigns. The red point represent the CRNP probe while the blue ones are the sampling soil locations. **(A)** the calibration procedure described by Heidbüchel et al. (2016) (T1 and T2 samples); **(B)** new calibration procedure used in this study (T3, C1, and C2 samples).

Water equivalent of the belowground hydrogen content pools was obtained by considering composite samples for the six different soil depths from all sample locations (∼2 g of soil from each location) (Heidbüchel et al., 2016). These soil samples were sieved through a 200 µm mesh size, oven-dried for 24 h at 105°C and weighted to determine the gravimetric water content. Subsequently, the soil samples were consecutively heated at 400, 700, and 1,000°C during 24 h to determine the contents of soil organic matter and lattice water. We included an intermediate step (700°C) to account for weight losses due to thermal break-down of carbonates at temperatures above 430°C because of the high carbonate content of the soil. Soil organic matter and root biomass content of each soil sample was obtained from the weight difference between the 105 and 400°C, and lattice water content by the weight difference between 700 and 1,000°C.

Cosmic-ray sensor neutrons correction and calibration

The first step was to correct the mean daily arrival of neutrons by the different equations proposed by Zreda et al. (2012) in order to account for the influence of atmospheric pressure (Equation 9), incoming neutrons (Equation 10) and air water

vapor (Equation 11):

$$N_p\,(t) = N_{raw} \times e^{\left(\frac{P-P_0}{L}\right)} \quad (9)$$

Where N_p is the number of neutrons corrected for atmospheric pressure (P_{atm}) variations. The gross neutron count (N_{raw}) is corrected for day specific air pressure variations, where P (hPa) is the daily pressure and P_0 (hPa) is the reference air pressure, calculated over the complete measurement period, and L is the mass attenuation length for high-energy neutrons (mbar or equivalent in g cm^{-2}) that varies progressively between ∼128 g cm^{-2} at high latitudes and 142 g cm^{-2} at the equator (Desilets and Zreda, 2003). The incoming neutron intensity was obtained from the Neutron Monitor Data Base (NMDB) of Castilla-La Mancha station (CALM), and the number of neutrons was in addition corrected to fluctuations in neutron intensity:

$$N_{pi}\,(t) = N_p \times \frac{Inn_{avg}}{Inn} \quad (10)$$

where N_{pi} is the number of neutrons corrected by the incoming neutron intensity, Inn_{avg} is the average neutron intensity over the measurement period and Inn is the day specific neutron intensity. Finally, the neutron count intensity is corrected for atmospheric humidity:

$$\boldsymbol{N_{pih\,(t)} = N_{pi\,(t)} \times [1 + 0.0054 \times (H - H_0)]} \quad (11)$$

N_{pih} is the number of neutrons corrected for air humidity variations, where H_0 is the average air humidity (g cm^{-3}) over the measurement period and H is the day-specific air humidity value (g cm^{-3}).

Once the incoming neutrons were corrected, these were converted into soil moisture ($O_{(t)}$) by using the following equation and calibration with help of measured soil moisture contents by each sampling campaign (O_g):

$$O_{(t)} = \left\{\left[a_0 \times \left(\frac{N_{pih}(t)}{N_0} - a_1\right)^{-1} - a_2\right] \times \rho_{bd}\right\} - W_L - (SOM + B_R) \quad (12)$$

where ρ_{db} is bulk density (g cm^{-3}),W_L is latice water (W_L, m^3 m^{-3}), SOM is the water equivalent of soil organic matter content (m^3 m^{-3}), B_R is root biomass (B_R, m^3 m^{-3}), $N_{pih}(t)$ is the corrected count neutrons; parameters a_0, a_1, and a_2 are 0.0808, 0.372, and 0.115, respectively, according to Desilets et al. (2010), and N_0 is the parameter to be optimized using *in-situ* soil moisture measurements.

N_0 was obtained from a non-linear optimization, minimizing the Root Mean Square Error (RMSE) between the soil moisture measured in the field (O_g) and calculated soil moisture content ($O_{(t)}$), according Equation 12.

The water content of the raindrops was not considered in the CRNP retrieval as this effect does not belong to the standard procedure, which only accounts for pressure, humidity and incoming neutrons (e.g., Zreda et al., 2012). Furthermore, rainfall events at the study site are not frequent and this study focuses on vegetation effects.

TABLE 2 | Classification according to the water content in the soil.

Sub-periods	Plot	O_{CRNP} (m^{-3} m^{-3})
WT	T	>0.178
TT		0.114–0.178
DT		<0.114
WC	C	>0.157
TC		0.1–0.157
DC		<0.1

WT and WC, are the periods when the soil is wet for thinned (T) and control (C) plots; TT and TC, are the periods when the soil is neither too wet nor too dry; DT and DC, are the ranges of water content in the soil for each class.

Considering the biomass effect

The correction for the influence of vegetation on the CRNP data was performed at each plot following Baatz et al. (2015). To that end, first, the number of base neutrons corresponding to total biomass (**Table 2**) was calculated according to Equation 13:

$$\boldsymbol{N_{0'} = -r \times Tb + N_{0,\,BWE=0}} \quad (13)$$

where r is the ratio between the hourly neutron count and the kg of water equivalent in the biomass (BWE, kg m^{-2}) and $N_{0,BWE=0}$ is the number of base neutrons when total biomass (Tb; kg m^{-2}) is not considered. Section Biomass calculation at plot scale specifies how Tb is calculated.

Subsequently, $N_{pihv(t)}$ was obtained by multiplying N_{pih} by a correction factor (f_{veg}) calculated as follows (Equation 14):

$$\boldsymbol{N_{pihv(t)} = N_{pih\,(t)} \times f_{veg} = N_{pih\,(t)} \times \left(1 - r/N_{0,BWE=0} \times BWE\right)^{-1}} \quad (14)$$

Finally, when N_{pihv} was obtained, the optimization of N_0 was carried out again, to check for the variation of RMSE when using the vegetation correction factor (f_{veg}).

Cosmic-Ray Neutron Probe Validation

The validation was carried out by comparing the CRNP and capacitance soil moisture estimations using two methodologies, the RMSE and the Kling-Gupta efficiency (KGE) (Gupta et al., 2009; Kling et al., 2012). This validation was independently developed for T and C plots, not only for the whole time series, but also for three different sub-periods. The semi-arid climate conditions of the study site are expected to provide soil moisture values within a wide range, which includes wet and very dry periods. Schreiner-McGraw et al. (2016) also studied the performance of CRNP in a semi-arid environment, and in spite of the good results, the worst performance was observed in wet and dry periods. Hence, with the aim to assess the CSR performance under very different soil moisture conditions, this study divides the soil moisture dataset according to the capacitance soil moisture values. This classification in sub-periods was done for each plot, by using the machine learning methodology K-Nearest Neighbor (kNN) (Cristianini and Shawe-Taylor, 2000; Chirici et al., 2016). As a result, three sub-groups (k = 3) per plot were

TABLE 3 | Summary of environmental variables for the complete time series period (A) and when considering the three sub-periods according to the kNN classification (W, wet period; T, transition period; D, dry period).

Period	Plot	Tr (mm)	Θ_{CRNP} (m^3m^{-3})	Θ_g (m^3m^{-3})	T (°C)	P_g (mm)	P_n (mm)	VPD (kPa)	RAD ($W\ m^{-2}$)
A	T	0.29	0.15	0.14	14.70	303.7	252.8	5.50	190.33
W		0.31	0.23	0.20	10.29	148.22	123.47	3.24	123.54
T		0.32	0.16	0.14	13.72	107.21	113.6	5.46	196.94
D		0.22	0.12	0.10	17.97	18.72	15.6	6.53	208.04
A	C	0.55	0.14	0.11	14.60	303.7	193	5.49	190.33
W		0.61	0.23	0.18	10.07	127.7	81.24	3.28	122.74
T		0.67	0.16	0.12	12.50	146.6	93.2	4.74	179.53
D		0.41	0.10	0.08	18.01	29	18.5	6.82	218.69

Plot: T is the treated area and C is the control area. Soil water content is presented as daily average for each sensor, Θ_{CNRP} for CRNP and Θ_g for capacitance probe. T (°C): is the average daily air temperature for the complete measurement period. P_g is the average annual gross precipitation. P_n is the average annual net precipitation. VPD is the average daily vapor pressure deficit. RAD is the average daily solar radiation.

obtained: wet (WT, WC), transition (TT, TC) and dry (DT, DC) (see **Table 2**).

The RMSE was calculated as the difference in soil moisture value measured by the capacitance method (Og) and the CRNP (O_{CRNP}):

$$RMSE = \sqrt{\frac{\sum_{i=1}^{n} (\Theta gi - \Theta CRNi)^2}{n}} \quad (15)$$

KGE uses the difference in the ratio between the modeled (O_{CRNP}) and observed (Og) soil moisture values ($\beta = O_{CRNP}/Og$) and the variability in their respective time series [$\gamma = (\sigma_{CRNP}/\mu_{CRNP})/(\sigma_g/\mu_g)$]; where modeled values are those obtained as described in sections Cosmic-ray sensor neutrons correction and calibration and Considering the biomass effect with the CRNP, and the observed ones are the mean values from the capacitance probes for each experimental plot. KGE was obtained according to Equation (16), where r is the correlation coefficient between modeled and observed values.

$$KGE = 1 - \sqrt{(r-1)^2 + (\beta - 1)^2 + (\gamma - 1)^2} \quad (16)$$

KGE ranges between 0 and 1, and 1 indicates a perfect result. The CRNP effective depth of each probe was calculated according Franz et al. (2012).

Statistical Analyses

The assumption of a Gaussian distribution of the different datasets was studied using a Kolmogorov-Smirnov (K-S) test with the Lilliefors correction. To analyze the correlations between soil moisture (capacitance and CRNP) and the environmental variables, a Pearson correlation test was done for variables for which the null hypothesis that these variables are Gaussian distributed was not rejected. On the other hand, a Spearman non-parametric correlation test was done for the variables for which the null hypothesis that they are Gaussian distributed was rejected. Both tests, Pearson and Sperman, were carried out at $p < 0.05$ level. Subsequently, the temporal lag between O and the environmental variables was studied by daily misplacing the environmental variables until the time lag with the greatest correlation and significance was found.

Finally, the technique of boosted regression trees (BRT) was used to study the capability of each methodology to register a physiological response to thinning. The BRT study was carried out following the methodology proposed by Elith et al. (2008), using as dependent variable stand transpiration and grouping the rest of the environmental variables in order to describe their importance: atmosphere (T, VPD, RAD, Ws), precipitation (P_g, P_n) and finally soil moisture (O_{CRNP} and O_g).

RESULTS

Environmental Conditions During the Study Period

The environmental variables showed a typical Mediterranean semi-arid climate with an average annual gross precipitation (P_g) over the measurement period of 304 mm, where 253 and 193 mm correspond to the net precipitation (P_n) for T and C plots, respectively. The average annual temperature was almost 15°C, with annual minimum and maximum daily averages of −1.3 and 30.3°C, and the annual average vapor pressure deficit is 0.97 kPa (see **Table 3**).

The measurements of soil moisture with capacitance probes during the study period (January 2017- December 2019) were significantly different between C and T, where T showed higher values ($p < 0.05$; see **Figure 3**). Likewise, the complete time series of stand transpiration (Tr) showed significant differences between C and T plots ($p < 0.05$), with higher values now for the C-plot and mean transpiration values of 0.63 vs. 0.39 mm day^{-1} for C and T, respectively.

Soil Characteristics

Tables 4, **5** show soil characteristics of the experimental plots. Soil has a loamy-clay texture with a high content of stones and a well-developed organic horizon (litter layer) mainly composed

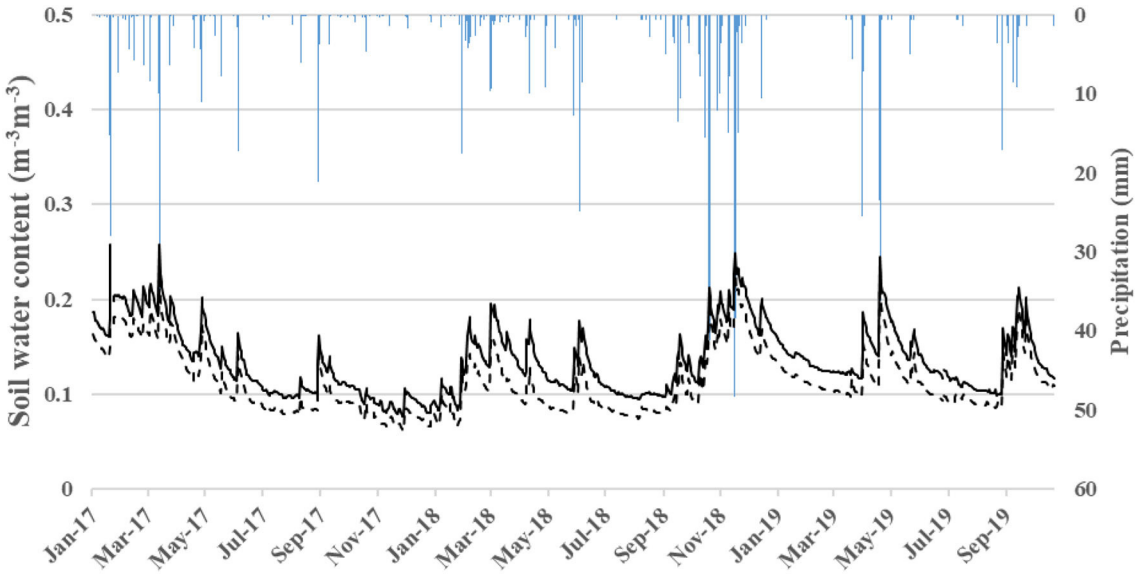

FIGURE 3 | Soil water content measured with capacitance probes in each plot. Blue bars represent the daily gross precipitation. Black line is the soil water content measured with capacitance probes in T-Plot. Black dashed line is the soil water content measured with capacitance probes in C-Plot.

TABLE 4 | Soil characteristics at the experimental plots.

Soil layer	Stoniness %	Root percentage %	$CaCO_3$ %	pH	TOC %
Litter layer	7.0 ± 8.3	0			
F/H layer	54.9 ± 23.4	0			
0–5 cm	33.7 ± 19.5	0.16 ± 0.06	27.9 ± 11.0	8.24 ± 0.17	5.1 ± 2.3
5–20 cm	20.3 ± 18.1	0.29 ± 0.13	34.2 ± 14.0	8.33 ± 0.17	2.3 ± 1.4
20–30 cm	5.3 ± 4.8	0.050 ± 0.04	39.6 ± 9.1	8.49 ± 0.06	1.0 ± 0.4
>30 cm	21.7 ± 4.3	0.01 ± 0.01	50.3 ± 0.8	8.51 ± 0.00	0.6 ± 0.1

TOC, Total Organic Carbon.

TABLE 5 | Organic material (g m^{-2}), depth (mm) and presence (%) of the litter layer in both experimental plots.

Plot	Depth	Presence	Woody debris	Miscelaneous > 2 mm	Needles	<2mm
T	2.9 ± 6.3	60	2,780 ± 2579	1,825 ± 513	506 ± 609	2,858 ± 2,529
C	3.1 ± 5.2	98	159 ± 131	1,573 ± 948	320 ± 385	1,323 ± 1,165

Values are mean ± standard deviation (n = 4 in each plot).

by needles. The C plot shows a more extended and thicker litter layer than the T plot (see **Table 5**).

Calibration and Validation of the CRNP

Calibration for Both Plots

The calibration was carried out following Bogena et al. (2013), with and without applying the vegetation correction factor, f_{veg} (see **Table 6**). The vegetation effect appears not to be significant in the T plot, where in spite of showing lower N_0 and RMSE, no significant differences were observed when comparing the O_{CRNP} values with and without the application of f_{veg}. On the contrary, the f_{veg} in the C plot did significantly decrease O_{CRNP} measurements (mean O_{CRNP} with and without f_{veg} of 0.144 and 0.216 $m^{-3}m^{-3}$, respectively) (see **Figure 4** and **Table 6**). The general validation of CRNP although showed a slight overestimation of O, resulted in KGE values of 0.84 and 0.40 for T and C plots, respectively, without applying the vegetation correction factor. When applying f_{veg}, the performance was not affected for the T plot, but the KGE value of C increased to 0.75 (see **Table 7** and **Figure 5**). Likewise, the validation for the

TABLE 6 | Soil characteristics and variables for CRNP calibration.

Date	Plot	S.S.	$\Theta_g + SOM_{Lw}$	P_{atm}	ρ_{bd}	Inn	a_0	a_1	a_2	No f_{veg}		Yes f_{veg}	
										N_0	RMSE	N_0	RMSE
3/20/17	T	T1	0.246	930	1.19	71.99	0.081	0.372	0.115	3795.0	0.013	3541.3	0.013
3/07/18		T2	0.270										
7/17/19		T3	0.167										
7/17/19	C	C1	0.193		1.23					1781.4	0.021	1030.4	0.007
9/19/19		C2	0.265										

Date is the soil sampling day. Plot: T is the treated plot and C is the control plot. S.S is the sampling soil in wet conditions (T1, T2, and C2) and dry conditions (T3 y C1). $\Theta_g + SOM_{Lw}$ is the gravimetric water + equivalent water of SOM+lattice water ($m^3\ m^{-3}$). P_{atm} is the average atmospheric pressure of all serie (hPa). ρ_{bd} is the bulk density for each plot ($g\ cm^{-3}$). Inn is the average of incoming neutrons from CALM station. a0, a1, and a2 are the parameters obtained by Desilets et al. (2010). N_0: optimized parameter. Yes and No f_{veg}: application or not of the vegetation correction. N_0: optimized parameter. RMSE is the root mean square error about the calibration with sampling point in each plot ($m^3\ m^{-3}$).

3 different sub-periods (wet, transition, and dry) showed only a significant effect of the vegetation correction factor for the control plot improving the performance (see **Table 7**).

As expected, the partial validation using the different sub-periods provided the lowest CRNP measurement accuracy during extreme soil water conditions (dry and wet) at both plots, whereas the best performance was found during the transition period (see **Table 6**). O_g at the different soil depths (15 cm, 30 cm and its averaged value) and Θ_{CRNP} were significantly correlated, for both plots, and for the wet and transition sub-periods. However, for the dry sub-period, O_{g-C} values did not show significant correlations. On the other hand, the effective depth of both CRNP ranged from 18.5 to 28.0 cm for T plot, and from 18.1 to 29.9 cm for C plot, indicating its suitability to be compared to O_g at 15 and 30 cm depth.

Relationship Between Soil Moisture (EC-5 and CRNP), Environmental Variables, and Stand Transpiration

According to **Table 8**, the general pattern of correlation among Θ and environmental variables was quite similar for both measurement methods when considering the entire measurement period, although the CRNP showed stronger correlations with the environmental variables. Likewise, the temporal dynamics of the three different EC-5 sensors was very similar in both plots and during all periods and sub-periods (see **Table 8**).

Correlations among O and the environmental variables varied between plots and sub-periods, but generally, T plot showed a better agreement between both methodologies than C plot. In this sense, O_{CRNP-T} only behaved differently during the dry period, where it was significantly correlated to all the environmental variables, while O_{g-T} was only correlated to air temperature, VPD, and RAD. On the contrary, O_{CRNP-C} and O_{g-C}, showed different relationships with the environmental variables during the three sub-periods (see **Table 8**).

CRNP measurements showed a significant correlation with RH and VPD at both plots and during all sub-periods, while EC-5 measurements were not always significantly related to these variables, and when they were, the sign of the correlation was not always the same. During the dry sub-period, CRNP for the control and thinning plots showed opposite relationships with RH (positive) and VPD (negative) than capacitance. Gross precipitation revealed a positive relationship with O_{CRNP-T} during all sub-periods, while the relationship with O_{CRNP-C} was only significant during the dry sub-period (see **Table 8**).

CRNP and EC-5 showed a positive relationship with Tr, if we consider the complete time series. It shows that higher soil moisture content is associated with higher transpiration. However, for the wet sub-period both soil moisture measurement techniques showed a negative correlation with transpiration. It seems that in the wet subperiod soil moisture availability is not a limitation for transpiration anymore. For the transition sub-period transpiration showed only a positive correlation with O_{g-C}, and no significant correlations with O_{g-T}, O_{CRNP-T}, and O_{CRNP-C}. The dry period also showed different behavior between measurement methods and plots. While O_{CRNP-C} did not have a significant correlation with transpiration, O_{g-C} was highly correlated to transpiration. On the contrary, O_{CRNP-T} was positively correlated to Tr, and so were O_{g-T} average at 15 cm, while 30 cm measures were negatively correlated to Tr (see **Table 8**).

Finally, the temporal lag of the correlation between O and the environmental variables, including transpiration at the C and T plots, was analyzed. According to this analysis, there was a differential behavior between plots and methodologies. The T plot showed similar temporal lags for both measurement techniques, while the C plot showed earlier responses of CRNP soil moisture to temperature, VPD and RH than soil moisture measured by capacitance probes. On the contrary, the response to cumulated precipitation (4 days) and solar radiation (1 day) was the same for the different plots and measurement techniques. No temporal lag of Tr nor RH was observed at T plot when using either CRNP or capacitance, while C plot showed a temporal lag of 1 day with Tr, and 0 and 1 day for RH with O_{CRNP-C} and O_{g-C}, respectively.

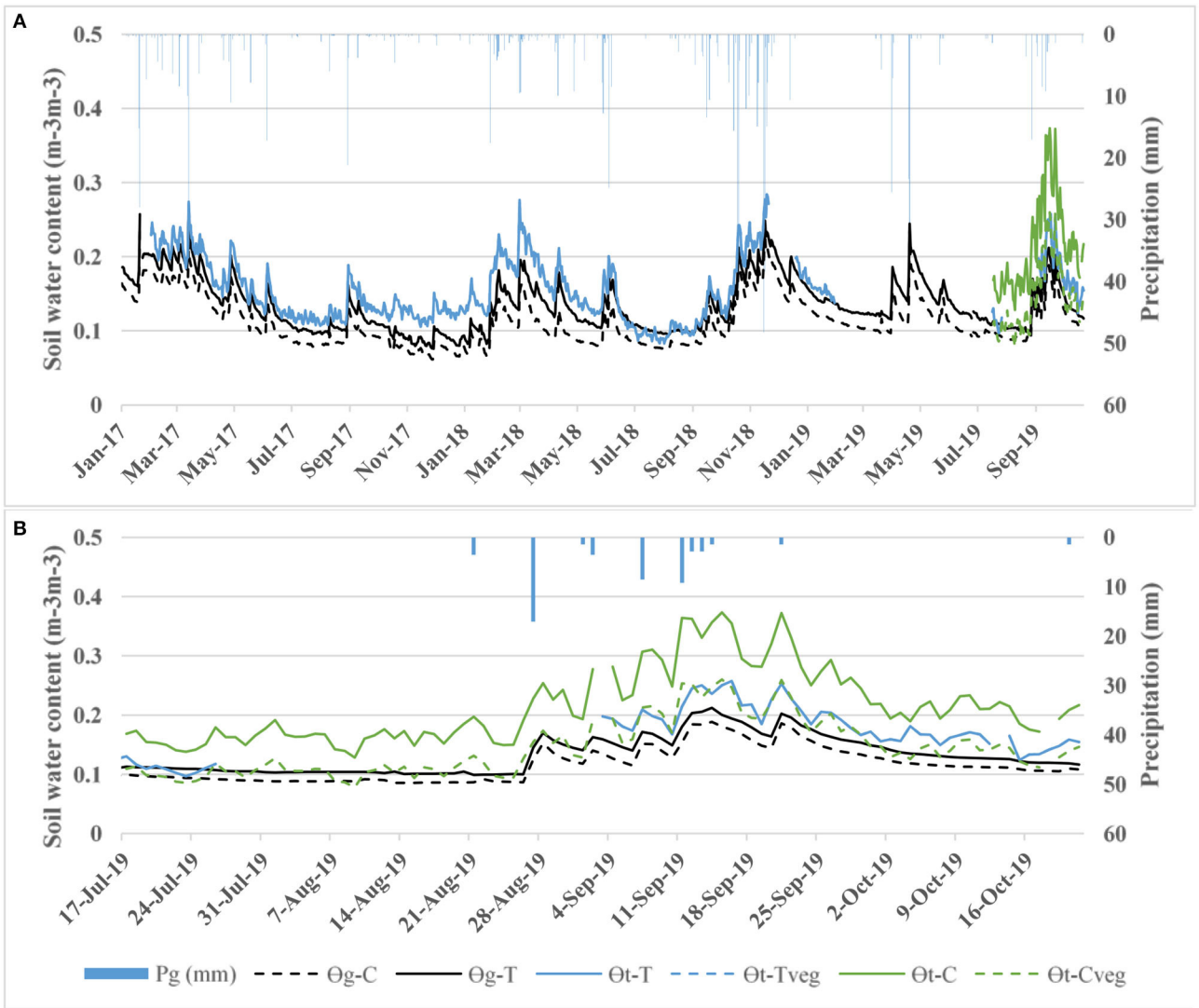

FIGURE 4 | (A) Comparison of soil water content values measured using capacitance probes (O_{g-T} and O_{g-C}) and CRNP at the T and C plots with the application of the vegetation correction factor f_{veg} ($O_{CRNP-Tfveg}$ and $O_{CRNP-Cfveg}$) and without the application of the vegetation correction factor (O_{CRNP-T} and O_{CRNP-C}). **(B)** Zoom of date comparison between plots.

TABLE 7 | Validation results of both CRNP probes.

Plot	Period	Without f_{veg}					With f_{veg}				
		Θ_{CRNP}	Θ_g	RMSE	R^2	KGE	Θ_{CRNP}	Θ_g	RMSE	R^2	KGE
T	A	0.15	0.14	0.03	0.86	0.84	0.15	0.14	0.03	0.86	0.84
	W	0.23	0.2	0.03	0.53	0.02	0.23	0.2	0.03	0.53	0.02
	T	0.16	0.14	0.03	0.63	0.48	0.16	0.14	0.03	0.63	0.48
	D	0.12	0.1	0.02	0.01	−0.06	0.12	0.1	0.02	0.01	−0.06
C	A	0.22	0.11	0.11	0.88	0.4	0.14	0.11	0.04	0.88	0.75
	W	0.33	0.18	0.16	0.75	−0.6	0.23	0.18	0.06	0.76	0.07
	T	0.24	0.12	0.12	0.68	0.16	0.16	0.12	0.04	0.68	0.63
	D	0.16	0.08	0.07	0.04	−0.03	0.1	0.08	0.02	0.04	0.01

Θ_t, Soil water content measured with CSR probe ($m^3\ m^{-3}$). Θ_g, Soil water content measured with capacitance probes ($m^3\ m^{-3}$). RMSE, root mean squared error ($m^3\ m^{-3}$). R^2, linear regression coefficient. KGE, Kling-Gupta efficiency value. A, complete period; W, wet period; T, Transition period; D, Dry period.

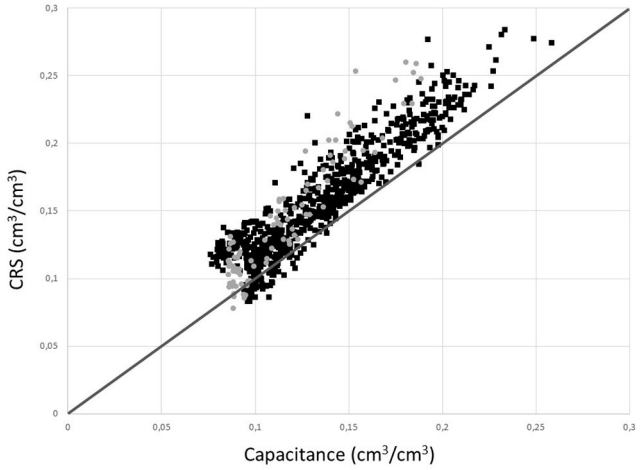

FIGURE 5 | Comparison of soil water content values measured using capacitance and CRNP probes at the T (black squares) and C (gray circles) plots after the vegetation correction.

Importance of Thinning Application on Stand Transpiration

The previous results pointed to a similar performance of CRNP and EC-5, although CRNP was consistently more affected by the atmospheric variables than EC-5. However, concerning stand transpiration, the difference between the two measurement techniques was larger, mainly for the control plot. With the aim to analyze this difference, two transpiration models were studied considering either CRNP or EC-5 measurements by means of boosted regression trees (BRT). To this end, transpiration was used as a dependent variable to determine the importance of thinning, and two different transpiration models were generated, one with O_{CRNP} values and another one with O_g values as independent variables together with meteorological and rainfall partitioning variables. The BRT models showed different degrees of fitting (CRNP-model: cv-correlation = 0.96, R^2 = 0.92; EC-5-model: cv-correlation = 0.97, R^2 = 0.95) that indicated a good performance of both models. The relative importance of each variable is shown in **Table 9**. The results showed once again the similarity between both measurement techniques, although a slightly stronger correlation in the CRNP-model with atmospheric variables was confirmed, as the CRNP-model relied more on atmosphere and less on soil moisture and thinning than the EC-5-model.

DISCUSSION

This study focused on the performance of CRNP for obtaining reliable soil moisture values in a semi-arid forest, and on the sensitivity of CRNP to forest management by comparing thinned and non-thinned forest experimental plots.

In general, calibration (RMSE: 0.013 and 0.007 m^3 m^{-3} for T and C plots, respectively) and validation (KGE: 0.84 and 0.75 for T and C plots, respectively) procedures showed values that indicate a good performance of CRNP, which in the case of the non-thinned forest (C-plot), improved with the application of the vegetation correction factor. These values are comparable to those obtained in other studies such as that of Bogena et al. (2013); they obtained a RMSE value of 0.025 m^3 m^{-3} for a forested area, and Li et al. (2019), who found a RMSE value of 0.025 m^3 m^{-3} for a semi-arid environment, or Lv et al. (2014), who found RMSE values varying between 0.011 and 0.023 m^3 m^{-3} for a humid forest (gross precipitation of 950 mm y^{-1}). However, when comparing O_{CRNP} to O_g, there is a general overestimation by CRNP that can be attributed to the influence of biomass and the different measurement depths of both methodologies and changes under the different subperiods (**Figure 5**). In fact, a closer analysis by dividing the time series into O sub-periods revealed that this general performance decreases when dealing with extreme O values. In this sense, this study found the CRNP performed worst in both wet and dry sub-periods, where O was overestimated in both plots, and even reaching negative KGE values for the T plot. Schreiner-McGraw et al. (2016) studied the performance of CRNP in two semi-arid catchments and also obtained the worst results during dry and wet periods. As stated by these authors, the worst performance under extreme soil water conditions could indicate that O_{CRNP} has a tendency to dry less quickly during some rainfall events, and therefore overestimate O values. Schreiner-McGraw et al. (2016) attributed this behavior to landscape features such as nearby channels and their associated zones of soil water convergence that remain wetter than areas measured by the distributed sensor network. However, in our case, there are no nearby channels, but a thick and continuous litter layer (**Table 4**) capable of retaining a significant amount of water, and probably increasing O_{CRNP} values (Heidbüchel et al., 2016). In agreement with this, O_{CRNP} values showed more and stronger correlations with the environmental variables, which probably indicate the effect of this litter layer, whose wetting-drying dynamics are more strongly related to precipitation than deeper soil layers (Bogena et al., 2013). During the dry sub-period, these relationships were even opposite to those of the capacitance sensor, and therefore closer to the faster wetting-drying dynamics of surface water (see **Table 8**).

The different measurement depths of the EC-5 sensors and CRNP could also explain this performance variation. The effective penetration depth of CRNP is dynamic, as it strongly depends on SWC, decreasing non-linearly from around 76 cm in dry soils to ∼12 cm in saturated soils (Zreda et al., 2012). Our data showed an effective penetration depth between 18 and 30 cm. These values are very close to the location of the capacitance probes, and therefore, the correlations between O_{CRNP} and O_g at 15 and 30 cm depth might not be significantly different. Accordingly, when comparing these values (O_{CRNP} and O_g, at 15 and 30 cm depth), no clear differences were found between them. The CRNP is most sensitive to soil moisture within the first centimeters and this sensitivity decreases non-linearly with increasing depth (Schrön et al., 2017). Correspondingly, the shallower capacitance measurements (O_g at 15 cm) always showed the strongest relationship with O_{CRNP} (see **Table 8**), but the correlation with O_g at 30 cm was also significant at both plots and during all sub-periods, except for the dry sub-period,

TABLE 8 | Matrix of Spearman correlations among soil water content measured with capacitance (O_g) and CSR (O_{CRNP}) probes and the environmental variables at thinned (T) and control (C) plots: Average temperature (Tm), Gross precipitation (Pg), accumulated precipitation (Pac), vapor pressure deficit (VPD), radiation (RAD), and stand transpiration (Tr).

Period	Plot	Variables		P_g	T	RH	VPD	RAD	Tr	O_g			Effective depth (cm)
										15 cm	30 cm	Average.	
A	C	O_{CRNP}		0.38**	−0.54**	0.63**	−0.71**	−0.67**	0.38**	0.87**	0.87**	0.87**	25.6 ± 4.6
		O_g	Average	0.34**	−0.36**	0.33*	−0.41**	−0.48**	0.34**				
			15 cm	0.33**	−0.35**	0.33*	−0.41**	−0.48**	0.34**				
			30 cm	0.32**	−0.39**	0.33*	−0.43**	−0.49**	0.36**				
	T	O_{CRNP}		0.27**	−0.57**	0.21**	−0.50**	−0.41**	.25**	0.89**	0.87**	0.89**	24.4 ± 4.0
		O_g	Average	0.20**	−0.40**	0.15**	−0.34**	−0.25**	0.24**				
			15 cm	0.19**	−0.39**	0.15**	−0.33**	−0.24**	0.27**				
			30 cm	0.23**	−0.42**	0.15**	−0.35**	−0.27**	0.16**				
W	C	O_{CRNP}		–	–	0.92*	−0.88**	–	−0.82**	0.87**	0.85**	0.87**	18.1 ± 1.5
		O_g	Average	0.64*	–	0.85**	−0.88**	–	−0.82**				
			15 cm	0.66*	–	0.86**	−0.88**	–	−0.82**				
			30 cm	–	–	0.84**	−0.87**	–	−0.81**				
	T	O_{CRNP}		0.53**	–	0.60**	−0.20*	−0.43**	−0.46**	0.66**	0.66**	0.72**	18.5 ± 1.1
		O_g	Average	0.26**	–	0.31*	–	−0.22**	–				
			15 cm	0.20*	–	0.25**	−0.19*	–	–				
			30 cm	0.30**	–	0.37**	–	−0.48**	−0.34**				
T	C	O_{CRNP}		–	–	0.47**	−0.35*	–	–	0.81**	0.81**	0.81**	23.4 ± 2.7
		O_g	Average	–	0.44**	–	–	0.47**	0.34*				
			15 cm	–	0.45**	–	–	0.50**	0.33*				
			30 cm	–	0.40**	–	–	0.40**	0.38*				
	T	O_{CRNP}		0.22**	−0.44**	0.22**	−0.41**	−0.31**	–	0.78**	0.72**	0.81**	23.0 ± 2.2
		O_g	Average	0.17**	−0.27**	0.15**	−0.27**	−0.25**	–				
			15 cm	0.12**	−0.24**	0.13**	−0.24**	−0.21**	–				
			30 cm	0.25**	−0.30**	0.17**	−0.30**	−0.30**	–				
D	C	O_{CRNP}		0.35*	−0.70**	0.73**	−0.80**	−0.58**	–	–	–	–	29.9 ± 1.9
		O_g	Average	–	0.36*	−0.49**	0.40*	0.38*	0.98**				
			15 cm	–	0.37*	−0.47**	0.38*	0.37*	0.97**				
			30 cm	–	–	−0.54**	0.43**	.038*	0.99**				
	T	O_{CRNP}		0.21**	−0.64**	0.11*	−0.53**	−0.49**	0.31**	0.20**	0.46**	0.29*	28.0 ± 2.0
		O_g	Average	–	0.29**	–	0.15**	0.49**	0.29**				
			15 cm	–	0.33**	–	0.18**	0.48**	0.45**				
			30 cm	–	0.23**	–	0.11*	0.47**	–				

**Sig. < 0.01; **Sig. <0.05; –no significant. A, complete study period; T, transition days; W, wet days; D, dry days. Effective depth of CRNP probes is expressed as mean ± standard deviation.*

where the behavior changes in both plots. During this period, the effective measurement depth of CRNP also reached its maximum value (28 cm), and in the case of the T plot, the correlation with O_g at 30 cm was higher than that of at 15 cm. Regarding the C plot, despite the fact that the maximum of the CRNP effective penetration depth was also 30 cm, no significant correlations were found for any of the measurement depths. This fact could be attributed to the low O_g values registered during this period (0.09 ± 0.004 m^3 m^{-3}), although this value was just slightly lower than that of T plot during the same sub-period, where the correlations were significant. Thus, the reason could not be the low soil moisture but difference in processes between the two plots. Looking closely to the comparison between both methodologies during this sub-period, O_{CRNP-T} and O_{gT} show a very similar variation, while on the contrary, in spite of the short measurement period, O_{CRNP-C} shows a standard deviation (0.012 m^3 m^{-3}) one order of magnitude higher than O_{gC} (0.004 m^3 m^{-3}). Schreiner-McGraw et al. (2016) and Heidbüchel et al.

TABLE 9 | Relative importance (%) of the different variables considered in the transpiration models using boosted regression trees.

Variable	CRNP-model	Capacitance-model
Soil water content	3.0	5.7
Thinning treatment	51.4	53.4
Precipitation	0.0	0.0
Atmosphere	37.5	34.4

Both models considered the same independent variables (except for rainfall partitioning, estimated for each plot) but used different data for the soil water content: either CRNP-model and Capacitance-model.

(2016) reported that the CRNP measurement signal is more strongly influenced by the first 5 soil cm depth, and Lv et al. (2014) reported a more sensitive response of CRNP to small rainfall events than soil moisture measured by TDR at 10 cm depth. Thus, soil water dynamics that CRNP is registering might probably correspond more to the upper 5–10 cm, including the litter layer, whose wetting-drying dynamics is significantly faster than that of deeper soil layers [see Bogena et al. (2013)].

When analyzing the performance of CRNP with and without forest management, a differential behavior of both plots was observed. In general, O_{CRNP} from T plot adjusted better to O_g values, and was not significantly affected by the vegetation correction factor. This is related to the low biomass present in the T plot (1.4 kg m^{-2}). According to Hawdon et al. (2014), values lower than 5 kg m^{-2} may have little influence on the neutron count rate. Higher biomass also implies higher water interception, which also affects the neutron count and may cause an overestimation of soil moisture (Heidbüchel et al., 2016; Jakobi et al., 2018). The litter layer of the C plot is practically continuous and thicker than that for the T plot (**Table 4**), and may have a similar effect as rainfall interception, increasing the possibility of overestimating O after rainfall events. Hence, the better performance of CRNP-T could be attributed to the biomass effect (both, soil and vegetation), but also to spatial and temporal representativeness. As shown in **Figure 1**, the T plot includes most of CRNP horizontal footprint, whereas for the C-plot this is <50% (Schrön et al., 2017). Thus, since the C plot capacitance probes were installed only within this non-thinned area, comparing these values with those that include other conditions (CRNP-C) could undermine actual CRNP performance. In terms of temporal representativeness, the time series of the T plot was significantly longer than that of the C plot, which only covered the summer period. Furthermore, during this study period a high number of rainy days occurred with high soil moisture conditions in which, as seen before, the CRNP showed its worst performance. Therefore, the investigation period of the C plot may have been too short to adequately test the performance of the CRNP.

Despite the fact that the performance of the CRNP-C was worse than for CRNP-T, O_{CRNP-C} values showed a higher correlation with environmental variables than O_{CRNP-T}. This difference between the plots could be due to the influence of biomass on the fast neutron intensity (e.g., by rainfall interception of the vegetation or the litter layer), i.e., by hydrogen pools other than soil moisture (Heidbüchel et al., 2016). However, on the other hand, O_{g-C} values were more correlated to environmental variables than O_{g-T}. In this case, biomass may also be responsible of this difference, but in a different way. Soil moisture in semi-arid forests is an important water source for the vegetation development (Castillo et al., 2003; Seeger et al., 2004), and changes in this variable highly affect the forest dynamic. In the same way, changes in vegetation (thinning) affect rainfall partitioning and tree water consumption, which directly affects soil moisture. This effect of forest management has already been pointed out by del Campo et al. (2019b) for this study site, as the thinning had significantly influenced rainfall partitioning by reducing water interception and increasing soil moisture. Thus, this effect together with the significant decrease in tree water competition increases soil water availability and therefore decreases the dependence of soil moisture dynamics on environmental variables.

The stand transpiration also showed different correlations with soil moisture for the plots, and in this case the C-plot is the one that showed significant relationships with both O_{CRNP-T} and O_{g-T}, while in the T plot the correlations were weaker or non-significant, such as during the transition sub-period. Furthermore, in contrast to the environmental variables, the highest correlation values were found for O_{g-C} in this case, probably due to the biomass influence on the CRNP and the different measurement support of the two methods both in terms of footprint and penetration depth. During the dry and transition sub-periods, O_{CRNP-C} did not show significant correlations with transpiration, while O_{g-C} values (at both measurement depths) were significantly correlated with transpiration. Probably, during these sub-periods, the trees were significantly transpiring more water from deeper soil layers, which would enhance the relationship with O_g at 15–30 cm.

Furthermore, the differential behavior of both soil moisture measurement methods when comparing between plots is probably related to the significant effect of thinning on rainfall partitioning, as already observed by del Campo et al. (2019b). The increase of O together with the diminishing of tree water competition allows trees to transpire whenever the combination between water availability and atmospheric demand is present. This relationship is possibly due to the fragile equilibrium between water supply and demand that exists in semi-arid forests, where the water in the soil is what limits the transpiration (del Campo et al., 2014). Nevertheless, since O is higher in the T plot, the limiting role of the soil is significantly reduced, and therefore the tree water consumption would be more related to the atmospheric demand.

CONCLUSIONS

The results presented in this study confirmed the overall reliability of CRNP in obtaining soil moisture in semi-arid forests, but a lower measurement accuracy was found for very dry and wet conditions. Furthermore, our results also show the relevance of spatial heterogeneity within the measuring

footprint to the CRNP measurements. Since the CRNP has a much larger measuring volume compared to capacitance sensors, this difference must be considered when comparing the two measurements. Furthermore, it has to be considered that in forests other processes, e.g., the interception of the litter layer or the vegetation, can influence the comparison with capacitance-based *in-situ* sensors. The CRNP showed stronger relationships with environmental variables (T, HR, VPD, and RAD), which were attributed to the effect of the soil litter layer together with the high sensitivity of the CRNP to the top 5–10 cm of soil. Both soil moisture measurement methods showed a similar correlation with tree transpiration, only insignificantly stronger for capacitance sensors. Both methods were affected by biomass management, although probably to different extents. The capacity sensors were directly affected by the increasing net precipitation following forest management, while the CRNP was also affected by precipitation interception, as this reduced neutron intensity leading to overestimation of soil moisture during rainfall and shortly afterwards. In either case, both methods were able to capture the physiological response of trees to thinning, which was reflected in the increase in the correlation between transpiration and soil moisture.

DATA AVAILABILITY STATEMENT

The datasets presented in this article are not readily available because the data set is available under request, and its usage is condition to previous agreements such as paper authorship. Requests to access the datasets should be directed to María González-Sanchis, macgonsa@gmail.com.

AUTHOR CONTRIBUTIONS

MG-S analyzed the results and wrote the paper. JG-S calibrated the CRS and helped with to build the paper and with the analysis of the results. AM contributed writing the paper and analyzing the results. AL and IB did the soil sampling campaigns and analyzed the samples. ER worked with the raw data and did the first calibration approach. HB, and H-JH contributed with both CRS probes and usage and calibration support. AC is the coordinator of the whole project. All authors contributed to the article and approved the submitted version.

FUNDING

This study is a component of the research projects: E-HIDROMED (CGL2014-58127-C3) and CEHYRFO-MED (CGL2017-86839-C3-2-R) funded by the Spanish Ministry of Science and Innovation and FEDER funds, and LIFE17 CCA/ES/000063 RESILIENTFORESTS. AM is beneficiary of an APOSTD fellowship (APOSTD/2019/111) funded by the Generalitat Valenciana.

ACKNOWLEDGMENTS

The authors are grateful to TERENO funded by the Helmholtz Association and the Federal Ministry of Education and Research of Germany for providing the CRNP, the Valencia Regional Government (CMAAUV, Generalitat Valenciana), the VAERSA staff, the Natural Park staff and the communal authority of Serra for their support and allowing the use of the Natural Park experimental forest.

REFERENCES

Andreasen, M., Jensen, K. H., Desilets, D., Franz, T. E., Zreda, M. G., and Bogena, H. R. (2017). Status and perspectives of the cosmic-ray neutron method for soil moisture estimation and other environmental science applications. *Vadose Zone J.* 16:86. doi: 10.2136/vzj2017.04.0086

Baatz, R., Bogena, H. R., Hendricks Franssen, H. J., Huisman, J. A., Montzka, C., and Vereecken, H. (2015). An empirical vegetation correction for soil water content quantification using cosmic ray probes. *Water Resour. Res.* 51, 2030–2046. doi: 10.1002/2014WR016443

Bell, D. M., Bradford, J. B., and Lauenroth, W. K. (2014). Mountain landscapes offer few opportunities for high-elevation tree species migration. *Glob. Chang. Biol.* 20, 1441–1451. doi: 10.1111/gcb.12504

Berdanier, A. B., Miniat, C. F., and Clark, J. S. (2016). Predictive models for radial sap flux variation in coniferous, diffuse-porous and ring-porous temperate trees. *Tree Physiol.* 36, 932–941. doi: 10.1093/treephys/tpw027

Bogena, H. R., Huisman, J. A., Baatz, R., Hendricks Franssen, H.-J., and Vereecken, H. (2013). Accuracy of the cosmic-ray soil water content probe in humid forest ecosystems: the worst case scenario: cosmic-ray probe in humid forested ecosystems. *Water Resour. Res.* 49, 5778–5791. doi: 10.1002/wrcr.20463

Bogena, H. R., Huisman, J. A., Güntner, A., Hübner, C., Kusche, J., Jonard, F., et al. (2015): Emerging methods for non-invasive sensing of soil moisture dynamics from field to catchment scale: a review. *WIREs Water* 2, 635–647. doi: 10.1002/wat2.1097

Brown, P., and Wu, R. (2005). Climate and disturbance forcing of episodic tree recruitment in a southwestern ponderosa pine landscape. *Ecology* 86, 3030–3038. doi: 10.1890/05-0034

Burgess, S. S. O., Adams, M. A., Turner, N. C., Beverly, C. R., Ong, C. K., Khan, A. A. H., et al. (2001). An improved heat pulse method to measure low and reverse rates of sap flow in woody plants. *Tree Physiol.* 21, 589–598. doi: 10.1093/treephys/21.9.589

Castillo, V. M., Gomez-Plaza, A., and Martinez-Mena, M. (2003). The role of antecedent soil water content in the runoff response of semiarid catchments: a simulation approach. *J. Hydrol.* 284, 114–130. doi: 10.1016/S0022-1694(03)00264-6

Chirici, G., Mura, M., McInerney, D., Py, N., Tomppo, E. O., Waser, L. T., et al. (2016). A meta-analysis and review of the literature on the k-nearest neighbors technique for forestry applications that use remotely sensed data. *Remote Sens. Environ.* 176, 282–294. doi: 10.1016/j.rse.2016.02.001

Coops, C. N., Waring, R. H., and Law, B. E. (2005). Assessing the past and future distribution and productivity of ponderosa pine in the Pacific Northwest using a process model, 3-PG. *Ecol. Modell.* 183, 107–124. doi: 10.1016/j.ecolmodel.2004.08.002

Cristianini, N., and Shawe-Taylor, J. (2000). *An Introduction to Support Vector Machines and Other Kernel-based Learning Methods, 1st Edn.* New York, NY: Cambridge University Press.

del Campo, A. D., Fernandes, T. J. G., and Molina, A. J. (2014). Hydrology-oriented (adaptive) silviculture in a semiarid pine plantation: how much can be modified the water cycle through forest management? *Eur. J. For. Res.* 133, 879–894. doi: 10.1007/s10342-014-0805-7

del Campo, A. D., González-Sanchis, M., García-Prats, A., Ceacero, C. J., and Lull, C. (2019a). The impact of adaptive forest management on water fluxes and growth dynamics in a water-limited low-biomass oak coppice. *Agric. Forest Meteorol.* 264, 266–282. doi: 10.1016/j.agrformet.2018.10.016

del Campo, A. D., González-Sanchis, M., Lidón, A., Ceacero, C. J., and García-Prats, A. (2018). Rainfall partitioning after thinning in two low-biomass semiarid forests: impact of meteorological variables and forest structure on the effectiveness of water-oriented treatments. *J. Hydrol.* 565, 74–86. doi: 10.1016/j.jhydrol.2018.08.013

del Campo, A. D., González-Sanchis, M., Lidón, A., García-Prats, A., Lull, C., Bautista, I., et al. (2017). "Ecohydrological-based forest management in semi-arid climate," in *Ecosystem Services of Headwater Catchments* (Cham: Springer), 45–57.

del Campo, A. D., González-Sanchis, M., Molina, A. J., García-Prats, A., Ceacero, C. J., and Bautista, I. (2019b). Effectiveness of water-oriented thinning in two semiarid forests: The redistribution of increased net rainfall into soil water, drainage and runoff. *For. Ecol. Manage.* 438, 163–175. doi: 10.1016/j.foreco.2019.02.020

Desilets, D., and Zreda, M. (2003). Spatial and temporal distribution of secondary cosmic-ray nucleon intensities and applications to in-situ cosmogenic dating. *Earth Planet. Sci. Lett.* 206, 21–42. doi: 10.1016/S0012-821X(02)01088-9

Desilets, D., Zreda, M., and Ferré T. (2010). Nature's neutron probe: Land surface hydrology at an elusive scale with cosmic rays. *Water Resour. Res.* 46, 21–42. doi: 10.1029/2009WR008726

Detty, J. M., and McGuire, K. J. (2010). Threshold changes in storm runoff generation at a till-mantled headwater catchment: threshold changes in runoff generation. *Water Resour. Res*. 46, 1–15. doi: 10.1029/2009WR008102

Elith, J., Leathwick, J. R., and Hastie, T. (2008). A working guide to boosted regression trees. *J. Anim. Ecol.* 77, 802–813. doi: 10.1111/j.1365-2656.2008.01390.x

Flinn, K. M., and Marks, P. L. (2007). Agricultural legacies in forest environments: Tree communities, soil properties, and light availability. *Ecol. Appl*. 17, 452–463. doi: 10.1890/05-1963

Franz, T. E., Zreda, M., Rosolem, R., and Ferré, T. P. A. (2012). Field validation of a cosmic-ray neutron sensor using a distributed sensor network. *Vadose Zone J.* 11, 46–56. doi: 10.2136/vzj2012.0046

Gardner, C. M. K., Dean, T. J., and Cooper, J. D. (1998). Soil water content measurement with a high-frequency capacitance sensor. *J. Agric. Eng. Res.* 71, 395–403. doi: 10.1006/jaer.1998.0338

González-Sanchis, M., Ruiz-Pérez, G., Del Campo, A. D., Garcia-Prats, A., Francés, F., and Lull, C. (2019). Managing low productive forests at catchment scale: considering water, biomass and fire risk to achieve economic feasibility. *J. Environ. Manage.* 231, 653–665. doi: 10.1016/j.jenvman.2018.10.078

Gupta, H. V., Kling, H., Yilmaz, K. K., and Martinez, G. F. (2009). Decomposition of the mean squared error and NSE performance criteria: implications for improving hydrological modelling. *J. Hydrol.* 377, 80–91. doi: 10.1016/j.jhydrol.2009.08.003

Hawdon, A., McJannet, D., and Wallace, J. (2014). Calibration and correction procedures for cosmic-ray neutron soil moisture probes located across Australia. *Water Resour. Res.* 50, 5029–5043. doi: 10.1002/2013WR015138

Hawley, M.E., Jackson, T. J., and McCuen, R. H. (1983). Surface soil moisture variation on small agricultural watersheds. *J. Hydrol*. 62, 179–200. doi: 10.1016/0022-1694(83)90102-6

Heidbüchel, I., Güntner, A., and Blume, T. (2016). Use of cosmic-ray neutron sensors for soil moisture monitoring in forests. *Hydrol. Earth Syst. Sci.* 20, 1269–1288. doi: 10.5194/hess-20-1269-2016

Jakobi, J., Huisman, J. A., Vereecken, H., Diekkrüger, B., and Bogena H. R. (2018). Cosmic-ray neutron sensing for simultaneous soil water content and biomass quantification in drought conditions. *Water Resour. Res*. 54, 7383–7402. doi: 10.1029/2018WR022692

Jana, R. B., Ershadi, A., and McCabe, M. (2016). Examining the relationship between intermediate-scale soil moisture and terrestrial evaporation within a semi-arid grassland. *Hydrol. Earth Syst. Sci.* 20, 3987–4004. doi: 10.5194/hess-2016-186

Kling, H., Fuchs, M., and Paulin, M. (2012). Runoff conditions in the upper danube basin under an ensemble of climate change scenarios. *J. Hydrol.* 424-425, 264–277. doi: 10.1016/j.jhydrol.2012.01.011

Li, D., Schrön, M., Köhli, M., Bogena, H., Weimar, J., Jiménez Bello, M. A., et al. (2019). Can drip irrigation be scheduled with cosmic-ray neutron sensing? *Vadose Zone J.* 18:190053. doi: 10.2136/vzj2019.05.0053

Lv, L., Franz, T. E., Robinson, D. A., and Jones, S. B. (2014). Measured and modeled soil moisture compared with cosmic-ray neutron probe estimates in a mixed forest. *Vadose Zone J.* 13, 1–13. doi: 10.2136/vzj2014.06.0077

MAPA (1994) *Métodos Oficiales de Análisis de Suelos y Aguas*. Madrid: Ministerio de Agricultura, Pesca y Alimentación.

Mast, J., Fule, P., Moore, M., Covington, W., and and, Waltz, A. (1999). Restoration of presettlement age structure of an Arizona ponderosa pine forest. *Ecol. Appl.* 9, 228–239. doi: 10.1890/1051-0761(1999)0090228:ROPASO2.0.CO;2

McJannet, D., Franz, T., Hawdon, A., Boadle, D., Baker, B., Almeida, A., et al. (2014). Field testing of the universal calibration function for determination of soil moisture with cosmic-ray neutrons. *Water Resour. Res*. 50, 5235–5248. doi: 10.1002/2014WR015513

Molina, A. J., Latron, J., Rubio, C. M., Gallart, F., and Llorens, P. (2014). Spatio-temporal variability of soil water content on the local scale in a Mediterranean mountain area (Vallcebre, North Eastern Spain). How different spatio-temporal scales reflect mean soil water content. *J. Hydrol.* 516, 182–192. doi: 10.1016/j.jhydrol.2014.01.040

Nelson, D. W., and Sommers, L. E. (1982). "Total carbon, organic carbon and organic matter," in *Methods of Soil Analysis. Part 2. Chemical and Mineralogical Properties* (Madison: American Society of Agronomy), 539–579.

Rehfeldt, G., Jaquish, B., Saenz-Romero, C., Joyce, D., Leites, L., St Clair, J., et al. (2014). Comparative genetic responses to climate in the varieties of Pinus ponderosa and Pseudotsuga menziesii: reforestation. *For. Ecol. Manage*. 324,147–157. doi: 10.1016/j.foreco.2014.02.040

Rodríguez-Iturbe, I., and Porporato, A. (2007). *Ecohydrology of Water-Controlled Ecosystems*: *Soil Moisture and Plant Dynamics*. Cambridge: Cambridge University Press

Rosolem, R., Hoar, T., Arellano, A., Anderson, J. L., Shuttleworth, W. J., Zeng, X., et al. (2014). Translating aboveground cosmic-ray neutron intensity to high-frequency soil moisture profiles at sub-kilometer scale. *Hydrol. Earth Syst. Sci*. 18, 4363–4379. doi: 10.5194/hess-18-4363-2014

Ruiz-Peinado, R., del Rio, M., and Montero, G. (2011). New models for estimating the carbon sink capacity of Spanish softwood species. *Forest Syst*. 20, 176–188. doi: 10.5424/fs/2011201-11643

Savage, M., Brown, P., and Feddema, J. (1996). The role of climate in a pine forest regeneration pulse in the southwestern United States. *Ecoscience* 3, 310–318. doi: 10.1080/11956860.1996.11682348

Schreiner-McGraw, A. P., Vivoni, E. R., Mascaro, G., and Franz, T. E. (2016). Closing the water balance with cosmic-ray soil moisture measurements and assessing their relation to evapotranspiration in two semiarid watersheds. *Hydrol. Earth Syst. Sci*. 20, 329–345. doi: 10.5194/hess-20-329-2016

Schrön, M., Köhli, M., Scheiffele, L., Iwema, J., Bogena, H. R., Lv, L., et al. (2017). Improving calibration and validation of cosmic-ray neutron sensors in the light of spatial sensitivity. *Hydrol. Earth Syst. Sci*. 21, 5009–5030. doi: 10.5194/hess-21-5009-2017

Seeger, M., Errea, M. P., Begueria, S., Arnáez, J., Mart, I. C., and Garcia-Ruiz, J. M. (2004). Catchment soil moisture and rainfall characteristics as determinant factors for discharge/suspended sediment hysteretic loops in a small headwater catchment in the Spanish Pyrenees. *J. Hydrol.* 288, 299–311. doi: 10.1016/j.jhydrol.2003.10.012

Seyfried, M. S., and Murdock, M. D. (2001). Response of a new soil water sensor to variable soil, water content, and temperature. *Soil Sci. Soc. Am. J.* 65, 28–34. doi: 10.2136/sssaj2001.65128x

Topp, G. C., and Ferré, T. P. (2006). "Measuring soil water content," in *En Encyclopedia of Hydrological Sciences* Vol. 2, ed M. G. Anderson (Chichester: Wiley). p. 1077–1088.

van Mantgem, P. J., Stephenson, N. L., Byrne, J. C., Daniels, L. D., Franklin, J. F., Fulé, P. Z., et al. (2009). Widespread increase of tree mortality rates in the western United States. *Science* 323, 521–524. doi: 10.1126/science.1165000

Vereecken, H., Huisman, J. A., Bogena, H. R., Vanderborght, J., Vrugt, J. A., and Hopmans, J. W. (2008). On the value of soil moisture measurements in vadose zone hydrology. *A review. Water Resour. Res*. 44:W00D06. doi: 10.1029/2008WR006829

Wang, E., Smith, C. J., Macdonald, B. C., Hunt, J. R., Xing, H., Denmead, O. T., et al. (2018). Making sense of cosmic-ray soil moisture measurements and eddy covariance data with regard to crop water use and field water balance. *Agr. Water Manag*. 204, 271–280. doi: 10.1016/j.agwat.2018.04.017

Williams, A. P., Allen, C. D., Macalady, A. K., Griffin, D., Woodhouse, C. A., Meko, D. M., et al. (2013). Temperature as a potent driver of regional forest drought stress and tree mortality. *Nat. Clim. Change* 3, 292–297. doi: 10.1038/nclimate1693

Zreda, M., Desilets, D., Ferré, T. P. A., and Scott, R. L. (2008). Measuring soil moisture content non-invasively at intermediate spatial scale using cosmic-ray neutrons. *Geophys. Res. Lett.* 35:L21402. doi: 10.1029/2008GL035655

Zreda, M., Shuttleworth, W. J., Zeng, X., Zweck, C., Desilets, D., Franz, T., et al. (2012). COSMOS: the cosmic-ray soil moisture observing system. *Hydrol. Earth Syst. Sci.* 16, 4079–4099. doi: 10.5194/hess-16-4079-2012

Conflict of Interest: The authors declare that the research was conducted in the absence of any commercial or financial relationships that could be construed as a potential conflict of interest.

frontiers in Water

ORIGINAL RESEARCH
published: 28 January 2021
doi: 10.3389/frwa.2020.544847

Soil Moisture and Air Humidity Dependence of the Above-Ground Cosmic-Ray Neutron Intensity

Markus Köhli[1,2*], *Jannis Weimar*[1], *Martin Schrön*[3], *Roland Baatz*[4†] *and Ulrich Schmidt*[1]

[1] Physikalisches Institut, Heidelberg University, Heidelberg, Germany, [2] Physikalisches Institut, University of Bonn, Bonn, Germany, [3] Helmholtz Centre for Environmental Research-UFZ, Leipzig, Germany, [4] Agrosphere (IBG-3), Forschungszentrum Jülich GmbH, Jülich, Germany

Investigations of neutron transport through air and soil by Monte Carlo simulations led to major advancements toward a precise interpretation of measurements; they particularly improved the understanding of the cosmic-ray neutron footprint. Up to now, the conversion of soil moisture to a detectable neutron count rate has relied mainly on the equation presented by Desilets and Zreda in 2010. While in general a hyperbolic expression can be derived from theoretical considerations, their empiric parameterization needs to be revised for two reasons. Firstly, a rigorous mathematical treatment reveals that the values of the four parameters are ambiguous because their values are not independent. We found a three-parameter equation with unambiguous values of the parameters that is equivalent in any other respect to the four-parameter equation. Secondly, high-resolution Monte-Carlo simulations revealed a systematic deviation of the count rate to soil moisture relation especially for extremely dry conditions as well as very humid conditions. That is a hint that a smaller contribution to the intensity was forgotten or not adequately treated by the conventional approach. Investigating the above-ground neutron flux through a broadly based Monte-Carlo simulation campaign revealed a more detailed understanding of different contributions to this signal, especially targeting air humidity corrections. The packages MCNP and URANOS were used to derive a function able to describe the respective dependencies, including the effect of different hydrogen pools and the detector-specific response function. The new relationship has been tested at two exemplary measurement sites, and its remarkable performance allows for a promising prospect of more comprehensive data quality in the future.

Keywords: Monte Carlo, neutron, soil moisture, air humidity, cosmic-ray neutron sensing, MCNP, URANOS

OPEN ACCESS

Edited by:
Jianzhi Dong,
United States Department of Agriculture, United States

Reviewed by:
Andreas Güntner,
Helmholtz Centre Potsdam, Germany
Tyson Ochsner,
Oklahoma State University, United States
Nolwenn Lesparre,
Université de Strasbourg, France
Trenton Franz,
University of Nebraska-Lincoln, United States

***Correspondence:**
Markus Köhli
koehli@physi.uni-heidelberg.de

†ORCID:
Roland Baatz
orcid.org/0000-0001-5481-0904

Specialty section:
This article was submitted to Water and Hydrocomplexity, a section of the journal Frontiers in Water

Received: *22 March 2020*
Accepted: *30 November 2020*
Published: *28 January 2021*

Citation:
Köhli M, Weimar J, Schrön M, Baatz R and Schmidt U (2021) Soil Moisture and Air Humidity Dependence of the Above-Ground Cosmic-Ray Neutron Intensity. Front. Water 2:544847. doi: 10.3389/frwa.2020.544847

1. INTRODUCTION

Techniques for determining the environmental water content are mostly bound to local instrumentation or remote sensing products, neither of which meet the typical correlation lengths for soil moisture. This lack of spatial coverage makes the interpretation of available data difficult (Vereecken et al., 2008), and it is called the intermediate scale gap (Robinson et al., 2008). The method of Cosmic-Ray Neutron Sensing (CRNS) (Kodama et al., 1985; Zreda et al., 2008; Desilets, 2012) is a promising tool for hydrological and environmental applications, such as irrigation (Li et al., 2019), water resource management (Franz et al., 2016), and predictions

of hydrological extremes like floods, droughts, and snow height measurements (Schattan et al., 2017, 2019). Its non-invasive nature in combination with a horizontal footprint radius in the order of 200 m (Köhli et al., 2015; Schrön et al., 2017) extending down to 75 cm (Desilets and Zreda, 2013) makes it attractive for hydrological modeling (Shuttleworth et al., 2013) and a large variety of hydrological applications. Moreover, the CRNS technique is increasingly applied in arid to semi-arid climates to support farming, irrigation, and hydro- and meteo services. CRNS is based on the principle that neutrons in the epithermal-to-fast energy range (1–10^5 eV) are highly sensitive to hydrogen, which turns neutron detectors into efficient proxies for changes of the environmental water content. It follows an inverse relationship between the above-ground epithermal-to-fast cosmic-ray neutron intensity N and the surrounding amount of hydrogen atoms, i.e., predominantly the volumetric water content θ (cm^3/cm^3). The originally proposed N_0 method by Desilets et al. (2010)

$$\theta(N) = \frac{a_0}{N/N_0 - a_1} - a_2 \tag{1}$$

included the fitting parameters a_i. Bogena et al. (2013) further suggested to multiply it with the dry soil bulk density ϱ_{bd} in order to convert gravimetric to volumetric moisture. N has to be corrected for air pressure and incoming cosmic-ray variation, leading to the quantity N_{pi}. A third correction factor $C_h = 1 + 0.00054\,h$ is used to account for the water vapor in the air column above the sensor (Rosolem et al., 2013). One free calibration parameter N_0 represents the intensity over dry soil at a reference location (Zreda et al., 2012). This transfer function from neutrons to soil moisture, however, has been developed for homogeneous soil and under idealized conditions, while its parameters were validated empirically from only a few measurements.

To date, many studies were carried out for finding a sensor calibration routine and to compare the performance to conventional instruments (Rivera Villarreyes et al., 2011; Franz et al., 2012a; Almeida et al., 2014; Coopersmith et al., 2014; Hawdon et al., 2014). The authors found a good agreement between measured neutron flux and soil moisture determinations. However, it was reported that unexplained features in the CRNS data could not be described by the Desilets equation (Desilets et al., 2010). Some authors explained the deviations by additional hydrogen pools or hydrological uncertainties (Franz et al., 2013a; Baatz et al., 2014; Baroni and Oswald, 2015). Others tried to fit the parameters of the hyperbola according to their data (Rivera Villarreyes et al., 2011; Lv et al., 2014; Heidbüchel et al., 2016; Sigouin and Si, 2016), which achieved a better correlation at the cost of site-specific calibrations. In their overview, Iwema et al. (2015) provided a comparison between existing $N(\theta)$ methods, especially at the Santa Rita site used in this work as well, finding that there is no conclusive solution for soil moisture retrieval. As shown in Rosolem et al. (2013), the Desilets equation remains not steep enough to consequently follow the change in intensity, particularly for dry conditions with soil moisture below $10\%_{\mathrm{Vol}}$.

The CRNS probe is usually mounted 1–2 m above the ground surface and equipped with two detection units—one bare counter for determining the thermal neutron flux and one counter enclosed by a moderator of 25 mm polyethylene. This makes the system most suited for rate changes in the epithermal-to-fast energy range. The energy sensitivity of the detector, the so-called response function, extends, however, into the thermal as well as the fast neutron regime (Köhli et al., 2018). Therefore, the moderated detector is partly sensitive to high energy neutrons, which partly accounts for the "road effect" (Schrön et al., 2018). It also suffers from the thermal neutron contamination that constitutes up to 20% of its signal. Both categories exhibit a different and much smaller dependence on the environmental hydrogen content than epithermal-to-fast neutrons. Desilets et al. (2010) and Andreasen et al. (2016), therefore, already suggested to disentangle the signals to provide a higher contrast. Although recent studies tried to make use of spectral information (Baatz et al., 2015; Tian et al., 2016) by comparing the two signals, the correlation between both signals and different environmental conditions is yet to be investigated in detail.

To assess the complex nature of neutron interactions, Monte-Carlo-based n-body simulations have proven to be the only efficient tool to support and interpret neutron observations in hydrology (Desilets et al., 2006; McKinney et al., 2006; Desilets and Zreda, 2013; Franz et al., 2013a; Shuttleworth et al., 2013). The first calculations for typical environmental conditions have been carried out by Zreda et al. (2008) in simplified domains using the MCNPX code (Waters et al., 2007). More precise calculations regarding the CRNS footprint for various scenarios with homogeneous domains have shown the complex neutron transport conditions (Köhli et al., 2015; Schrön et al., 2017).

Since the previously recognized approach is often based on site-specific parameters and shows weaknesses under dry conditions, we will fundamentally revisit the search for the relationship between water content and neutron count rate. The aim is to find a function that is as generally valid as possible, which combines all physically relevant processes, and which, generally formulated, gets by with as few free parameters as possible. In this context, we look at the relationship between neutrons and soil moisture as well as air humidity.

2. METHODS

The scope of the paper is to develop an analytical intensity relation for various environmental conditions. The general shape of such a function is motivated theoretically and parameterized. With the help of neutron transport simulations, this model is fitted to the synthetic data sets and finally evaluated using timeseries from field sites.

The simulation toolkits used in this study are MCNP 6.2 (Werner et al., 2018) and URANOS (Köhli et al., 2015). MCNP (**M**onte **C**arlo **N**-**P**article) is a general-purpose software that can simulate the propagation and interaction of neutrons, electrons, protons, pions, and others. Versions until MCNP4 (Briesmeister, 2000) were capable of simulating neutrons up to 20 MeV. Since the release of MCNPX (Waters

et al., 2007), it is capable to simulate the propagation of particles in the Earth's atmosphere by extension of the energy range for many isotopes up to 150 MeV and some to GeV by using the continuously improved Cascade-Exciton Model (CEM) (Gudima et al., 1983) and the Los Alamos Quark-Gluon String Model (LAQGSM) (Gudima et al., 2001). MCNPX in particular was used in several studies to understand the CRNS signal (Desilets, 2012; Rosolem et al., 2013; Andreasen et al., 2016). With version 6 (Werner et al., 2018), the MCNPX branch was merged into the main development line featuring an optional cosmic-ray source (McKinney, 2013). The Monte Carlo code URANOS (**U**ltra **Ra**pid **N**eutron-**O**nly **S**imulation) was developed at the Physikalisches Institut, Heidelberg University, in collaboration with the UFZ Leipzig. This code has been specifically tailored to the needs of the CRNS method. It is based on a voxel engine and excludes any particles other than neutrons replacing them with effective models. Thereby, URANOS is a computationally efficient code that allows us to simulate the large environmental setups typically found in the context of CRNS on standard desktop computers. It uses the validated near-ground cosmic-ray neutron spectrum by Sato (2016). The code was employed for CRNS footprint revision by Köhli et al. (2015) and Schrön et al. (2017), in roving (Schrön et al., 2018) and irrigation studies (Li et al., 2019) as well as understanding the signal for snow height measurements (Schattan et al., 2019).

MCNP allows us to exchange the standard physics interaction cross-sections and also the use of different high-energy models. In this study, the standard databases ENDF/B-VII.1 (Chadwick et al., 2011) and ENDF/B-VIII.0 (Brown et al., 2018) were employed as well as JEFF 3.2 (Koning et al., 2011) and JENDL-4/HE (High Energy) (Shibata et al., 2011). URANOS couples to a combination of the ENDF/B-VII.1 and JENDL/HE 2007 (Watanabe et al., 2011) database. This JENDL/High Energy database includes cross-sections up to 3 GeV, but the data above 150 MeV were simply evaluated by JAM (Niita, 2002), an intra-nuclear cascade model. As this model leads to larger deviations for highest energies, in the JENDL-4.0/High Energy release the limit was set back to 200 MeV. This database was evaluated by CCONE (Iwamoto et al., 2016), which is a more sophisticated model compared to INCL (Boudard et al., 2013) and JAM but with many adjustable parameters based on experimental data.

The use of both toolkits enables the simulation of a wide range of typical environmental conditions, which have different effects at different stages of neutron transport. In MCNP we included the most relevant particles participating in the generation of hadrons, that is neutrons, protons, pions, and muons. We also implemented their typical energy spectra in order to achieve a representative spectrum. Protons are much less abundant at sea level, but they produce on average three neutrons. Muons are responsible for only a few percent of the neutron production; however, their attenuation length is twice as long.

The air medium consists of 78%$_{\mathrm{Vol}}$ nitrogen, 21%$_{\mathrm{Vol}}$ oxygen, and 1%$_{\mathrm{Vol}}$ argon usually at a pressure of 1,020 mbar. The soil extends to a depth of 1.6 m and the air to 1,000 m. The vertical dimensions are chosen to cover the tracks for the relevant above-ground flux to at least 99.9%. Both soil and air are typically represented by planes of infinite extension, which can have subdomains, either to create an in-depth density profile or to add specific entities like water or a detector. The soil consists of 50%$_{\mathrm{Vol}}$ solids and a scalable amount of H_2O. The solid domain is comprised of 75%$_{\mathrm{Vol}}$ SiO_2 and 25%$_{\mathrm{Vol}}$ Al_2O_3 at a compound density of 2.86 g/cm^3. Thus, the total densities vary from 1.43 to 1.93 g/cm^3 for 0%$_{\mathrm{Vol}}$ and 50%$_{\mathrm{Vol}}$ soil moisture, respectively. Chemical constituents regarding rock types are not relevant for the characteristics in the epithermal regime (Franz et al., 2012a; Zreda et al., 2012); however, the amount of chemically bound water in rocks lies in the order of a few percent. Cutoff rigidity and air pressure variations have not been studied and require an independent treatment, the latter being also analyzed in Köhli et al. (2015).

The input spectrum used in this work relies on the cosmic-ray propagation models by Sato and Niita (2006) and Sato et al. (2008), which are based on PHITS (Iwase et al., 2002) and PARMA (Sato et al., 2008). The latest version (Sato, 2015) provides an energy- and angle-dependent spectrum of cosmic-ray neutrons for a variety of altitudes, cutoff-rigidities, solar modulation potentials, and surface conditions. These simulations have been validated with various independent measurements, i.e., Goldhagen et al. (2004) and Gordon et al. (2004), at different altitudes and locations on Earth. Moreover, the analytical formulations of the spectra turned out to be effective in use for subsequent calculations. The presented energy-dependent flux $\phi(E)$ is described by a mean basic spectrum ϕ_{B} and a modifier f_{G} for the geometry of the interface, which is defined by the ratio in comparison to a hypothetical spectrum of a semi-infinite atmosphere. In order to take into account air humidity effects, spectra were released at a height of usually 450 and 650 m for the simulations with atmospheric gradients.

3. THEORETICAL UNDERSTANDING

In order to support the analytical relationship derived later in this work (15), we discuss and merge the basic theoretical concepts behind neutron transport and interaction.

3.1. Spatial Transport

It is important to realize that the diffusive spatial transport of epithermal neutrons in air follows an exponential law, which mainly determines the influence of air on neutrons. Considering a point source in an infinite medium, the integral version of the transport equation (Beckurts and Wirtz, 1964) reduces to a description of the radial flux $\Phi(r)$:

$$\Phi(r) = \underbrace{Q\frac{e^{-\Sigma_t r}}{4\pi r^2}}_{\text{transient} := \Phi_{\mathrm{tr}}} + \underbrace{\int \Sigma_s \Phi(r') \frac{e^{-\Sigma_t |r-r'|}}{4\pi (r-r')^2}\, \mathrm{d}V'}_{\text{diffusive transport} := \Phi_{\mathrm{dt}}}, \qquad (2)$$

with Σ_t being the total cross section and Σ_s the scattering cross section for changes from $E \longrightarrow E'$ in the volume $\mathrm{d}V'$. The first term describes the direct "geometric" transport without any collision from a source of strength Q to a surface proportional to r^2. At larger distances the integration of the second term leads to

the asymptotic solution of

$$\Phi_{\mathrm{dt}}(r) \approx \frac{e^{-\kappa r}}{r}, \tag{3}$$

with κ being a function of the ratio of the cross sections. The derivation can be found in Glasstone and Edlund (1952). In systems of weak absorption the absorption cross section Σ_a is much smaller than Σ_s. In other words the total cross section Σ_t is approximately the scattering cross section Σ_s and κ can be written as

$$\kappa^2 = 3\Sigma_a\Sigma_t. \tag{4}$$

In general such terms have to fulfill the diffusion equation, which can be described by a transport equation for the neutron balance in a specific volume:

$$\mathrm{div}\,\Phi + \Sigma_a\Phi = S. \tag{5}$$

Hence, in order to describe a plane or a volume source, Φ has to be described by terms for which the integration over the total volume in spherical coordinates $\mathrm{d}V = r^2 \sin\vartheta\,\mathrm{d}\vartheta\,\mathrm{d}\phi\mathrm{d}r$ converges. Therefore, terms in Φ involving $\exp(-r)/r^n$ fulfill the norm $\|\cdot\|_{\mathcal{L}^1}$ for $n \leq 2$. In the case of (2) with $\Phi \propto \exp(-r)/r^2$ and $\Phi \propto \exp(-r)/r$ this is satisfied. In general, solutions in the form of

$$\Phi(r) = \sum_i S_i \frac{e^{-r/L_1^{(i)}}}{r^{1+e^{-r/a_2^{(i)}}}} \tag{6}$$

can also be allowed within individual parameters describing a diffusion length $L_1^{(i)}$ and absorption-to-scattering ratios $a_1^{(i)}$ and overall source contributions S_i, for example, for different energies. For a simple diffusion approach the resulting transport equation can characterize Φ by a sum of exponential functions. Such has been found in Köhli et al. (2015) and Schrön et al. (2017) with two terms, one describing a long-range transport from high energy neutrons mainly over the air and a second describing the transient near-field contribution. For a more complex configuration with a two-medium interface, a spectral range for the source emission energies and the detector acceptance energy and an exponentially described volume source there is no simple general solution using Fermi Age transport theory; nevertheless, the exponential range dependency of the footprint can be motivated by the approach presented here.

3.2. Intensity Relation

The mean logarithmic reduction of the neutron energy E per collision, ξ, is an important quantity in slowing-down theory that describes the rate of energy loss per interaction in the elastic scattering regime (Dobrzynski and Blinowski, 1994):

$$\xi := \ln\frac{E_0}{E} = 1 + \frac{(A-1)^2}{2A}\ln\left(\frac{A-1}{A+1}\right) \approx \frac{2}{A+1}, \tag{7}$$

where A is the atomic mass number of the considered element. The logarithm represents the fact that, by elastic collisions, not an absolute quantity but always a fraction of the kinetic energy is lost. This formulation can be directly linked to the number of collisions, n_{col}, necessary to slow a neutron of energy E_0 down to E_1:

$$n_{\mathrm{col}} = \frac{u}{\xi}, \quad \text{where} \quad u = \ln\frac{E_0}{E_1}. \tag{8}$$

The variable u is called lethargy and ξ represents the average change in lethargy per collision. Following these relationships, it can be estimated that fast neutrons ($\approx 10^6$ eV) need ≈ 18 collisions with hydrogen to get thermalized below 10^{-5} eV, whereas collisions with large nuclei like iron take more than 500 collisions. This is the reason why the effect of metallic cases around the moderator of the detector is negligible. According to Equation (7), the lethargy is a property of a material and decreases with increasing nuclide mass. An overview of different atoms is provided in **Table 1**.

TABLE 1 | Slowing down of neutrons by interaction with different isotopes from 2 MeV to thermal and to an exemplary energy relevant for CRNS.

			Avg. no. collisions n_{col}	
Element	**Mass (u)**	**Log. energy decrement ξ**	**to thermal**	**To 100 eV**
H	1	1	18	10
H_2O	–	0.92	20	11
N	14	0.134	135	73
O	16	0.12	153	82
Al	27	0.0723	255	137
Si	28	0.0698	264	142
Fe	56	0.0353	522	280
SiO_2	–	0.11	166	90
Air (dry)	–	0.135	135	73

For an inhomogeneous medium, the effective $\overline{\xi}$ is an average of material-specific ξ_i weighted by their elastic cross sections σ_i:

$$\overline{n_{\mathrm{col}}} = u/\overline{\xi} = u\left(\frac{\Sigma_i\,\sigma_i\,\xi_i}{\Sigma_i\,\sigma_i}\right)^{-1} \tag{9}$$

In a macroscopic medium with the material density ϱ we can consider the macroscopic cross section, $\Sigma = \varrho\cdot\sigma$. Hence, a typical ground medium can be described with the macroscopic cross sections of Σ^{soil} plus a fraction w of added water Σ^{water}:

$$n_{\mathrm{col}}^{\mathrm{ground}} = u\,\frac{\Sigma^{\mathrm{soil}} + w\,\Sigma^{\mathrm{water}}}{\Sigma^{\mathrm{soil}}\,\xi^{\mathrm{soil}} + w\,\Sigma^{\mathrm{water}}\,\xi^{\mathrm{water}}} \tag{10}$$

Since the neutron flux $\Phi_{\mathrm{el,\,epith}}$ in the relevant energy range of 0.5 eV to 0.5 MeV is proportional to the number of scatterings required for thermalization (n_{col}), we can conclude that the above-ground neutron intensity is inversely proportional to the water fraction w:

$$I(\theta) \propto \Phi_{\mathrm{epith}}(H_2O) \propto n_{\mathrm{col}}^{\mathrm{ground}} \propto \left(\Sigma^{\mathrm{soil}}\,\xi^{\mathrm{soil}} + w\,\Sigma^{\mathrm{water}}\,\xi^{\mathrm{water}}\right)^{-1} \tag{11}$$

As a consequence, the relationship between above-ground neutron intensity and soil water content is hyperbolic and scales with the combined lethargy of soil and water. This concept is already expressed in the conventional N_0 method (1) and will be also used for a revised approach in this work. The statements here are to be regarded as basic analytical approaches. They only apply to homogeneous transport problems. For the combination of different media interface effects have to be taken into account.

3.3. Cosmic-Ray Neutron Transport on the Ground

The cosmic-ray neutron spectrum (see **Figure 1**) exhibits a triple peak structure. The rightmost peak at ∼100 MeV makes up neutrons generated in atmospheric cascades from mainly extrasolar particles or spallation reactions induced by protons in the upper atmosphere. The flux of these particles directed toward the ground is attenuated by several orders of magnitude. On their path, high-energy protons and neutrons also excite nuclei, which evaporate neutrons at energies around 1 MeV. Resonant nuclear excitations are responsible for the comb-like structure of this peak. Toward lower energies, elastic scattering becomes the dominant interaction as long as neutrons are epithermal. Due to the mass of hydrogen being nearly equal to that of the neutron, this following energy band is most sensitive to water and organic molecules and thus most relevant for the method of cosmic-ray neutron sensing. Below 1 eV the kinetic energy of the target, which is usually in thermal equilibrium (25 meV), significantly contributes to the neutron's energy during a collision. As a consequence, neutrons finally become thermalized and perform a random walk until they are absorbed.

In the air, the mean free path for neutrons is ∼1,000 times greater than in the soil. In an artificial scenario aiming to visualize the transport at the interface, a flux column is released onto the ground. By focusing such a "neutron beam" onto one spot, on the surface, the three-dimensional spatial distribution can be seen more directly, as the flux of the cosmic-ray neutron spectrum of **Figure 1** is otherwise mostly omnidirectional. A rather dry condition is chosen in order to show a more spatially extended distribution. **Figure 2** shows the tracks of all neutrons in the domain in three different energy regimes. Most high-energy neutrons entering the soil are scattered in a forward direction, and the possibility of leaving the ground is therefore considerably low; the exception is those originating from evaporation processes, which emit secondary particles nearly isotropically. However, only neutrons within the top few dozen centimeters below the interface border exhibit a significant probability of leaving. In general, this also leads to slant soil emission angles being suppressed. Epithermal neutrons below 1 MeV behave rather diffusively until they are moderated to thermal energies. As a first-order approach, one can expect neutrons to behave as a diffusive gas, as it was formulated by Glasstone and Edlund (1952), and applied to a footprint estimate by Desilets and Zreda (2013). But since every collision results in an energy loss for the neutrons, their mean free path between collisions changes and pure diffusion theory loses validity. The Fermi Age theory, e.g., applied in Barkov et al. (1957), accounts for these energy losses in a diffusive system, but analytical solutions exist only for mono-energetic particles and are not feasible for the cosmic-ray neutron spectrum exposed to a wide range of environmental conditions with different cross-sections. The cosmic-ray spectrum is partly also made up of neutrons slowed down in the air, which have a higher probability of being emitted back into the air. For thermalized neutrons, the soil can be regarded as a source. It can be explained by the fact that the moderation due to the presence of hydrogen is effective and no isotope with a large capture cross-section is present, unlike the case of air in which argon and especially nitrogen are comparably strong absorbers.

4. CALCULATION MODEL

4.1. Above-Ground Neutron Flux

In order to analyze the above-ground neutron intensity relation to the environmental variables soil moisture θ and absolute air humidity h, simulations were carried out for a set of 11×11 values from $\theta = 1$ to 50% and $h = 1$ to 35 g/m^3 with 10^6–10^7 initial neutrons each. A detector layer was placed at a height of 1.3–1.5 m, and it records the tracks of neutrons passing through. The energy sensitivity of this layer can be adjusted. In this study the following two settings have been used: a fixed energy window (THL) scores neutrons from 1 eV to 10 keV and a more realistic approach, which employs the detector response function (drf) from Köhli et al. (2018). The discussion does not explicitly distinguish between incoming and albedo flux; however, in order to interpret the signal changes as a function of environmental variables, it is necessary to understand the transport paths of neutrons to the detector. Besides the fraction of incoming radiation, which acts as a background, there are three main types of transport processes: so-called geometric transport from the soil surface directly to the detector and typical mid-range transport of neutrons which cross the air-ground interface several times. The far-field transport can be understood as neutrons originating from a remote ground location and being transported mainly over the air with long path lengths. A set of such tracks is exemplarily visualized in the simulated detector of **Figure 3**.

4.2. Calculation of Particle Fluxes

4.2.1. The Effect of the Cross Section Database

Neutron simulation toolkits provide very similar results for the well-understood physics below 20 MeV. Yet, there are differences with respect to the cross-section database and the high energy transport models. Most resources agree with each other and exhibit differences on the level of a few percent on the low energy cross-section. By far the best-known isotope is ^{1}H with an uncertainty of 0.3%. In a first study, we compared different cross-section databases, which extend into the range above 20 MeV. However, as described in section 2, most of the necessary high-energy interactions are calculated by specific models. Therefore, the exchange of cross-section databases does not exclusively determine the result of a cosmic-ray neutron transport study. A broader overview of available toolkits can be found in Köhli (2019).

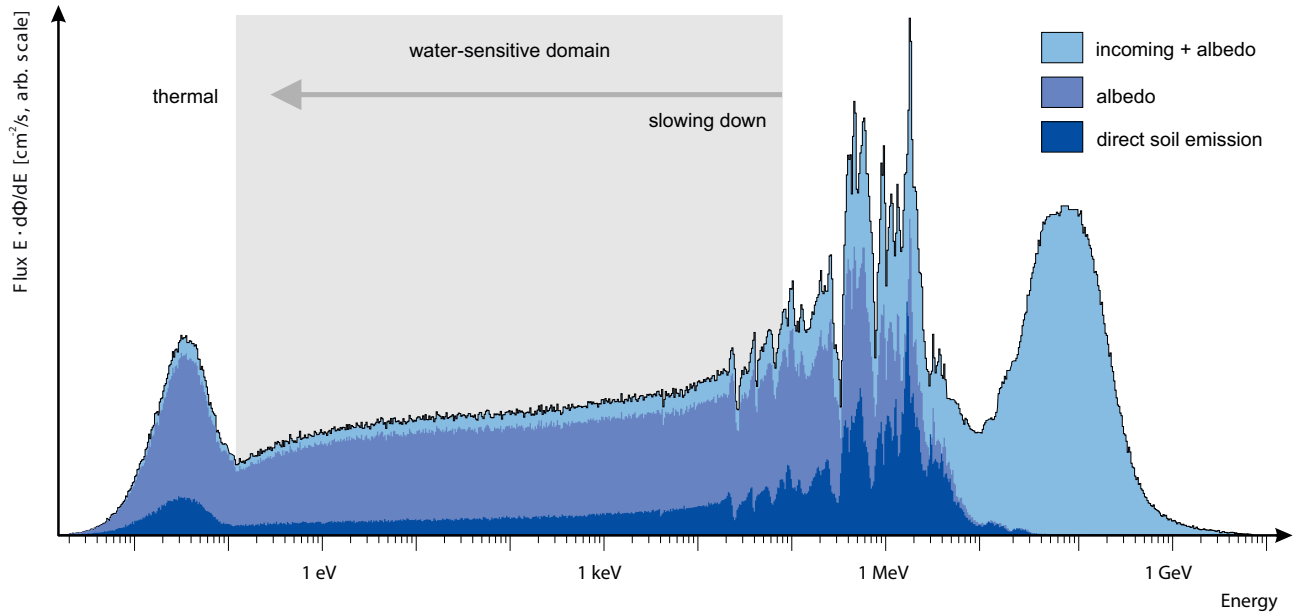

FIGURE 1 | Cosmic-ray neutron spectrum above dry ground. Three distinct peaks can be observed, which correspond to three physical processes. High-energy neutrons are generated in cascades in the upper atmosphere with energies up to several GeV. By interaction with atoms in the air or ground evaporation, neutrons are emitted with energies around 1 MeV. Finally, by elastic scattering, neutrons are slowed down until they are in thermal equilibrium with their environment. The total spectrum (black outline) can be separated into one part comprising albedo neutrons that have been in the soil (blue) and therefore carry soil moisture information and the incoming fraction (light blue), which can be considered a background. The spectrum which is emitted from the soil ("direct soil emission," dark blue), mainly due to neutrons which have been generated in the ground, shows that the overall intensity is the result of several oscillations around the air-ground interface.

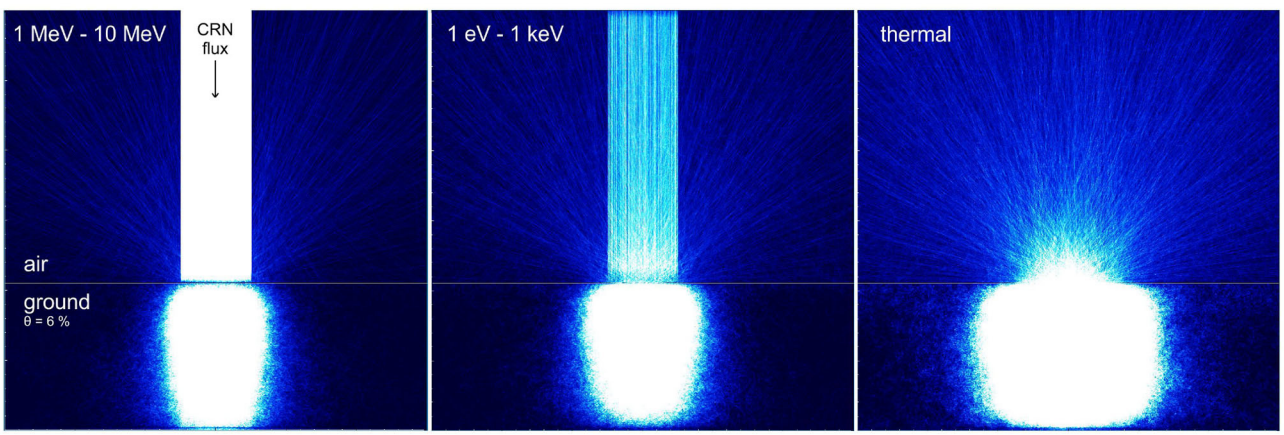

FIGURE 2 | Flux calculation of an air-ground interface in which neutrons are artificially released centered straight down but with a CR spectrum according to **Figure 1**. The simulated neutron tracks from evaporation (MeV) to absorption (thermal) of $80{\cdot}10^4$ histories are displayed in a domain of 3 × 3 × 3 m with a track density scaling from dark blue to white (Köhli, 2019).

The ensemble of different cross-section databases with the same high-energy model (**Table 2**) leads to a relative variation of the predicted flux by 3% for a range of dry and wet conditions. The deviation of URANOS and MCNP6 is found to be ∼2%, which amounts to a relative difference of 10%. There is a clear difference for both toolkits between the predicted flux for air humidity and soil moisture changes. URANOS produces an attenuation length in air, depending on the cutoff rigidity, of $\lambda_{air} = 150–160\,g/cm^2$, similar to MCNP6. Yet, the attenuation length in water is $\lambda_{water} \approx 135\,g/cm^2$. In MCNP6 for a neutron-only transport scenario one finds $\lambda_{water} \approx 110\,g/cm^2$, and if protons, pions, and muons are included, $\lambda_{water} \approx 120\,g/cm^2$. Cosmogenic nuclide studies, however, suggest values rather in the order of $130\,g/cm^2$ (Nesterenok and Naidenov, 2012). As a result in MCNP6 high-energy neutrons are attenuated faster and the relative production of evaporation neutrons in the top soil layers

TABLE 2 | Comparison of the scaling of $I(\theta, h)$ for different simulation toolkits.

	MCNP6						URANOS	
	ENDF8		JEFF3.2		JENDL4		ENDF7/JENDL-HE	
Simulation setting from condition → to condition	**THL**	**drf**	**THL**	**drf**	**THL**	**drf**	**THL**	**drf**
1% → 50%, 1 g/m^3	0.218	0.309	0.224	0.315	0.213	0.301	0.248	0.342
1 g/m^3 → 35 g/m^3, 1%	0.831	0.847	0.828	0.845	0.821	0.842	0.794	0.810
1%, 1 g/m^3 → 50%, 35 g/m^3	0.185	0.267	0.190	0.271	0.184	0.263	0.197	0.285

MCNP6 was additionally coupled to different cross-section databases. The change from dry to moist conditions has been analyzed for fixed upper and lower detection limits 1 eV to 10 keV (THL) and a detector response function (Köhli et al., 2018) for a standard sensor (drf). Each run provided enough statistics that all digits are significant. The provided ratios cover a range of soil moisture values at a fixed air humidity and a range of air humidity at a fixed soil moisture value, while both quantities have been increased from the lower to the upper bound.

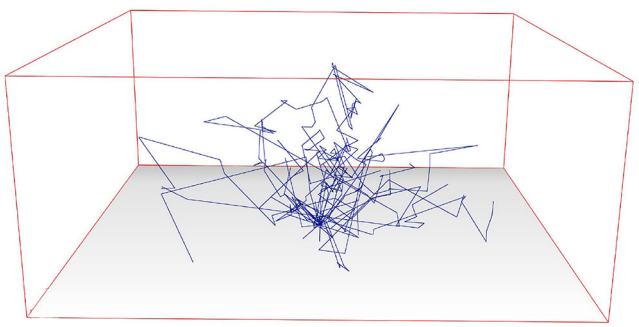

FIGURE 3 | Transport of cosmic-ray neutrons within a domain of 600 × 600 × 250 m. A detector is placed in the center at a height of 1.5 m. The tracks that are shown in blue correspond to 35 neutrons that probed the soil at some point on the plane and ended up in the detector volume. These exemplary tracks show typical paths neutrons travel until detection. Besides the importance of air as a transport medium it is noteworthy that most last scatterings occur in the direct vicinity of the sensor.

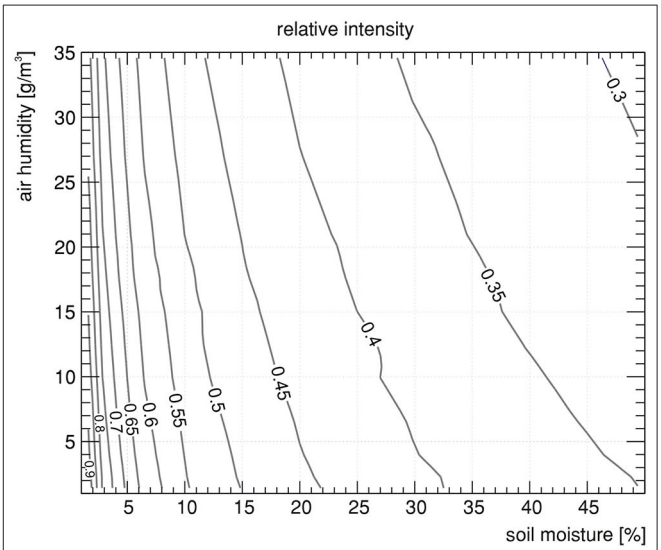

FIGURE 4 | Above-ground neutron intensity as a function of air humidity and soil moisture simulated by URANOS applying a simulated detector response function. The contour lines show the extrapolated intensity change in steps of 5%. For dry soils air humidity has a stronger effect as neutrons travel over longer distances. The effect of water vapor is non-linear.

is higher. This could lead to a larger difference in the flux between dry and moist conditions.

4.2.2. The Effect of the Detector Response Function

Taking into account the actual detector response function significantly reduces the predicted flux change, whereas the energy window method leads to a factor of ∼4.5 for a soil moisture change from 1 to 50%, including the response function reduces this by 40% to a factor of about 3. This can be attributed to the fact, that the energy bands above and below the water-sensitive domain are less affected by environmental hydrogen changes (see **Figure 1**). The detector is susceptible to contamination by thermal neutrons, which scale differently with environmental water, and on the other hand, the evaporation peak includes more neutrons, which have never probed the soil (Köhli et al., 2018). A more comprehensive analysis of the detector response function can furthermore be found in Weimar et al. (2020).

4.2.3. The Effect of Air Humidity Profiles

As air humidity can be distributed vertically inhomogeneous in a second simulation set, a humidity profile with an e-fold length of 2.3 km was assumed according to Rosolem et al. (2013). The results are shown in **Table 3**. One finds, that using a vertically inhomogeneous atmosphere especially has an effect on the soil moisture scaling and less on air humidity variations. In that scenario, MCNP and URANOS agree well with each other for the predicted flux changes. However, it does not agree with the results of Rosolem et al. (2013), especially it is interesting to note that even with ten times larger statistics the MCNP6 runs still have larger uncertainties than shown in the referenced publication.

5. RESULTS AND DISCUSSION

5.1. Global Intensity Scaling

The relative reduction in neutron intensity at the surface for different soil moisture conditions when humid atmosphere layers

TABLE 3 | Comparison of the scaling of $I(\theta, h)$ for different simulation toolkits.

	MCNP6			URANOS		
	Profile		Th. shield	Profile		Th. shield
Simulation setting from condition → to condition	**THL**	**drf**	**drf**	**THL**	**drf**	**drf**
1% → 50%, 1 g/m^3	0.264	0.350	0.266	0.254	0.350	0.290
1 g/m^3 → 35 g/m^3, 1%	0.825	0.827	0.833	0.794	0.818	0.800
1%, 1 g/m^3 → 50%, 35 g/m^3	0.207	0.292	0.226	0.203	0.291	0.231

The change from dry to moist conditions has been analyzed for fixed upper and lower detection limits 1 eV to 10 keV (THL) and a detector response function (Köhli et al., 2018) for a standard sensor (drf) and a sensor with thermal neutron shield (shielded). For the setting "Profile," the air humidity was scaled like in Rosolem et al. (2013). The provided ratios cover a range of soil moisture values at a fixed air humidity and a range of air humidity at a fixed soil moisture value, while both quantities have been increased from the lower to the upper bound.

are added is shown in **Figure 4**. The plots do not qualitatively change for simulations using the energy window settings or the detector response function and likewise not for URANOS or MCNP6. For humid compared to dry air the maximum achievable count rate is reduced by 20% in case of dry soil conditions. This quantitatively agrees with Rosolem et al. (2013) who studied the change from dry to 22 g/m^3. However, a strictly linear relationship for water vapor cannot be verified. The presented reduction rate of 0.0054 per gram air humidity in Rosolem et al. (2013) seems to hold only for dry conditions. The scaling to moist soils is non-linear, as seen by the contour lines in **Figure 4**. Within the parameter space of this study, the relative intensity change for scaling water vapor lies in all cases in the order of 20% for 1 g/m^3 → 35 g/m^3 (see **Table 2**). This observation can be attributed to the fact that, for dry conditions, neutrons travel much longer paths and start with higher energies, both of which increase the transport through air, which, in case of a decreasing vertical humidity profile, is even amplified. The results presented in **Figure 5** also show that using fixed upper and lower boundaries for scoring the neutron flux (energy window), the intensity scaling as a function of soil moisture is significantly higher. While the latter reduces the intensity by ∼75% from dry to wet soils, using a detector response function reduces the measured flux by 65%. In Franz et al. (2013b) the authors already experimentally found a scaling factor of 2.5–3 between wet and dry conditions by comparing the data of ∼ 40 COSMOS stations. This disparity could imply that further studies with fixed lower and upper energy boundaries would overstate intensity changes regarding soil moisture. Yet, applying the response function of a neutron detector using a shield, which absorbs more than 90% of the thermal neutron spectrum, yields a scaling between both cases. This study finds, based on **Table 3**, that the performance of CRNS detectors with regard to the measured intensity differences can be improved by at least 20% using such a thermal neutron shield. Although it reduces the overall measured flux, the improvement in the steepness of the $I(\theta)$ relation can be beneficial especially for moist conditions.

The major outcome of this study is that the N_0 method (1) is not steep enough to describe measurements, especially in dry regions. The hyperbolic characteristics reflect well local gradients, which is the reason why different adaptations of the parameters of this equation led to site-specific solutions. If the neutron intensity at a specific station does not change significantly, a locally adapted hyperbola like (1) can lead to an acceptable fit quality given the fact that there are most often unknown systematic errors. In different studies, including the literature cited here, typical calibration plots indicate a more steep $I(\theta)$ relation than can be achieved by (1). Especially when calibrated to rather moist conditions, the gradient from the Desilets equation is able to follow the simulations over a broad range of the variable space (see **Figure 5** left). The reason is that the solution (15) for the above-ground neutron flux can require an additional exponential term (6), which leverages the intensity changes especially for dry conditions (see section 3). The possibility of such a description had already been indicated by Köhli (2019). COSMIC (Shuttleworth et al., 2013) relies on an exponential description for $I(\theta)$ and is able to better reproduce the intensity changes as can be seen for an exemplary evaluation in **Figure 5**. Yet, one can likewise ascertain a limited steepness for dry conditions. In conclusion, the findings here underline that for CRNS two important factors have to be taken into account. First, air humidity corrections are non-linear, yet the relative changes can be linearized, and second, the intensity scaling is much steeper than until now assumed based on the N_0 method.

5.2. Revision of the Intensity Relation

We have shown in section 3 that a hyperbolic formulation is reasonable to express the relationship between neutron intensity and soil moisture (see relation 11). The Desilets equation (1) satisfies this condition; however, it is mathematically overdefined. The four parameters (a_0, a_1, a_2, and N_0) are correlated, i.e., one of them is redundant. Any attempt to optimize or fit the parameters will lead to multiple, non-unique solutions as a hyperbola is defined by only three parameters. We believe that this is one of the reasons why different researchers found different parameter sets for their sites.

For a rigorous treatment, and to allow for unique fitting solutions, it is necessary to reduce the hyperbolic part to three parameters. We start from the Desilets Equation (1):

$$\theta(N) = \frac{a_0}{N/N_0 - a_1} - a_2 = \tilde{a}_0 \frac{1 - N/N_{\max}}{\tilde{a}_1 - N/N_{\max}}, \qquad (12)$$

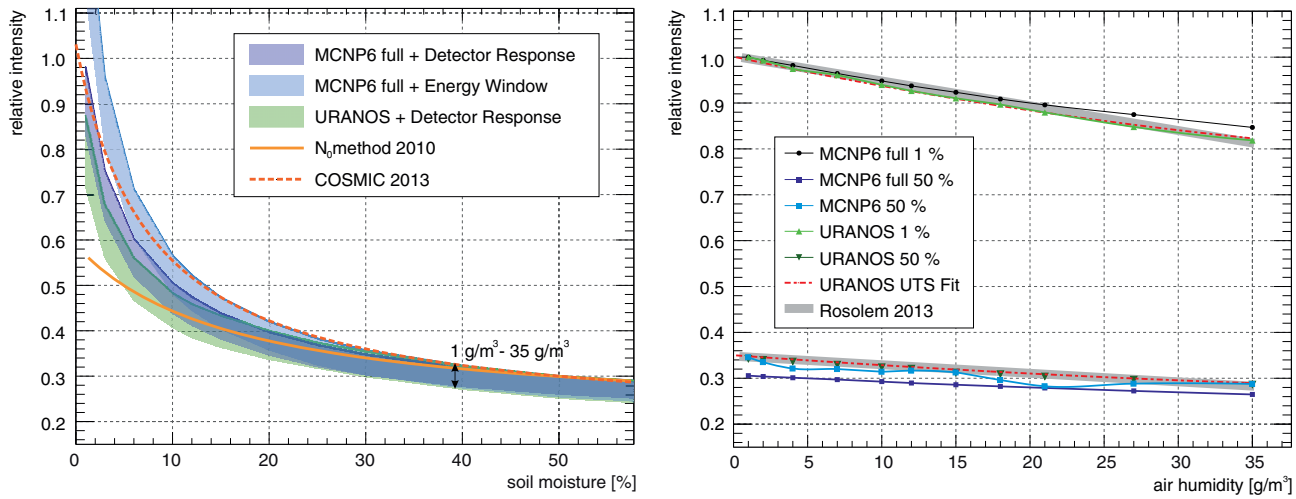

FIGURE 5 | CRN intensity scaling for a simulation set with MCNP and URANOS in comparison with MCNP6, indicating a neutron-only simulation and MCNP6 full including all particle species. (Left) The intensity scaling with the shaded area indicating the variation from minimum to maximum air humidity shows the N_0 method (1), the COSMIC forward operator and different simulations with flux recording set to fixed lower and upper bounds (energy window), or using a typical detector response function. (Right) The water vapor correction is compared to simulations of 1 and 50% soil moisture, which all use the detector response function. The UTS fit for URANOS is shown exemplarily.

where the new parameters $\tilde{a}_0$, $\tilde{a}_1$, and N_{max} can be expressed in terms of the classic parameters:

$$\tilde{a}_0 = -a_2, \qquad \tilde{a}_1 = \frac{a_1 a_2}{a_0 + a_1 a_2}, \qquad N_{\text{max}} = N_0 \, \frac{a_0 + a_1 a_2}{a_2}. \tag{13}$$

Here, N_{max} is slightly larger than N_0 and represents the absolute upper bound of the above-ground neutron flux. With these three, instead of four, parameters, this function is now uniquely defined and should be much better suited for calibration and optimization methods.

The inverse relation can be expressed as

$$I(\theta, h) \equiv N(\theta, h) = N_{\text{max}} \cdot \frac{\tilde{a}_0 + \tilde{a}_1 \, \theta}{\tilde{a}_0 + \theta} \sim (\tilde{a}_0 + \theta)^{-1} \tag{14}$$

As explained in section 3, there are reasons to assume a strong link between above-ground neutron flux and soil moisture as well as air humidity. For this reason, we propose to extend this function with physically reasonable terms that express this complex relationship. The intensity scaling in the water-sensitive domain can be very well-described by a hyperbolic expression like (14), which originates from the stopping power of the medium slowing down the neutrons as described in (11). An offset can be added that amounts for the 'incoming' part of the neutron spectrum. The diffusive spatial transport of neutrons in an absorbing medium however can be described by an exponential law like (6). These are the main effects that contribute to the above-ground neutron flux. As a rigorous analytical solution would be too complex, we use these findings as a mathematical structure and evaluate their different contributions by fitting this generalized approach to a simulation data set.

As Rosolem et al. (2013) have shown that the influence of water vapor, h, in the air column above the sensor can be expressed by a correction factor C_h, which is, in a first-order approximation, linear in h and especially accounts for the increased density. We found that the linear relationship is not enough to account for the changes in the very dry air regime, attributed to the long-range neutrons which probed the soil at distances of 100 m and beyond. Those neutrons are exceptionally exposed to air humidity above the surface and also interact with the soil 2–3 times on their way to the detector (Köhli et al., 2015). Therefore, we propose a non-linear correction factor using at least a 2nd order Taylor expansion.

The equation in the final form becomes

$$I(\theta, h) = N_D \left(\frac{p_1 + p_2 \, \theta}{p_1 + \theta} \left(p_0 + p_6 \, h + p_7 \, h^2 \right) + e^{-p_3 \, \theta} \left(p_4 + p_5 \, h \right) \right). \tag{15}$$

This *universal transport solution* (UTS) is a general description of $I(\theta, h)$. The parameters p_i are derived from a two-dimensional fit on simulated data sets (see also **Table A1**). The scaling constant N_D accounts for the average specific detector count rate and can be determined with any combination of I, θ, and h. For soil moisture retrieval $\theta(I, h)$ has to be inverted numerically (e.g., using the Newton-Raphson method), which is beyond the scope of this work. UTS can be used with volumetric or gravimetric soil moisture by rescaling θ.

5.3. Experimental Evidence

Every parameter set from different simulation settings for the presented function has its own justification depending on a specific site and detector conditions. It is beyond the scope of this work to conclusively clarify which function would be generally best suited for CRNS applications, as it would require

a statistically sound study with a large set of data from various stations around the world.

We exemplarily pick two distinct sites to illustrate the general performance of the proposed UTS approach compared to the conventional relationship. The first site is the COSMOS station at the Santa Rita Experimental Range (SRER) in Arizona, US, which is exposed to a very dry climate with rapidly changing air humidity (Zreda et al., 2008; Franz et al., 2012b). For example, SRER provided the data basis of the works by Franz et al. (2013b) and Rosolem et al. (2013). SRER has also been used by Iwema et al. (2015) for a study concerning a new $N(\theta)$ approach since the N_0 method was known to not perform well enough at this site. We would expect to see a stronger dependency of the neutron intensity on soil moisture and air humidity in very dry periods.

The second data set is from the Rollesbroich grassland test site in Central Europe, part of the TERENO Rur Observatory (Bogena et al., 2018) and with contrasting climatic conditions compared to SRES. Annual precipitation of 1,037 mm (2012) is distributed throughout the year, while evapotranspiration focusses on the months April to September and sums to 480 mm in 2012 (Gebler et al., 2015). Dry aboveground biomass is negligible with 0.2 kg/m^2 (Baatz et al., 2015). The Rollesbroich test site features a network of 84 nodes with each three TDT (Time Domain Transmissometry) sensors installed in 5, 20, and 50 cm depth (Qu et al., 2016). The grassland is structured into several smaller fields which are in part and irregularly subject to management activities (mowing, manuring). Both soil moisture intensity conversions well represent soil moisture dynamics. The TDT data of both sites were weighted horizontally and vertically according to Schrön et al. (2017). In the rather wet and humid climate, we would expect no substantial difference to the performance of the conventional N_0 approach, except for a slightly stronger influence of air humidity according to **Figure 4**.

The SRER data set, however, incorporates systematic uncertainties, which are significant at the level of the achieved precision. The supplement data provided by T. Franz compensates for the partial lack of environmental data by the sensor itself. However, there are small differences to the level 0 website data in relative air humidity and temperature as well as a noticeable pressure offset in 2011 by 2 mbar. With none of the *in situ* probes being closer to the sensor, the large contribution from the near-field remains unknown. As the uppermost TDT data is retrieved from a depth of 10 cm, the weighted soil moisture is dominated by this layer. Given that in deserts the largest dynamics can be observed at the surface, especially great signal deviations are therefore expected for hourly data. For the periods of extremely dry conditions the uncertainty on the lattice water, which can constitute half of the measured moisture, also becomes a relevant quantity. As there is no neutron monitor close to the experimental site or worldwide at the same cutoff rigidity we analyzed several stations statistically for their correction significance. We found that data from the NEWK station (Newark) slightly outperformed the data from the conventional JUNG station (Jungfraujoch), especially during Forbush decreases (Cane, 2000).

For each of the settings described in section 4.2, Equation (15) was fitted to the full set of simulation data with an atmospheric profile of water vapor in height h according to $\exp(-h/(2{,}300\,\mathrm{m}))$. The resulting parameter sets are provided in the **Table A1**. UTS provides an excellent agreement with the data outperforming by far the hitherto used approach of the Desilets equation (1) with the water vapor correction (Rosolem et al., 2013) (see **Figures 6**, **7**). It is especially interesting to notice that the short-term variation in the data seems to be entirely due to air humidity changes. This can also be concluded from the statistical analysis of hourly and daily accumulation intervals (see **Table A1**), in which the latter show much better agreement. In another parameter set (not shown) in which we doubled the air humidity scaling, we could achieve a better statistical significance. We therefore deduce that the water vapor changes at this site are much higher than actually measured by ground-based instruments. It could also mean that atmospheric profiles, at least under such extreme conditions, can play a role in precise soil moisture retrieval. An underestimation of the surface moisture dynamics might also be the reason why the energy window functions show a slightly better agreement to the measured neutron intensity. As the uppermost TDT probe depth is located 10 cm below the surface, the near-ground variations may enforce larger intensity fluctuations than is actually reflected by the data set. As URANOS and MCNP6 provide comparable results in order to analyze the best detector representation further sites will be necessary for testing.

The UTS approach proposed here shows significantly higher skill in soil moisture representation for all three measures, KGE, RMSE, NSE (**Figure 8**) compared to the traditional four-parameter approach. Several periods show varying performance but the "MCNP drf" approach is consistently closer to the observed reference neutron flux throughout most of the year. Short-term offsets, such as those in May and August, could be explained by unmonitored management. Considering high humidity and rather wet soils, the here proposed method based on "MCNP drf" is a promising advance to previous soil moisture neutron intensity conversions.

6. CONCLUSIONS

In this study, we investigated the relationship between near-surface epithermal neutron intensity and water content in the soil and atmosphere. The analytical form has been derived from physical principles while the parameter sets were determined from neutron transport simulations for various types of model setups. We demonstrated the performance of our approach exemplarily at a dry and a wet instrument site using data from cosmic-ray neutron sensors and soil moisture monitoring networks.

A variety of modeling concepts have been evaluated using MCNP6 vs. URANOS, different cross-section databases, and different detector energy response functions (**Tables 2**, **3**). MCNP simulations greatly benefited from the inclusion of protons and muons while they showed good agreement to URANOS on the level of 2–10%. The discrepancy might be attributed to the

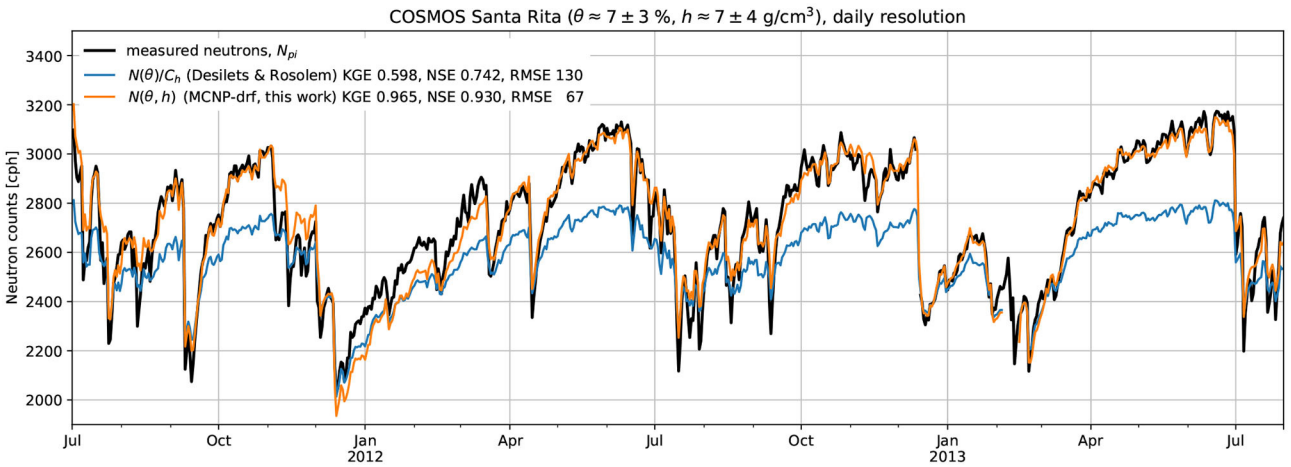

FIGURE 6 | The COSMOS site "Santa Rita" exhibits periods of extremely dry soil and air. The measured neutron flux N_{pi} (black) was corrected for air pressure and incoming radiation. Daily aggregation is applied on all data. Soil moisture θ from the surrounding TDT network has been converted to neutron intensity using two approaches: (blue) the equation from Desilets et al. (2010) with the inverse water vapor correction from Rosolem et al. (2013), and (orange) the formula (15) presented in this work, using the parameter set "MCNP drf." Kling-Gupta Efficiency (KGE), Nash-Sutcliffe Efficiency (NSE), and root mean square error (RMSE) are reported with respect to N_{pi}. Note that the Desilets fit (blue) has been shifted by −200 cph to better illustrate the poor performance toward dry conditions (i.e., high neutron counts).

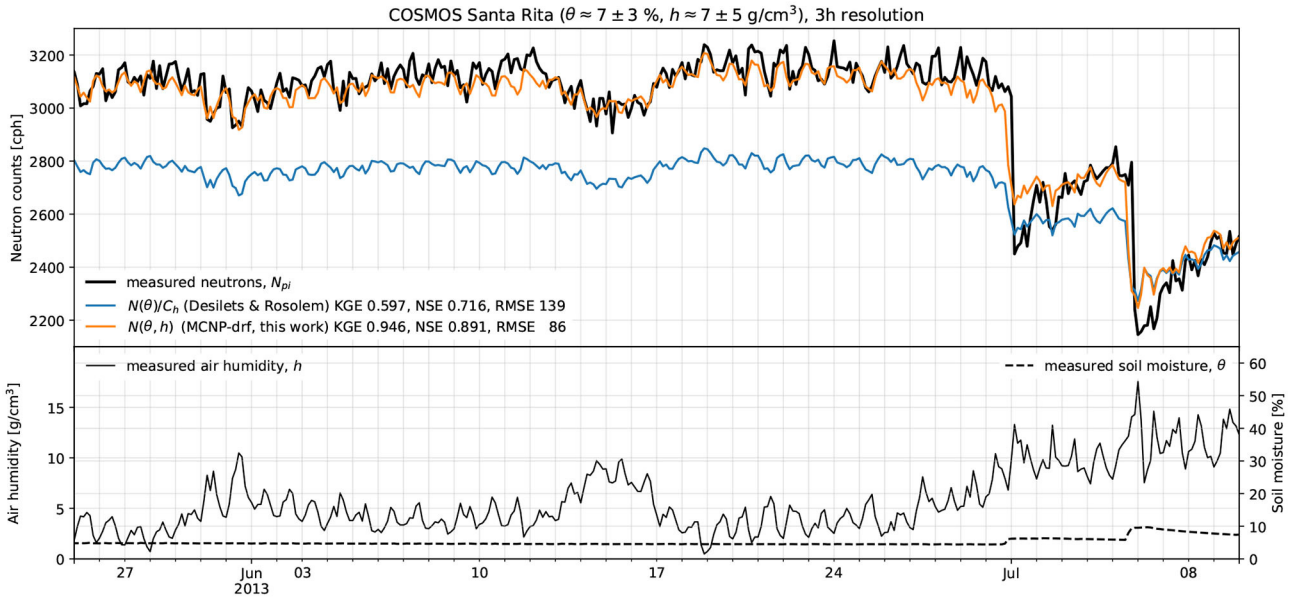

FIGURE 7 | Cutout section of the data sequence in **Figure 6** with a temporal aggregation of 3 h for the summer period of 2013, where soil moisture is almost constant and the diurnal variations of air humidity are predominantly influencing the count rate. Note that the Desilets fit (blue) has been shifted by −200 cph to better illustrate the poor performance toward dry conditions (i.e., high neutron counts).

missing consensus about the effective attenuation length in water, which will be investigated in future research. The choice of the right detector response is crucial to the relationship between neutrons and soil moisture. For example, the dynamic range of $N(\theta)$ would be reduced by up to 40% using the detector-specific response function compared to the conventional energy-window approach. Additional shielding material would be able to exclude thermal neutrons and to partly restore this dynamic range.

The neutron response to air humidity has been investigated using homogeneous, exponential, and heterogeneous atmospheric profiles. Similar to Rosolem et al. (2013) we found that only the lowest 600 m are relevant for CRNS modeling. Our experimental results also suggest that complex atmospheric profiles could have previously undiscovered effects on CRNS measurements under dry conditions. Our simulations also suggest that the neutron response to water vapor depends on soil moisture itself. Hence, we recommend a non-linear

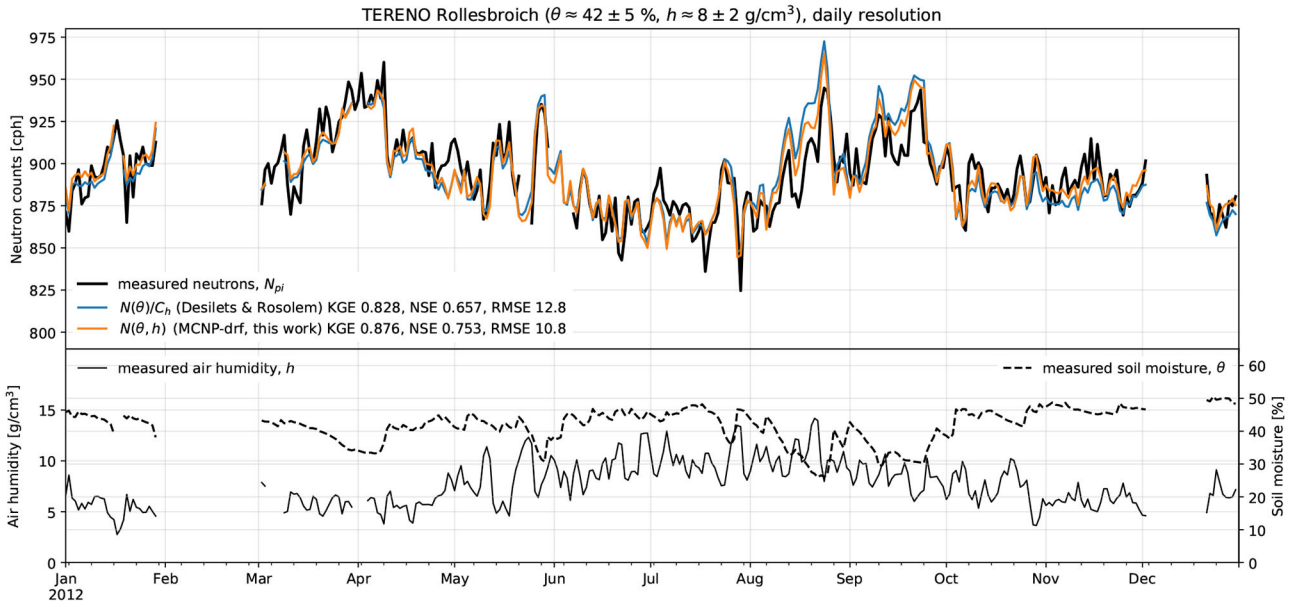

FIGURE 8 | The TERENO site "Rollesbroich" features a humid climate with wet grassland soils. The measured neutron flux N_{pi} (black) was corrected for air pressure and incoming radiation with data aggregated in daily intervals. Soil moisture θ from the surrounding TDT network has been converted to neutron intensity using two approaches: (blue) the equation from Desilets et al. (2010) with the inverse water vapor correction from Rosolem et al. (2013) and (orange) the formula (15) presented in this work using the parameter set "MCNP drf."

correction approach as an alternative to the conventional method from Rosolem et al. (2013).

The hitherto accepted $N(\theta, N_0)$ approach was found to be overdefined by one redundant parameter. This might be one of the reasons for the growing number of studies proposing site-specific parameter calibrations. Furthermore, our revised simulations with MCNP and URANOS showed a significantly steeper neutron response to soil moisture at the dry end. Based only on our simulations, we deduced a new *universal transport solution* (UTS, Equation (15)) that implicitly includes the correction for air humidity. The parameters only depend on the physical model used, except for the detector-specific scaling parameter N_D. A reversed formulation, $\theta(I, h)$, could be performed numerically. We hope that this solution could contribute to a more general and unique sensor calibration.

Our new approach has been evaluated at dry and a wet site in Arizona (US) and Germany, respectively, which cover a wide range of soil moisture (1–50%$_{\mathrm{Vol}}$) and air humidity (1–25 g/m^3). At both sites, the UTS led to significantly improved CRNS performance compared to the conventional Desilet's equation (e.g., KGE 0.60 $\rightarrow$ 0.97). Future studies are encouraged to investigate the performance of this approach on a larger number of locations. The UTS function can serve as a base description for further CRNS related studies, such as biomass effects or hydrological profiles, which look for rather small deviations from the overall signal.

DATA AVAILABILITY STATEMENT

The raw data supporting the conclusions of this article will be made available by the authors, without undue reservation.

AUTHOR CONTRIBUTIONS

MK and US wrote the manuscript. JW provided the MCNP simulations. MS and RB provided the experimental verification data. MS conducted the analysis on the field data. All authors contributed to the article and approved the submitted version.

FUNDING

URANOS was developed within the project Neutron Detectors for the MIEZE method and Forschung und Entwicklung hochauflösender Neutronendetektoren, funded by the German Federal Ministry for Research and Education (BMBF), grant identifier: 05K10VHA and 05K16PD1. The project Large-scale and high-resolution mapping of soil moisture on field and catchment scales boosted by cosmic-ray neutrons was funded within the DFG research group Cosmic Sense FOR 2694. The TERrestrial Environmental Observatory (TERENO) was funded by the Helmholtz Association and the Federal Ministry of Education and Research. We acknowledge financial support by the Baden-Württemberg Ministry of Science, Research and Arts and by Ruprecht-Karls-Universität Heidelberg.

ACKNOWLEDGMENTS

MK and MS acknowledge Trenton Franz for providing the extended Santa Rita data set and Lena Scheiffele for the weighting of the *in situ* soil moisture data.

REFERENCES

Almeida, A., Dutta, R., Franz, T., Terhorst, A., Smethurst, P., Baillie, C., et al. (2014). Combining cosmic-ray neutron and capacitance sensors and fuzzy inference to spatially quantify soil moisture distribution. *IEEE Sens. J.* 14, 3465–3472. doi: 10.1109/JSEN.2014.2345376

Andreasen, M., Jensen, H. K., Zreda, M., Desilets, D., Bogena, H., and Looms, C. (2016). Modeling cosmic ray neutron field measurements. *Water Resour. Res.* 52, 6451–6471. doi: 10.1002/2015WR018236

Baatz, R., Bogena, H., Hendricks-Franssen, H.-J., Huisman, J., Montzka, C., and Vereecken, H. (2015). An empirical vegetation correction for soil water content quantification using cosmic ray probes. *Water Resour. Res.* 51, 2030–2046. doi: 10.1002/2014WR016443

Baatz, R., Bogena, H., Hendricks-Franssen, H.-J., Huisman, J., Qu, W., Montzka, C., et al. (2014). Calibration of a catchment scale cosmic-ray probe network: a comparison of three parameterization methods. *J. Hydrol.* 516, 231–244. doi: 10.1016/j.jhydrol.2014.02.026

Barkov, L., Makarin, V., and Mukhin, K. (1957). Measurement of the slowing down of neutrons in the energy range 1.46–0.025 eV in water. *J. Nucl. Energy* 4, 94–102. doi: 10.1016/0891-3919(57)90124-9

Baroni, G., and Oswald, S. (2015). A scaling approach for the assessment of biomass changes and rainfall interception using cosmic-ray neutron sensing. *J. Hydrol.* 525, 264–276. doi: 10.1016/j.jhydrol.2015.03.053

Beckurts, K., and Wirtz, K. (1964). *Neutron Physics*. Berlin; Heidelberg: Springer Berlin Heidelberg.

Bogena, H., Huisman, J., Baatz, R., Hendricks-Franssen, H.-J., and Vereecken, H. (2013). Accuracy of the cosmic-ray soil water content probe in humid forest ecosystems: the worst case scenario. *Water Resour. Res.* 49, 5778–5791. doi: 10.1002/wrcr.20463

Bogena, H., Montzka, C., Huisman, J., Graf, A., Schmidt, M., Stockinger, M., et al. (2018). The TERENO-Rur hydrological observatory: a multiscale multi-compartment research platform for the advancement of hydrological science. *Vadose Zone J.* 17:180055. doi: 10.2136/vzj2018.03.0055

Boudard, A., Cugnon, J., David, J.-C., Leray, S., and Mancusi, D. (2013). New potentialities of the Liège intranuclear cascade model for reactions induced by nucleons and light charged particles. *Phys. Rev. C* 87:014606. doi: 10.1103/PhysRevC.87.014606

Briesmeister, J. (2000). *MCNP-A General Monte Carlo N-Particle Transport Code*. Los Alamos, NM: Los Alamos National Laboratory.

Brown, D., Chadwick, M., Capote, R., Kahler, A., Trkov, A., Herman, M., et al. (2018). ENDF/B-VIII.0: The 8th major release of the nuclear reaction data library with CIELO-project cross sections, new standards and thermal scattering data. *Nucl. Data Sheets* 148, 1–142. doi: 10.1016/j.nds.2018.02.001

Cane, H. (2000). Coronal mass ejections and forbush decreases. *Space Sci. Rev.* 93, 55–77. doi: 10.1023/A:1026532125747

Chadwick, M., Herman, M., Obložinský, P., Dunn, M., Danon, Y., Kahler, A., et al. (2011). ENDF/B-VII.1 nuclear data for science and technology: cross sections, covariances, fission product yields and decay data. *Nucl. Data Sheets* 112, 2887–2996. doi: 10.1016/j.nds.2011.11.002

Coopersmith, E., Cosh, M., and Daughtry, C. (2014). Field-scale moisture estimates using COSMOS sensors: a validation study with temporary networks and leaf-area-indices. *J. Hydrol.* 519, 637–643. doi: 10.1016/j.jhydrol.2014.07.060

Desilets, D. (2012). "Probe background, technology, calibration, MCNP," in *Third COSMOS Workshop* (Tucson, AZ).

Desilets, D., and Zreda, M. (2013). Footprint diameter for a cosmic-ray soil moisture probe: theory and Monte Carlo simulations. *Water Resour. Res.* 49, 3566–3575. doi: 10.1002/wrcr.20187

Desilets, D., Zreda, M., and Ferré, T. (2010). Nature's neutron probe: land surface hydrology at an elusive scale with cosmic rays. *Water Resour. Res.* 46:W11505. doi: 10.1029/2009WR008726

Desilets, D., Zreda, M., and Prabu, T. (2006). Extended scaling factors for in situ cosmogenic nuclides: new measurements at low latitude. *Earth Planet. Sci. Lett.* 246, 265–276. doi: 10.1016/j.epsl.2006.03.051

Dobrzynski, L., and Blinowski, K. (1994). *Neutrons and Solid State Physics*. New York, NY; London: Prentice Hall.

Franz, T., Wahbi, A., Vreugdenhil, M., Weltin, G., Heng, L., Oismueller, M., et al. (2016). Using cosmic-ray neutron probes to monitor landscape scale soil water content in mixed land use agricultural systems. *Appl. Environ. Soil Sci.* 2016:4323742. doi: 10.1155/2016/4323742

Franz, T., Zreda, M., Ferré, T., and Rosolem, R. (2013a). An assessment of the effect of horizontal soil moisture heterogeneity on the area-average measurement of cosmic-ray neutrons. *Water Resour. Res.* 49, 6450–6458. doi: 10.1002/wrcr.20530

Franz, T., Zreda, M., Ferré, T., Rosolem, R., Zweck, C., Stillman, S., et al. (2012a). Measurement depth of the cosmic ray soil moisture probe affected by hydrogen from various sources. *Water Resour. Res.* 48:8515. doi: 10.1029/2012WR011871

Franz, T., Zreda, M., Rosolem, R., and Ferré, T. (2012b). Field validation of a cosmic-ray neutron sensor using a distributed sensor network. *Vadose Zone J.* 11:vzj2012.0046. doi: 10.2136/vzj2012.0046

Franz, T., Zreda, M., Rosolem, R., and Ferré, T. (2013b). A universal calibration function for determination of soil moisture with cosmic-ray neutrons. *Hydrol. Earth Syst. Sci.* 17, 453–460. doi: 10.5194/hess-17-453-2013

Gebler, S., Hendricks-Franssen, H.-J., Pütz, T., Post, H., Schmidt, M., and Vereecken, H. (2015). Actual evapotranspiration and precipitation measured by lysimeters: a comparison with eddy covariance and tipping bucket. *Hydrol. Earth Syst. Sci.* 19, 2145–2161. doi: 10.5194/hess-19-2145-2015

Glasstone, S., and Edlund, M. (1952). *The Elements of Nuclear Reactor Theory*. Princeton, NJ; New York, NY: D. Van Nostrand Company.

Goldhagen, P., Clem, J., and Wilson, J. (2004). The energy spectrum of cosmic-ray induced neutrons measured on an airplane over a wide range of altitude and latitude. *Radiat. Protec. Dosimetry* 110, 387–392. doi: 10.1093/rpd/nch216

Gordon, M., Goldhagen, P., Rodbell, K., Zabel, T., Tang, H., Clem, J., et al. (2004). Measurement of the flux and energy spectrum of cosmic-ray induced neutrons on the ground. *IEEE Trans. Nucl. Sci.* 51, 3427–3434. doi: 10.1109/TNS.2004.839134

Gudima, K., Mashnik, S., and Sierk, A. (2001). *User Manual for the Code LAQGSM*. Los Alamos, NM: Los Alamos National Laboratory.

Gudima, K., Mashnik, S., and Toneev, V. (1983). Cascade-exciton model of nuclear reactions. *Nucl. Phys. A* 401, 329–361. doi: 10.1016/0375-9474(83)90532-8

Hawdon, A., McJannet, D., and Wallace, J. (2014). Calibration and correction procedures for cosmic-ray neutron soil moisture probes located across Australia. *Water Resour. Res.* 50, 5029–5043. doi: 10.1002/2013WR015138

Heidbüchel, I., Güntner, A., and Blume, T. (2016). Use of cosmic-ray neutron sensors for soil moisture monitoring in forests. *Hydrol. Earth Syst. Sci.* 20, 1269–1288. doi: 10.5194/hess-20-1269-2016

Iwamoto, O., Iwamoto, N., Kunieda, S., Minato, F., and Shibata, K. (2016). The CCONE code system and its application to nuclear data evaluation for fission and other reactions. *Nucl. Data Sheets* 131, 259–288. doi: 10.1016/j.nds.2015.12.004

Iwase, H., Niita, K., and Nakamura, T. (2002). Development of general-purpose particle and heavy ion transport Monte Carlo code. *J. Nucl. Sci. Technol.* 39, 1142–1151. doi: 10.1080/18811248.2002.9715305

Iwema, J., Rosolem, R., Baatz, R., Wagener, T., and Bogena, H. (2015). Investigating temporal field sampling strategies for site-specific calibration of three soil moisture–neutron intensity parameterisation methods. *Hydrol. Earth Syst. Sci.* 19, 3203–3216. doi: 10.5194/hess-19-3203-2015

Kodama, M., Kudo, S., and Kosuge, T. (1985). Application of atmospheric neutrons to soil moisture measurement. *Soil Sci.* 140, 237–242. doi: 10.1097/00010694-198510000-00001

Köhli, M. (2019). *The CASCADE ^{10}B thermal neutron detector and soil moisture sensing by cosmic-ray neutrons* (Doctoral thesis), Physikalisches Institut, Heidelberg University, Heidelberg, Germany.

Köhli, M., Schrön, M., and Schmidt, U. (2018). Response functions for detectors in cosmic ray neutron sensing. *Nucl. Instr. Methods Phys. Res. Sect. A Acceler. Spectrom. Detect. Assoc. Equip.* 902, 184–189. doi: 10.1016/j.nima.2018.06.052

Köhli, M., Schrön, M., Zreda, M., Schmidt, U., Dietrich, P., and Zacharias, S. (2015). Footprint characteristics revised for field-scale soil moisture monitoring with cosmic-ray neutrons. *Water Resour. Res.* 51, 5772–5790. doi: 10.1002/2015WR017169

Koning, A., Bauge, E., Dean, C., Dupont, E., Nordborg, C., Rugama, Y., et al. (2011). Status of the JEFF nuclear data library. *J. Korean Phys. Soc.* 59, 1057–1062. doi: 10.3938/jkps.59.1057

Li, D., Schrön, M., Köhli, M., Bogena, H., Weimar, J., Jiménez Bello, M., et al. (2019). Can drip irrigation be scheduled with cosmic-ray neutron sensing? *Vadose Zone J.* 18:190053. doi: 10.2136/vzj2019.05.0053

Lv, L., Franz, T., Robinson, D., and Jones, S. (2014). Measured and modeled soil moisture compared with cosmic-ray neutron probe estimates in a mixed forest. *Vadose Zone J.* 13:vzj2014.06.0077. doi: 10.2136/vzj2014.06.0077

McKinney, G. (2013). *MCNP6 Cosmic and Terrestrial Background Particle Fluxes*. Los Alamos, NM: Los Alamos National Laboratory.

McKinney, G., Lawrence, D., Prettyman, T., Elphic, R., Feldman, W., and Hagerty, J. (2006). MCNPX benchmark for cosmic ray interactions with the Moon. *J. Geophys. Res. Planets* 111:E06004. doi: 10.1029/2005JE002551

Nesterenok, A., and Naidenov, V. (2012). *In situ* formation of cosmogenic ^{14}c by cosmic ray nucleons in polar ice. *Nucl. Instr. Methods Phys. Res. Sect. B Beam Interact. Mater. Atoms* 270, 12–18. doi: 10.1016/j.nimb.2011.09.026

Niita, K. (2002). QMD and JAM calculations for high energy nucleon-nucleus collisions. *J. Nucl. Sci. Technol.* 39, 714–719. doi: 10.1080/00223131.2002.10875198

Qu, W., Bogena, H., Huisman, J., Schmidt, M., Kunkel, R., Weuthen, A., et al. (2016). The integrated water balance and soil data set of the rollesbroich hydrological observatory. *Earth Syst. Sci. Data* 8, 517–529. doi: 10.5194/essd-8-517-2016

Rivera Villarreyes, C., Baroni, G., and Oswald, S. (2011). Integral quantification of seasonal soil moisture changes in farmland by cosmic-ray neutrons. *Hydrol. Earth Syst. Sci.* 15, 3843–3859. doi: 10.5194/hess-15-3843-2011

Robinson, D., Campbell, C., Hopmans, J., Hornbuckle, B., Jones, S., Knight, R., et al. (2008). Soil moisture measurement for ecological and hydrological watershed-scale observatories: a review. *Vadose Zone J.* 7, 358–389. doi: 10.2136/vzj2007.0143

Rosolem, R., Shuttleworth, W., Zreda, M., Franz, T., Zeng, X., and Kurc, S. (2013). The effect of atmospheric water vapor on neutron count in the cosmic-ray soil moisture observing system. *J. Hydrometeorol.* 14, 1659–1671. doi: 10.1175/JHM-D-12-0120.1

Sato, T. (2015). Analytical model for estimating terrestrial cosmic ray fluxes nearly anytime and anywhere in the world: extension of PARMA/EXPACS. *PLoS ONE* 10:e0144679. doi: 10.1371/journal.pone.0144679

Sato, T. (2016). Analytical model for estimating the zenith angle dependence of terrestrial cosmic ray fluxes. *PLoS ONE* 11:e0160390. doi: 10.1371/journal.pone.0160390

Sato, T., and Niita, K. (2006). Analytical functions to predict cosmic-ray neutron spectra in the atmosphere. *Radiat. Res.* 166, 544–555. doi: 10.1667/RR0610.1

Sato, T., Yasuda, H., Niita, K., Endo, A., and Sihver, L. (2008). Development of PARMA: PHITS-based analytical radiation model in the atmosphere. *Radiat. Res.* 170, 244–259. doi: 10.1667/RR1094.1

Schattan, P., Baroni, G., Oswald, S., Schöber, J., Fey, C., Kormann, C., et al. (2017). Continuous monitoring of snowpack dynamics in alpine terrain by aboveground neutron sensing. *Water Resour. Res.* 53, 3615–3634. doi: 10.1002/2016WR020234

Schattan, P., Köhli, M., Schrön, M., Baroni, G., and Oswald, S. (2019). Sensing area-average snow water equivalent with cosmic-ray neutrons: the influence of fractional snow cover. *Water Resour. Res.* 55, 10796–10812. doi: 10.1029/2019WR025647

Schrön, M., Köhli, M., Scheiffele, L., Iwema, J., Bogena, H., Lv, L., et al. (2017). Improving calibration and validation of cosmic-ray neutron sensors in the light of spatial sensitivity. *Hydrol. Earth Syst. Sci.* 21, 5009–5030. doi: 10.5194/hess-21-5009-2017

Schrön, M., Rosolem, R., Köhli, M., Piussi, L., Schröter, I., Iwema, J., et al. (2018). Cosmic-ray neutron rover surveys of field soil moisture and the influence of roads. *Water Resour. Res.* 54, 6441–6459. doi: 10.1029/2017WR021719

Shibata, K., Iwamoto, O., Nakagawa, T., Iwamoto, N., Ichihara, A., Kunieda, S., et al. (2011). JENDL-4.0: a new library for nuclear science and engineering. *J. Nucl. Sci. Technol.* 48, 1–30. doi: 10.1080/18811248.2011.9711675

Shuttleworth, J., Rosolem, R., Zreda, M., and Franz, T. (2013). The COsmic-ray Soil Moisture Interaction Code (COSMIC) for use in data assimilation. *Hydrol. Earth Syst. Sci.* 17, 3205–3217. doi: 10.5194/hess-17-3205-2013

Sigouin, M., and Si, B. (2016). Calibration of a non-invasive cosmic-ray probe for wide area snow water equivalent measurement. *Cryosphere* 10, 1181–1190. doi: 10.5194/tc-10-1181-2016

Tian, Z., Li, Z., Liu, G., Li, B., and Ren, T. (2016). Soil water content determination with cosmic-ray neutron sensor: correcting aboveground hydrogen effects with thermal/fast neutron ratio. *J. Hydrol.* 540, 923–933. doi: 10.1016/j.jhydrol.2016.07.004

Vereecken, H., Huisman, J., Bogena, H., Vanderborght, J., Vrugt, J., and Hopmans, J. (2008). On the value of soil moisture measurements in vadose zone hydrology: a review. *Water Resour. Res.* 44:W00D06. doi: 10.1029/2008WR006829

Watanabe, Y., Kosako, K., Kunieda, S., Chiba, S., Fujimoto, R., Harada, H., et al. (2011). Status of JENDL high energy file. *J. Korean Phys. Soc.* 59, 1040–1045. doi: 10.3938/jkps.59.1040

Waters, L., McKinney, G., Durkee, J., Fensin, M., Hendricks, J., James, M., et al. (2007). The MCNPX Monte Carlo radiation transport code. *AIP Conf. Proc.* 896, 81–90. doi: 10.1063/1.2720459

Weimar, J., Köhli, M., Budach, C., and Schmidt, U. (2020). Large-scale boron-lined neutron detection systems as a ^{3}He alternative for cosmic ray neutron sensing. *Front. Water* 2:16. doi: 10.3389/frwa.2020.00016

Werner, C., Bull, J., Solomon, C., Brown, F., McKinney, G., Rising, M., et al. (2018). *MCNP Version 6.2 Release Notes*. Technical report, Los Alamos National Lab. (LANL), Los Alamos, NM, United States.

Zreda, M., Desilets, D., Ferré, T., and Scott, R. (2008). Measuring soil moisture content non-invasively at intermediate spatial scale using cosmic-ray neutrons. *Geophys. Res. Lett.* 35:L21402. doi: 10.1029/2008GL035655

Zreda, M., Shuttleworth, W., Zeng, X., Zweck, C., Desilets, D., Franz, T., et al. (2012). COSMOS: The COsmic-ray Soil Moisture Observing System. *Hydrol. Earth Syst. Sci.* 16, 4079–4099. doi: 10.5194/hess-16-4079-2012

Conflict of Interest: The authors declare that the research was conducted in the absence of any commercial or financial relationships that could be construed as a potential conflict of interest.

The reviewer AG declared a past co-authorship with the authors MK and MS to the handling editor.

APPENDIX

The results for the χ^2 minimization of the simulated data sets using (15) are presented in the following **Table A1**. Simulations for the parameter sets relied on soil with a bulk density of $\rho_{bd}^{sim} = 1.43\,g/cm^3$. In order to rescale UTS to different local bulk densities ρ_{bd}^{loc} it is necessary to convert soil moisture to $\theta^{loc} = \theta \cdot \rho_{bd}^{sim}/\rho_{bd}^{loc}$ and use θ^{loc} instead.

TABLE A1 | Parameter sets p_i for the UTS-equation (15) fitted to simulation results.

Set	p_0	p_1	p_2	p_3	p_4	p_5	p_6	p_7
1: MCNP drf (full)	1.0940	0.0280	0.254	3.537	0.139	−0.00140	−0.0088	0.0001150
2: MCNP THL (full)	1.2650	0.0259	0.135	1.237	0.063	−0.00021	−0.0117	0.0001200
3: URANOS drf	1.0240	0.0226	0.207	1.625	0.235	−0.00290	−0.0093	0.0000740
4: URANOS THL	1.2230	0.0185	0.142	2.568	0.155	−0.00047	−0.0119	0.0000920

The simulated setups are: (1) MCNP6 and a detector response function, (2) MCNP and energy window thresholds, (3) URANOS and a detector response function, (4) URANOS and energy window thresholds. The latter being defined as 1 eV to 10 keV and the response function is taken from Köhli et al. (2018).

Advantages of publishing in Frontiers

OPEN ACCESS
Articles are free to read for greatest visibility and readership

FAST PUBLICATION
Around 90 days from submission to decision

HIGH QUALITY PEER-REVIEW
Rigorous, collaborative, and constructive peer-review

TRANSPARENT PEER-REVIEW
Editors and reviewers acknowledged by name on published articles

Frontiers
Avenue du Tribunal-Fédéral 34
1005 Lausanne | Switzerland

Visit us: www.frontiersin.org
Contact us: frontiersin.org/about/contact

REPRODUCIBILITY OF RESEARCH
Support open data and methods to enhance research reproducibility

DIGITAL PUBLISHING
Articles designed for optimal readership across devices

FOLLOW US
@frontiersin

IMPACT METRICS
Advanced article metrics track visibility across digital media

EXTENSIVE PROMOTION
Marketing and promotion of impactful research

LOOP RESEARCH NETWORK
Our network increases your article's readership